

Dissertation
submitted to the
Combined Faculty of Mathematics, Engineering and Natural Sciences
of Heidelberg University, Germany
for the degree of
Doctor of Natural Sciences

Put forward by
B.Sc. Weiyu Zhang

born in: Taiyuan, China

Oral examination: 30-04-2025

Time-Resolved Fragmentation of Methane in Strong Laser Fields

Referees: Prof. Dr. Thomas Pfeifer (Priv.-Doz. Dr. Robert Moshhammer)
Priv.-Doz. Dr. Wolfgang Quint

This work is licensed under a Creative Commons
“Attribution-NonCommercial-NoDerivs 3.0 Unported”
license.



Abstract

The ionization and dissociation dynamics of methane (CH_4) in strong laser fields are studied in a series of near-infrared (NIR) pump-probe experiments with a Reaction Microscope (ReMi) [1].

Upon few-cycle strong NIR pump pulses, methane is ionized to different cationic states and undergoes the Jahn-Teller distortions, leading to multiple dissociation pathways. A time-delayed NIR probe pulse then induces Coulomb explosion (CE), leading to the rapid dissociation of the molecule into two or three fragments. In CE, the initial internuclear distances can be determined by measuring the final kinetic energy release (KER). Combined with the angular distribution of the fragments, four distinct fragmentation processes are identified and analyzed. Through the time-resolved study of methane photofragmentation, ‘molecular movies’ are reconstructed, enabling the investigation of the ultrafast molecular rearrangement dynamics.

In two-body fragmentation, atomic hydrogen dissociates from methane as either neutral hydrogen (H^0) or a proton (H^+), each exhibiting distinct angular emission characteristics. Comparing features observed in atomic and molecular hydrogen dissociation provides insight into molecular structural dynamics.

Moreover, while molecular hydrogen is observed as a product in two-body fragmentation, it can also act as an intermediate species, contributing to the three-body dissociation channel ($\text{CH}_4 \rightarrow \text{CH}_2^+ + \text{H}^+ + \text{H}^+$). Finally, the unexpected detection of H_3^+ raises fundamental questions regarding its formation mechanism under strong-field conditions, suggesting new directions for future research.

Zusammenfassung

Die Ionisations- und Dissoziationsdynamik von Methan, CH_4 , in starken Laserfeldern wird in einer Reihe von nahinfraroten (NIR) Pump-Probe-Experimenten mit einem Reaktionsmikroskop (ReMi) untersucht [1].

Durch starke NIR-Pumpulse mit wenigen Zyklen wird Methan in verschiedene kationische Zustände ionisiert und erfährt Jahn-Teller-Verzerrungen, die zu mehreren Dissoziationspfaden führen. Ein zeitverzögerter NIR-Probepuls induziert eine Coulomb-Explosion (CE), die zur raschen Dissoziation des Moleküls in zwei oder drei Fragmente führt. Bei der CE können die anfänglichen internuklearen Abstände durch die Messung der endgültigen Freisetzung kinetischer Energie (engl. Kinetic Energy Release, KER) bestimmt werden. In Kombination mit der Winkelverteilung der Fragmente werden vier verschiedene Fragmentierungsprozesse identifiziert und analysiert. Durch die zeitaufgelöste Untersuchung der Methan-Photofragmentierung wird ein „molekularer Film“ rekonstruiert, der die Untersuchung ultraschneller molekularer Umlagerungsdynamiken ermöglicht.

Bei der Zweikörperfragmentierung dissoziiert atomarer Wasserstoff aus Methan entweder als neutrales Wasserstoffatom (H^0) oder als Proton (H^+), wobei beide unterschiedliche Charakteristiken hinsichtlich ihrer Winkelverteilung aufweisen. Der Vergleich der Dissoziationsmerkmale von atomarem und molekularem Wasserstoff liefert Einblicke in die molekulare Struktur- und Dynamik.

Darüber hinaus wird molekularer Wasserstoff zwar als Produkt der Zweikörperfragmentierung beobachtet, kann aber auch als Zwischenzustand zum Dreikörperdissoziationskanal beitragen ($\text{CH}_4 \rightarrow \text{CH}_2^+ + \text{H}^+ + \text{H}^+$). Schließlich wirft der unerwartete Nachweis von H_3^+ grundlegende Fragen zu seinem Bildungsmechanismus in starken Laserfeldern auf und deutet auf neue Richtungen für zukünftige Forschung hin.

Contents

Abstract	vii
Zusammenfassung	ix
Contents	xi
1 Introduction	1
2 Molecules in Strong Laser Fields	7
2.1 Theoretical Background	7
2.1.1 Born-Oppenheimer Approximation and Jahn-Teller Effect	7
2.1.2 Franck-Condon Principle	9
2.2 Molecular Imaging	9
2.2.1 Coulomb Explosion Imaging	10
2.2.2 Coulomb Explosion Imaging with Hydrogen	10
2.3 CH_4 Molecule and CH_4^+ Cation	11
2.3.1 Symmetry	11
2.3.2 Studies of the Jahn-Teller Effect in Methane Cations	15
2.3.3 The Fragmentation Studies of Methane	16
2.4 The H_2 Molecule	16
2.4.1 Floquet Picture	16
2.4.2 Bond Softening and Bond Hardening	17
2.4.3 Sequential Dissociation, Charge Resonance Enhanced Ionization and Non-Sequential Dissociation	18
3 Pulse Shaping	21
3.1 Pulse Generation and Propagation	21
3.1.1 Mathematical Description of Laser Fields	21
3.1.2 Kerr Effect	22
3.1.3 Pulse Propagation and Dispersion	23

3.1.4	Femtosecond Laser System	24
3.2	Laser Pulse Shaping	27
3.2.1	Spectral Pulse Shaping with SLM	27
3.2.2	‘4f’ Fourier Plane Setup	28
3.2.3	Phase and Amplitude Modulation	31
3.2.4	Calibration Process	32
3.3	Software Realization of Phase Control	34
3.3.1	Phase Modulation Function	35
3.3.2	Phase-controlled Program	36
3.4	Pulse Characterization	37
3.4.1	Autocorrelation Measurements	38
3.4.2	Combination of SLM with Auto-Correlation Measurement	39
3.4.3	Pulse Characterization with a Reaction Microscope	40
4	Reaction Microscope	43
4.1	Working Principle	43
4.1.1	Vacuum System and Supersonic Gas Jet	45
4.1.2	Time and Position Sensitive Detectors and Spectrometer	46
4.2	Data Acquisition and Data Analysis	49
4.2.1	Data Acquisition	49
4.2.2	Momentum Reconstruction	49
4.2.3	Coincidence Measurement	52
5	Atomic and Molecular Hydrogen Ejection from Two-body Fragmentation of CH_4^+	59
5.1	Identification of Possible Fragments	60
5.2	Comparison between Neutral Hydrogen and Proton Ejection	61
5.2.1	Characterization of Fragmentation Pathways from Single Pulse Measurement	62
5.2.2	Time-dependent Proton Ejection	66
5.3	H_2^+ Formation from CH_4^+ Dissociative Ionization	70
5.3.1	Characterization of Fragmentation Pathways from Single Pulse Measurement	71
5.3.2	Time-dependent Molecular Hydrogen Ejection	73
5.4	Comparison: Proton Ejection vs Molecular Hydrogen Formation	76
5.5	Summary of this Chapter	80

6	Three-Body Fragmentation of CH₄	83
6.1	Separating Fragmentation Pathways Using Two-Proton Energy Correlation	83
6.1.1	Pathway Separation	86
6.2	Concerted Fragmentation	90
6.3	Sequential Fragmentation through Hydrogen Release	93
6.4	Sequential Fragmentation through Molecular Hydrogen Release	99
6.5	Connections between Different Pathways	105
6.6	Simulation	108
6.6.1	Simulation Methods	108
6.6.2	Simulation Results	110
6.7	Conclusion	118
7	H₃⁺ Formation from CH₄ Photodissociation	119
7.1	Experimental H ₃ ⁺ Observations	120
7.2	Time-independent Channel	121
7.3	Time-dependent Channel	125
8	Summary and Outlook	127
A	Coincident Channel of CH⁺ + H₂⁺ + H⁺	131
B	Experiments with Horizontally Polarized Pulses	133
B.1	Single-pulse Measurement	133
B.1.1	Hydrogen Emission	133
B.1.2	Molecular Hydrogen Emission	135
B.2	Pump-Probe Measurements: Comparison of Atomic Hydrogen and Molecular Hydrogen Emission	136
B.3	Three Body Coincidence	141
B.3.1	Energy Correlation between Two H ⁺	141
B.3.2	Characteristics of the Four Pathways	141
B.4	The Formation of H ₃ ⁺	144
C	SLM Alignment Procedure	145
C.1	Alignment with Optics	145
C.2	Grating Alignment	146
C.3	SLM Installation	147
C.4	Fine-Tuning and Final Verification	147
C.4.1	Optical Methods	147
C.4.2	Dispersion Measurement	147

C.4.3	Alignment Examination with the Reaction Microscope	149
D	Supplemented classical simulations	151
D.1	Region 1	152
D.2	Region 2	155
	Bibliography	157
	Acknowledgements	171

Chapter 1

Introduction

In the 5th century BC, Leucippus and his student Democritus proposed that matter is composed of small, indivisible particles, which they named atoms [2]. Over the following centuries, atomic theory evolved as a philosophical concept, but it remained without experimental validation. It was not until 1803 that Dalton [3] introduced a scientific atomic theory, providing evidence for the existence of atoms and establishing them as the fundamental building blocks of matter. Nearly a century later, in 1904, J.J. Thomson [4], introduced the Plum Pudding Model, in which negative and positive charges are distributed uniformly across the atom. However, in 1911, Ernest Rutherford's gold foil scattering experiment [5] disproved the Plum Pudding model. Instead, he revealed that electrons orbit a tiny, dense, positively charged nucleus. A major shortcoming of the Rutherford model was that classically the atom could not be stable. Since the electron is an accelerating charge, it should continuously lose energy through radiation and eventually crash into the nucleus. Only with the advent of quantum mechanics, a viable model finally emerged. Bohr developed a semi-classical model [6], which explained the discrete energy spectra of hydrogen atomic radiation. However, it relied on assumptions, such as electrons following fixed orbits, which were later shown to be incorrect. Modern physics has since extended the exploration of microscopic particles to include leptons, quarks, gluons, and others [7]. This long history reveals how challenging it is to achieve even incremental progress in expanding our understanding of the atomic world, but also how fascinating and rewarding the topic is for humanity's curiosity and technological progress.

Through the long journey of scientific investigation, major achievements in our understanding of the micro-cosmos of nature were made possible by the development of groundbreaking techniques. In the case of atomic physics, one such development was the invention of the laser [8, 9]. Its subsequent developments have found widespread application across various fields [10].

Among the advancements in laser technology, significant progress has been made over

the past decades towards high-power, ultra-short pulse generation. The Nobel Prize in 2018 was awarded to Donna Strickland and Gérard Mourou for their invention of chirped pulse amplification (CPA) techniques [11], which enables the generation of femtosecond pulses (fs, $1 \text{ fs} = 10^{-15} \text{ s}$) with high peak intensity in laboratory setups, such as the Ti:Sapphire crystal femtosecond lasers employed in this thesis. The development of laser techniques has significantly enhanced the ability to resolve molecular motions in chemical reactions both in space and in time, including bond formation and bond breaking [12]. For pioneering this field, now known as ‘femtochemistry’, Ahmed Zewail was awarded the Nobel Prize in 1999 [13].

Besides its applications in chemistry, lasers have played a crucial role in advancing fundamental studies of atoms and molecules. With the advent of strong laser fields, extensive investigations into ionization mechanisms have been conducted. Among them, the ‘three-step’ model [14, 15] has been adapted to explain the motion of electrons in intense laser fields. In parallel with this model, the high-harmonic generation (HHG) process [16, 17] was observed, ultimately enabling the generation of attosecond (as, $1 \text{ as} = 10^{-18} \text{ s}$) pulses [18]. This breakthrough has created new opportunities to resolve the even faster motion of electrons in matter [19]. In recognition of their pioneering experimental contributions to this field, Pierre Agostini, Ferenc Krausz, and Anne L’Huillier were awarded the 2023 Nobel Prize in Physics [20]. Furthermore, several free-electron laser facilities, such as FLASH and EuXFEL in Hamburg, have been constructed and are now operational worldwide, providing high-power lasers in the X-ray regime. With these sources, the temporal resolutions for a ‘molecular movie’ have been significantly improved, as reviewed by Linda Young *et al.* [21] and Ueda *et al.* [22].

Imaging techniques have also developed rapidly and were equally important as lasers in advancing our understanding of atoms and molecules. By combining knowledge from collision physics, the invention of the ‘Reaction Microscope’ [23] has enabled coincidence measurements between multiple particles with complete momentum reconstruction. Similarly, Velocity Mapping Imaging (VMI) [24] facilitates fast detection of electron and ion velocity distributions. A series of experimental studies have been conducted using these advanced detection systems [25] [26] [27].

By combining well-established techniques with theoretical models, molecular dynamics can be explored at a deeper level. Over the past few decades, extensive studies have focused on the simplest molecular systems, H_2 . Under strong laser fields, H_2 exhibits rich phenomena such as bond softening [28], bond hardening [29], above-threshold ionization [30], and electron localization [31]. Significant progress has also been made with other molecules, including tomographic imaging of molecular N_2 [32], structural studies of CF_3I using diffraction techniques [33], and ring-opening dynamics [34]. Additionally, advancements have

extended to protein imaging, offering new insights into complex biological structures [22].

During light-matter interaction, molecular structural distortion can be triggered by electronic excitation, ionization, and photofragmentation. These distortions occur when a non-linear molecule reaches a degenerate electronic state, a phenomenon known as the Jahn-Teller effect [35], which will be introduced in **Chapter 2**. As one of the simplest nonlinear molecules, methane serves as an ideal system for studying the Jahn-Teller effect in its cation [36–38].

Due to the Jahn-Teller distortion, the methane cation cannot remain stable in its tetrahedral T_d geometry but instead reaches different configurations. With different geometries, methane cation undergoes different fragmentation processes. The main goal of this thesis is to resolve the different fragmentation dynamics of methane under strong laser fields with the Coulomb explosion imaging (CEI) technique, which will also be introduced in **Chapter 2**.

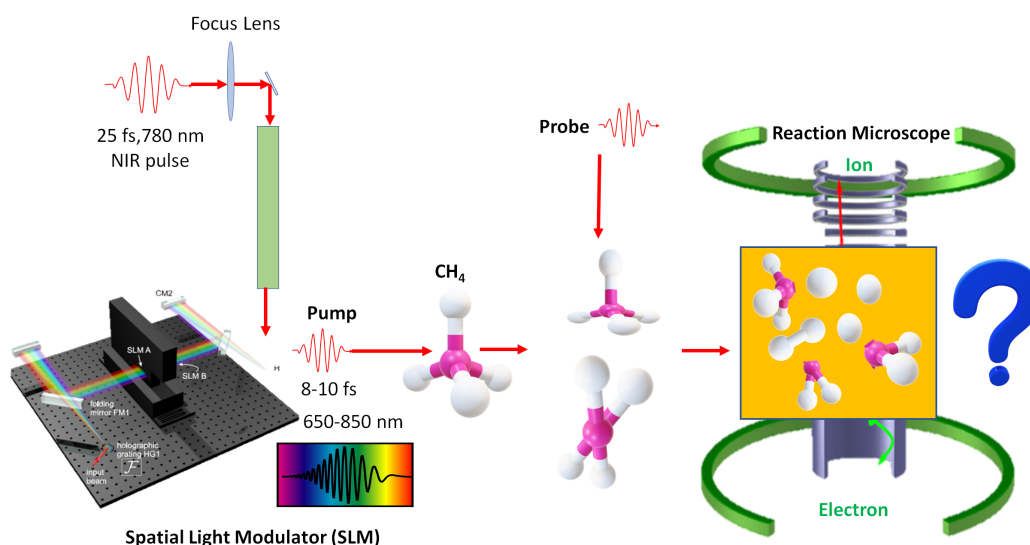


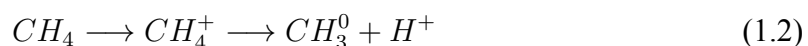
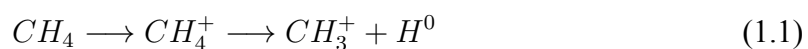
Figure 1.1. Illustration of the experimental setup: A commercial Ti:Sapphire laser system generates 25-fs NIR pulses. The spectrum is broadened by passing through a hollow-core fiber filled with noble gases. The broadband pulses are then sent to the SLM for pulse shaping. The SLM compresses the pulses to 10 fs and generates two pulses with controllable time delays, serving as pump and probe pulses separately. Finally, the laser pulses interact with the target gas, and the resulting ionic fragments are collected in the Reaction Microscope. In this thesis, methane is used as the target gas. The first (pump) pulse ionizes it into different ionic states, leading to structural rearrangements. A time-delayed probe pulse further ionizes the methane cation, resulting in multiple fragmentation pathways that produce distinct fragments for analysis. The SLM picture is taken from [39].

In this thesis, multiple fragmentation pathways are investigated through time-resolved pump-probe experiments on methane, conducted using lab-based near-infrared (NIR, 780 nm) pulses with a duration of 8–10 fs. A spatial light modulator (SLM) was employed to compress and shape the few-cycle laser pulses. At a peak intensity of 3×10^{14} W/cm², different ionization, and dissociation pathways emerge in methane molecules. A Reaction Microscope was used to detect the full momentum of all resulting ions coincidentally, providing detailed insights into the fragmentation dynamics. This experimental setup as shown in Fig. 1.1 ensures long-term stability and enables the acquisition of high-quality, well-resolved data with robust statistics. This setup facilitates detailed analysis of time-resolved three-ion coincidence measurements, advancing our understanding of molecular dynamics on top of previous studies. The setup of SLM and the reaction microscope will be introduced in **chapter 3** and **chapter 4** separately.

In methane’s photon-dissociative ionization process, two or three fragments are produced in coincidence. These ion fragments originate from multiple dissociation pathways, encoding information about molecular structural dynamics. This makes methane an ideal prototype for studying complex molecular breakups triggered by strong-field ionization, where multiple dissociation pathways happen simultaneously. Three distinct fragmentation dynamics are explored in Chapters 5 to 7, separately.

Fragmentation Processes (I) and (II): Atomic and Molecular Hydrogen Ejection from Two-body Fragmentation of CH₄⁺

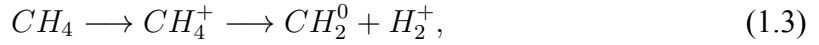
As the simplest fragment, hydrogen can dissociate through two different pathways:



In these processes, molecular rearrangement and Jahn-Teller-induced geometric distortions are imprinted in the motion of the emitted neutral hydrogen and proton.

From single-pulse measurements, neutral hydrogen (H^0) and charged hydrogen (the proton, H^+) exhibit distinct angular distributions: H^0 is emitted isotropically, while the proton is predominantly emitted along the laser polarization axis. Furthermore, the branching ratio between these two pathways indicates that the H^0 channel, measured in coincidence with CH_3^+ , is the dominant fragmentation pathway. This distinction in angular distribution allows for the differentiation between the two pathways in a pump-probe scheme, where the channels are mixed. Additionally, by examining the time-dependent angular distributions and yield variations, it is observed that the H^0 dissociation channel is suppressed at short time delays in the pump-probe experiment.

Furthermore, the second reaction outcome, ejection of molecular hydrogen, is conceptually comparable to the first one, therefore they are grouped within the same chapter. Similar angular dependencies are observed for neutral (H_2^0) and charged (H_2^+) molecular hydrogen from the following pathways:



Time-resolved detection of H_2^+ has revealed that carbon-hydrogen bond breaking in methane and subsequent bond formation between two hydrogen atoms occur within 10 fs.

By mapping atomic hydrogen dissociation and molecular hydrogen formation to the Jahn-Teller (JT)-induced structural evolution, we gain insights into how the NIR field modifies the molecular potential energy surface and facilitates coupling between electronic and nuclear dynamics through the JT effect.

Chapter 5 provides a detailed discussion of how these processes are observed in experiments.

Fragmentation Process (III): Three-body fragmentation of methane

In parallel to these two-body fragmentation processes, the time-resolved three-body fragmentation channel of $CH_2^+ + H^+ + H^+$ is detected. This channel is mixed by four distinct pathways, resulting from different intermediate charge states (x), which can be summarized as follows:



Among these processes, two concerted pathways are directly coming from CH_4^{3+} , and two sequential pathways are passing through methane cation CH_4^+ . Moreover, different stretching modes of CH_4^+ lead to these two distinct sequential dissociation channels. The one with a symmetric stretching mode (C_{2v} geometry) of CH_4^+ leads to H_2 formation. Two protons detected from this pathway exhibit typical features of strong-field ionization in H_2 , such as charge resonance-enhanced ionization (CREI) [40]. The presence of CREI provides insights into bond-formation timescales and the influence of laser intensity on molecular dynamics.

All features of these channels are presented in **Chapter 6**, supported by both experimental observations and classical calculations.

Fragmentation Process (IV): H_3^+ formation from methane photodissociation

Furthermore, the H_3^+ formation is observed in the photodissociation in parallel to the dissociation pathways mentioned above as:



Both time-independent and time-dependent dissociation channels are identified in **Chapter 7**. For the time-independent H_3^+ channel, the roaming mechanism of molecular H_2 is introduced. However, determining the roaming mechanism requires further evidence from both experimental observations and theoretical calculations. For the time-dependent H_3^+ channel, there is not yet a clear explanation. The unexpected observation of H_3^+ formation raises questions and opens new avenues for future research.

Chapter 8 concludes this comprehensive study on methane fragmentation, enabled by the combination of intense few-cycle NIR pump-probe pulses and a Reaction Microscope (ReMi). Additionally, it provides an outlook on simulations and further experiments that could complement and support the findings of this thesis.

Atomic units (a.u.) are used throughout this thesis.

Chapter 2

Molecules in Strong Laser Fields

This chapter introduces the basic theoretical background for understanding the concept of the Jahn-Teller effect.

To bridge theoretical concepts with practical applications, this section discusses current progress in molecular imaging, with a particular emphasis on the Coulomb Explosion Imaging (CEI) technique employed in this thesis. CEI provides great insights into the study of molecular structure and dynamics [41] [25].

Methane and its cation are introduced in terms of their symmetry and the corresponding Jahn-Teller effect. Relevant background studies on methane are also presented. Finally, the typical characteristics of H_2 in strong laser fields are introduced, serving as a basis for the discussions in Chapter 6, where H_2 appears as a fragment resulting from methane dissociation.

2.1 Theoretical Background

Potential energy surfaces are essential for understanding molecular dynamics. Computing them at a more accurate level is challenging due to the computation resource limitation and the complexity of molecular states. Born-Oppenheimer approximation is the foundation for potential energy surface calculations [42]. However, several non-adiabatic effects cannot be resolved within the basic approximation. The Jahn-Teller effect, for example, is one of those cases beyond the Born-Oppenheimer approximation, which arises due to the coupling between many electronic states and the nuclear motion in molecules.

2.1.1 Born-Oppenheimer Approximation and Jahn-Teller Effect

In the 1920s, the Born-Oppenheimer approximation [42] was introduced to simplify the description of molecular dynamics by treating nuclear motion and electronic motion sepa-

rately. In the time-independent Schrödinger equation, the Hamiltonian can be written as:

$$H(\vec{r}, \vec{R}) = T_n(\vec{R}) + T_e(\vec{r}) + V_n(\vec{R}) + V_e(\vec{r}) + V_{ne}(\vec{r}, \vec{R}) \quad (2.1)$$

where $\vec{r} = \{\vec{r}_i\}$ stands for all electron coordinates, and $\vec{R} = \{\vec{R}_i\}$ stands for all nuclear coordinates. $T_n(\vec{R})$ and $T_e(\vec{r})$ represent the kinetic energy of the nuclei and electrons, respectively. $V_n(\vec{R})$ and $V_e(\vec{r})$ are the potential energy terms for the nuclei and electrons at a fixed nuclear position \vec{R}_0 , and $V_{ne}(\vec{r}, \vec{R})$ is the interaction between the nuclei and electrons.

By separating the Hamiltonian into two parts and neglecting the interaction term $V_{ne}(r, R)$, the wave function can be expressed as:

$$\psi(\vec{r}, \vec{R}) = \psi_{\text{electron}}(\vec{r}; \vec{R}) \cdot \chi_{\text{nuclear}}(\vec{R}) \quad (2.2)$$

where ψ_{electron} is the electronic wave function with its eigen energy \mathcal{E}_i , dependent on both the electronic coordinates \vec{r} and the nuclear coordinates \vec{R} , and χ_{nuclear} is the nuclear wave function, dependent only on the nuclear coordinates \vec{R} .

The basis of this approximation is that nuclei are at least 1836 times heavier than electrons, resulting in electron motion being significantly faster than nuclear motion. This allows electrons to adjust to their new configuration almost instantaneously, relative to nuclear motion. Thus, the potential is calculated assuming fixed nuclear coordinates.

Back to equation (2.1), when the nuclei position deviates from \vec{R}_0 , the potential $V_{ne}(\vec{r}, \vec{R})$ between the nuclei and electrons can be Taylor-expanded around the nuclear coordinate \vec{R}_0 :

$$\tilde{V}(\vec{r}, \vec{R}) = \sum_{k=0}^{\infty} \frac{1}{k!} \sum_{i=1}^{3N-6} \left(\frac{\partial^k \tilde{V}}{\partial R_i^k} \right)_0 (R_i - R_0)^k \quad (2.3)$$

Rewriting the Schrödinger equation for nuclear motion using the diabatic electronic wavefunction $\psi_i(r)$, beyond the Born-Oppenheimer approximation (where Equation (2.2) is not satisfied), yields:

$$[\tilde{H}_n + \mathcal{E}_i(\vec{R}) + W_{ii}(\vec{R})]\chi_i(\vec{R}) + \sum_{i \neq j} W_{ij}\chi_j(\vec{R}) = E\chi_i(\vec{R}) \quad (2.4)$$

$$W(\vec{r}, \vec{R}) = v(\vec{r}, \vec{R}) - v(\vec{r}, \vec{R}_0) \quad (2.5)$$

Here, $W(\vec{r}, \vec{R})$ describes the coupling between vibrational states. The Born-Oppenheimer approximation is a special case of this equation when the coupling term $W(\vec{r}, \vec{R})$ becomes zero. Considering nuclear motion, this term cannot be neglected. Thus the Schrödinger equation (2.4) exhibits coupling between the electron and nuclei wavefunctions.

This non-negligible coupling happens in different scenarios: when nuclei are highly excited and move rapidly, or when electronic states become degenerate. The latter one leads to the **Jahn-Teller effect**.

In 1937 and 1938, the theorem of Jahn and Teller [43] [44] states the following:

“A configuration of a polyatomic molecule for an electronic state having an orbital degeneracy cannot be stable with respect to all displacements of the nuclei unless, in the original configuration, the nuclei all lie on a straight line.”

In an electronically degenerate molecule influenced by the Jahn-Teller (JT) effect, the non-linear molecule undergoes a series of distortions to reduce its symmetry and reach the potential energy minimum. Once the stabilization energy becomes comparable to the vibrational energies, the molecule evolves along several equivalent vibrational modes to reach the potential minima. During this process, different vibrational modes can be exchanged through tunneling [35].

The JT effect can be seen as a special case of conical intersections, where electronic states intersect in nuclear coordinate space. With the Taylor expansion of the potential at a reference geometry, Jahn-teller theory is also applied to non-adiabatic potential surface calculations [45].

The JT effect plays an essential role in solid-state physics and chemistry [46–48]. With various molecular geometries or different point groups, the JT effect has been studied intensively [35].

In Section 2.3, the JT effect of methane cations will be introduced.

2.1.2 Franck-Condon Principle

A set of vibrational states belongs to every given electronic state. During a photon absorption or emission process, similar to the Born-Oppenheimer approximation, the electronic transition happens faster than the vibrational transition. As a result, the electronic transition can be represented as a vertical line in the potential-energy diagram, independent of the nuclear distance [49]. This approximation is called the Franck-Condon principle. The Franck-Condon factor quantifies the transition probability by calculating the overlap between the vibrational wavefunctions of the initial and final electronic states.

2.2 Molecular Imaging

Over the past decades, advancements in imaging, vacuum, electronics, and laser techniques have been developed and integrated, enabling the imaging of individual atoms with sub-Ångström[Å] resolution and the resolution of atomic and molecular dynamics on timescales of a few femtoseconds or even attoseconds [21] [22].

Using laboratory-based few-cycle femtosecond pulses, vibrational wavepackets in H_2 molecules have been measured with a Reaction Microscope [50]. Progress in X-ray diffraction has further enabled the capturing of snapshots of complex molecules [51]. With differ-

ent laser pulses or electron pulses, many molecular processes have been studied, including chiral molecules [52], ring-opening reactions [34], hydrogen migration [53], etc. Additionally, the range of target systems has expanded beyond the gas phase to include liquids [54], solids [55], clusters [56], nanodroplets [57], etc. Today, the concept of a ‘molecular movie’ has evolved into an achievable reality [58].

2.2.1 Coulomb Explosion Imaging

In this thesis, one of the advanced techniques, known as ‘Coulomb Explosion Imaging’ (CEI) [41], is employed. CEI begins by introducing an external field to ionize the system, such as strong laser pulses, or electron collisions, resulting in multiple charges and very fast dissociation. Under electrostatic repulsion, these charged fragments repel each other instantaneously. The inter-nuclear distances between them can be determined by measuring their final momenta. Combined with the angular distribution of the fragments, the molecular structure can be reconstructed. By applying CEI to pump-probe measurements, the evolution of molecular geometry can be visualized as a function of time [41], creating the so-called molecular ‘movie’.

The limitation of CEI happens when molecules often fragment partially, rather than all atoms being ionized and repelling each other. Consequently, there is no guarantee that instantaneous Coulomb explosion is the only process responsible for the detected fragments. Post-ionization effects, such as delayed-dissociative ionization or the metastable ionic states, can also contribute. These post-dynamics can distort the molecular geometry, meaning the detected momenta may not accurately reflect the true nuclear distances immediately after the ionizing pump pulse. Furthermore, the ability to detect all charged particles coincidentally is constrained by the efficiency of the detector. In this sense, higher intensity pulses increase the chance of full ionization, and higher efficiency detectors and good reconstruction strategies help with detection [59].

2.2.2 Coulomb Explosion Imaging with Hydrogen

Hydrogen is critical in encoding key information about molecular dynamics since it is the most common component of molecules and the lightest atom. Consequently, the task of creating a ‘molecular movie’ is often focused on observing hydrogen motion.

Combining CEI with a reaction microscope, Till Jahnke *et al.* [25] revealed molecular rearrangement processes by employing the emitted proton as a messenger. X. Li *et al.* [59] investigated the nuclear wavepacket dynamics of iodomethane, with a five-ion coincidence measurement. Wang *et al.* [53] compared proton transfer and electron transfer pathways in ethanol dications. Chelsea E. Liekhus-Schmaltz, *et al.* [60] has recorded the acetylene

isomerization process with deuterons.

2.3 CH₄ Molecule and CH₄⁺ Cation

Methane is the target molecule in this thesis. With an ionization potential of (12.61 ± 0.01) eV [61] and a photon energy of 1.57 eV from the laser used in this thesis, neutral CH₄ must absorb at least eight photons to ionize to CH₄⁺.

To study the dynamical processes of CH₄⁺, it is essential to understand its molecular geometry and electronic structure. Before delving into methane, a brief introduction to molecular symmetry and the necessary notations used in the subsequent chapters is provided. In addition, the relevant studies on methane are introduced.

2.3.1 Symmetry

The concept of symmetry is defined through specific transformation operations, such as rotations, reflections, and inversions. In this context, point groups consist of symmetry operations that leave a molecule unchanged before and after the operation.

Symmetry Operations

- **identity E**: The operation that leaves the system unchanged. It can be represented as a unit matrix.
- **n-fold rotation C_n**: The system is rotated around a certain axis by $360 \text{ deg}/n$. The principle axis is referred to as the axis with the largest n in the molecule. The rotation matrix in the xy-plane for a C_n operation is:

$$\begin{pmatrix} \cos\left(\frac{2\pi}{n}\right) & \sin\left(\frac{2\pi}{n}\right) & 0 \\ -\sin\left(\frac{2\pi}{n}\right) & \cos\left(\frac{2\pi}{n}\right) & 0 \\ 0 & 0 & 1 \end{pmatrix} \begin{pmatrix} x \\ y \\ z \end{pmatrix} = \begin{pmatrix} x' \\ y' \\ z' \end{pmatrix}$$

- **reflection/mirror plane σ** : Reflects all points across the defined mirror plane (here, x-y plane), and can be described as:

$$\begin{pmatrix} 1 & 0 & 0 \\ 0 & 1 & 0 \\ 0 & 0 & -1 \end{pmatrix} \begin{pmatrix} x \\ y \\ z \end{pmatrix} = \begin{pmatrix} x' \\ y' \\ z' \end{pmatrix}$$

- **inversions i**: Referred to as the opposite action. Each coordinate (x, y, z) is inverted through the center of the molecule, resulting in: $(x, y, z) \rightarrow (-x, -y, -z)$

- **improper rotation S_n**: A combination of rotation and reflection, meaning a rotation by 360 deg / *n* and then a reflection with the plane perpendicular to the rotation axis.

The translation matrix is:

$$\begin{pmatrix} \cos\left(\frac{2\pi}{n}\right) & \sin\left(\frac{2\pi}{n}\right) & 0 \\ -\sin\left(\frac{2\pi}{n}\right) & \cos\left(\frac{2\pi}{n}\right) & 0 \\ 0 & 0 & -1 \end{pmatrix} \begin{pmatrix} x \\ y \\ z \end{pmatrix} = \begin{pmatrix} x' \\ y' \\ z' \end{pmatrix}$$

Point Groups

Here two examples of common point groups are listed.

- *C_n*: *C_n* means the group with *n*-fold axis.
C_{nv}: On top of an *n*-fold axis, the molecule has a vertical mirror plane *σ_v*.
- *D_n*: *D_n* is referred to as a molecule that owns an *n*-fold symmetry axis with *n* axis perpendicular to *C_n*.

Irreducible Representations, Character Table

Irreducible representation describes how vibrational modes or orbitals transform under the symmetry operations of the molecule's point group, often denoted with *A₁*, *A₂*, *B₁*, *B₂*, etc.

For example, a character table 2.1 for the *C_{2v}* (which is the potential-energy minimum for methane cation) point group is:

Symmetry Operations	E	C ₂	σ _v (xy)	σ _v ' (xz)
A₁	1	1	1	1
A₂	1	-1	1	-1
B₁	1	1	-1	-1
B₂	1	-1	-1	1

Table 2.1. Character table for the point group *C_{2v}*.

Symmetry of CH₄

Methane consists of a central carbon atom bonded to four identical hydrogen atoms in a tetrahedral geometry of *T_d*. According to hybridization theory, the electronic structure of carbon is *1s²2s²2p²*, with two unpaired *2p* electrons, namely *2p_x* and *2p_y*, which can accept two external electrons from other atoms to form a molecule. However, experimentally, methane is observed to be able to bind with four external electrons. This is explained by

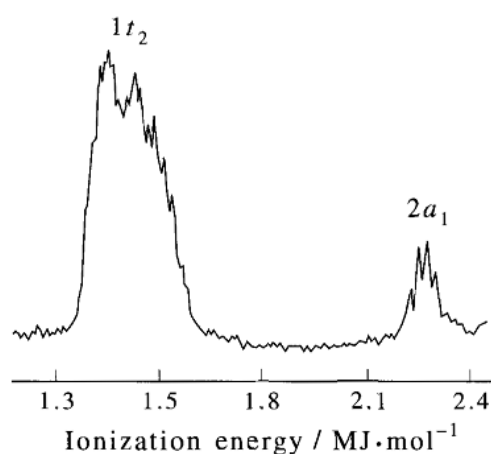


Figure 2.1. Photoelectron spectrum of methane. The two distinct peaks are coming from separate $2a_1$ and $1t_2$ orbitals, corresponding to energy values around 14 eV and 22 eV. The broadened spectrum comes from different vibrational states. The figure is taken from [62], p388.

the excitation of one $2s$ electron to the empty $2p_z$ orbital through perturbation, resulting in one unpaired $2s$ electron and three unpaired $2p$ electrons. These orbitals combine to form four equivalent sp^3 hybrid orbitals. In methane, the four $1s$ electrons from hydrogen bond with the four sp^3 hybrid orbitals of carbon. While sp^3 hybridization explains the tetrahedral geometry of methane, it does not agree with the valence electron ionization spectrum observed by McQuarrie and Simon [62], p. 388, where two distinct energy levels for the valence electrons are detected as shown in Fig. 2.1. In molecular orbital theory, this problem is solved by considering the phase of orbitals during their combination, as described by the linear combination of atomic orbitals (LCAO). Depending on the phase, different types of bonds can form. In the case of methane, two kinds of molecular orbitals are created, namely $2a_1$ and $1t_2$ as shown in Fig. 2.2. The $2a_1$ orbital forms when the hydrogen $1s$ orbitals interact with the carbon $2s$ electrons, resulting in a spherical bonding orbital with an ionization energy of 22.8 eV. In contrast, the $1t_2$ orbital forms when the hydrogen $1s$ orbitals interact with the carbon $2p$ electrons, creating a degenerate p-like bonding orbital with an ionization energy of 14.0 eV [63].

Symmetry of CH₄⁺

When methane gets ionized from the $1t_2$ and $2a_1$ orbitals, the cation is noted as the X ground state $(1t_2)^{-1}$ and the A excited state $(2a_1)^{-1}$ respectively. Due to the degeneracy of the $1t_2$ orbital, the X-state cation undergoes a rapid Jahn-Teller distortion process. This geometry

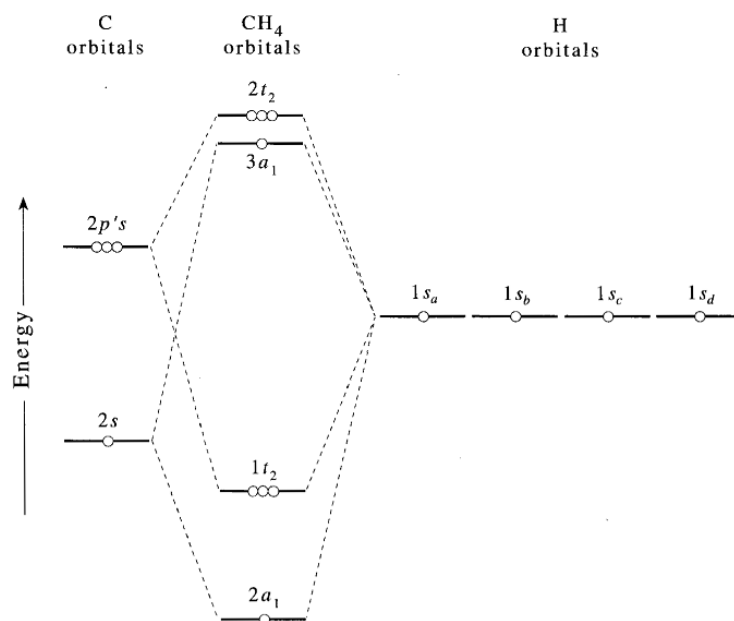


Figure 2.2. Molecular-orbital energy level diagram for methane valence electrons. The $2a_1$ and $1t_2$ are occupied. The figure is taken from [62], p388.

distortion destroys the T_d symmetry of neutral methane. Subsequently, the molecule can undergo geometries with C_{3v} , C_{2v} , or D_{2d} symmetry, as illustrated in Fig. 2.3.

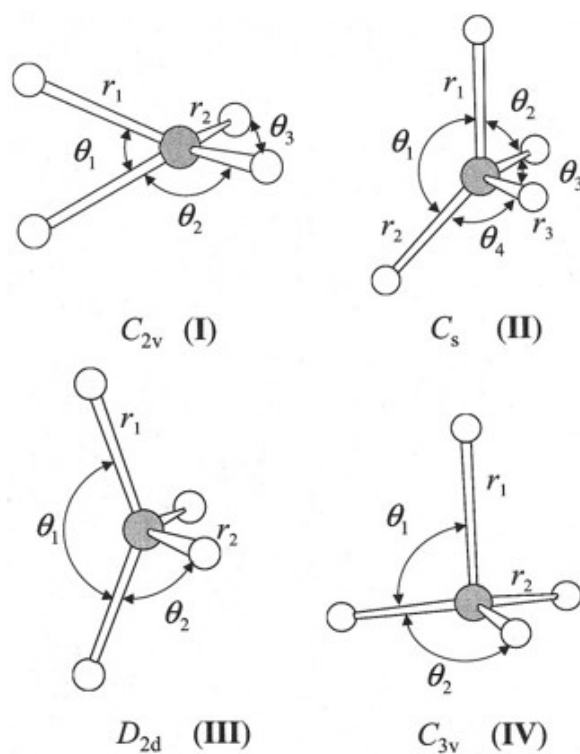


Figure 2.3. Calculated equilibrium geometry for CH₄⁺ with different symmetry as noted under the corresponding representation. The figure is taken from [64].

In a triply degenerate $(1t_2)^{-1} X$ ground state, two kinds of vibrational modes are active, one is called e -mode with double degeneracy and another is the f -mode with triple degeneracy. Along these vibrational modes, CH₄⁺ reach different geometry of C_{3v} , C_{2v} , or D_{2d} as mentioned above. One example of how the distortion process happens to reach a potential minimum is shown in Fig. 2.4, which is studied by H. Wörner et. al in [35].

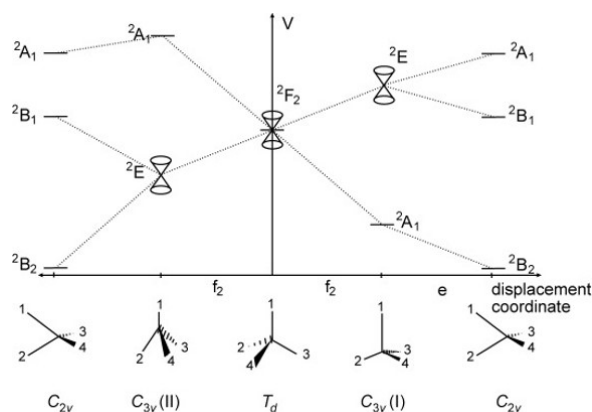


Figure 2.4. Schematics of the JT effect evolution in methane cation, taken from [35]. The vertical axis represents the potential energy, and the horizontal axis shows nuclei displacement.

2.3.2 Studies of the Jahn-Teller Effect in Methane Cations

Starting from the last century, the Jahn-Teller effect in methane cations has been studied extensively, both experimentally and theoretically [36] [37]. There has been considerable discussion about the geometry distortion caused by the non-adiabatic effect, with several vibrationally excited states being reached due to this effect [38], which has triggered significant interest.

In recent years, with rapid advancements in the field, many more accurate studies have been conducted on the Jahn-Teller effect in methane cations. A study by F. Remacle's group in 2021 [65] theoretically demonstrated that, upon ionization by XUV pulses, the methane cation undergoes a Jahn-Teller-driven distortion from its T_d geometry to a D_{2d} configuration within a few femtoseconds, followed by further rearrangement to a C_{2v} geometry. Another experimental study, conducted in 2021 by Li's group [66], showed that methane cations dissociate into different products as they pass through a conical intersection on the potential surface. By identifying and extracting the fragment time dynamics, they estimated the evolution time from the C_{3v} geometry to the C_{2v} geometry to be approximately 20 ± 7 fs. Leone's group, in 2023 [67], demonstrated that methane cations, starting from the T_d ground state, undergo Jahn-Teller distortion to reach the C_{2v} minimum within (10 ± 2) fs. This process is followed by 60 fs coherent oscillations in vibrational modes, notably in the asymmetric

scissoring mode.

2.3.3 The Fragmentation Studies of Methane

The fragmentation channels of methane are widely discussed within different experiments. With methane dications, Auger electrons are measured in coincidence with photodissociated ions in [68]. Collision induced by Ar^{9+} ions on neutral methane has revealed the internal energies carried by the sequential fragments [69]. In addition, collision-induced H_3^+ is observed in B. Wei's group [70]. Various experimental observations have been explored for different fragmentation pathways of methane [71] [72] [73] [74].

2.4 The H_2 Molecule

H_2 is a fragmentation product of the methane cation and one of the most well-studied molecular systems [75]. Here, a brief overview of studies on H_2 is presented.

2.4.1 Floquet Picture

The Floquet picture is used to describe systems under periodic driving, such as the modification of molecular potential energy curves by a strong laser field (10^{13} W/cm²) [76] [77]. By introducing a periodic electric field, the dipole interaction term $V(t) = -\mathbf{D} \cdot \mathbf{E}(t)$ is incorporated into the Hamiltonian (where \mathbf{D} is the molecular dipole moment, and $\mathbf{E}(t)$ represents the electric field of the laser field). After diagonalizing the potential matrix, the system's potential splits into a series of quasi-energy levels separated by the photon energy $h\omega$. For $1s\sigma_g$ (potential is noted as $V_g(R)$) and $2p\sigma_u$ ($V_u(R)$) states of H_2^+ , the potential matrix for single photon interaction is:

$$V(R) = \begin{bmatrix} V_g(R) + \hbar\omega & V_{gu}(R) \\ V_{gu}(R) & V_u(R) \end{bmatrix} \quad (2.6)$$

$V_{gu}(R)$ are the coupling term between two curves through the laser field. The eigenvalues are:

$$E_{\pm}(R) = \frac{V_g(R) + V_u(R) + \hbar\omega}{2} \pm \frac{1}{2} \sqrt{[V_g(R) - V_u(R) + \hbar\omega]^2 + [4V_{gu}(R)]^2} \quad (2.7)$$

Compared to the original molecular potential, the coupling with the laser field can modify the potential energy curves, leading to avoided crossings, conical intersections, and other phenomena.

2.4.2 Bond Softening and Bond Hardening

Using the Floquet picture, the calculated H_2^+ $1s\sigma_g$ and $2p\sigma_u$ potential curves under different laser field couplings are presented in Fig. 2.5.

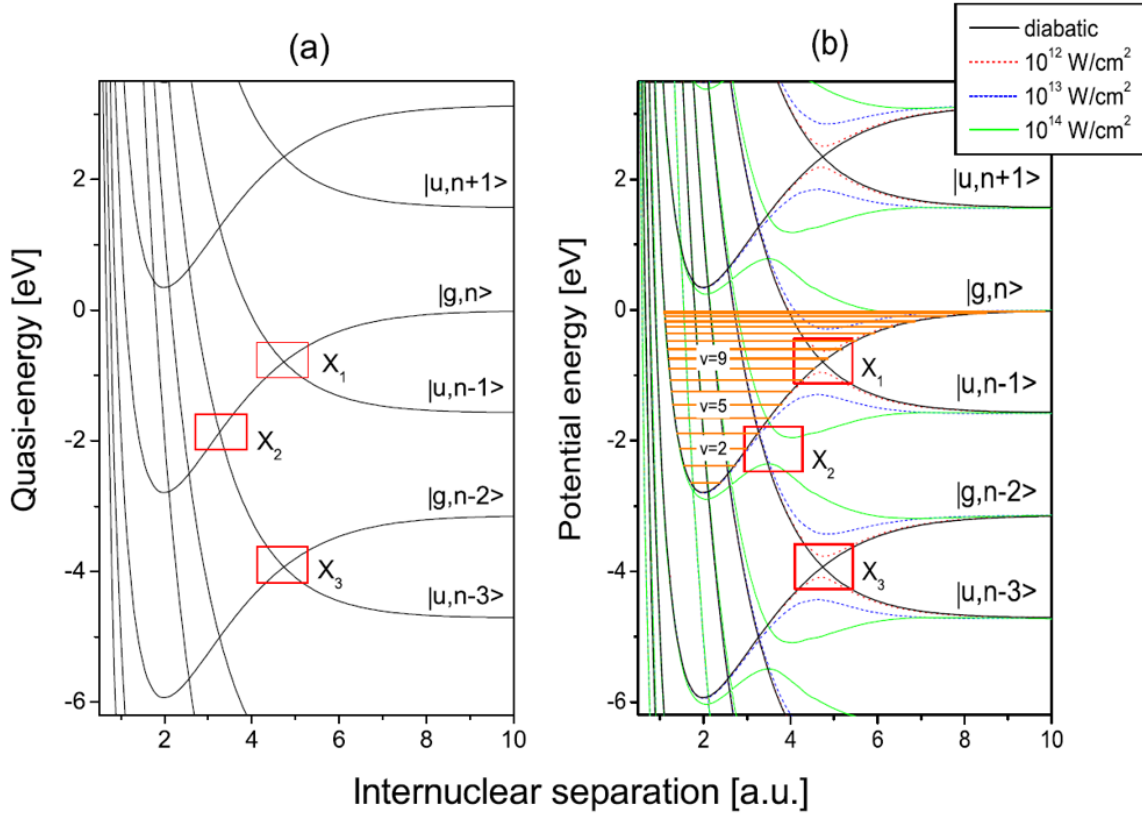


Figure 2.5. Calculated H_2^+ electronic states potential curves in the Floquet picture. X_1 , X_2 , and X_3 are marked for curve-crossing. (a) The $1s\sigma_g$ and $2p\sigma_u$ potential curves are dressed by $n = 1, 2, 3, \dots$ photons. (b) At different laser intensities, adiabatic potential curves in green are modified due to the coupling of $1s\sigma_g$ and $2p\sigma_u$ states. The figure is taken from [78].

The coupling term $V_{gu}(R)$ depends on the laser intensity and polarization, expressed as:

$$V_{gu}(R) = -\frac{1}{2}E(t)D(R)\cos\theta(t), \quad (2.8)$$

where $E(t)$ is the electric field, $D(R)$ is the transition dipole moment, and $\theta(t)$ is the angle between the molecular axis and the laser field.

As shown in Fig. 2.5, with increasing laser intensity (around 10^{13} W/cm²), more crossings and openings occur. Some originally bound vibrational levels can dissociate as the openings increase, a phenomenon known as **bond softening** [28]. The bound states above the E_+ curve are stabilized by curve bending, referred to as **bond hardening** [29]. At this trapping point, if the laser intensity suddenly decreases, the molecule can dissociate by transitioning to the $1s\sigma_g$ curve. Conversely, if the laser intensity increases, the potential is lifted, allowing the vibrational states to dissociate with nearly zero energy.

When the laser intensity reaches about 10^{14} W/cm², the vibrational states at $|u, n - 3\rangle$ follow the potential curve until they reach the crossing with $|g, n - 2\rangle$. At this point, the molecule can transition to $|g, n - 2\rangle$ by emitting a photon. The complete process is then a two-photon process. During the process, the molecules absorb more photons than the ionization potential needed, which is referred to as **above threshold dissociation** [79] [80].

2.4.3 Sequential Dissociation, Charge Resonance Enhanced Ionization and Non-Sequential Dissociation

Several well-studied mechanisms lead to molecular hydrogen dissociation [27], as shown in Fig. 2.6. These serve as a reference for comparison with molecular hydrogen dissociated from methane.

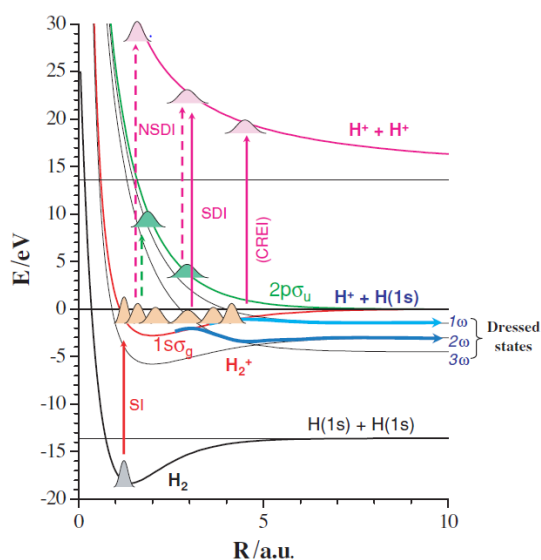


Figure 2.6. Schematics of H_2 dissociative ionization in 800 nm NIR field from A. Rudenko [27]. $1s\sigma_g$ and $2p\sigma_u$ dressed states of H_2^+ with $n=1,2,3$ photons. SDI: sequential double ionization; NSDI: non-sequential double ionization; CREI: charge resonance-enhanced ionization.

Charge Resonance-Enhanced Ionization (CREI) [40] refers to the phenomenon where the maximum ionization yield of molecules occurs at a specific internuclear distance. For H_2 , this distance is approximately 3.5 to 7 a.u., depending on the laser intensity. The mechanism is based on the electron being localized between one of the nuclei. Due to dipole interactions, when the molecule is aligned with the electric field, the detected ions exhibit polarization dependence.

In contrast, atomic-like sequential dissociation competes with CREI when the laser pulse duration reaches the few-cycle regime. This process appears without polarization depen-

dence [81].

Additionally, the non-sequential process is dominated by a recollision mechanism, where the laser field drives back the first ionized electron to excite another bound electron, which is subsequently ionized in the second step. The fragments from this process appear with the highest kinetic energy, as it occurs within a single laser cycle [27] [82].

Chapter 3

Pulse Shaping

Commercial Titanium:Sapphire (Ti:Sa) laser systems have become a standard tool for generating femtosecond laser pulses with pulse energies of a few millijoules. These systems have enabled extensive studies of atomic and molecular dynamics [83] [84] [85]. However, directly controlling the temporal pulse shape in the femtosecond regime is challenging due to the limitations of electronic response times.

Spatial light modulators (SLM) enable pulse shaping in the spectral domain [86–88]. This technique significantly expands the possibilities for controlling nonlinear and multi-photon light-matter interaction processes on the femtosecond time scale at high laser intensities exceeding 10^{13} W/cm² [89].

This chapter is structured as follows: Firstly, an overview of femtosecond pulse generation and propagation effects is provided in Section 3.1. In Section 3.2, the experimental methodology for realizing femtosecond laser pulse shaping with the spatial light modulator (SLM) is presented. The software realization of phase control is briefly discussed in Section 3.3. Finally, in Section 3.4, the pulse characterization methods and results are presented.

3.1 Pulse Generation and Propagation

3.1.1 Mathematical Description of Laser Fields

The electric field of a linearly polarized laser pulse in the temporal domain $\tilde{E}(t)$ can be written as:

$$\tilde{E}(t) = \tilde{E}_0(t) \cdot e^{-i\phi(t)} \quad (3.1)$$

$\tilde{E}_0(t)$: the complex envelope of the laser field can describe how the laser intensity changes with time. The intensity is given by the squared modulus of the electric field amplitude.

$\phi(t)$: The time-dependent phase, which can be expressed with a Taylor expansion:

$$\phi(t) = \phi_0 + \frac{\partial\phi}{\partial t}t + \frac{1}{2}\frac{\partial^2\phi}{\partial t^2}t^2 + \dots = \phi_0 + \omega_0 t + \psi(t) \quad (3.2)$$

ϕ_0 is the constant phase, called as carrier-envelope phase (CEP), describing the relative shift of the carrier wave to the envelope. ω_0 is the central frequency, and $\psi(t)$ contains higher order terms, leading to the frequency change:

$$\omega(t) = \frac{d\phi(t)}{dt} = \omega_0 + \frac{d\psi(t)}{dt} \quad (3.3)$$

If $\frac{d\psi}{dt} \neq 0$, the instantaneous frequency will change over time, leading to a chirped pulse.

With the Fourier transform, the laser pulses in the frequency domain and time domain can be written respectively as:

$$\tilde{E}(\omega) = \frac{1}{\sqrt{2\pi}} \int_{-\infty}^{\infty} \tilde{E}(t)e^{-i\omega t} dt \longleftrightarrow \tilde{E}(t) = \frac{1}{\sqrt{2\pi}} \int_{-\infty}^{\infty} \tilde{E}(\omega)e^{i\omega t} d\omega \quad (3.4)$$

Furthermore, the complex form of $\tilde{E}(\omega)$ is:

$$\tilde{E}(\omega) = A(\omega)e^{i\phi(\omega)} \quad (3.5)$$

Where $A(\omega)$ is the spectrum amplitude of the electric field in the frequency domain. $\phi(\omega)$ indicates how phase varies across different frequencies. Combining the equation (3.5) and (3.1), the time domain formulae can be expressed with frequency form as:

$$\tilde{E}(t) = \frac{1}{\sqrt{2\pi}} \int_{-\infty}^{\infty} A(\omega)e^{i(\phi(\omega)+\omega t)} d\omega \quad (3.6)$$

One important insight from the formula is that a short pulse in the time domain corresponds to a broad spectrum, and vice versa. This relationship can be understood through the uncertainty principle between time and energy, expressed as $\delta E \cdot \delta t \geq \frac{1}{2}$, where $E = \hbar\omega$. For a given bandwidth spectrum, there is a minimum achievable time duration, referred to as the Fourier-limited pulse:

$$\delta\omega \cdot \delta t \geq \frac{1}{2} \quad (3.7)$$

More generally, any signal function is composed of sine or cosine waves. The sharper or more localized the function is in the time domain, the more oscillatory components are required for its representation through superposition.

3.1.2 Kerr Effect

Since the Fourier limit imposes a constraint on the product of temporal duration and spectral width, achieving shorter pulse durations requires spectral broadening. One approach for broadening the spectrum is based on the optical Kerr effect [90]. This effect describes how

the refractive index $n(t, \omega_0)$ of a material changes in response to the instantaneous intensity of the pulses passing through it.

$$n(t, \omega_0) = n_0(\omega_0) + n_2(\omega_0) \cdot I(t) \quad (3.8)$$

Taking a Gaussian pulse as an example, where $t = 0$ is defined as the moment of maximum peak intensity, the intensity profile of the pulse can be described as:

$$I(t) = I_0 \exp\left(-\frac{t^2}{\tau^2}\right) \quad (3.9)$$

The nonlinear effect leads to self-phase modulation (SPM), where the temporal phase changes by propagation through a fixed distance L :

$$\phi(\omega_0, t) = \frac{2\pi}{\lambda} n_2(\omega_0) I(t) L \quad (3.10)$$

Correspondingly, it introduces an instantaneous frequency shift:

$$\Delta\omega(t) = -\frac{d\phi(t)}{dt} = \frac{4\pi}{\lambda} n_2 L \frac{t}{\tau^2} I_0 e^{-\frac{t^2}{\tau^2}} \quad (3.11)$$

This instantaneous frequency shift (chirp), introduced by self-phase modulation (SPM), broadens the spectrum of the pulse. The leading edge of the pulse experiences a red shift, while the trailing edge experiences a blue shift. This chirping effect is fundamental for generating short pulses.

The Kerr effect not only influences the temporal shape of pulses but also affects their spatial profile. For Gaussian pulses, the intensity is highest at the center, leading to a larger refractive index at the center compared to the edges. This spatially dependent refractive index generates varying focal points for the pulses in space, acting as a lens known as the Kerr lens. This phenomenon is utilized in oscillator cavities to achieve mode-locked pulse generation.

3.1.3 Pulse Propagation and Dispersion

When a laser propagates through a medium, the phenomenon where the refractive index varies with frequency is known as dispersion. The electric field in the frequency domain, propagating along the z -direction, can be expressed as:

$$\tilde{E}(z, \omega) = \int_{-\infty}^{\infty} A(z, \omega) \cdot \exp[i(\omega t - \phi(z, \omega))] d\omega \quad (3.12)$$

The spectral phase, $\phi(z, \omega)$, depends on the properties of the medium through which the pulse propagates and is related to the refractive index via $n(\omega) = \frac{c}{V_p(\omega)}$. By Taylor-expansion:

$$\begin{aligned} \phi(z, \omega) &= \phi(\omega_0) + (\omega - \omega_0) \left. \frac{\partial \phi}{\partial \omega} \right|_{\omega_0} + \frac{1}{2} (\omega - \omega_0)^2 \left. \frac{\partial^2 \phi}{\partial \omega^2} \right|_{\omega_0} + \dots \\ &= \phi(\omega_0) + (\omega - \omega_0) GD + \frac{1}{2} (\omega - \omega_0)^2 GDD + \frac{1}{6} (\omega - \omega_0)^3 TOD \dots \end{aligned} \quad (3.13)$$

Where

$$\phi(\omega_0) = \frac{2\pi n(\omega_0)}{\lambda_0} \cdot L$$

is the constant phase induced by the refractive index n for the central frequency ω_0 , and the higher-order terms correspond to dispersion effects.

- **Group Delay (GD):**

$$GD = \frac{dk}{d\omega}$$

The group delay is induced by the group velocity v_g of the pulse, where $\frac{dn}{d\omega}$ represents the slope of the refractive index n with respect to frequency ω . k is the wave vector.

The group velocity is determined as:

$$v_g = \frac{d\omega}{dk} = \frac{1}{\frac{dn}{d\omega}}$$

- **Group Delay Dispersion (GDD):**

$$GDD = \frac{d^2k}{d\omega^2}$$

Group delay dispersion is caused by different frequencies traveling through a material at different group velocities. Normal dispersion, also called positive chirp, occurs when $GDD > 0$, meaning higher frequency components travels slower than lower frequency components, introducing a temporal broadening of the pulse.

- **Third-Order Dispersion (TOD):**

$$TOD = \frac{d^3k}{d\omega^3}$$

Third-order dispersion becomes significant for ultra-short pulses, where the pulse broadens in more complex ways due to higher-order dispersion effects.

To compensate for the effects of dispersion, optical elements such as prisms, gratings, and chirped mirrors are commonly used in femtosecond laser setups to mitigate pulse broadening.

3.1.4 Femtosecond Laser System

For this work, a commercially available Ti: Sapphire laser system from Femtolasers Company is used, centered at 785 nm, generating 25 fs laser pulses with an energy of 1 millijoule, and operating at a repetition rate of 3 kHz. The system contains three major components as shown in Fig. 3.1: the oscillator, the amplifier and the compressor.

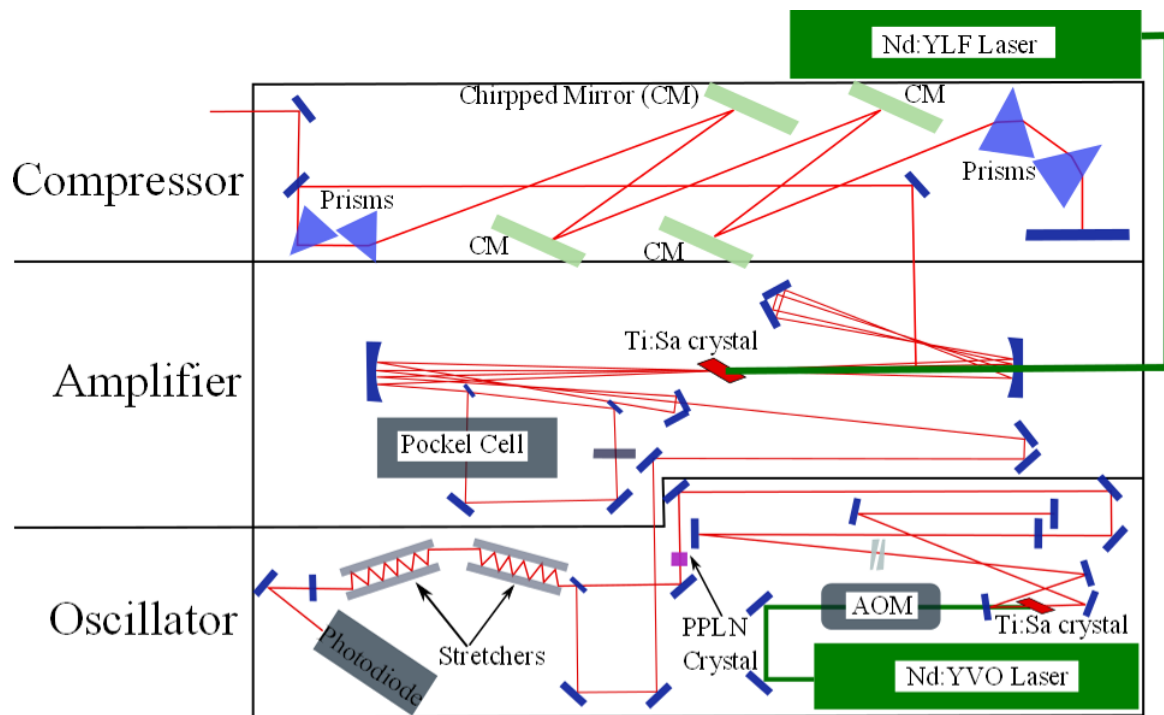


Figure 3.1. Schematic of a femtosecond laser system, adapted from [84]. The three main components are: the oscillator, amplifier, and compressor.

- Oscillator** Pumped by a 3 W Nd: YVO continuous laser at 532 nm, Ti^{3+} ions in the Ti:Sapphire crystal absorb pump photons, which excites them to higher electronic states. These ions then undergo fast non-radiative relaxation, allowing them to populate the upper lasing level. This process creates a population inversion between the upper and lower lasing levels, which is essential for laser operation. Once the population inversion is established, stimulated emission occurs, leading to the emission of laser photons. The Ti^{3+} ions transition from the upper lasing level to the lower lasing level, releasing energy in the form of NIR laser light, typically centered around 785 nm.

Initially, light is emitted in continuous wave (CW) mode, where many longitudinal modes propagate with random, unrelated phases within the cavity defined by the cavity mirrors. When a small external perturbation is manually introduced into the cavity, it causes a slight increase in intensity in a specific region relative to the background. This intensity spike in the crystal triggers the Kerr effect due to its nonlinear properties. The Kerr effect acts as an intensity-dependent iris, allowing the pulses to self-focus within the crystal. As a result, the more intense regions overlap more effectively with the cavity's optical mode, leading to more efficient amplification.

Simultaneously, self-phase modulation (SPM) broadens the spectrum by generating new frequencies. These newly generated frequencies interfere with the existing longitudinal modes, causing their phases to lock with each other. This phase-locking process leads to the generation of ultrashort pulses within the cavity.

The output pulses from the oscillator have a temporal duration of 5-8 fs, with a repetition rate of 80 MHz and a pulse energy of a few nanojoules.

- **Amplifier** The output intensity of pulses from the oscillator is insufficient to ionize atoms and molecules. A common approach to increasing amplification is to pass the pulses through the gain medium—the Ti:Sapphire crystal multiple times. However, further amplification is limited by the damage threshold of the gain medium, which is affected by thermal effects induced by high-intensity lasers. To overcome this, chirped pulse amplification (CPA) [11], a technique awarded the 2018 Nobel Prize, is developed to achieve higher amplification.

The key principle of CPA is to introduce additional chirp thereby stretching the pulse in time. This reduces the peak intensity of the pulses, thereby preventing damage to the crystal while allowing the pulses to be amplified. As shown in Fig. 3.1, a stretcher composed of thick glass elements is used to introduce this chirp dispersion to the pulses before they enter the amplification stage.

In the amplification process, a 532 nm Nd: YLF laser operating at a 3 kHz repetition rate is used to pump the Ti: Sapphire crystal. The beam passes through the Ti: Sapphire crystal nine times to achieve the desired amplification. After the first four passes, a Pockels cell, combined with a polarizer, acts as an optical switch to reduce the pulse repetition rate from 80 MHz to 3 kHz.

- **Compressor** A pair of prisms, and two pairs of chirped mirrors compensate for the dispersion introduced during stretching and amplification stages, reducing the pulse duration to 25 fs, which is close to the Fourier limitation decided by the spectrum bandwidth.

At this stage, a 25-fs pulse duration is achieved with a pulse energy of 1 mJ. To achieve even shorter pulses, the laser spectrum needs to be broadened through self-phase modulation (SPM) with a **hollow-core fiber**.

The output beam from the femtosecond laser system, approximately 1 cm in diameter, is focused into a 1 m-long hollow-core fiber with an inner diameter of 250 μm , filled with argon gas (other rare gases, such as neon, can achieve a similar effect.). As the laser beam propagates through the fiber, nonlinear self-phase modulation leads to spectral broadening. Fig. 3.2 compares the resulting spectra with and without argon gas in the hollow-core fiber.

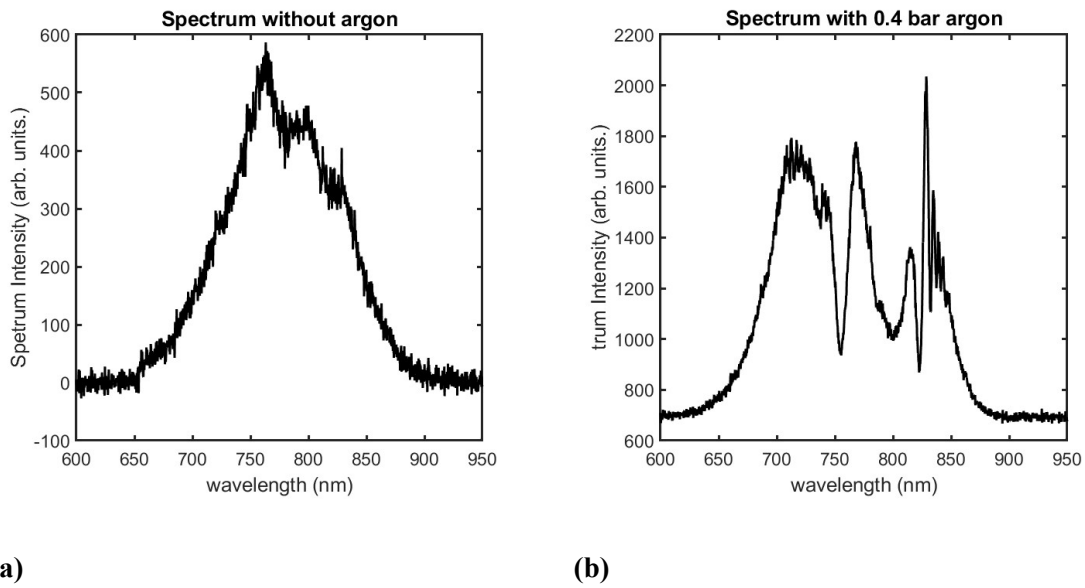


Figure 3.2. Spectrum after the hollow-core fiber. (a) Spectrum without argon gas. (b) Spectrum with 0.4 bar of argon gas.

3.2 Laser Pulse Shaping

Pulse shaping refers to the control of laser pulses in terms of time, frequency, spatial profile, and polarization to achieve desired output characteristics. Several experimental devices have been developed for laser pulse shaping, including acousto-optic modulators (AOMs) [91], deformable mirrors (DMs) [92], and liquid crystal display (LCD)-based spatial light modulators (SLMs) [88].

3.2.1 Spectral Pulse Shaping with SLM

As described in the previous chapter, the temporal shape of laser pulses can be connected to the spectral domain through the Fourier transformation. This gives us a useful way to shape the pulse field regarding its phase, amplitude, and polarization.

Mathematically, the input laser field \tilde{E}_{in} can be modified by a transformation matrix $\tilde{\mathcal{M}}(\omega)$ to get the output shaped pulses \tilde{E}_{out} as: $\tilde{E}_{out} = \tilde{\mathcal{M}}(\omega)\tilde{E}_{in}$. More specifically, the transformation matrix $\tilde{\mathcal{M}}(\omega)$ can be written as:

$$\tilde{\mathcal{M}}(\omega) = |\mathcal{M}(\omega)| \exp[i\phi_{mod}(\omega)] \quad (3.14)$$

Connected with the Fourier transform, applying a modification to the spectral components lead to a shaped pulse in the time domain as:

$$\tilde{E}(t) \xrightarrow{\mathcal{F}} \tilde{E}(\omega)_{in} \xrightarrow{\tilde{\mathcal{M}}(\omega)} \tilde{E}_{in}(\omega) = \tilde{E}_{out} \xrightarrow{\mathcal{F}^{-1}} \tilde{E}(t)_{out} \quad (3.15)$$

If $|\mathcal{M}(\omega)| = 1$ for all frequencies and only the ϕ_{mod} is changing, it is called **spectral phase shaping**. If $|\mathcal{M}(\omega)| < 1$, then the relative spectra amplitude of different frequencies will be changed and thus the temporal profile of pulses will also be changed, which is called **spectral amplitude shaping**. For **polarization shaping**, in reality, is often done by modifying the phase of two orthogonal linear components, which can be described by:

$$\widetilde{\mathcal{M}}(\omega) = \begin{bmatrix} |M|_{xx}(\omega)e^{i\phi_{xx}(\omega)} & |M|_{xy}(\omega)e^{i\phi_{xy}(\omega)} \\ |M|_{yx}(\omega)e^{i\phi_{yx}(\omega)} & |M|_{yy}(\omega)e^{i\phi_{yy}(\omega)} \end{bmatrix} \quad (3.16)$$

3.2.2 ‘4f’ Fourier Plane Setup

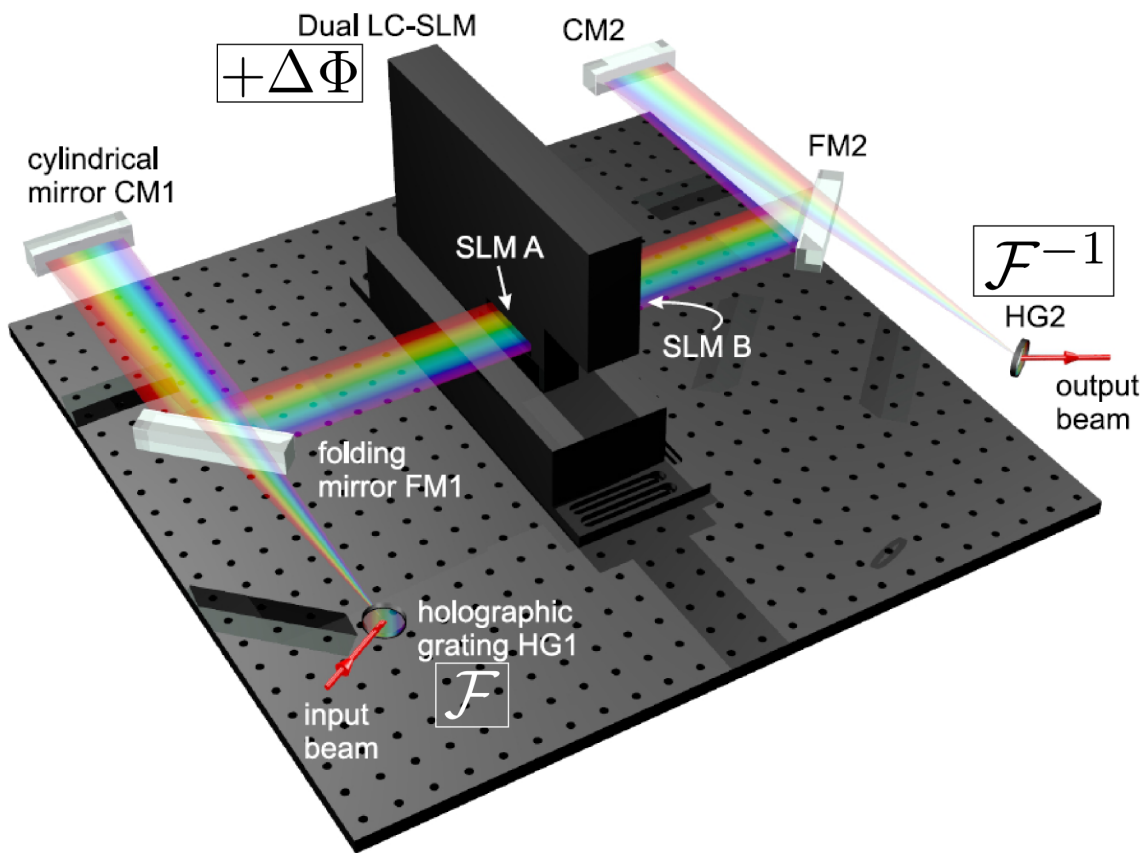


Figure 3.3. Schematic of a zero-dispersion compressor in a reflective 4f setup. This system is designed symmetrically and includes several key components. Two transmission gratings (TG1 and TG2) are used for coupling the beam in and out, while two planar folding mirrors (FM1 and FM2) and two cylindrical mirrors (CM1 and CM2), with focal length f , direct and focus the beam. In the Fourier plane, a two-layer liquid crystal modulator (Dual LC-SLM) serves as the spatial mask, splitting the input pulse into two stages. The pulse first interacts with SLM A and subsequently with SLM B. Between the two transmission gratings, the beam travels a total distance of $4f$. The figure is taken from ref. [39].

Since the 1970s, SLM has been applied to the picosecond regime [93] [94]. As shown

in Fig. 3.3, the technical details of a whole SLM set-up are presented. The input broadband pulses are guided into a holographic transmission grating, different frequency components are then split in space and collimated by a cylindrical mirror CM1. The cylindrical mirror is placed at a distance f which corresponds to the focal length $f = 22.5\text{cm}$. After guiding by a plane folding mirror FM1, all the spectral components are collimated and then focused at the Fourier plane. The liquid crystal display (LCD) placed at the Fourier plane is then adding spectral phases to individual frequency components. The second plane mirror FM2, the cylindrical mirror CM2, and the recombination grating then lead symmetrically to recombine all frequencies to be the output pulses. Considering a perfect alignment with idealized optics, this set-up is dispersion-free. From the complete set-up, the incoming pulses travel four times focal lengths, so this geometry is called the ‘4f’ set-up. The entire setup is referred to as a ‘pulse shaper’.

Holographic Transmission Grating

Volume-phase holographic transmission gratings are utilized in the setup. These gratings are fabricated by exposing a photosensitive material to the interference pattern of two coherent laser beams. Unlike traditional diffraction gratings with periodic surface structures, volume-phase gratings achieve diffraction within the grating’s volume. This is accomplished through a periodic refractive index modulation inside the gelatin or glass material, resulting in an enhanced diffraction efficiency.

Littrow configuration is employed, where the incident angle equals the diffracted angle for the first order. This way, the maximum efficiency of the grating for a specific wavelength can be realized. It satisfies:

$$2a \sin(\alpha) = m\lambda \quad (3.17)$$

m is the diffraction order, λ the wavelength, a the grating spacing, and α the incident/diffraction angle. Here, the grating lines density is $g = 1500$ lines/mm, and the incidence angle is 10.8° .

Liquid Crystal Display

The LCD-based modulator located at the Fourier plane consists of two layers, namely SLM-A and SLM-B, each made up of liquid crystal cells in the nematic phase exhibiting uniaxial birefringence, as illustrated in Fig. 3.4. The optical axis of each liquid crystal cell is naturally aligned along the alignment layer in the x-direction, as depicted in Fig. 3.4. Each layer features a pixel structure composed of 640 electrically isolated, strip-shaped electrodes. By applying external voltage to different pixels px , the liquid crystal molecules within these pixel areas are rotated in the z-direction by an angle $\theta[U(px)]$. The extraordinary refractive index $n_e(\omega, U)$ in both LCDs affects light with polarization aligned parallel to the main

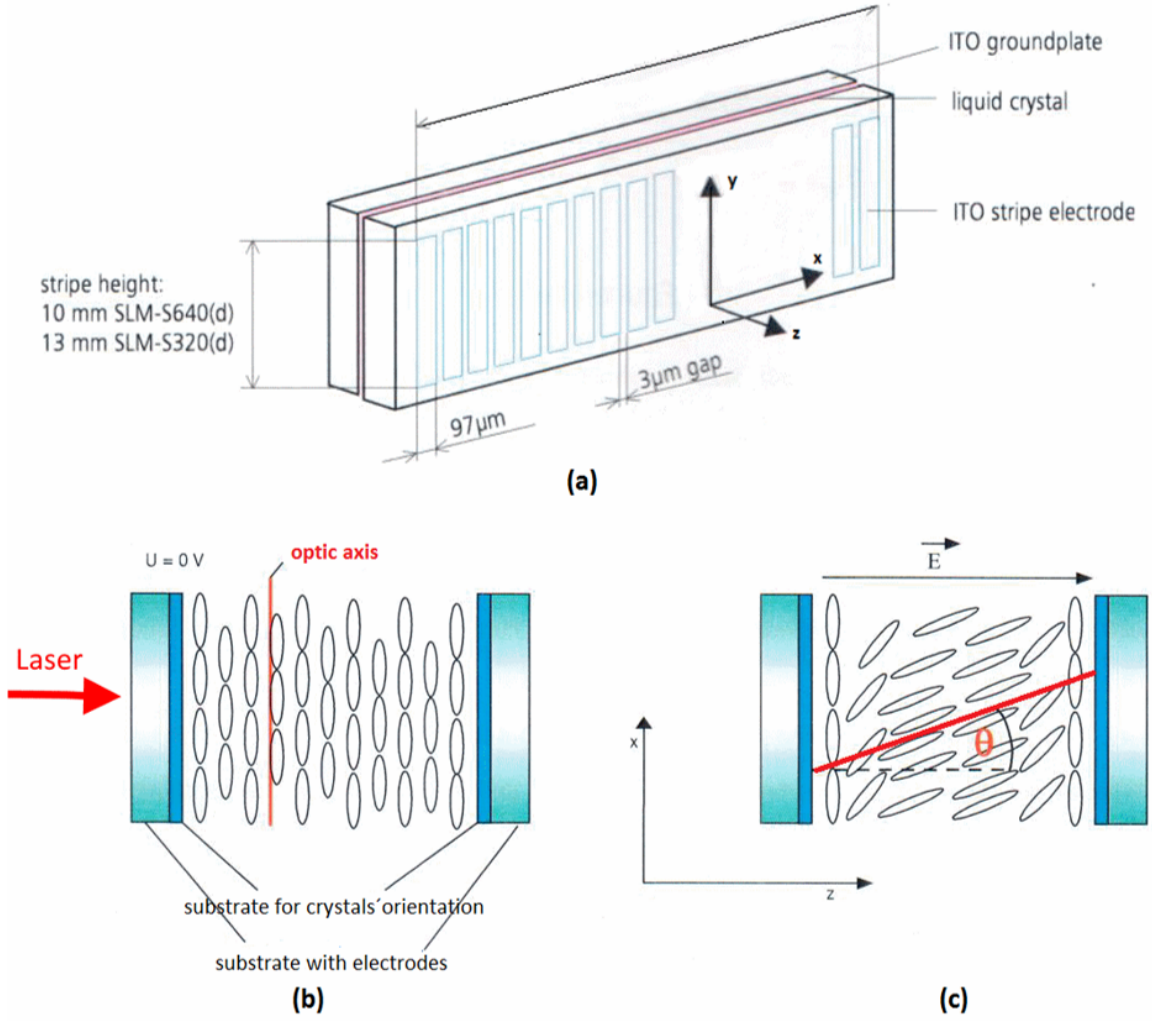


Figure 3.4. Structure of the two-layer liquid crystal display [95]. (a) Schematic of a liquid crystal (LC) cell. The pixel structure of the LCD is achieved through 640 stripe-shaped and electrically separated electrodes. The alignment of the liquid crystal molecules in the nematic phase without external voltages is presented in (b). By applying voltages, the alignment rotates as shown in (c).

section, defined as the plane spanned by the laser propagation direction (z -direction) and the optical axis. In contrast, light polarized perpendicular to this plane retains a constant refractive index $n_o(\omega)$ and remains unaffected by the external voltage:

$$\frac{1}{n(\omega, U)} = \frac{\cos^2 \theta(U)}{n_o^2(\omega)} + \frac{\sin^2 \theta(U)}{n_e^2(\omega)} \quad (3.18)$$

Thus, the modulated phases added to o - or e -ray are:

$$\phi_o = \frac{\omega}{c} [n_o(\omega)] d \quad (3.19)$$

$$\phi_e = \frac{\omega}{c} [n(\omega, \theta(U))] d \quad (3.20)$$

Where d is the thickness of the liquid crystal. The phase difference between the ordinary and extraordinary polarized light is:

$$\Delta(\omega, U) = \phi_e - \phi_o = \frac{\omega}{c} [n(\omega, \theta(U)) - n_o(\omega)] d \quad (3.21)$$

3.2.3 Phase and Amplitude Modulation

The two-layer crystal cells are oriented $\pm 45^\circ$ to the optical table normal. When a linearly p-polarized input pulse $\tilde{\tilde{E}}_{in}(\omega) = \tilde{E}_{in}(\omega) \begin{pmatrix} 1 \\ 0 \end{pmatrix}$ travels through the modulator, it is split into two orthogonal components with equal amplitude. Then, one component is modulated by SLM A with $\phi_A(\omega)$, while the other is modulated solely by SLM B with $\phi_B(\omega)$. The total transformation matrix is then:

$$\begin{aligned} \tilde{\tilde{E}}_{mod}(\omega) &= \begin{bmatrix} \cos(\frac{\pi}{4}) & \sin(\frac{\pi}{4}) \\ -\sin(\frac{\pi}{4}) & \cos(\frac{\pi}{4}) \end{bmatrix} \begin{bmatrix} 1 & 0 \\ 0 & \exp(i\Delta\phi_B(\omega)) \end{bmatrix} \begin{bmatrix} \cos(-\frac{\pi}{4}) & \sin(-\frac{\pi}{4}) \\ -\sin(-\frac{\pi}{4}) & \cos(-\frac{\pi}{4}) \end{bmatrix} \\ &\times \begin{bmatrix} \cos(-\frac{\pi}{4}) & \sin(-\frac{\pi}{4}) \\ -\sin(-\frac{\pi}{4}) & \cos(-\frac{\pi}{4}) \end{bmatrix} \begin{bmatrix} 1 & 0 \\ 0 & \exp(i\Delta\phi_A(\omega)) \end{bmatrix} \begin{bmatrix} \cos(\frac{\pi}{4}) & \sin(\frac{\pi}{4}) \\ -\sin(\frac{\pi}{4}) & \cos(\frac{\pi}{4}) \end{bmatrix} \\ &= \exp \left[i \left(\frac{\Delta\phi_A(\omega) + \Delta\phi_B(\omega)}{2} \right) \right] \begin{bmatrix} \cos \left[\frac{\Delta\phi_A(\omega) - \Delta\phi_B(\omega)}{2} \right] \\ \sin \left[\frac{\Delta\phi_B(\omega) - \Delta\phi_A(\omega)}{2} \right] \exp \left(i \frac{\pi}{2} \right) \end{bmatrix} \cdot \tilde{E}_{in}(\omega) \end{aligned} \quad (3.22)$$

By installing a horizontal polarizer at the output pulse, the combination of amplitude and phase modulation can be realized:

$$\tilde{\tilde{E}}_{mod}(\omega) = \exp \left[i \left(\frac{\Delta\phi_A(\omega) + \Delta\phi_B(\omega)}{2} \right) \right] \cos \left[\frac{\Delta\phi_A(\omega) - \Delta\phi_B(\omega)}{2} \right] \cdot \tilde{E}_{in}(\omega) \begin{bmatrix} 1 \\ 0 \end{bmatrix} \quad (3.23)$$

The modified pulse amplitude is:

$$|\tilde{\tilde{E}}_{mod}(\omega)| = |\tilde{E}_{in}(\omega)| \cos \left[\frac{\Delta\phi_A(\omega) - \Delta\phi_B(\omega)}{2} \right] \quad (3.24)$$

The modified pulse phase is:

$$\phi_{mod}(\omega) = \frac{\Delta\phi_A(\omega) + \Delta\phi_B(\omega)}{2} \quad (3.25)$$

The phases added to two layers are:

$$\Delta\phi_A(\omega) = \phi_{mod}(\omega) + \arccos \left[\frac{|\tilde{\tilde{E}}_{mod}(\omega)|}{|\tilde{E}_{in}(\omega)|} \right] \quad (3.26)$$

$$\Delta\phi_B(\omega) = \phi_{mod}(\omega) - \arccos \left[\frac{|\tilde{\tilde{E}}_{mod}(\omega)|}{|\tilde{E}_{in}(\omega)|} \right] \quad (3.27)$$

In the same way, if a vertical polarizer is installed at the output, the field is then:

$$\begin{aligned} \vec{E}_{mod}(\omega) = & \exp \left[i \left(\frac{\Delta\phi_A(\omega) + \Delta\phi_B(\omega)}{2} \right) \right] \\ & \times i \sin \left[\frac{\Delta\phi_B(\omega) - \Delta\phi_A(\omega)}{2} \right] \cdot \vec{E}_{in}(\omega) \begin{bmatrix} 0 \\ 1 \end{bmatrix} \end{aligned} \quad (3.28)$$

3.2.4 Calibration Process

Phase-Voltage Calibration

Phase modulation is achieved by varying the refractive index, which is controlled by an external voltage. Therefore, it is necessary to determine the relationship between these two:

$$\begin{aligned} \Delta n(\omega, U) &= n(\omega, \theta(U)) - n_0(\omega) \\ &= n_0(\omega) \left(\frac{\frac{n_e(\omega)}{n_0(\omega)}}{\sqrt{1 + \left(\frac{n_e(\omega)}{n_0(\omega)} \right)^2 - 1}} \cos^2(\theta(U)) - 1 \right) \\ &= n_0(\omega) f(U) \end{aligned} \quad (3.29)$$

Here, $f(U)$ describes the relation between the voltage and the phase change $\Delta\phi(U, \omega)$.

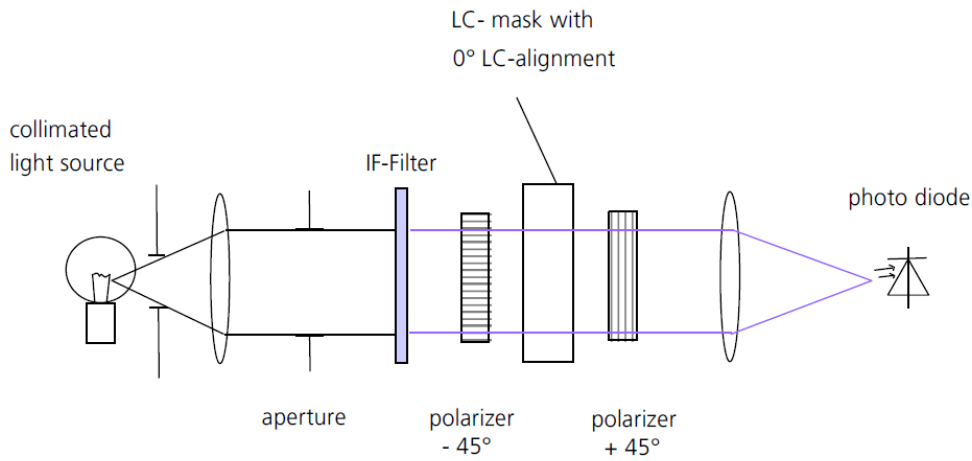


Figure 3.5. The schematic of the setup used to measure the transmission-voltage curves, taken from [95]. Two polarizers, oriented at $\pm 45^\circ$ relative to the table normal, are placed before and after the SLM. The transmitted power of a monochromatic laser (HeNe laser diode) is recorded using a photodiode sensor. The SLM A is positioned to face the incident laser light.

Fig. 3.5 shows the experimental setup to measure the function. T is the transmitted beam power measured by a photo-diode. By varying the voltages U_A and U_B , the transmission

signal changes accordingly:

$$T(U_A, U_B, \omega) = \sin^2 \left(\frac{\Delta\phi_B(U_B) - \Delta\phi_A(U_A)}{2} + k\pi \right), \quad k \in \mathcal{Z} \quad (3.30)$$

During the calibration, for each layer of the liquid crystal modulator, the driving voltage applied to each pixel varies continuously over 4096 points. Two voltage range modes can be selected. A low voltage range corresponds to $U \in [0, 5 \text{ V}]$, while a high voltage range corresponds to $U \in [0, 8 \text{ V}]$. Meanwhile, a constant voltage is applied to all pixels of the other SLM layer.

Based on the measured transmission-voltage curves, the corresponding phase-voltage relationship can be calculated:

$$\Delta\phi_A(U_A, U_{\text{ref}}, \omega_{\text{ref}}) = \Delta\phi_B(U_{\text{ref}}) \pm 2a \sin [T(U, U_{\text{ref}}, \omega_{\text{ref}})] + 2\pi k_A, \quad k_A \in \mathcal{Z} \quad (3.31)$$

$$\Delta\phi_B(U_B, U_{\text{ref}}, \omega_{\text{ref}}) = \Delta\phi_A(U_{\text{ref}}) \pm 2a \sin [T(U, U_{\text{ref}}, \omega_{\text{ref}})] + 2\pi k_B, \quad k_B \in \mathcal{Z} \quad (3.32)$$

The calibration is measured with a specific frequency (HeNe laser with $\lambda_{\text{ref}} = 633 \text{ nm}$). Extending it to other wavelengths as follows:

$$\Delta\phi(U, \lambda) = \Delta\phi(U, \lambda_{\text{ref}}) \frac{\lambda_{\text{ref}}}{\lambda} \frac{\Delta n(\lambda)}{\Delta n(\lambda_{\text{ref}})} \quad (3.33)$$

Fig. 3.6 shows the transmission-voltage and phase-voltage calibration curves for the SLM set-up employed in this thesis, which were carried out by Dr. Stefanie Kerbstadt from the University of Oldenburg.

Pixel-Wavelength Calibration

To achieve precise pulse shaping, an additional calibration is required to map spectral components to individual pixels, known as pixel-wavelength calibration. Based on the geometric relationship derived in [39]:

$$\lambda(px) = d \left\{ \sin(\gamma_{in}) + \sin \left[\arcsin \left(\frac{\lambda_o}{d} + \gamma_{out} \right) \right] - \arctan \left(\frac{px_{center} - px}{f} \Delta_{px} \right) \right\} \quad (3.34)$$

γ_{in} is the incident angle to the grating, γ_{out} the angle exit of the grating. Following the Littrow configuration mentioned in Section 3.2.2, $\gamma_{in} = \gamma_{out}$ is fulfilled. px_{center} is the central pixel which is hit by the central wavelength λ_o . Δ_{px} is the pixel width and $d = 1/g$ [mm] is the grating lines spacing.

In practice, the calibration can be performed by placing two horizontal polarizers (parallel to the table surface) separately before and after the SLM screens, with the input light being p-polarized. A spectrometer is positioned after the second grating to record the spectrum.

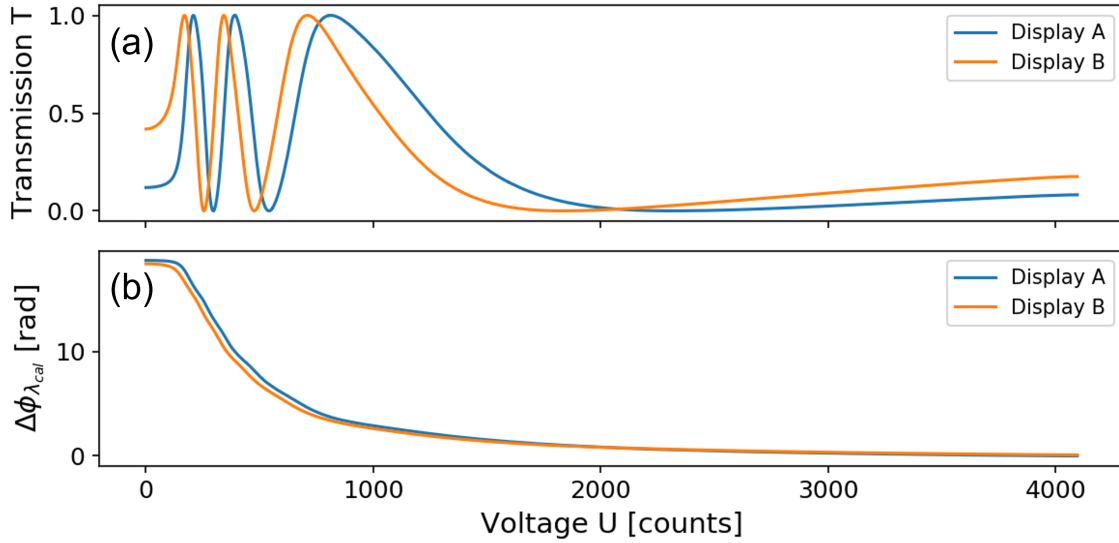


Figure 3.6. Calibration curves taken from ref. [83]. (a) The transmission-voltage calibration curve was measured with a HeNe laser $\lambda_{ref} = 633nm$. (b) The phase-voltage calibration curve.

To achieve calibration, all pixels are initially set to the ‘dark’ state, corresponding to minimum transmission. Then, each of the 640 pixels is activated sequentially, allowing maximum transmission for the selected pixel while keeping all other pixels in the ‘dark’ state. In this way, the spectrometer detects a narrow spectral peak across the broad spectrum.

By employing a peak-finding algorithm, each narrow spectral peak is associated with its corresponding central wavelength, determined by the position of the maximum peak intensity. An example of the calibration result is shown in Fig. 3.7.

It is important to note that the wavelength-pixel calibration must be repeated if the beam position shifts. Otherwise, unexpected phases would be added to misassigned wavelengths, creating distorted chirps to the pulses.

3.3 Software Realization of Phase Control

To make use of the pulse shaper, one application is to compress the pulse with a broad spectrum to reach its temporal limit. Another application of SLM is to independently shape two orthogonal components, allowing for a pump-probe experiment. The key point is to determine and optimize the parameters for the phase.

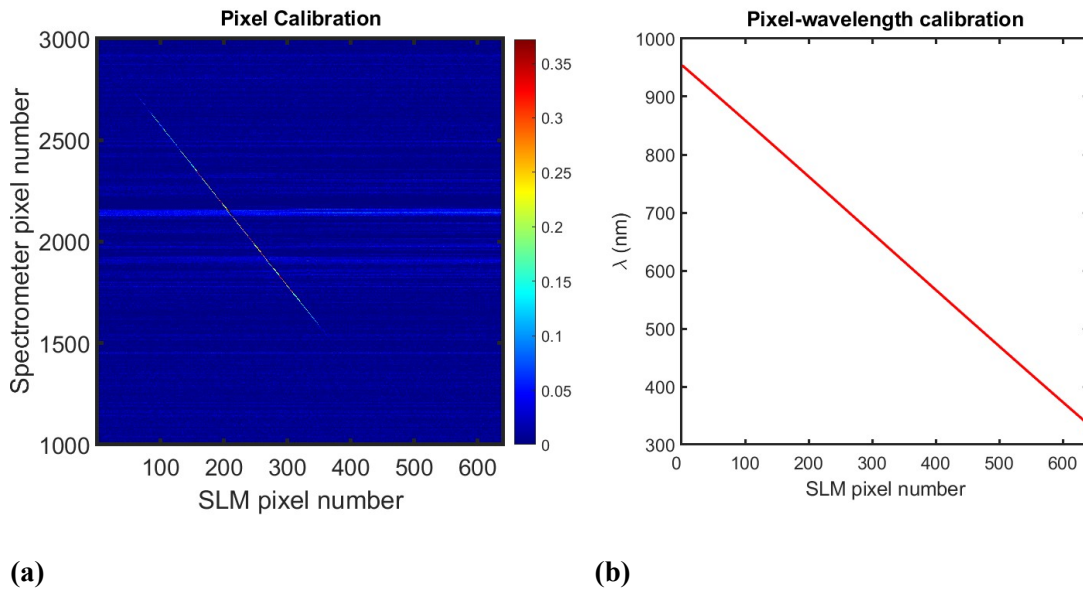


Figure 3.7. Pixel to wavelength calibration with the current beamline. (a) Spectrum measured for switching each pixel. (b) Pixel-wavelength fitted curve, the details can be viewed in [39].

3.3.1 Phase Modulation Function

Polynomial Function

The polynomial function is mentioned in Section 3.1, where the phase can be written as Taylor expansion:

$$\phi_{mod}(\omega) = \Phi_0 + \Phi_1\omega + \frac{\Phi_2}{2}\omega^2 + \frac{\Phi_3}{6}\omega^3 + \mathcal{O}(\omega^4) \quad (3.35)$$

where Φ_n is the n -th order derivative of the phase with respect to the frequency. As explained, the first order is the group delay, the second is the group delay dispersion(GDD), and the third one is called third-order dispersion(TOD). Usually, GDD and TOD play a crucial role in fs-pulse compensation.

Sinusoidal Phase Modulation

By Jacobi-Anger expansion, the phase function can be expanded to a series of Bessel functions:

$$e^{iA \sin(\omega t)} = \sum_{n=-\infty}^{\infty} J_n(A) e^{in\omega t} \quad (3.36)$$

Here, A is the amplitude of the modulation, and J_n is the n th harmonic. With sinusoidal modulation, a pulse train can be tuned separately in time.

3.3.2 Phase-controlled Program

Two programs are used for **pulse compensation**, and a third program is employed for **generating and controlling time delays** between two pulses. The initial program, developed by the group of Prof. Wollenhaupt at the University of Oldenburg, has been modified for different experimental purposes [39] [96].

For pulse compensation, the goal is to apply an optimal phase to correct the pulse chirps. The optimization criterion is based on the ionization count rates measured in the reaction microscope which will be introduced in Chapter 4. When the count rates reach their maximum, the pulse achieves its highest intensity, corresponding to its shortest temporal duration.

GDD-TOD Program

Group delay dispersion (GDD) and third-order dispersion (TOD), as introduced in Section 3.1, are the primary factors contributing to pulse broadening in the temporal domain. To achieve optimal values for GDD and TOD, a two-dimensional scan is performed. The scan range and step size are defined based on prior experience.

The procedure is illustrated in Fig.3.8, where the phase parameters are optimized using the ionization count rate measured by the Reaction Microscope.

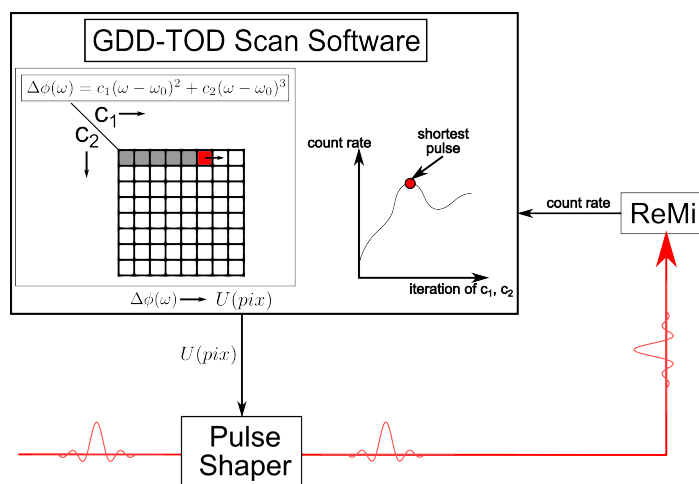


Figure 3.8. The working scheme for GDD-TOD optimization program. The figure is taken from [83].

Evolution Program

A genetic algorithm [97, 98] is designed to automatically find the optimal phase compensation parameters. A random initial solution is given at the beginning. Then a fitness function is used to evaluate the current parameters set by comparing the ionization count rates in the

reaction microscope. At every iteration, random variations based on the temporal solution are made, thus the search range gets enlarged until the best fitness function is reached.

Time Delay Scan

As described in the previous section, two orthogonal pulses are generated due to the birefringence of the SLM crystal. These orthogonal components can be used as pump and probe pulses, with an accurate time delay introduced between them. The time delay is achieved by applying equivalent phase shifts: for SLM A, no phase shift is applied ($\Delta\phi_A(\omega) = 0$), while for SLM B, a linear phase $\Delta\phi_B(\omega) = \tau(\omega - \omega_0)$ is introduced. Here, $\tau = \frac{\partial\phi}{\partial\omega}$ represents the time delay, and ω_0 is the central angular frequency of the laser spectrum.

It is important to note that the two pulses generated by the SLM are orthogonally polarized, oriented at $\pm 45^\circ$ relative to the table normal.

To obtain two parallel beams with identical polarization, a broadband polarizer is used to align the beam polarization along either the y-axis (spectrometer axis) or the x-axis (jet direction).

3.4 Pulse Characterization

With the advancement of modern electronics, devices with response times in the nanosecond and picosecond range have become widely utilized in various applications. For instance, transistors based on Gallium Nitride (GaN) [99] or Indium Phosphide (InP) [100] can operate at frequencies of hundreds of gigahertz, corresponding to response times of just a few picoseconds. However, no electronic devices currently allow for the femtosecond regime.

Several indirect methods have been developed over the past decades to measure pulse durations in the femtosecond range and sub-fs regime. These include autocorrelation, frequency-resolved optical gating (FROG) [101], spectral phase interferometry for direct electric-field reconstruction (SPIDER) [102], and techniques specific to attosecond pulses, such as attosecond streaking [103]. The core concept of these methods is to utilize short pulses to either measure a replica of themselves or to characterize other short pulses.

One disadvantage of autocorrelation and other pulse duration measurement techniques is that they require precise alignment and depend on the accuracy of curve fitting. In practical applications, real-time feedback is necessary to determine the phase compensation parameters discussed in Section 3.3. In this experiment, the ionization count rate serves as a reliable feedback signal.

3.4.1 Autocorrelation Measurements

The autocorrelation method works by splitting a pulse into two identical replicas, introducing a variable time delay between them, and then overlapping them spatially and temporally in a nonlinear medium to generate a second-harmonic (SHG) signal. By varying the time delay and measuring the SHG intensity as a function of the delay, the temporal characteristics of the original pulse can be extracted. More specifically, there are two types of auto-correlation methods, one is called intensity autocorrelation, and another is called interferometric autocorrelation.

Intensity Autocorrelation

With a time delay τ , the two separated beams are overlapped in the second harmonic generation (SHG) crystal to generate the pulse at 2ω frequency, thus the signal depends only on the intensity of the pulses, not on their electric field interference:

$$I_{AC}(\tau) = \int_{-\infty}^{\infty} |E(t)E(t - \tau)|^2 dt = \int_{-\infty}^{\infty} I(t)I(t - \tau) dt \quad (3.37)$$

In which, $I(t)$ is the intensity of the pulses, measured by a power meter. One feature of intensity autocorrelation is that the measured pulse duration is always longer than the actual value.

In the case of a Gaussian pulse:

$$I(t) = I_0 \exp\left(-\frac{4 \ln 2 \cdot t^2}{\tau_p^2}\right) \quad (3.38)$$

The corresponding autocorrelation signal is:

$$I_{AC}(\tau) = I_0 \exp\left(-\frac{4 \cdot \ln 2 \tau^2}{\tau_A^2}\right) \quad (3.39)$$

In which $\tau_A = \sqrt{2}\tau_p$, meaning the actual pulse duration is shorter than the autocorrelation trace by a factor of $\sqrt{2}$. The factor is varied for different input pulse shapes. Thus, assuming a reasonable pulse shape is needed beforehand.

One thing that needs to be noticed is that the autocorrelation is unambiguous since the phase information is not included in the measurement.

Interferometric Autocorrelation

Another alternative method that includes phase information is called interferometric autocorrelation. As the name suggests, this method allows the two beams to interfere, generating

second-harmonic generation (SHG), as shown in Fig. 3.9. This way, the phase information is recorded by the SHG oscillation:

$$\begin{aligned}
 I_{AC}(\tau) &= \int_{-\infty}^{\infty} |[E(t) - E(t - \tau)]|^2 dt \\
 &= \int_{-\infty}^{\infty} I^2(t) + I^2(t - \tau) dt + 4 \cdot \int_{-\infty}^{\infty} I(t)I(t - \tau) dt \\
 &\quad - 2 \cdot \int_{-\infty}^{\infty} [I(t) + I(t - \tau)] E(t)E^*(t - \tau) dt + \int_{-\infty}^{\infty} E^2(t)E^{2*}(t - \tau) dt
 \end{aligned} \tag{3.40}$$

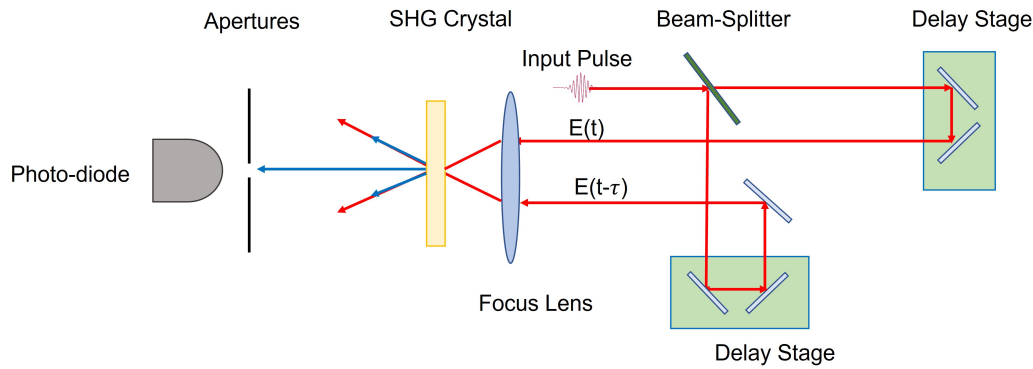


Figure 3.9. Schematics for an interferometric autocorrelation measurement set-up.

Similar to the intensity mode, the pulse duration and phase information are the curve-fitting results from the given pulse shapes. Different from the intensity mode, the peak signal amplitude to the background level in the intensity is 8:1.

3.4.2 Combination of SLM with Auto-Correlation Measurement

Autocorrelation measurements were performed to verify the alignment of the zero-dispersion 4-f geometry implemented with the SLM. Zero-dispersion means without any phase given by the SLM, the temporal profile of input and output pulses before and after the 4-f setup should be the same. Any distortion is an indication of a bad alignment or bad optics. If additional dispersion is introduced by misalignment of the optics within the 4-f geometry, the measured autocorrelation pulse duration will differ before and after the pulse shaper. For instance, if the pulse duration before the pulse shaper is 25 fs, and the pulse measured after the pulse shaper is significantly longer or shorter than 25 fs, or if the pulse shape is distorted with additional pre-pulse structures, the alignment must be readjusted. This examination also serves as the fine alignment procedure for the SLM, which is detailed in Appendix C.

In addition to measuring pulse duration, autocorrelation traces are also used as a method for examining time delays. When two pulses with a separation of τ pass through the autocorrelator, the autocorrelation trace will display three peaks with a time interval of τ between them.

3.4.3 Pulse Characterization with a Reaction Microscope

A Reaction Microscope not only provides the count rate as a criterion for pulse compression but also enables the measurement of pulse duration by recording the ionization count rate as a function of the added phase delay. As a cross-checking method, it serves as the final step in the SLM alignment procedure, detailed in Appendix C.

In addition to its role as a pulse-duration measurement device, the Reaction Microscope also records ion momentum distributions. This allows for extracting additional pulse characteristics, such as polarization states and phase delays.

As described in the previous section, the time-delay function of the pulse shaper is achieved by introducing a phase delay between two orthogonal pulses. To verify its effectiveness, the two pulses are kept orthogonal, with a $\lambda/2$ waveplate installed after the SLM, rotated by 22.5° relative to the table normal. Over one laser cycle, the polarization vector of these two components varies depending on the relative phases, as shown in Fig. 3.10.

As will be discussed in Chapter 5, part of the H^+ dissociated from methane always aligns with the laser polarization. In this context, it is shown that the H^+ emission direction changes with the phase delay. When the phase shift $\Delta\phi = 0$, the light is linearly polarized along the TOF direction, causing the H^+ to be dissociated along the TOF axis. When the phase shift $\Delta\phi = \pi$, the light is linearly polarized along the jet direction (y-axis), resulting in H^+ dissociation along the y-axis. For intermediate phase shifts, the dissociated H^+ ions are emitted in an elliptical way.

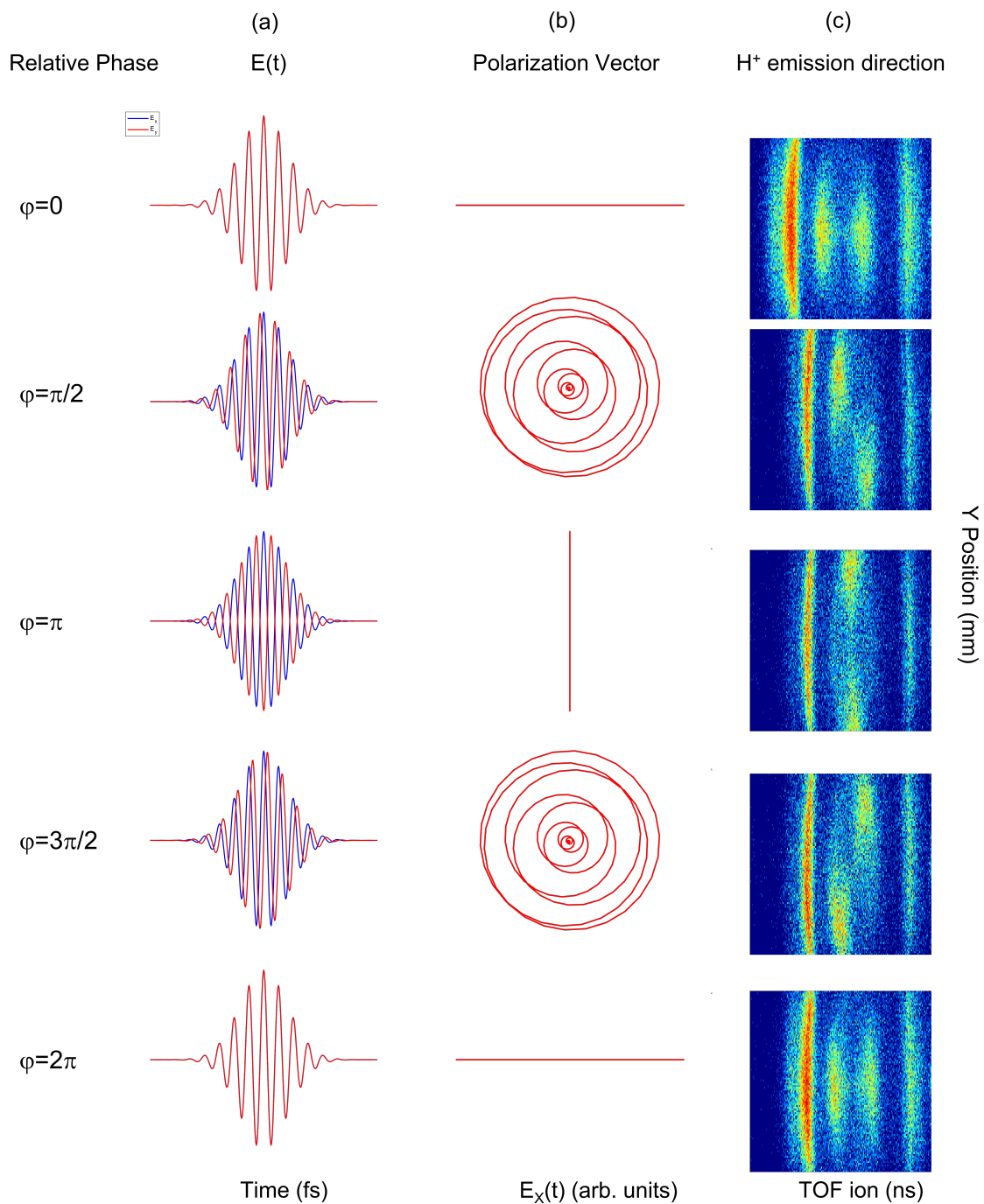


Figure 3.10. The schematics of the laser polarization within one laser cycle and the corresponding observation of dissociated H^+ . (a) The two laser fields in time with a variable phase shift. (b) The polarization vector of $E_x(t)$ and $E_y(t)$. (c) The corresponding dissociated H^+ imaging in the light polarization plane.

Chapter 4

Reaction Microscope

Atomic or molecular fragments can result from various processes, such as ionization, collision, or detachment [22, 104]. To study the complete dynamics of these processes, a full measurement of the multi-particle final momenta must be recorded using high-resolution spectroscopy. Over the past decades, several techniques and experimental apparatus have been developed to achieve this goal. For example, a supersonic gas jet has been incorporated to facilitate Cold Target Recoil-Ion Momentum Spectroscopy (COLTRIMS) [105].

Electrons, being significantly lighter than ions, often possess higher kinetic energy, which increases the possibility of them colliding with the chamber walls before reaching the detector. To overcome this, a pair of Helmholtz coils have been designed and installed outside the chamber to generate a homogeneous magnetic field. This field confines the electron motion, enabling efficient collection and ensuring 4π acceptance across a wide energy range for electron-ion coincidence measurements.

By combining these advanced techniques, a state-of-the-art setup called the ‘Reaction Microscope’ (ReMi) has been developed. The ReMi is often referred to as ‘a bubble chamber for atomic and molecular physics’ [23, 106]. This apparatus has facilitated numerous studies, such as non-sequential ionization [1], electron-impact double ionization [26], molecular Coulomb explosion [59], etc.

This chapter begins by introducing the working principle of the ReMi, followed by a detailed explanation of its key components. Additionally, it provides background knowledge on data analysis techniques that will be used in the subsequent discussion of results.

4.1 Working Principle

The general working principle of a reaction microscope is illustrated in Fig. 4.1. With a **supersonic gas jet**, a cold atomic or molecular target beam is sent into the interaction region, where it overlaps with a focused laser beam or a projectile beam. Guided by an external

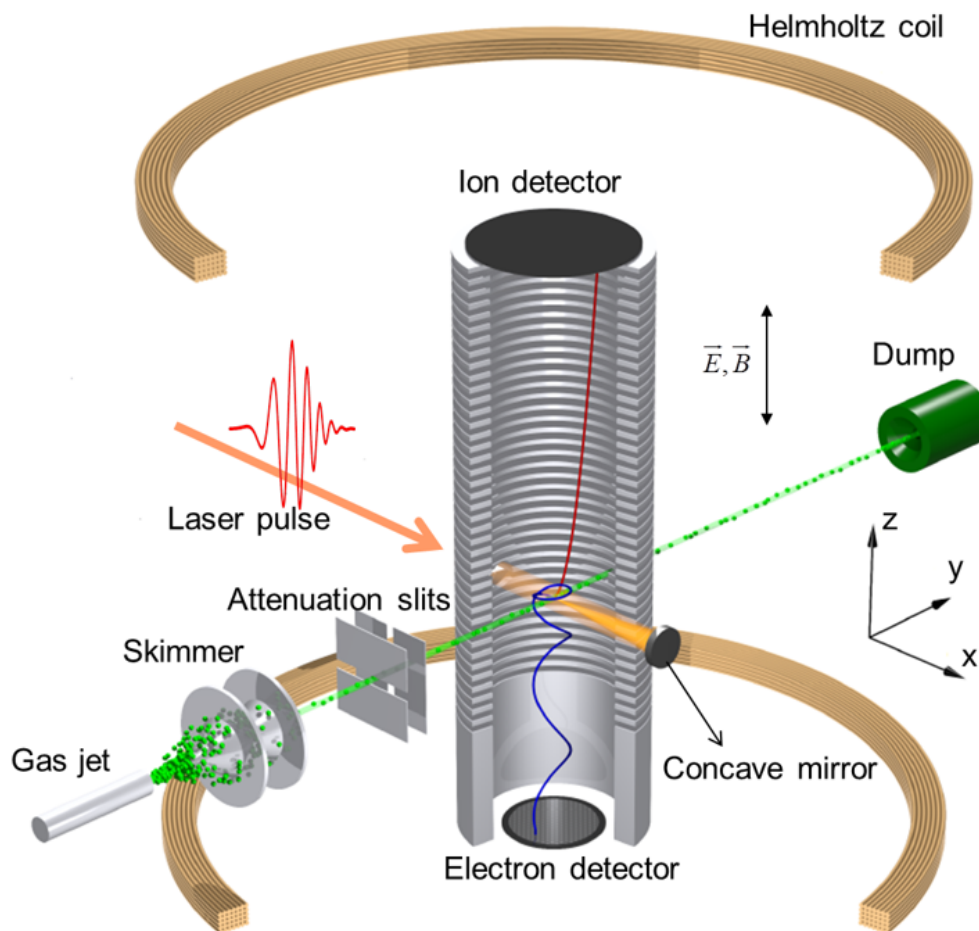


Figure 4.1. Schematic of a Reaction Microscope: The supersonic gas jet is aligned along the y-axis. The Z-axis is the direction of the spectrometer. The X-axis corresponds to the laser propagation direction. This figure is taken from Fechner [85].

electric field in the **spectrometer**, charged particles are accelerated toward the **position-sensitive detector**.

Simultaneously, electrons undergo a spiral motion due to the combined effect of a weak magnetic field and the external electric field. By measuring the time of flight (TOF) of each particle and the position at which it impacts the detector, a full 3-D momentum reconstruction of the particle can be achieved.

It is worth noting that, with a reaction microscope, coincidence measurements of multiple particles can be achieved under the conditions of a cold jet implementation, an ultra-high vacuum environment below 10^{-11} mbar, a high-speed data acquisition system, and an optimized combination of electric and magnetic fields.

4.1.1 Vacuum System and Supersonic Gas Jet

To give a more technical view of the set-up with the complete vacuum requirement, the schematic is given in Fig. 4.2.

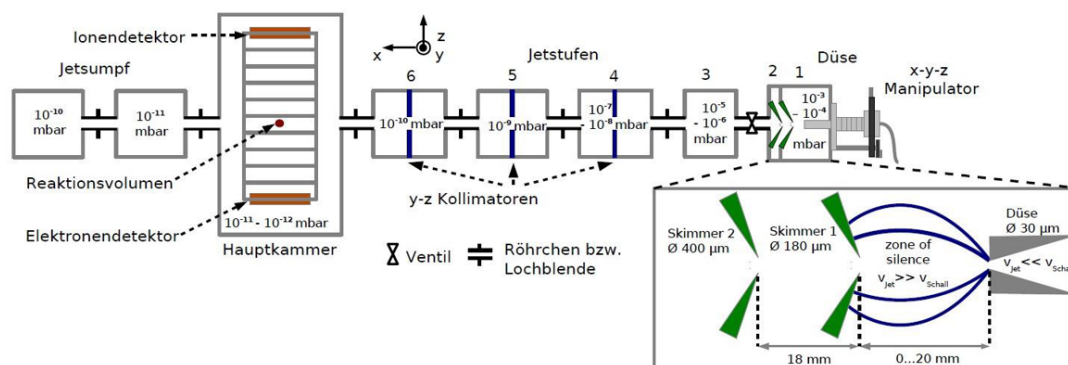


Figure 4.2. Schematic of the complete vacuum system. The figure is taken from Nicolas Camus [107].

Supersonic Jet

The resolution of momentum measurements strongly depends on the initial momentum spread of the target beams. A supersonic gas jet, as illustrated in Fig. 4.2, is designed to achieve a small momentum spread and a well-defined target size. The gas is initially prepared at room temperature with a typical pressure of a few bars and then passed through a nozzle with an orifice size ranging from 10 to 100 μm into a vacuum chamber. Upon passing through the nozzle, the gas undergoes adiabatic expansion, where its internal energy is converted into kinetic energy. This process accelerates the gas to supersonic velocities, exceeding the speed of sound, while simultaneously cooling it to very low temperatures, typically a few Kelvin. As the cold jet interacts with the background hot gas, its velocity reaches a limit, resulting in the formation of a discontinuous flow. This discontinuity creates a shock wavefront and a ‘zone of silence’, where the gas stream is highly collimated and cold.

To ensure optimal jet quality, skimmers—typically conical or cylindrical in shape—are placed at the nozzle exit. These skimmers select only the central portion of the collimated jet to pass through, effectively filtering out the peripheral gas and helping to maintain the vacuum between successive stages.

Key factors in the supersonic jet design include the skimmer-to-nozzle distance and the pumping speed in the first differential pumping stage. To facilitate fine alignment and ensure optimal jet performance across different gas species and pressures, the nozzle is mounted

on a three-dimensional (3-D) translation stage. This setup allows precise adjustment for optimal alignment at the dump chamber.

To further control the gas delivered to the spectrometer, an adjustable slit is installed before the main chamber, allowing control over the gas load. Additionally, differential pumping stages are equipped with connecting tubes to help maintain the vacuum. The residual gas after the reaction is directed toward a dump chamber, which is positioned at a slightly tilted angle relative to the jet's delivery direction.

This carefully engineered supersonic jet system ensures a high-quality target beam with minimal momentum spread, enabling precise momentum measurements in the spectrometer.

Alignment

To make sure the jet is passing through all the limited apertures along the long beam (the nozzle, skimmers, holes between the differential pumping stages, the slit control the gas load before the spectrometer, the hole at the spectrometer), can overlap with the laser focus and finally reach the dumping stage, one standard alignment procedure is needed.

The procedure begins by placing a telescope instead of the dump side before closing the chamber. The spectrometer, slit, and movable parts should be positioned so that the center of the telescope can pass through and finally can see the nozzle and skimmers by illuminating with white light.

The next step is to align the laser focus with the jet beam. This can be done by adjusting the position of the focusing mirror so that the laser-induced plasma in the air is visible along the alignment line from the telescope.

Finally, after closing the chamber, the jet can be fine-tuned by optimizing the pressure at the dump. In the ideal case, the main chamber pressure will not be affected whether the gas is passing or not and the dump pressure will increase by roughly one order to 10^{-10} mbar.

To maintain such a high vacuum, several measures need to be taken. For example, proper-speed turbo pumps must be installed at each stage. In addition, The baking process needs to be done to eliminate residual water efficiently.

4.1.2 Time and Position Sensitive Detectors and Spectrometer

Time and Position Sensitive Detectors

Each detector in the Reaction Microscope used in the thesis is made of two grids, two micro-channel plates(MCP) in a chevron configuration, and a delay-line anode.

Fig. 4.3 illustrates the structure of an MCP, which is made of a thin glass layer containing millions of microscopic channels. A high direct current (DC) voltage, typically around

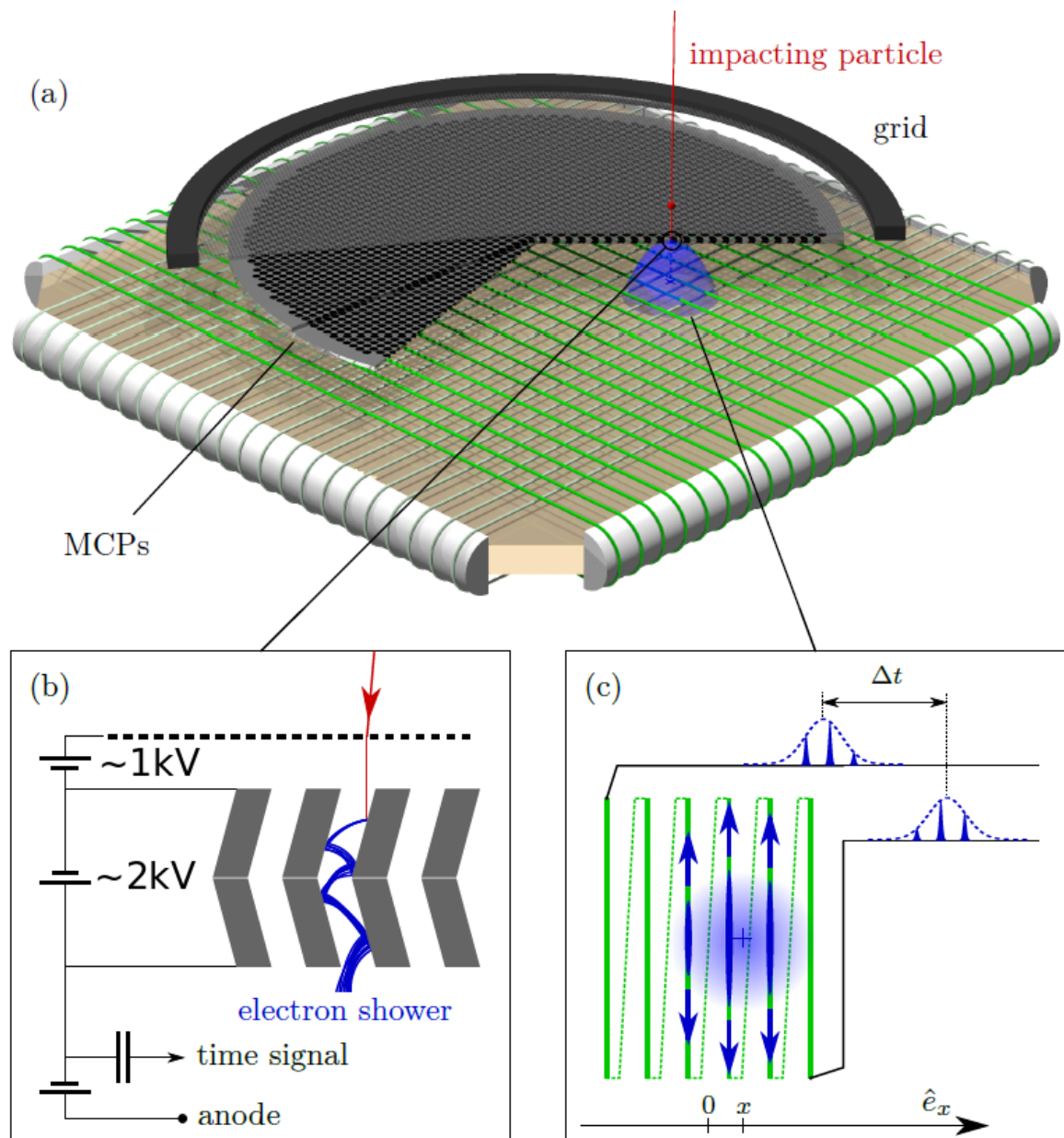


Figure 4.3. Schematics of MCPs in a Chevron configuration and a delay-line anode: (a) A particle impacts one channel of the MCP, generating electron clouds. (b) Under high voltage, secondary electrons are produced and undergo an avalanche amplification process. (c) Working principle of a delay-line anode: by measuring the arrival time difference at both ends of the wire, the original impinged position can be determined. This figure is adapted from [85].

2 kV, is applied between the front and back surfaces of the MCP to guide charged particles into the individual channels. Each channel is slightly tilted at a fixed angle relative to the plate's surface, ensuring that incoming particles efficiently impact the channel walls. The inner surfaces of the channels are coated with a semiconducting material, which facilitates the emission of secondary electrons when the primary particles collide with the walls.

These secondary electrons are then accelerated by the applied voltage, causing further collisions with the channel walls and generating additional secondary electrons. This cascading process, known as an avalanche effect, results in the release of thousands to millions of electrons for each incoming particle. The avalanche process significantly amplifies the initial signal, making MCPs highly efficient for detecting and amplifying charged particle signals in various experimental setups.

To get the position where the particle is hitting the detector, delay-line anodes are placed behind the MCPs. Two wires orthogonal to each other are wound with many turns with a spacing of about 0.5 mm. Taking x-direction as an example, by measuring the times when one signal reaches the two ends at t_{x1} and t_{x2} , the position of the original impact can be calculated:

$$x = (t_{x1} - t_{x2})v_{signal} \quad (4.1)$$

To increase the efficiency of detecting real signals instead of noise, in reality, two identical wires instead of one single wire are placed, so-called Lecher-cable. Both wires pick up noise, but one of the two Lecher cables is set to a slightly higher positive voltage than the other, making it more favorable for the real signal. This wire is referred to as the ‘signal wire’, while the other is called the ‘reference wire.’ Differential amplifiers are then installed to filter out background noise from real signals.

There is a concept called ‘dead time’, referring to the time the detector/ digitizer takes to register one hit and it can not process another hit during this time. The dead time for MCP is usually within 1 ns. For the anode, it is around 50 ns, depending on the size and design of the anode.

The feature of the anode is that for one hit, we get four values, namely t_{x1} , t_{x2} , t_{y1} , and t_{y2} . We just used the time difference between the arrival time of the signal at two ends to determine the position for each coordinate x and y . One more piece of information we can get from here is the sum of the time one signal takes to reach both ends. For one hit, the sum of t_{x1} and t_{x2} should be a constant. Using this fact, we could exclude some cases like when two hits are overlapping or the second hit arrives earlier than the first one. In addition, the dead time of the digitizers is typically around 5-10 ns.

Spectrometer

The spectrometer is shown in Fig. 4.1, where all the metal plates are connected via electrodes, fixed by four pillars with the ion detector on top and the electron detector on the bottom. The laser beam is focused by a focusing mirror $f=7.5$ cm which is placed on a 3D adjustable stage to the center of the spectrometer and intersects with the gas jet.

4.2 Data Acquisition and Data Analysis

4.2.1 Data Acquisition

Fast digitizers are needed to process multi-hit, multi-channel detectors. Here we use the fADC8 unit from Roentdek [108]. The trigger signal is given by a gating between the laser signal and the ion MCP time window, which is around $30 \mu\text{s}$ to include all the mass species we are interested in. The fADC8 unit allows the sampling of single analog traces, similar to those shown on an oscilloscope, converting analog signals to digital signals for further analysis. The sampling rate of the fADC8 in the ADC channels is 800 ps (or 400 ps or 200 ps if channels are combined).

4.2.2 Momentum Reconstruction

Longitudinal Momentum

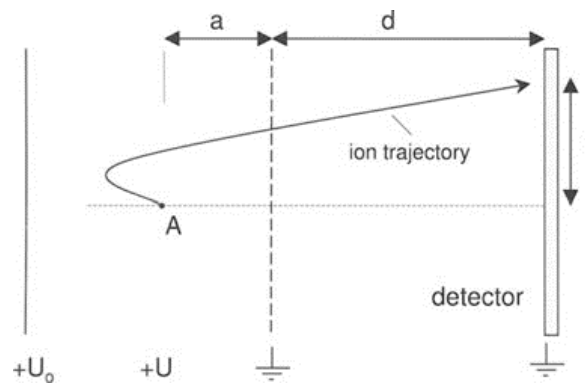


Figure 4.4. Schematics of a recoil-ion momentum spectrometer. The figure is taken from the book of Ullrich [104], P.35.

The longitudinal momentum P_{\parallel} , which is the momentum along the spectrometer axis, is determined by the particle's time of flight. Consider a recoil-ion spectrometer as shown in Fig. 4.4. The magnetic field, which is parallel to the spectrometer axis, does not affect the longitudinal momentum. After the interaction, particles acquire a longitudinal momentum P_{\parallel} and travel toward the detector under the influence of a homogeneous electric field. This field is applied in an acceleration region with a length a and a voltage U . On the electron side, a field-free region of length d is added following the acceleration region. The relationship between the time of flight t and the longitudinal momentum P_{\parallel} is given by:

$$t_{+/-} = m \left(\frac{2a}{\sqrt{P_{\parallel}^2 + 2mqU} \pm P_{\parallel}} + \frac{d}{\sqrt{P_{\parallel}^2 + 2mqU}} \right) \quad (4.2)$$

The ‘ \pm ’ means the particles fly toward/backward to the detector separately. q is the charge, and m is the mass. For $P_{\parallel} = 0$:

$$t(P_{\parallel} = 0) = \sqrt{2} \sqrt{\frac{m}{qU}} (2a + d) \quad (4.3)$$

This is the time of flight(ToF) peak position center for a specific m/q value. If the initial energy of the particles is small compared to the energy gained by the accelerating field, i.e. $qU \gg P_{\parallel}^2/m$, and the particles have an equal possibility to fly toward/backward to the detector, a Taylor-expansion can be carried out to extract the initial momentum distribution. This is not valid for light particles due to the large kinetic energy gained, e.g. protons or electrons due to the small mass. Since there is no drift region for the ion side, meaning $d = 0$, the equation can be written as:

$$P_{\parallel} = \frac{am}{t} - \frac{qU}{2a}t \quad (4.4)$$

In contrast to the ions, there is a drift region after the acceleration region for electrons, so the equation will not be valid. In this case, since there is no analytical solution, a numerical method is employed, e.g. Newton’s method.

Transverse Momentum

To calculate the transverse momentum, a combination of the time of flight (ToF) t from the MCP and the position information from the delay line anodes is required. As introduced in Section 4.1.2, the position for x and y coordinates can be calculated.

For **ions**, due to its large mass compared to electrons, the weak magnetic field can not provide enough Lorenz force to lead the spiral movement, so the magnetic field is neglected in most cases. Then, to get the transverse momentum reconstructed, one should first rotate the calculated x - y plane according to the anode’s orientation to the spectrometer and the jet position. The jet direction is aligned along the y -axis by rotating the coordinate system. By adding a mass-dependent constant, the jet displacement can be corrected so that the lab coordinate system matches the moving reference frame of the molecules in the jet. With the correct position, the transverse momentum can be calculated as:

$$P_{\perp} = m \cdot \frac{\sqrt{x^2 + y^2}}{t} \quad (4.5)$$

The working principle is the same for **electrons**, but the magnetic field must be included. The electron with momentum P_{\pm} travels with a radius R decided by the magnetic field B as:

$$R = \frac{P_{\perp}}{qB} \quad (4.6)$$

And the cyclotron frequency ω is:

$$\omega_c = \frac{qB}{m_e} = 2\frac{\pi}{T} \quad (4.7)$$

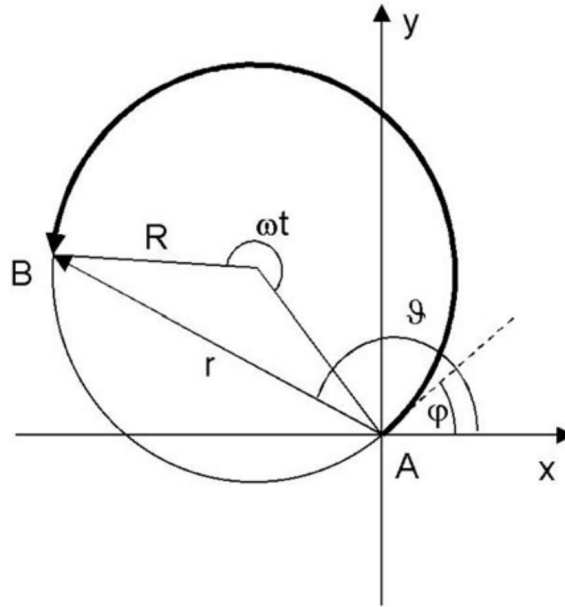


Figure 4.5. The electron trajectory view from detector plane, taken from [104], P. 53.

Now we consider the plane perpendicular to the magnetic field, as shown in Fig. 4.5, the electron with momentum P_{\pm} released at position A will be emitted with an angle ϕ to the positive x -axis direction. As mentioned before, the radius R is decided by the magnetic field B , and the arc-angle ωt in space is decided by the electron's time of flight. By reconstructing the geometry, we get:

$$R = \frac{r}{2|\sin(\omega t/2)|} \quad (4.8)$$

In practice, electrons undergo not just a single cyclotron turn but several turns (N). Consequently, the arc angle ω is determined by $\omega t - N \cdot 2\pi$. An important consideration is that electrons completing one or more entire turns will hit the detector at the origin (point A), making it impossible to obtain the transverse momentum anymore. These specific electron radii appear as node points when plotting the electrons' radius against their time of flight, as illustrated in Fig. 4.6. The distance between two consecutive nodes corresponds to the cyclotron period (T), providing a more precise measurement than any prior determination of the magnetic field. If the nodes carry physical information to be measured, slightly changing the magnetic field will help.

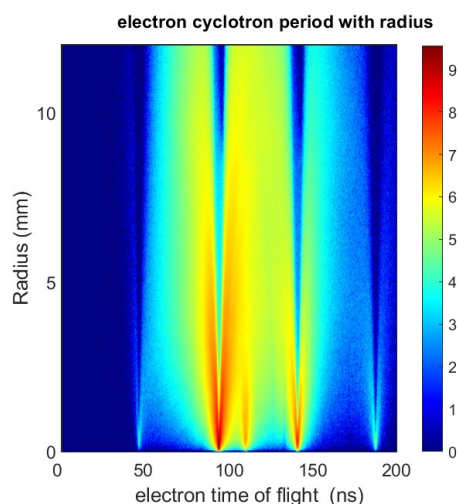


Figure 4.6. An example of electron counts as a function of ToF and radius on the detector.

4.2.3 Coincidence Measurement

A coincidence measurement involves detecting more than one fragment originating from the same ionization or dissociation event. As mentioned previously, the reaction microscope satisfies the necessary conditions for such measurements. Since this thesis focuses on the fragmentation process in molecules, the analysis of coincidence measurements is needed.

One of the initial steps in this analysis is to determine the types of fragmentation processes that have occurred by examining the correlation between the time-of-flight spectra of different ions. For events where more than two ions are detected, a Newton plot can be utilized to simplify the complexity of three-body problems, providing a clearer visualization of the fragmentation dynamics [109].

Time of Flight Correlation from Coincidence Measurement

A PIPICO plot, short for ‘Photo-ion Photo-ion Coincidence’ plot, represents the correlation between two ions originating from the same event. As the name suggests, it shows the relationship between the ToF of these two ions from the same event, referred to as coincident measurement. From a PIPICO plot, we can extract information such as identifying the fragmentation channels involved, whether a metastable state exists for certain fragments, etc. The reason why coincidence lines exist is as follows: taking two fragments come from the same dissociation process, one ion arrives on time t_1 with momentum p_0 , and the other one arrives on time t_2 with opposite momentum $-p_0$, due to momentum conservation, the sum of two ions TOF is:

$$t_1 + t_2 = t(p_0) + t(-p_0) = \frac{2a\sqrt{p^2 + 2mqU}}{qU} \quad (4.9)$$

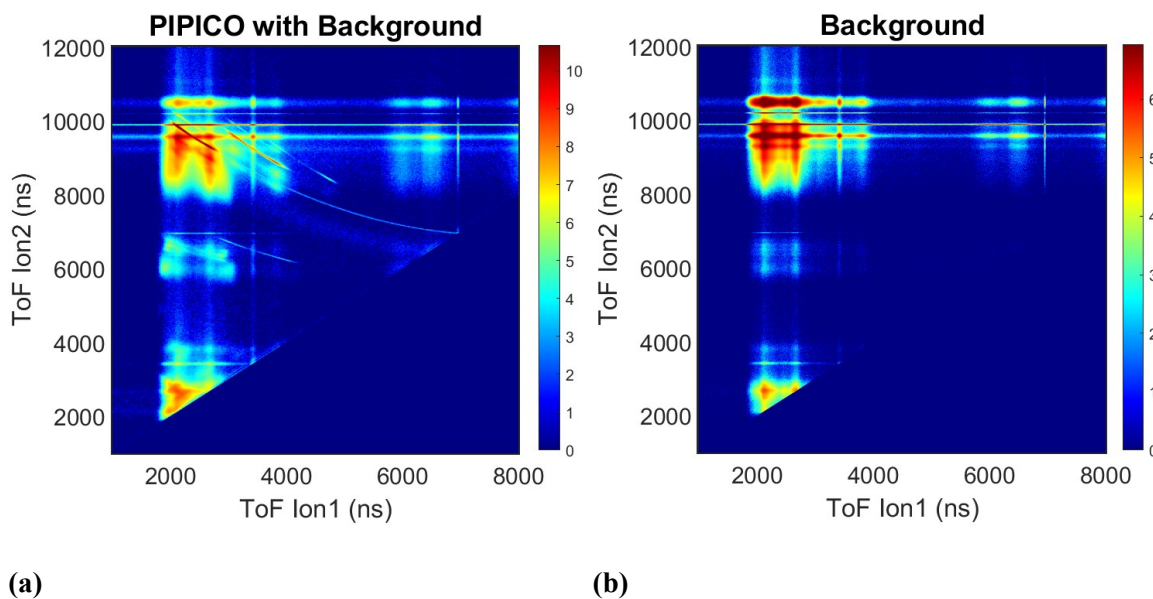


Figure 4.7. Photon-Ion-Photon-Ion Coincidence Plot (PIPICO plot). (a) Raw data PIPICO plot. (b) Reconstructed background of the PIPICO plot.

From equation (4.9), when the charge states $q_1 = q_2$, the sum of two ions' time of flight should be nearly a straight line depending on the distribution of p_0 .

As a result, each 'diagonal' line appearing in a PIPICO plot corresponds to a specific fragmentation process. By selecting these lines, one can identify the dissociation channels. An example from the methane fragmentation pump-probe measurement, which will be discussed in detail in Chapter 5, is shown in Fig.4.7 (a). Except for the coincidence lines, several lines result from false coincidences and noise. To remove the background, one can generate an artificial background plot by mismatching the t_1 and t_2 from different events, as shown in Fig. 4.7 (b). By background subtraction, a clearer PIPICO plot can be seen in Fig. 4.8.

In Fig. 4.8, the background subtracted PIPICO plot is shown. Several distinct fragmentation channels can be observed, like the marked ones as $CH_3^+ + H^+$, $CH_2^+ + H_2$, and so on.

This strategy can also be extended to three-body fragmentation processes. By treating two of the three particles as one, such as $t_1 + t_2$, and then plotting it against the third particle's time of flight, t_3 , this is referred to as the 'Tripico' coincidence plot shown in Fig. 4.9. Here is an example that will be discussed in Chapter 6.

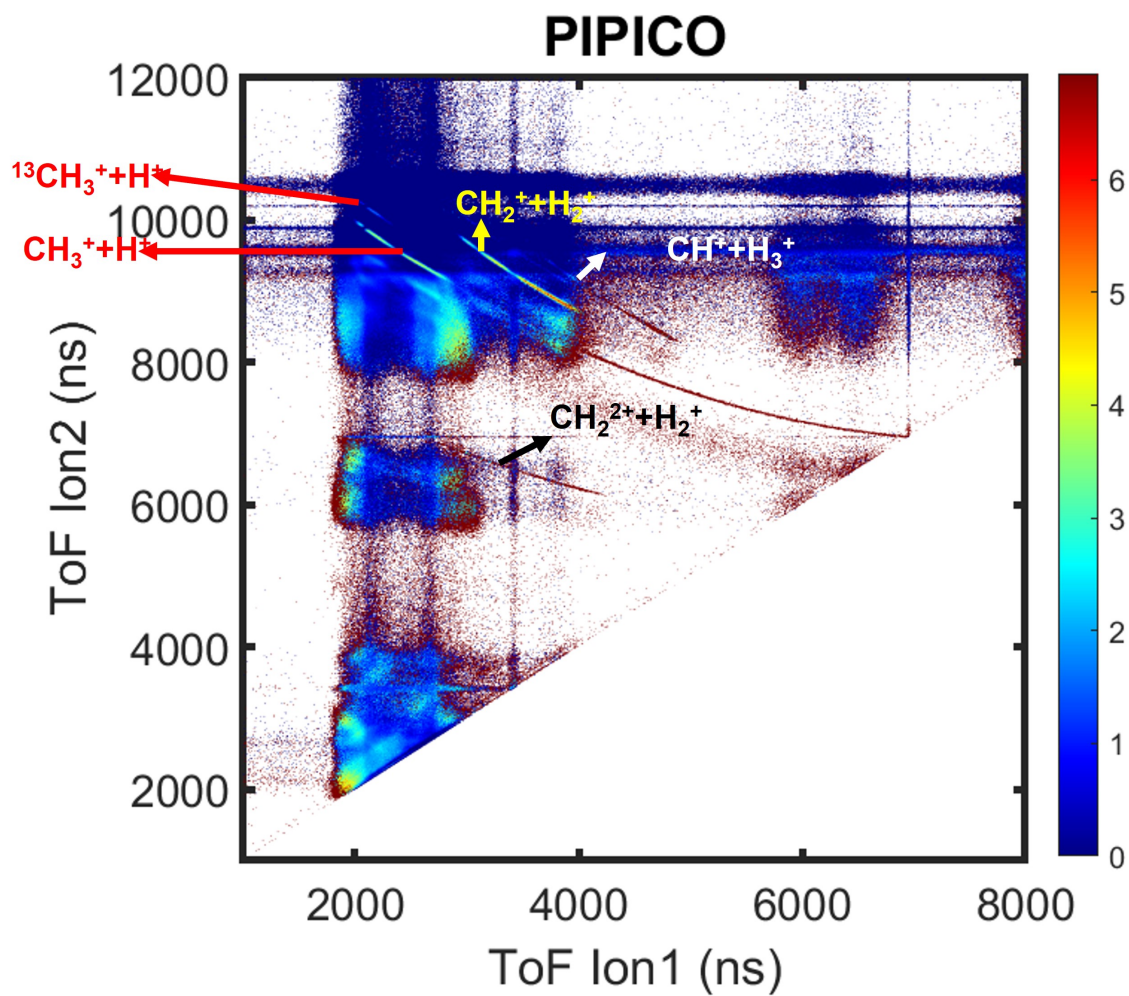


Figure 4.8. PIPICO plot with background removal. Arrows mark different dissociation channels.

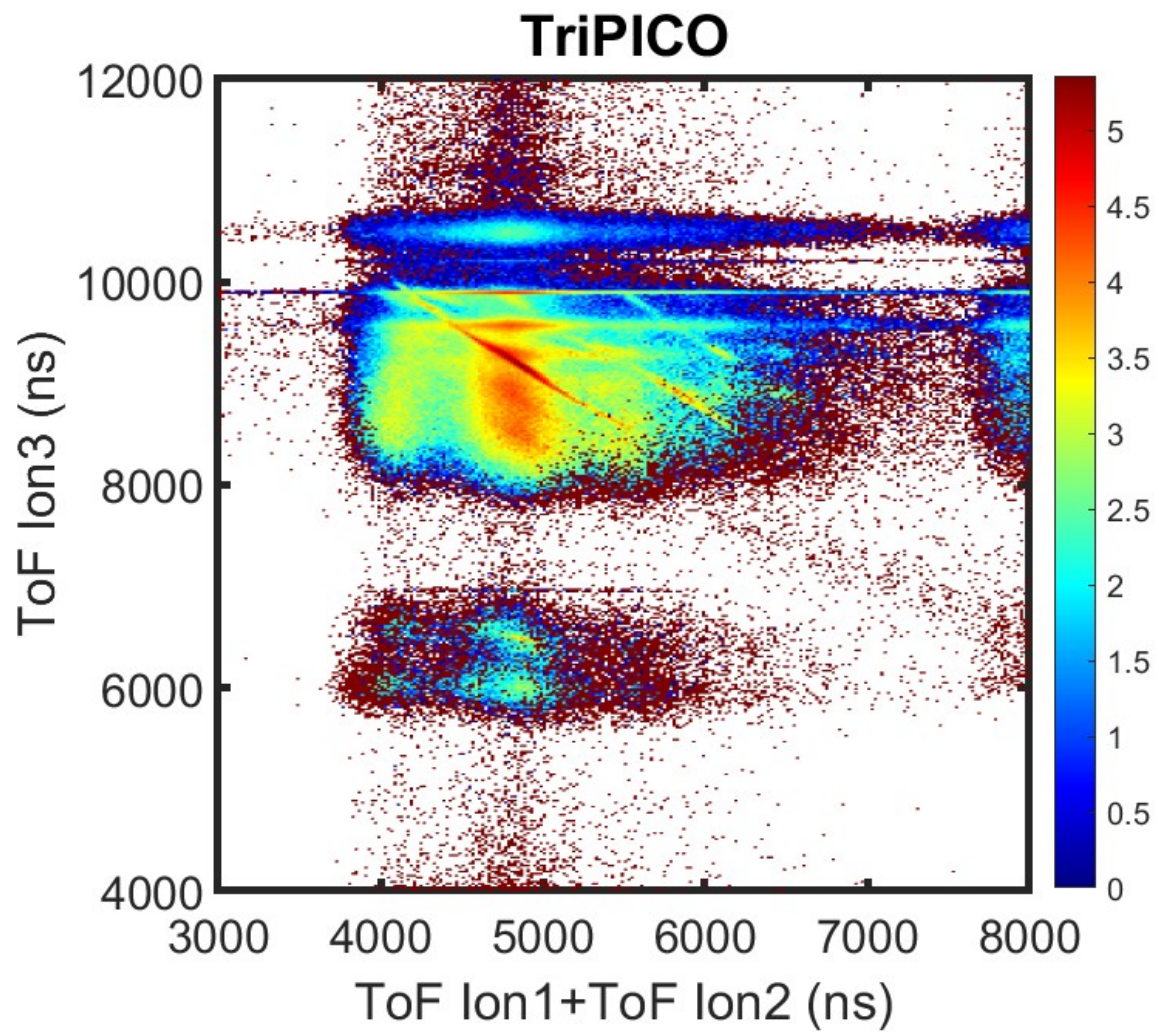


Figure 4.9. Three ions' coincidence TOF measurement with background removal. In this case, the $t_1 + t_2$ are the arrival-time sums of two H^+ ions. The red arrow shows the fragmentation channel $CH_2^+ + H^+ + H^+$ discussed in Chapter 6.

Newton Plot

One question in the three-body dissociation process is how to analyze momentum conservation and reflect the kinematic relationships between particles [109]. The Newton plot is a tool that serves this purpose and is widely used in nuclear physics and particle physics studies.

The core of a Newton plot lies in the momentum conservation equation $P_A + P_B + P_C = 0$, which confines the fragmentation process to a plane in the center-of-mass frame. Here, P_A , P_B , and P_C are the momenta of the three fragments A, B, and C, respectively. By rotating fragment A's momentum vector, P_A , to a fixed direction (usually along the x-axis), the momentum vectors P_B and P_C are rotated accordingly within the same plane with respect to the fixed P_A . This method allows the Newton plot to provide a clear visualization of the relationship between the fragments.

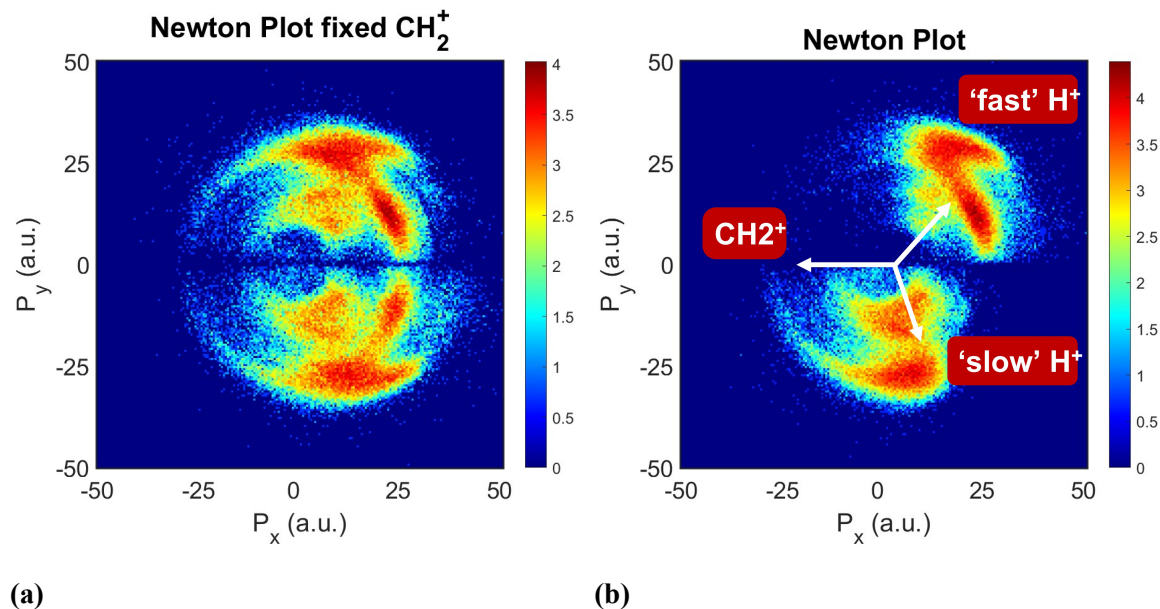


Figure 4.10. Newton plot for $CH_2^+ + H^+ + H^+$. (a) Newton plot without distinguishing between the two protons. (b) Newton plot with the selection of two protons: the 'fast' proton is displayed in the upper part of the plot, while the 'slow' proton is shown in the lower part. The definitions of 'fast' and 'slow' protons can be found in the text.

Here is an example from the three-ion coincidence channel $CH_2^+ + H^+ + H^+$, which will be discussed in detail in Chapter 6. As shown in Fig. 4.10, the momentum of CH_2^+ is fixed towards the negative x-axis direction. In panel (a), the two H^+ ions are plotted without any selection on the fragmentation plane: one is shown in the upper part of the figure, and the other in the lower half. (Since the two H^+ ions arrive at the MCP nearly simultaneously, there is no distinction between the first and second hits. Equivalently, the two H^+ ions are

considered identical if the detector is ideal.)

In panel (b), the two H^+ ions are sorted based on their final kinetic energy. The higher-energy ion is referred to as the ‘fast’ proton and is plotted in the upper part, while the lower-energy ion, referred to as the ‘slow’ proton, is shown in the lower part.

As shown in the picture, fixing one ion’s direction helps to understand the other two particles’ relative correlation.

Dalitz Plot

Another useful visualization tool is the Dalitz plot, which represents the energy sharing among three or more particles in a system. According to Viviani’s theorem, in a three-body system, the sum of the distances of the three particles from the center of mass remains constant [110]. Using two degrees of freedom, the energy sharing between two particles and the remaining energy for the third particle form an equilateral triangle:

$$X = \frac{\epsilon_1 - \epsilon_2}{\sqrt{3}} \quad (4.10)$$

$$Y = \epsilon_3 - \frac{1}{3} \quad (4.11)$$

Here, $\epsilon_i = \frac{|P_i|^2}{\sum |P_j|^2}$, where P_i is the momentum of the i -th fragment. The points $\epsilon_1 = 1$, $\epsilon_2 = 1$, and $\epsilon_3 = 1$ correspond to the right corner, left corner, and top point of the triangle, respectively. When the three particles share energy equally, the point appears at $(0, 0)$. Other correlations are distributed at various locations within the triangle, as shown in Fig. 4.11.

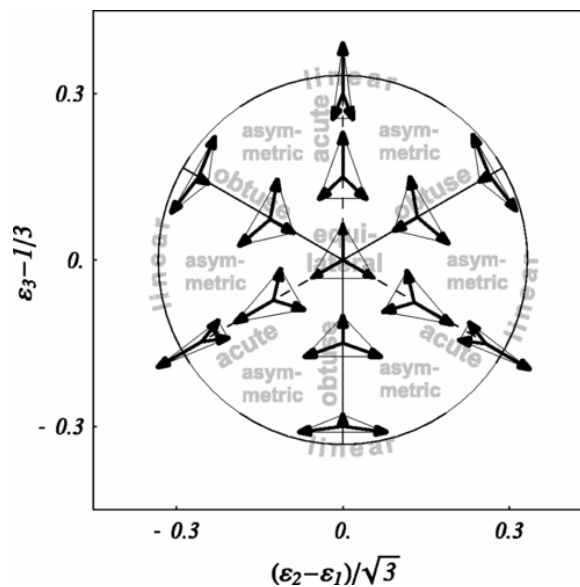


Figure 4.11. Momentum configurations in a Dalitz plot. The figure is taken from [111].

From the Dalitz plot, one can infer the energy distribution among particles [112], providing insights into possible geometric variations during the process. However, it is important

to note that the geometric configuration and the energy sharing represented in the Dalitz plot are not mapped one-to-one. This means that different geometries can produce the same Dalitz plot, and vice versa.

Here is one example Dalitz plot for $CH_2^+ + H^+ + H^+$ measured with the experiment, which will be analyzed in Chapter 6 further.

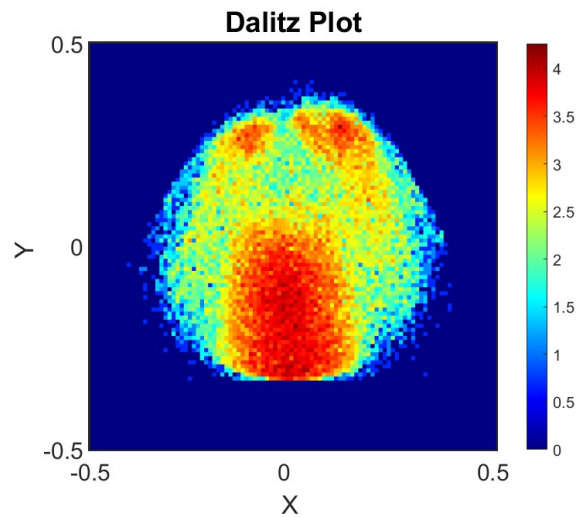


Figure 4.12. Dalitz Plot for $CH_2^+ + H^+ + H^+$, ϵ_1 and ϵ_2 are calculated for H^+ and ϵ_3 is for CH_2^+ .

Chapter 5

Atomic and Molecular Hydrogen Ejection from Two-body Fragmentation of CH_4^+

Proton motion in molecules has become a widely used method for studying molecular geometry rearrangement dynamics [25, 113].

Methane, as one of the simplest and lightest organic molecules, exhibits complex behavior under strong near-infrared (NIR) fields. Multiple fragmentation processes can occur, including proton dissociation and molecular hydrogen formation, as listed in Table 5.1.

Two-Body Fragmentation Channels of CH_4		
CH_4^+ (12.5 eV)		
$\text{CH}_3^+ + \text{H}^0$ (14.0 eV)	$\text{CH}_2^+ + \text{H}_2^0$ (15.1 eV)	
$\text{CH}_3^0 + \text{H}^+$ (18.1 eV)	$\text{CH}_2^0 + \text{H}_2^+$ (20.1 eV)	$\text{CH}^0 + \text{H}_3^+$
CH_4^{2+}	$\text{CH}_3^+ + \text{H}^+$ (27.8 eV)	$\text{CH}^+ + \text{H}_3^+$ (28.4 eV)
$\text{CH}_3^{2+} + \text{H}^0$ (33.3 eV)	$\text{CH}_2^+ + \text{H}_2^0$ (30.5 eV)	
$\text{CH}_3^{2+} + \text{H}^+$	$\text{CH}_2^{2+} + \text{H}_2^+$	$\text{CH}^{2+} + \text{H}_3^+$

Table 5.1. Possible Two-Body Fragmentation Channels of the CH_4 Molecule. This table lists the possible fragmentation channels [114] along with their respective threshold energies, which can occur under the laser conditions used in this thesis.

This chapter focuses on the two-body fragmentation pathways leading to proton and molecular hydrogen emission. It is structured as follows: Section 5.1 introduces the possible fragments identified from the ion time-of-flight spectra in a single-pulse measurement. Section 5.2 presents two pathways leading to neutral hydrogen H^0 and charged hydrogen H^+ (proton). These two channels exhibit distinct angular momentum distributions, which en-

ables the separation when they are mixed in a pump-probe experiment. Section 5.3 discusses the pathways responsible for molecular hydrogen formation in single-pulse and pump-probe schemes. Finally, Section 5.4 compares the proton and molecular hydrogen formation channels and examines their connection to the Jahn-Teller effect in methane cations.

5.1 Identification of Possible Fragments

Before studying time-resolved molecular fragmentation processes, it is essential first to identify the possible fragmentation channels occurring under a single pulse. Therefore, this section presents the results of single-pulse measurements, which serve as a reference for analyzing subsequent pump-probe experiments. All single-pulse measurements presented here are conducted with 10 fs laser pulses at an intensity of 3×10^{14} W/cm². The laser polarization is along the z-axis, which is parallel to the direction of the spectrometer. The electric field of the ReMi Spectrometer is 10 V/cm.

As introduced in Chapter 4 on the Reaction Microscope, different time-of-flight peaks represent different $\sqrt{m/q}$ values. The Time-of-Flight (ToF) spectra from the single-pulse measurement are presented here in Fig. 5.1. The highest peak corresponds to singly charged CH_4^+ , and all other fragments are determined by $\sqrt{m/q}$.

(a) Methane molecular ions: The most probable ion produced with this laser condition is the single ionization of methane, represented by the narrow peak of CH_4^+ at 9900 ns. The nearby sharp peak corresponds to the carbon isotope $^{13}CH_4^+$.

(b) Hydrocarbon fragment ions: : The peak between 7900 ns and 9810 ns corresponds to CH_3^+ , CH_2^+ , CH^+ , resulting from events where one, two, or three hydrogens are dissociated with certain momentum from the molecule, making all these peaks broader than the CH_4^+ peak. It is difficult to distinguish CH^+ from CH_2^+ , but this will be clearer in a PIPICO plot introduced in Chapter 4.

(c) Doubly ionized methane fragments: The peak at 5900 ns results from the double ionization of methane (CH_4^{2+}), while the peak slightly to the left originates from the dissociation of CH_4^{2+} into CH_2^{2+} . No distinct peak corresponding to CH_2^{3+} is observed, which agrees with theoretical studies suggesting that CH_2^{3+} does not possess a stable long lifetime [115].

(d) Hydrogen-related fragments: The peaks between 3000 ns and 4000 ns correspond to H_2^+ , while the peak below 3000 ns is attributed to H^+ . In the H^+ regime, two sets of peaks can be observed: outer peaks and inner peaks. The outer peaks are induced by the Coulomb explosion, where ions gain higher energy and reach the detector with a shorter or longer time of flight (ToF), depending on their initial velocity direction. Two inner peaks result from dissociation, which are typically slower than Coulomb processes.

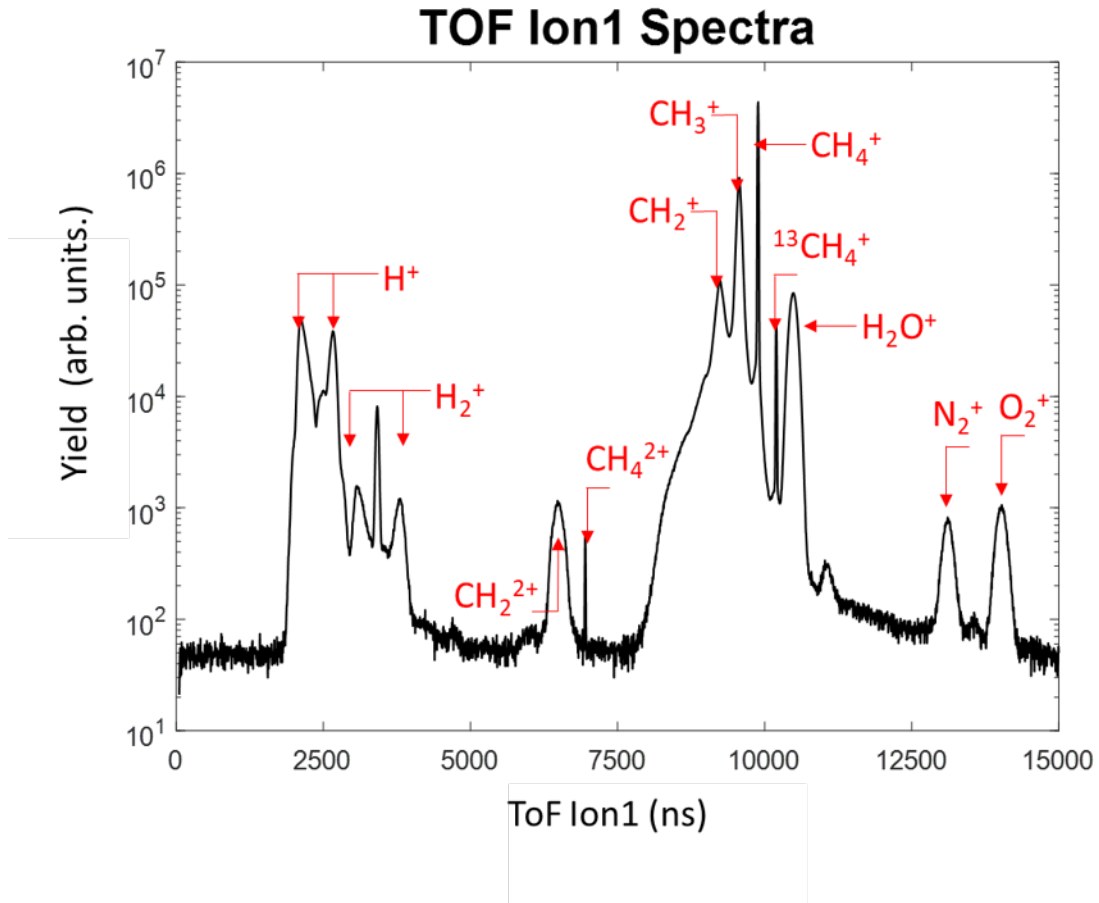


Figure 5.1. Time-of-flight spectrum for the first detected ion. Different peaks correspond to particles with different mass-to-charge ratios.

(e) **Background gas ionization** H_2O^+ , N_2^+ , O_2^+ : Broad peaks appearing beyond 10,000 ns correspond to ionization of residual gases, such as H_2O^+ , N_2^+ and O_2^+ .

5.2 Comparison between Neutral Hydrogen and Proton Ejection

It is observed in a **single-pulse** measurement that the methane cation (CH_4^+) can dissociate into either H^+ or H^0 . In this section, we analyze two dissociation pathways which produce H^+ and H^0 , respectively:



The dissociation pathway leading to neutral hydrogen (H^0) exhibits an isotropic emission direction, whereas the pathway resulting in a proton (H^+) shows a strong angular dependence on laser polarization.

This difference in angular distribution allows for clear differentiation between the two pathways. By characterizing these mixed pathways in a **pump-probe** scheme, it has been found that the pathway leading to neutral hydrogen production is delayed, as evidenced by changes in both time-dependent angular distributions and yield rate with time delays.

5.2.1 Characterization of Fragmentation Pathways from Single Pulse Measurement

In single-charged dissociative ionization, only one fragment is ionized, while the other, resulting from two-body fragmentation, remains neutral and cannot be directly detected with this setup. However, the momenta of neutral fragments can still be calculated from the cations, as the sum momentum of the charged fragment and the neutral part is conserved. For the single-charged dissociative ionization, two pathways from equation (5.1) and (5.2) are observed.

In these two channels, hydrogen is released from CH_4^+ either as a neutral hydrogen atom or as a proton. The kinetic energy release and momentum distribution are shown in Fig. 5.2 and Fig. 5.3, respectively.

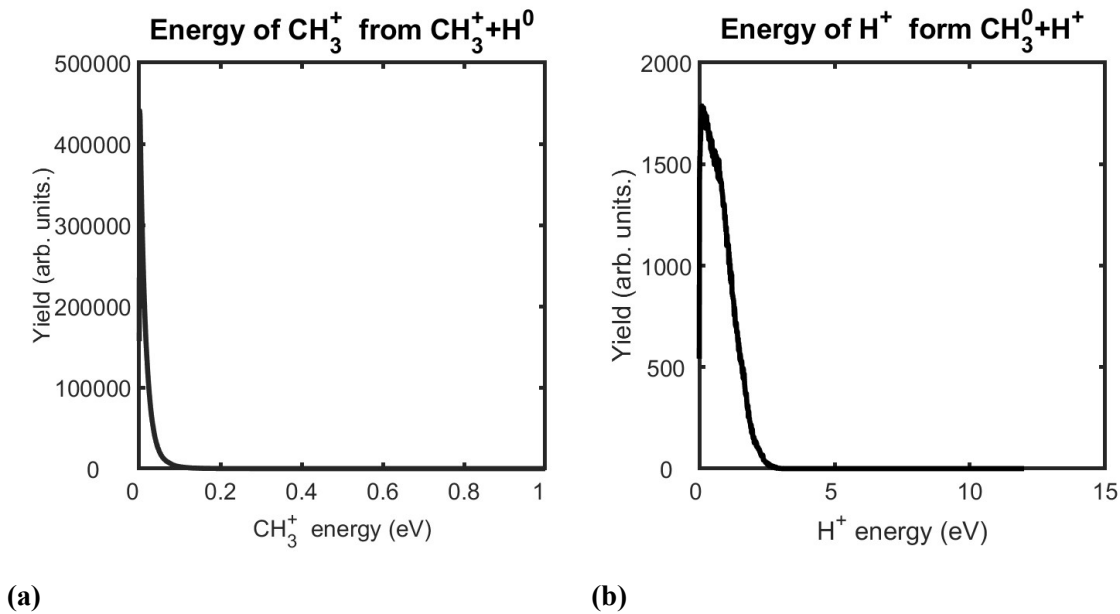


Figure 5.2. (a) Energy of CH_3^+ from channel $CH_4^+ \rightarrow CH_3^+ + H^0$. (b) Energy of H^+ from the channel $CH_4^+ \rightarrow CH_3^0 + H^+$.

Momentum Distribution

Fig. 5.3 (a) and (b) show the momentum distribution for channels (5.1) and (5.2). To quantify the ion emission angle relative to the laser polarization along the z-axis, the angular

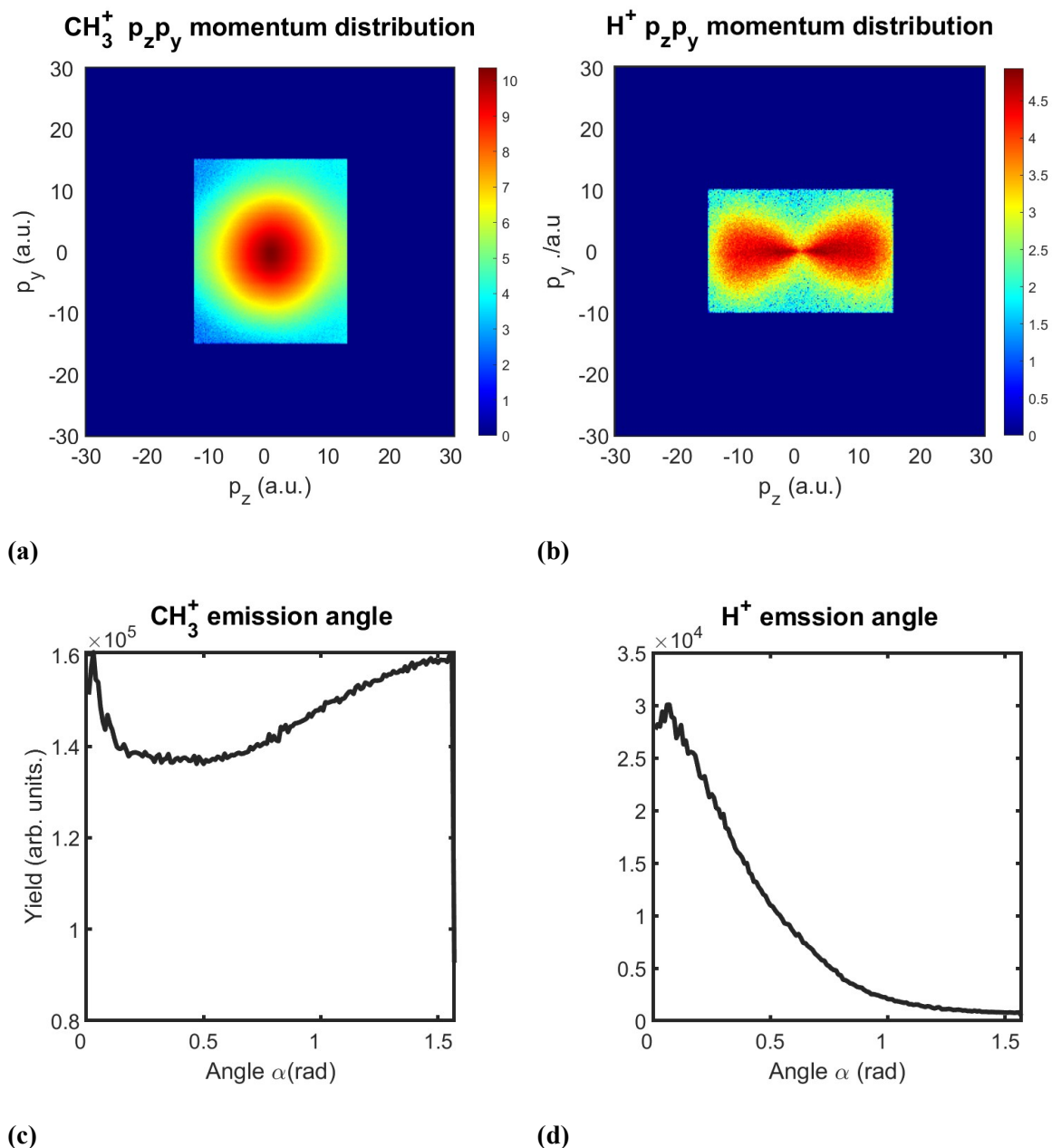


Figure 5.3. (a) Momentum distribution of CH_3^+ from the dissociation channel $CH_4 \rightarrow CH_3^+ + H^0$. (b) Momentum distribution of H^+ from the dissociation channel $CH_4 \rightarrow CH_3^0 + H^+$. (c) Yield of dissociated CH_3^+ as a function of the emission angle relative to the laser polarization. (d) Yield of dissociated H^+ as a function of the emission angle relative to the laser polarization.

distribution is plotted in Fig. 5.3 (c) and (d). It is clear that the momentum angular distribution of CH_3^+ from the fragmentation channel (5.1) is nearly isotropic, meaning the chance for the coincident fragment H being ejected in any direction is almost the same. However, for channel (5.2), the momentum distribution of the proton is strongly aligned with the polarization.

Branching Ratio

Fig. 5.4 shows the yield ratio of CH_3^+ from the dissociation channel (5.1) to H^+ from the dissociation channel (5.2) as a function of single-pulse intensity. The branching ratio between channels (5.1) and (5.2) is approximately 33.8:1 at an intensity of $3 \times 10^{14} \text{ W/cm}^2$, indicating that the channel $CH_3^+ + H^0$ dominates over the other. The branching ratio exhibits a strong dependence on pulse intensity, as shown in Fig. 5.4. As the laser intensity increases, the branching ratio decreases. In other words, at higher intensities, excitation to the methane cation's excited state becomes more probable, leading to dissociation into $CH_3^0 + H^+$. (The H^+ is produced exclusively from the excited A state, while H^0 is produced predominantly from the ground X state, as will be discussed next.)

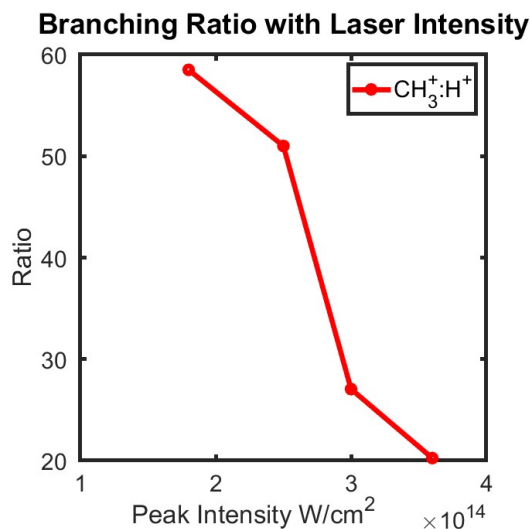


Figure 5.4. Branching ratio between dissociation channels $CH_3^+ + H^0$ and $CH_3^+ + H^+$ at different laser peak intensities.

To better understand these pathways, we present a schematic representation of the two dissociation channels in Fig. 5.5.

From Fig. 5.5, $CH_3^+ + H^0$ can originate from both the ground X state and the excited A state of the methane cation, whereas $CH_3^0 + H^+$ exclusively arises from the higher excited A state. The transition to the A state requires an additional 4.5 eV from the X state, corresponding to the absorption of three additional photons. This aligns with our observation that the $CH_3^0 + H^+$ channel is dominant. Furthermore, the decrease in the branching ratio with increasing laser intensity can be partially attributed to the increased population of the A state at higher intensities.

In addition, we conclude that the major part of $CH_3^+ + H^0$ observed in the measurements originates from the X state of CH_4^+ , as its ionization potential is lower. Next, we temporarily

neglect the contribution of the pathway $\text{CH}_4^+ \rightarrow \text{CH}_3^+ + \text{H}^0$ via the higher excited A state.

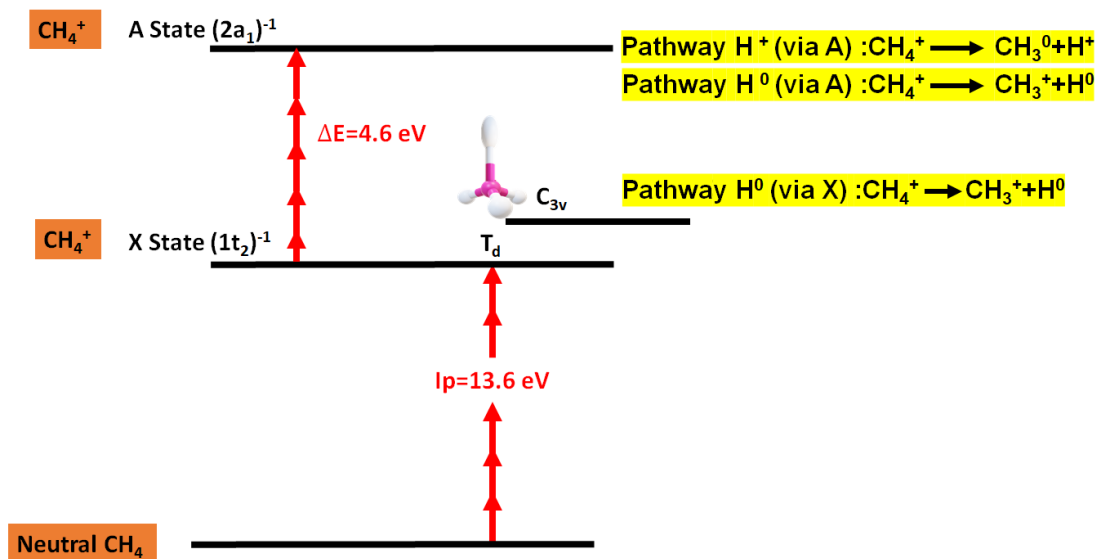


Figure 5.5. Schematic representation of pathways (5.1) and (5.2). The vertical ionization potential of neutral methane in its T_d symmetry ground state, $X(1t_2)^{-1}$, is 13.6 eV [65]. An additional 4.5 eV is needed to reach the excited $A(2a_1)^{-1}$ state [116]. The proton (H^+) is only created via the higher A state, while neutral hydrogen (H^0) can be generated from both the lower X state and A state [67].

5.2.2 Time-dependent Proton Ejection

The distinct differences in the angular momentum distribution between the two channels provide a direct way of distinguishing them when they are mixed in a pump-probe scheme. Now, the schematics mechanism is presented in Fig. 5.6.

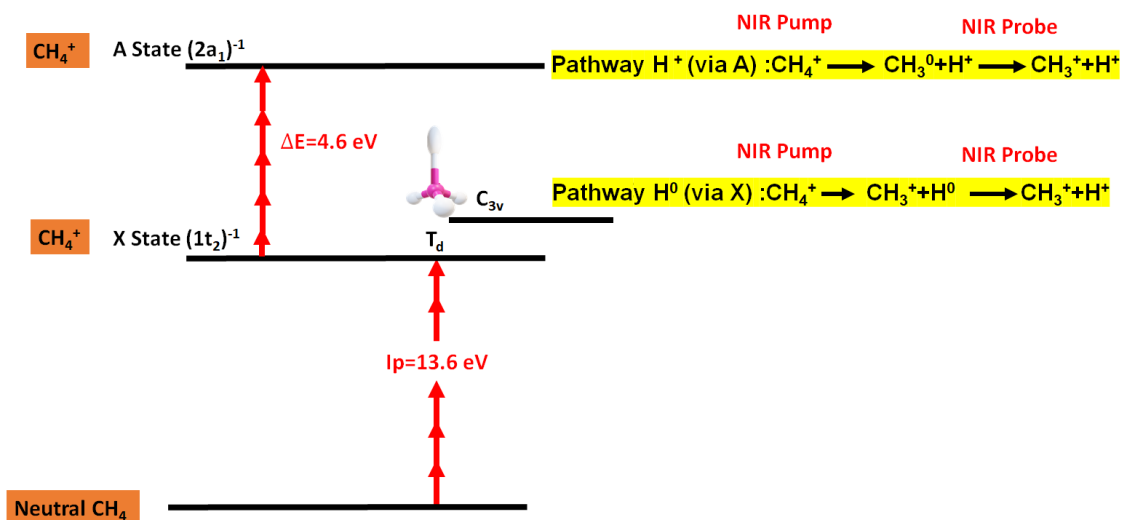


Figure 5.6. Schematic representation of pathways (5.3) and (5.4). In addition to the pump pulses shown in Fig. 5.5, a time-delayed probe pulse further ionizes the remaining neutral fragment. As a result, pathways (5.1) and (5.2) overlap, producing the same final fragments: $H^+ + CH_3^+$.

The pump-probe experiment was conducted with equal pump and probe intensities, each with $3 \times 10^{14} \text{ W/cm}^2$. The time delay was set between -50 fs and 1 ps, with a 1 fs step size, and both linear polarizations were aligned along the spectrometer z-axis.

Fig. 5.7 (a) shows the kinetic energy release (KER) plot as a function of the time delays. Two features appear: one is a constant KER of 5 eV. The time-independency indicates that two charged particles, CH_3^+ and H^+ , are created with only one pulse (either pump or probe), resulting in KER does not change with time delays. However, in Fig. 5.7 (a), the time-independent Coulomb explosion yield rate decreases with time delay. The reason is that the laser intensity decreases slightly with time delay, which is induced by the pulse shaper, as explained in Chapter 3. To correct for intensity variations, a measurement using a Mach-Zehnder interferometer was performed, as shown in Fig. 5.7 (b). While the peak laser intensity remains constant, the pulse duration in the Mach-Zehnder measurement is 25 fs. In this Mach-Zehnder data set, the count rate for the time-independent part is constant, suggesting a stable laser intensity over the entire time-delay range. This provides us with a more accurate data set.

Another feature is a time-dependent slope. A clearer visualization is provided in Fig. 5.8,

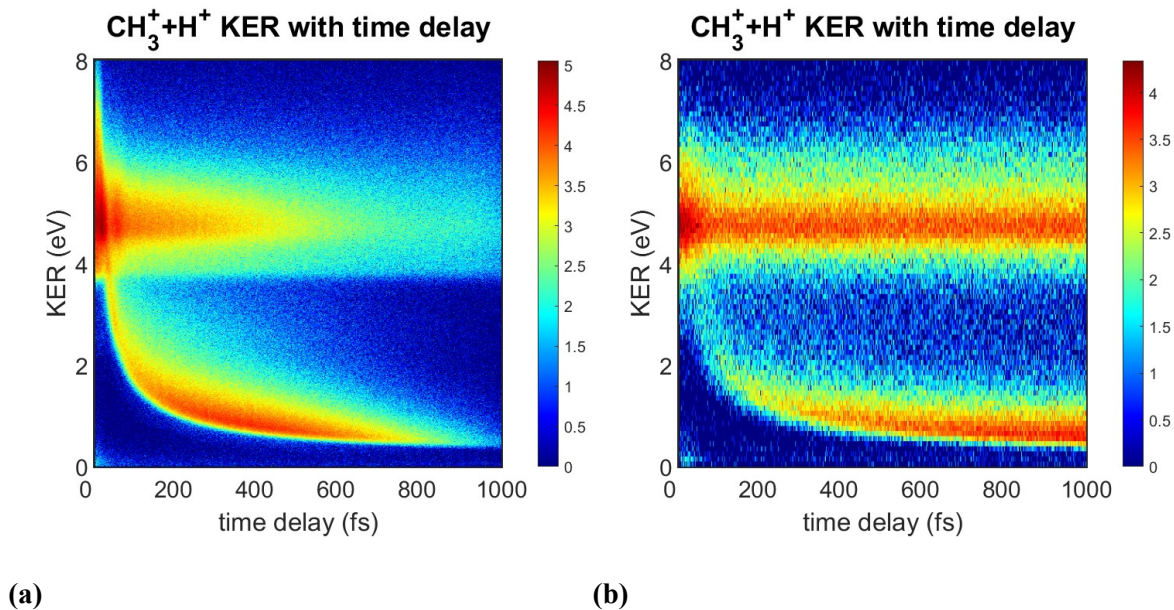


Figure 5.7. The kinetic energy release of the dissociation channel $CH_4^+ \rightarrow CH_3^+ + H^+$ with time delay. (a) Measurement with the pulse shaper. (b) Measurement with Mach-Zehnder interferometer.

where only the time-dependent events are selected and the count rate is plotted against the time delay. The count rate increases as the time delay grows for the delayed-dissociation part. Furthermore, even up to 1 ps, the count rate continues to increase. This enhancement is observed not only at a particular laser intensity but also across different intensities.

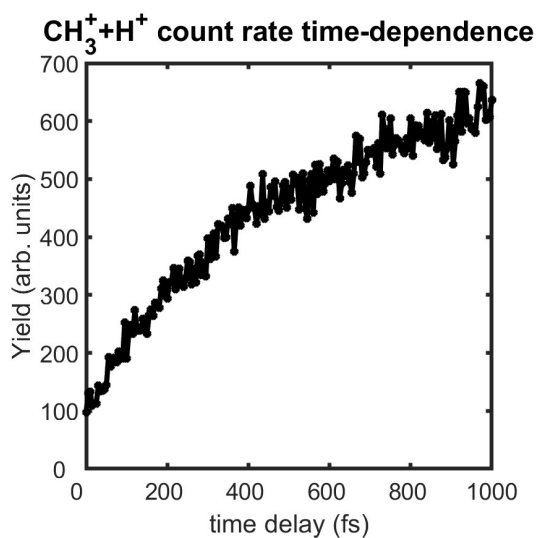
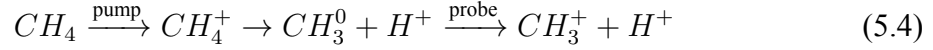
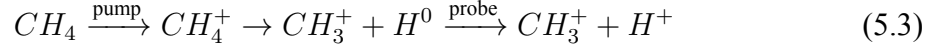


Figure 5.8. Count rate of the time-dependent dissociation part as a function of time delay from Fig. 5.7 (b).

Now, back to the topic of the fragmentation pathways that lead to this time-dependent slope. The time dependency suggests that the molecule has interacted with both the pump and probe pulses. In other words, the probe pulse further ionizes the system in addition to the single pulse measurement as shown in Fig. 5.6:



In these two cases, the methane molecule is ionized by the pump pulse, and the resulting CH_4^+ cation dissociates via different pathways. Before the probe pulse arrives, the dissociated fragments move apart from each other, with the distance R between them increasing over time. Once the probe pulse arrives, the fragments undergo the Coulomb explosion, with energy release proportional to $1/R$. Thus, the KER curve decreases with increasing time delay, as shown in Fig. 5.7.

However, the fragments of $CH_3^+ + H^+$ from two pathways are mixed in the same time-dependent KER curve. The next step is to distinguish between the two pathways described. In other words, the task is to figure out whether the intermediate fragment is H^+ or H^0 .

Here, the difference in the emission angle discussed in the last section is used to differentiate these two pathways. The momentum distribution of H^+ in Fig. 5.9 (a) shows the signal integrated over all time delays. To visualize the dynamics, time-resolved momentum distributions are presented at different time windows in Fig. 5.9 (b). From the plot, we see that at early time delays (e.g., between 0 to 50 fs and 50 to 100 fs), the H^+ ion is ejected most likely along the laser polarization direction, similar to the distribution observed for H^+ in the channel (5.2) as shown in Fig. 5.3 (b).

As time delays increase, the momentum distribution becomes more isotropic, similar to the distribution of CH_3^+ observed for the channel (5.1) as shown in Fig. 5.3 (a). This indicates that the H^+ dissociation channel (5.2) emerges earlier than the H^0 dissociation channel (5.1). The angular distribution of the H^+ yield for different time windows are shown in Fig. 5.10, where the dark blue curve represents events between 0 and 50 fs, the red curve corresponds to events between 50 and 100 fs, and so on. It is clear that as the time delay increases, the distribution becomes increasingly isotropic. This means that from 0 to 1000 fs, the **dominant channel** changes from $CH_4^+ \rightarrow H^+ + CH_3^0$ to $CH_4^+ \rightarrow H^0 + CH_3^+$. In other words, the branching ratio between these two pathways changes with time delays. However, in the single pulse measurement, we see the dominant one is $CH_4^+ \rightarrow H^0 + CH_3^+$.

Given that the two fragments are separated fast from each other (approximately 10 Å after 100 fs from the KER dependence), the probe pulse does not influence the alignment of the ions. Consequently, the observed angular distribution directly reflects the emission

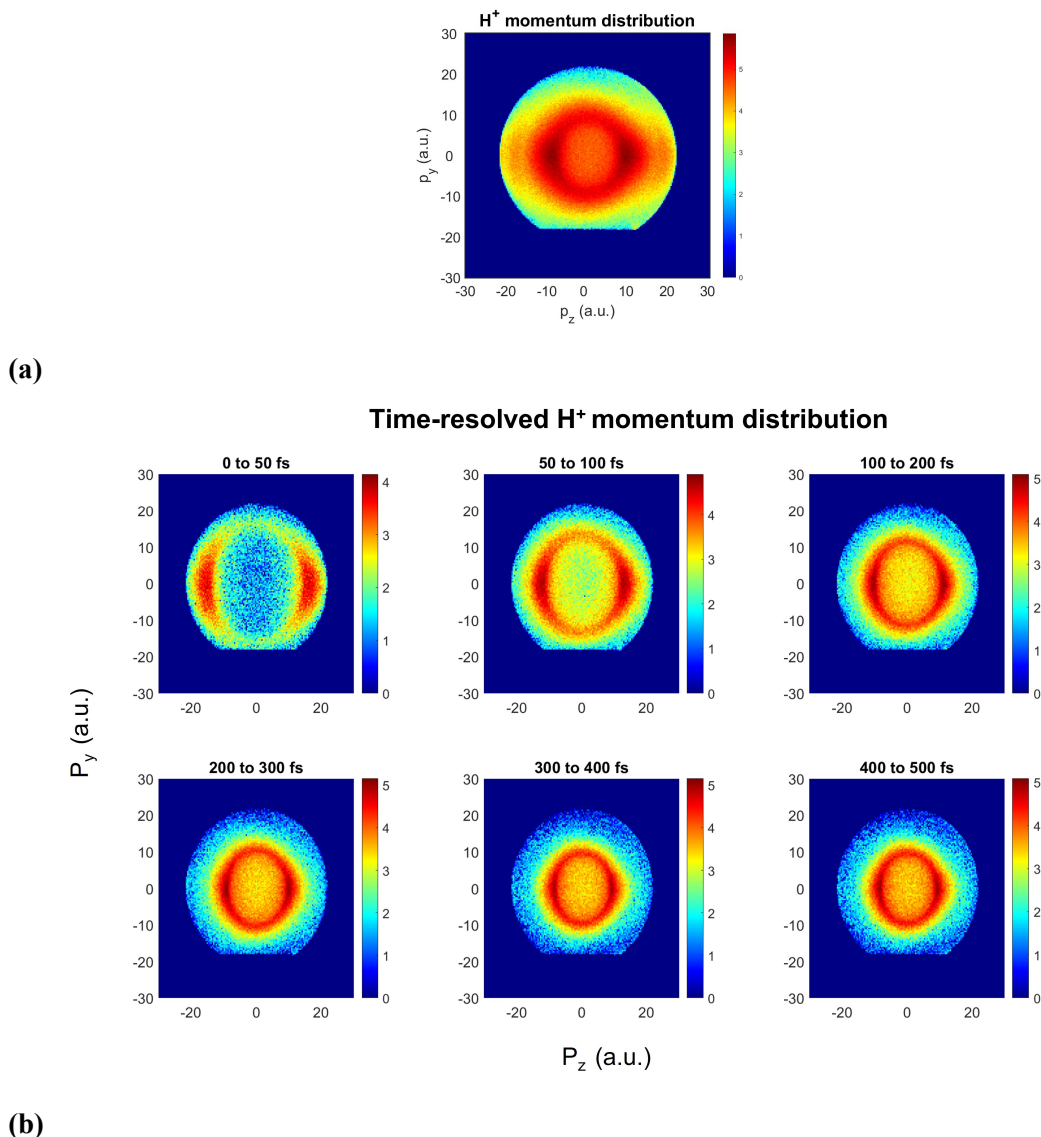


Figure 5.9. (a) H^+ momentum distribution integrated over all time delays. (b) H^+ momentum distribution at different time intervals.

directions of the dissociating fragments immediately after the pump pulse. As a result, the change of angular distribution is a direct reflection of the CH_4^+ molecular evolution with different configurations.

The observation of changes in the branching ratio suggests a plausible explanation: the two dissociation pathways are driven by different electronic states of the methane cation, namely the ground X state and the excited A state, as introduced in the last section. And for two different cation states, it takes different evolution times to dissociate into fragments. For pathway $CH_4^+(X) \rightarrow CH_3^+ + H^0$ occurs over a longer timescale compared to $CH_4^+(A) \rightarrow CH_3^0 + H^+$. This means the pathway leading to neutral hydrogen is initially suppressed. As a result, at very short time delays, $CH_4^+(X)$ cation does not dissociate into

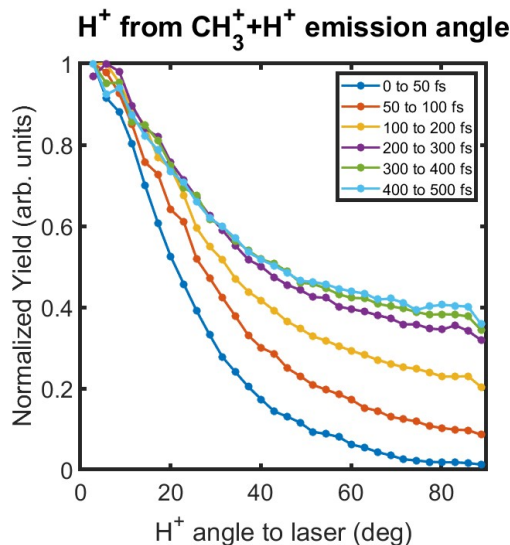


Figure 5.10. Yield of H^+ as a function of emission angle with respect to laser polarization axis at different time intervals. The deep blue curve represents the times from 0 to 50 fs, while the red, yellow, purple, green, and light blue curves correspond to additional time slices, as indicated in the legend in the top-right corner.

fragments, which may explain why this dominant channel is absent in the early stages, as well as why the isotropic distribution in momentum is missing. As the time delay increases, the dissociation process $CH_4^+(X) \rightarrow CH_3^+ + H^0$ is initiated, leading to an enhancement in the count rate and the emergence of additional features in the emission angular distribution.

5.3 H_2^+ Formation from CH_4^+ Dissociative Ionization

Now, we focus on the neutral molecular hydrogen H_2^0 and singly charged molecular hydrogen H_2^+ fragments observed in both single-pulse and pump-probe measurements. Similar to the hydrogen case, two pathways contribute to the formation of charged H_2^+ and neutral H_2^0 fragments.

For singly charged cations, the two dissociation channels are:



Once again, the emission angle of H_2^+ exhibits a dependence on the laser polarization (despite some mixing with a hydrogen background), whereas the neutral H_2^0 shows an isotropic distribution. This agrees with the theoretical calculation from the supplementary materials of [67] that $CH_2^0 + H_2^+$ is produced by the A state of CH_4^+ while $CH_2^+ + H_2^0$ is produced by the lower X state of CH_4^+ .

By applying this characteristic to the pump-probe scheme, it is observed that the dissociation pathway (5.5) leads to H_2^0 taking a longer time compared with the H_2^+ case in (5.6).

Another important observation is that H_2 formation involves both bond-breaking and bond-formation processes. From the pump-probe measurements, it can be seen that H_2^+ starts to show up in the KER plot within the first 10 fs.

5.3.1 Characterization of Fragmentation Pathways from Single Pulse Measurement

The analysis of protons as in Section 5.2 can be applied to the case of H_2 here.

The schematics for the pathways (5.5) and (5.6) are presented in Fig. 5.11.

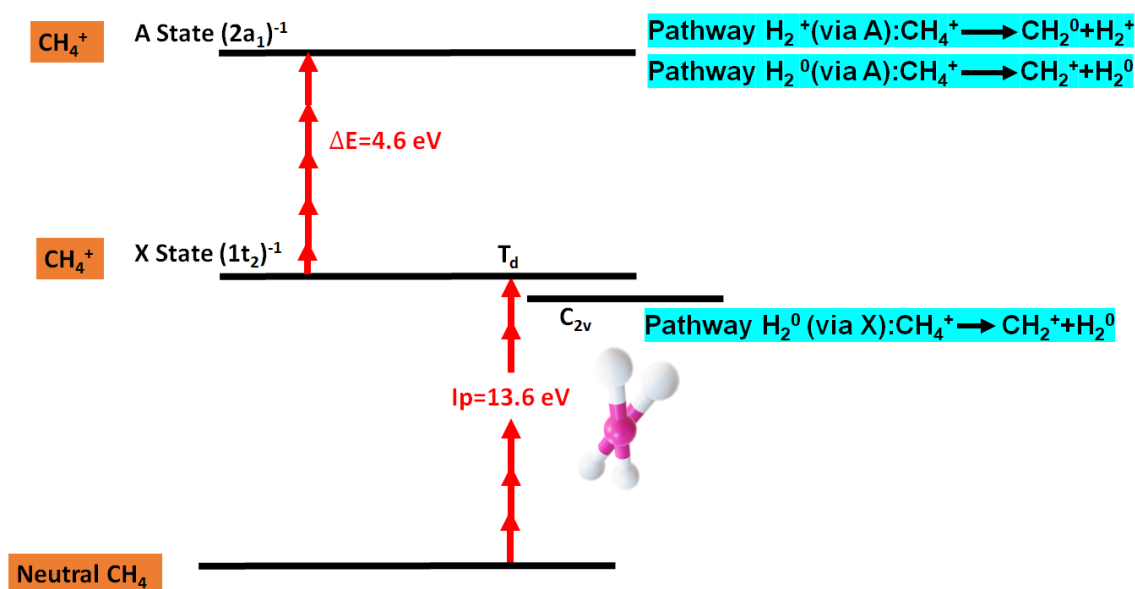


Figure 5.11. Schematic representation of dissociation pathways (5.5) and (5.6). Neutral molecular hydrogen can be formed via either the X or A state, while charged H_2^+ is only produced from the A state.

For the single-pulse measurement, the kinetic energy of the charged fragments and the momentum distributions are plotted in Fig. 5.12.

The emission angular dependency of molecular hydrogen is similar to that of protons, as shown in Fig. 5.13. In the momentum distribution plot, CH_2^+ (representing H_2^0) exhibits an almost isotropic distribution, while H_2^+ is ejected along the laser polarization. (One may notice that for H_2^+ , a strong isotropic component with nearly zero momentum is observed at the center, which is most likely due to residual gas in the chamber rather than dissociation from methane. Unfortunately, this cannot be entirely excluded from the data analysis. This can be seen better in the appendix under another laser polarization condition as Fig. B.2.

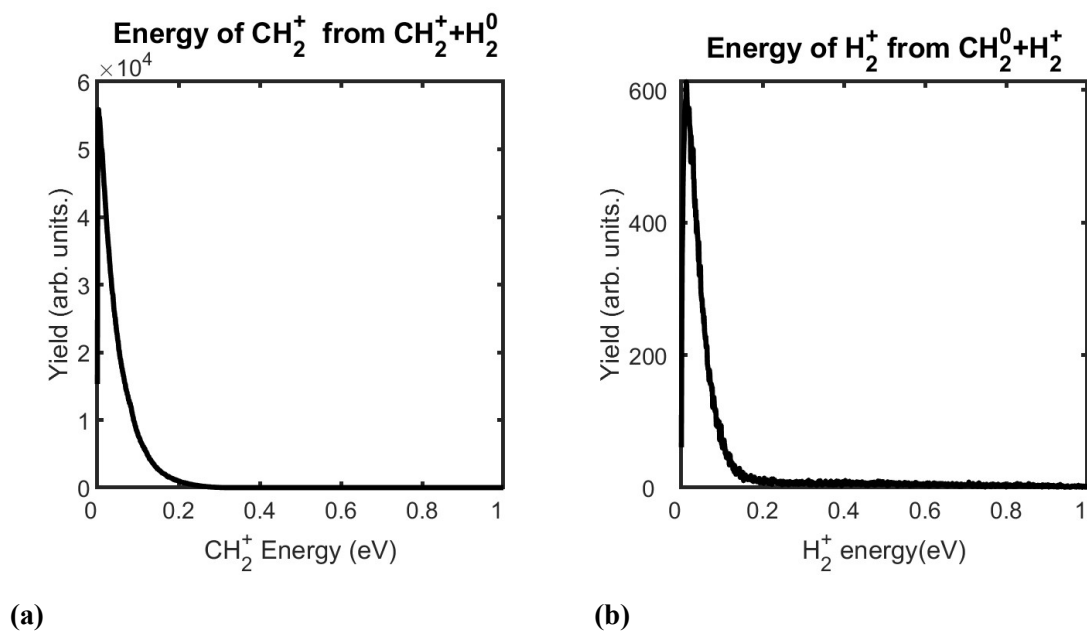


Figure 5.12. (a) Energy of CH_2^+ from channel $CH_4^+ \rightarrow CH_2^+ + H_2^0$. (b) Energy of H_2^+ from $CH_4^+ \rightarrow CH_2^0 + H_2^+$.

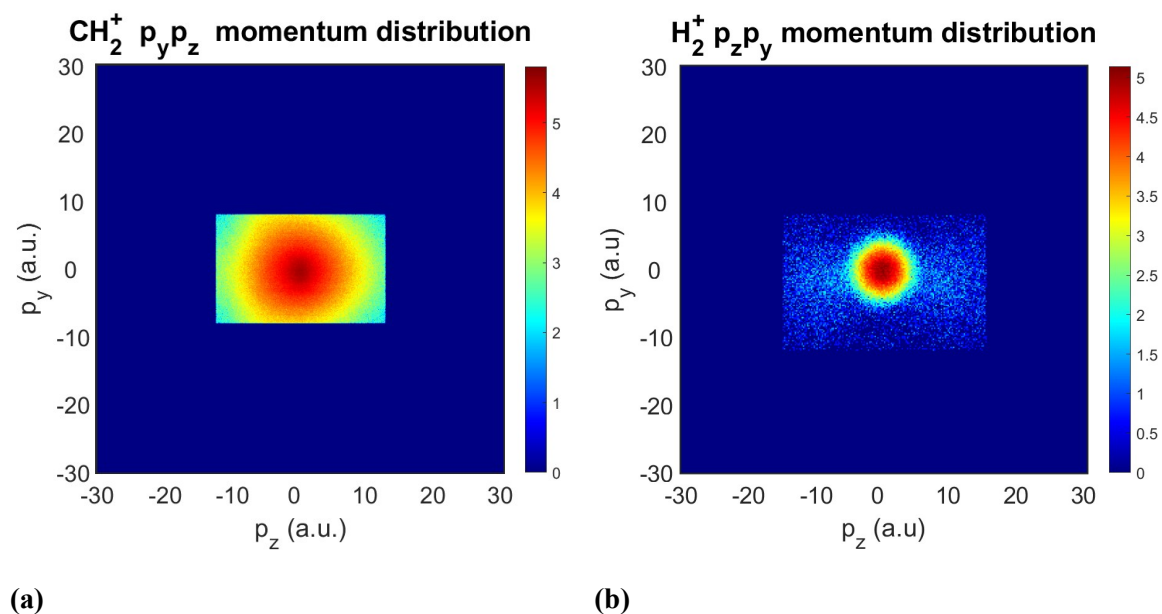
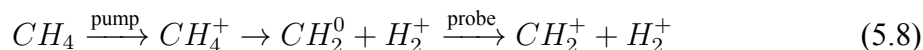
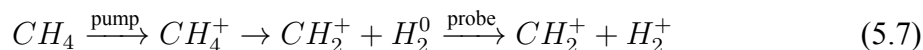


Figure 5.13. (a) CH_2^+ momentum distribution from channel $CH_2^+ + H_2^0$. (b) H_2^+ momentum distribution from channel $CH_2^0 + H_2^+$.

The branching ratio between the channels $CH_2^+ + H_2^0$ and $CH_2^0 + H_2^+$ is approximately 32:1, which is also similar to the branching ratio between channel (5.1) and channel (5.2), where the neutral hydrogen (CH_3^+) is dominated over the charged H^+ . Thus, the charged H_2^+ emission most likely originates from a higher CH_4^+ A state.

5.3.2 Time-dependent Molecular Hydrogen Ejection

The dissociation pathways of a singly charged methane cation that lead to hydrogen formation are:



Now, the schematics mechanism is presented in Fig. 5.14.

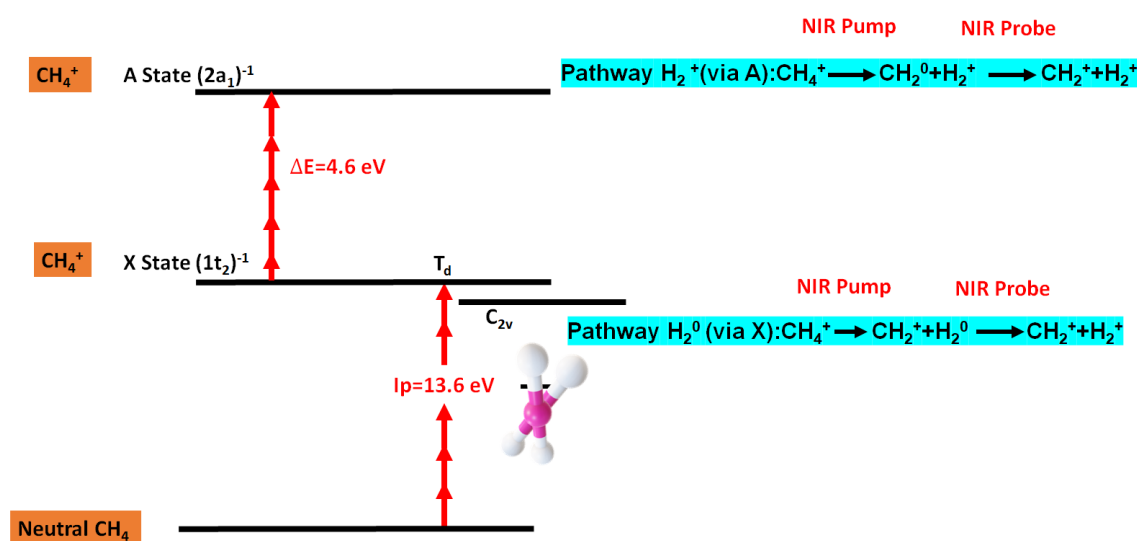


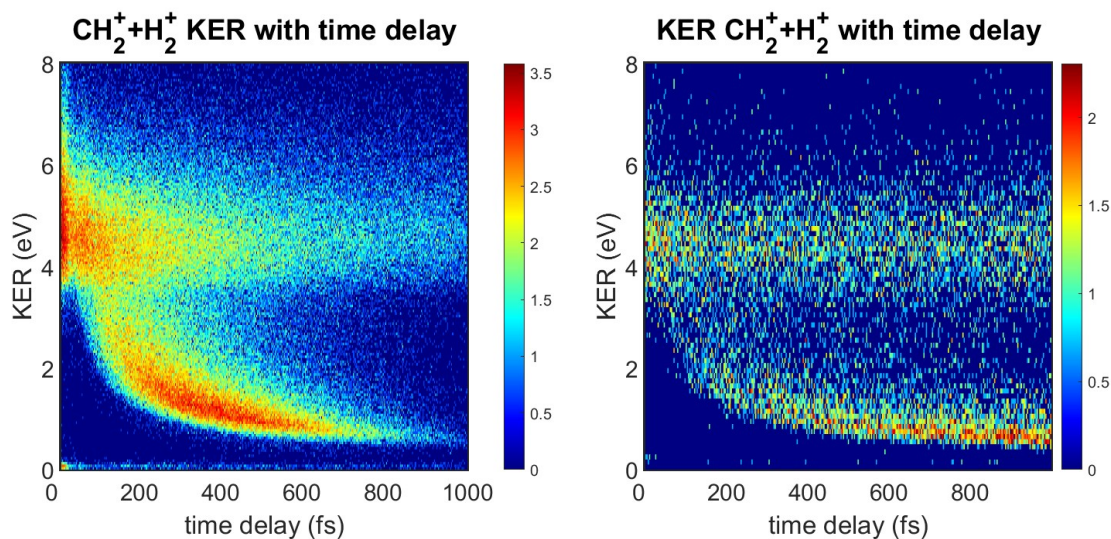
Figure 5.14. Schematic representation of dissociation channels (5.7) and (5.8). In addition to the pump pulse, the probe ionizes the residual neutral fragments, leading to the same final fragments $CH_2^+ + H_2^+$.

The kinetic energy as a function of time delay is shown in Fig. 5.15, where we observe a constant KER line corresponding to a single-pulse reaction, and a time-dependent curve resulting from sequential dissociation.

The momentum distribution of dissociated H_2^+ at different time delays is shown in Fig. 5.16 and Fig. 5.17.

From Fig. 5.16, Fig. 5.17, the behavior of $CH_2^+ + H_2^+$ is very similar to that of $CH_3^+ + H^+$: At the beginning, the ions are emitted primarily along the laser polarization. As the time delay increases, the ion emission becomes more isotropic. Based on the analysis from the previous section, the conclusion is that the isotropic channel of neutral hydrogen (coincidence detected with CH_2^+) is suppressed at the beginning, indicating that the dissociation is delayed at short time delays.

Another conclusion that can be demonstrated is that the formation time of H_2^+ is very short. The time-dependent curve shows that the H_2^+ signal appears after approximately 10 fs from Fig. 5.15 (b), which may correspond to the time needed for bond formation.



(a)

(b)

Figure 5.15. Kinetic energy release (KER) of the dissociation channel $CH_2^+ + H_2^+$ as a function of time delay. (a) Measurement using a pulse shaper. (b) Measurement using a Mach-Zehnder interferometer.

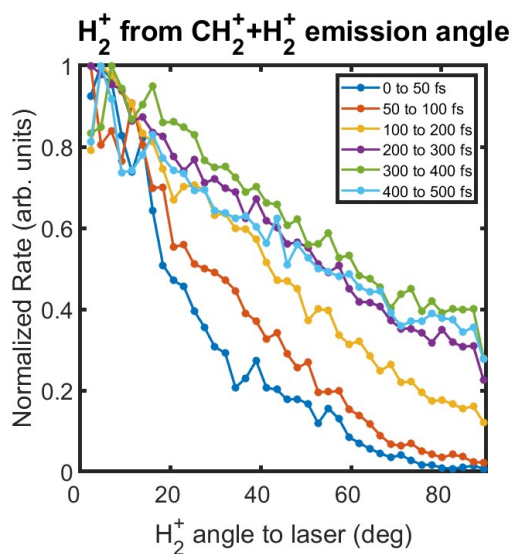
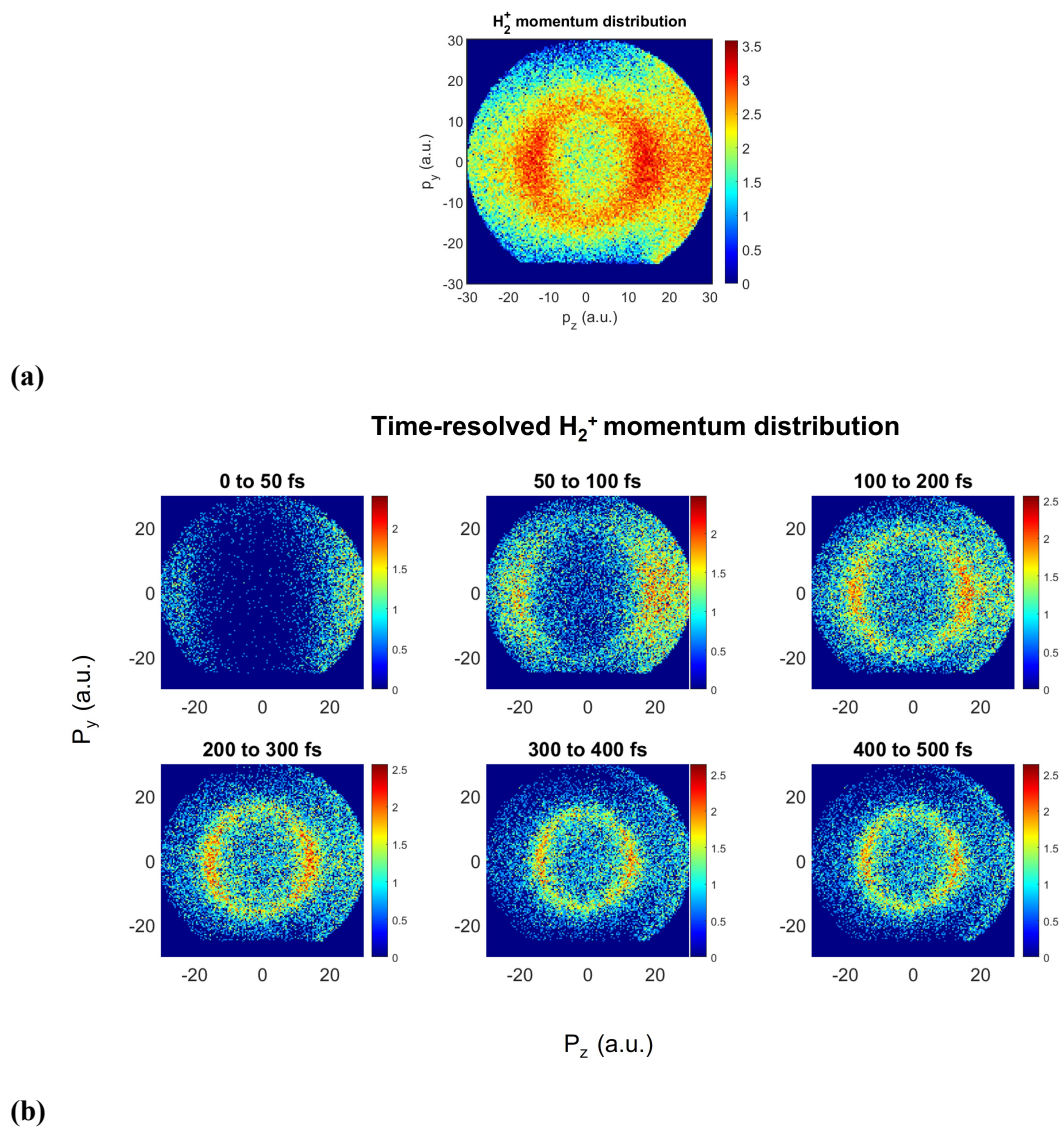


Figure 5.16. Yield of H_2^+ as a function of emission angle at different time intervals. The deep blue curve represents the time delay from 0 to 50 fs, while the red, yellow, purple, green, and light blue curves correspond to additional time slices, as indicated in the legend in the top-right corner.

The total lower yield for the H_2^+ compared with H^+ is partly due to the ionization potential for H_2^+ being higher from table 5.1.



5.4 Comparison: Proton Ejection vs Molecular Hydrogen Formation

In the previous two sections, the atomic hydrogen and molecular hydrogen dissociation channels were discussed separately in detail. In this section, their connection and comparison are analyzed.

First, dissociation velocities are examined by fitting the time-dependent KER curves. Next, variations in the count rates as a function of time delay are analyzed. Finally, potential geometric evolution including the influence of the Jahn-Teller effect is discussed.

Comparing the channels between proton ejection and molecular hydrogen formation can provide insights into the methane cation potential surface [66]. Under laser pulses, the molecule moves along potential surfaces modified by the external laser field, leading to different fragmentation pathways resulting in different fragments.

As shown in previous sections, these two channels are well analyzed separately. Here, we present these two channels together. Both channels show time-dependent and time-independent components. For the time-dependent dissociation parts, as discussed in Section 5.2.2, the probe pulse is supposed to induce a Coulomb explosion to methane cation, thus the evolution of internuclear distance R is mapping to the KER time-dependency. By fitting the time-dependent signal, the dissociating velocity can be determined using the formula:

$$E = \frac{1}{R_0 + v_0 t} + \frac{\mu}{2} v_0^2 \quad (5.9)$$

where R_0 is the initial molecular distance between the center mass of two fragments, v_0 is the fragment ejection velocity, t is the time delay, and μ is the reduced mass of the dissociating system.

As shown in Fig. 5.18c, for the case of $CH_3^+ + H^+$, if R_0 is fixed at 1.9278 a.u. based on the T_d geometry of the methane cation, the fitted dissociation velocity v_0 is 0.0065 a.u. Notably, even if the value of R_0 varies to match different methane cation geometries (e.g., R_0 from C_{3v} geometry is 1.989 a.u.), the fitted v_0 remains close at 0.0062 a.u.

Applying the same procedure to the $CH_2^+ + H_2^+$ channel, the dissociation velocity v_0 is 0.0057 a.u. if $R_0 = 1.37$ a.u. is taken from the T_d geometry.

Not only can the ejection velocity be obtained by fitting the time-dependent KER data, but the count rates for both channels are also accessible. As discussed in Section 5.2.2 and shown in Fig. 5.19, the count rate for $CH_3^+ + H^+$ increases continuously up to the longest time delay of 1 ps. In contrast, the count rate for $CH_2^+ + H_2^+$ reaches its plateau at approximately 200 fs. This difference suggests that the dissociation processes leading to proton and molecular hydrogen fragmentation evolve on different time scales.

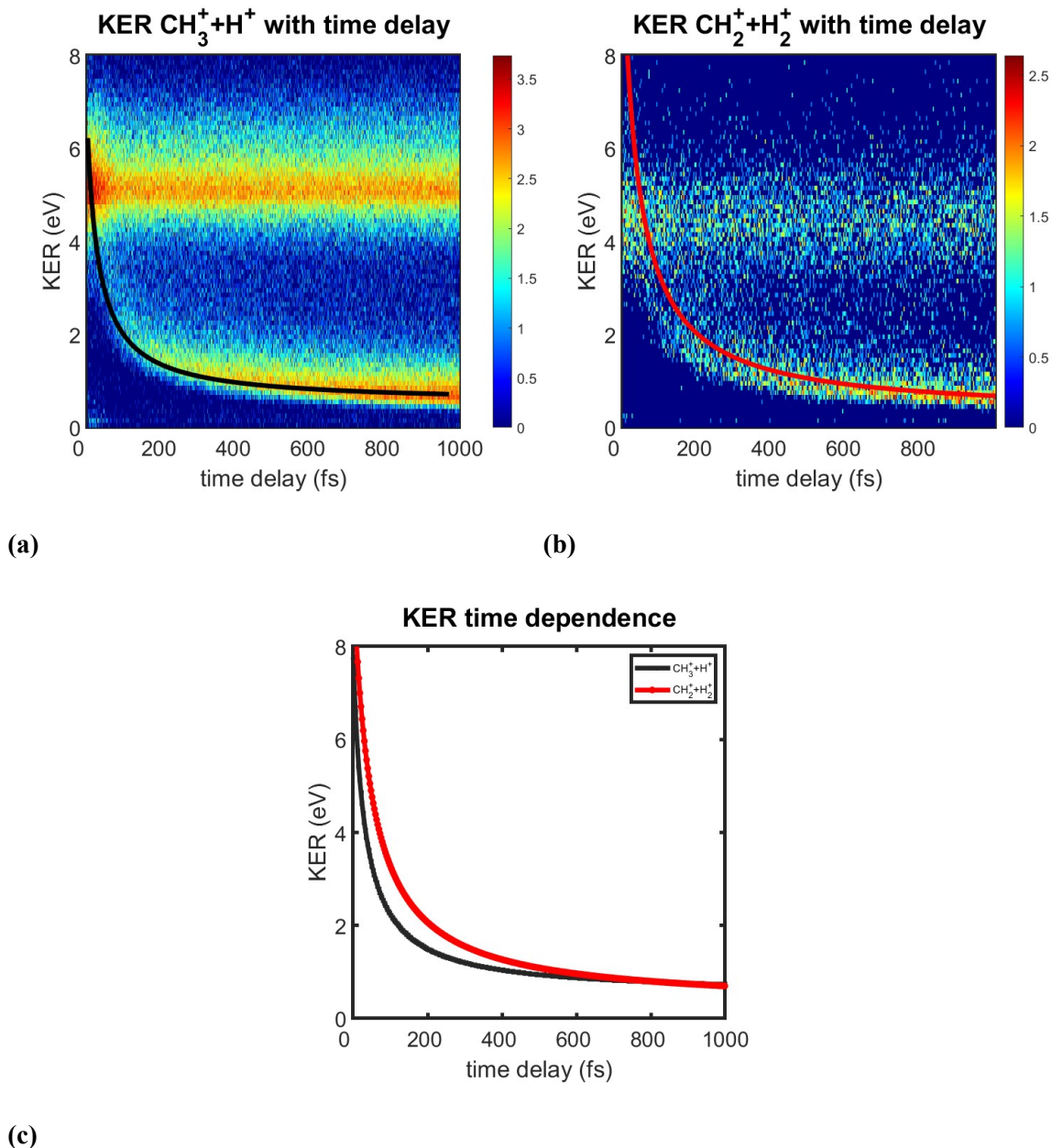


Figure 5.18. Kinetic energy release (KER) of two dissociation channels: (a) involving proton ejection ($CH_4 \rightarrow CH_3^+ + H^+$) and (b) involving charged molecular hydrogen ejection ($CH_4 \rightarrow CH_2^+ + H_2^+$). The black curve in (a) and the red curve in (b) are fitted separately with the equation $E = \frac{1}{R_0 + v_0 t} + \frac{\mu}{2} v_0^2$. (c) Fitted KER time-dependency.

As discussed in the previous section, the increase in yield with time delay is primarily attributed to the X state. Consequently, the differences in count rate between the proton and molecular hydrogen channels can be linked to JT-induced distortion processes within the X state.

Fig. 5.20 shows the combined schematics of these two channels. At the ground X state, CH_4^+ cannot maintain T_d symmetry and undergoes the Jahn-Teller induced nuclear rear-

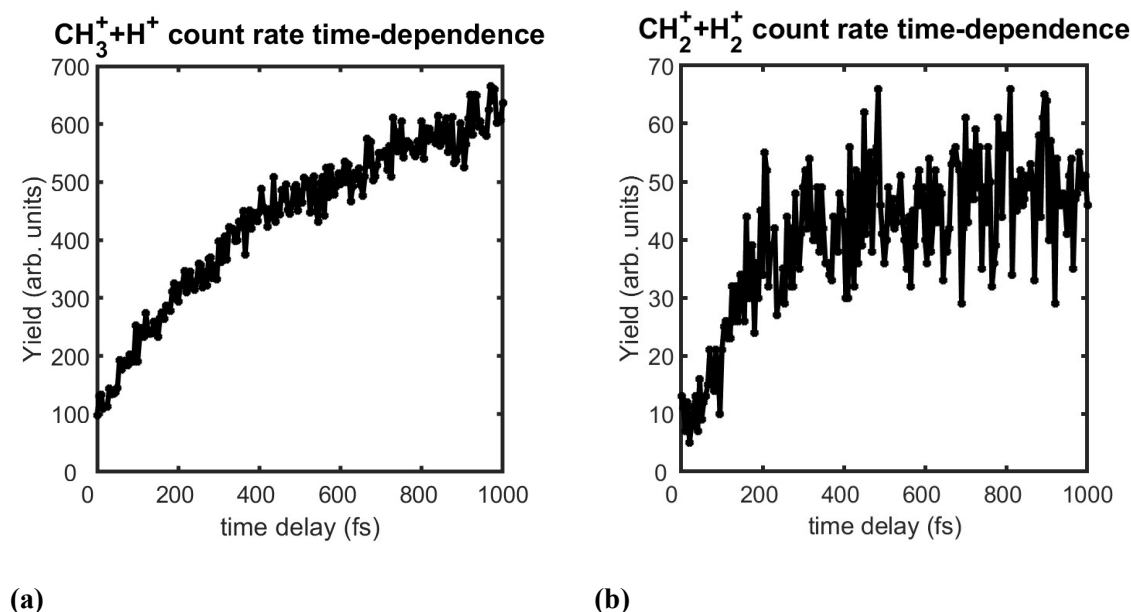


Figure 5.19. Yield as a function of time delay for the time-dependent dissociation events. (a) Channel $\text{CH}_3^+ + \text{H}^+$. (b) Channel $\text{CH}_2^+ + \text{H}_2^+$.

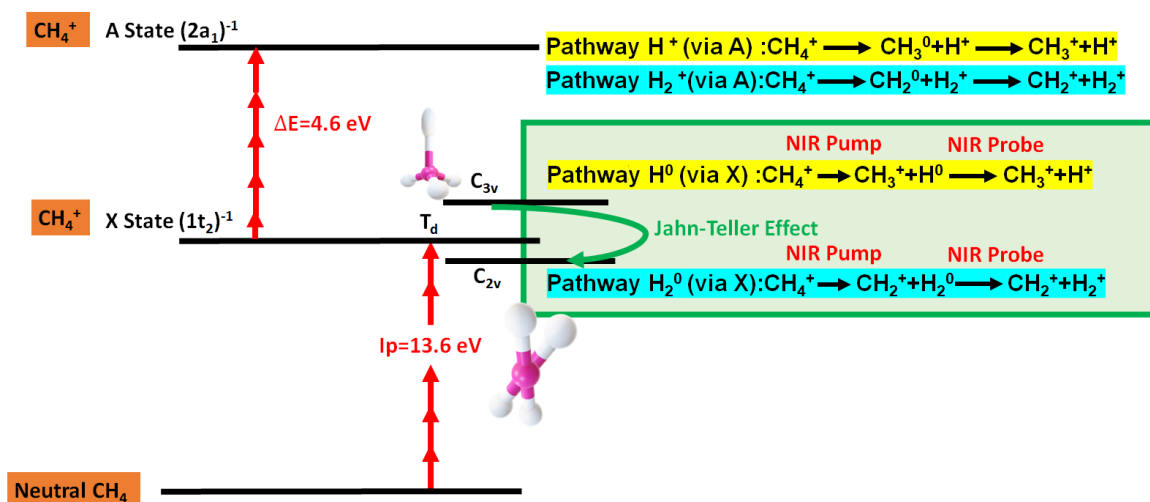


Figure 5.20. Schematic of the channels discussed in Sections 5.1, 5.2, 5.3, and 5.4. The X state of CH_4^+ , which exhibits three-fold degeneracy, undergoes Jahn-Teller (JT) distortion when exposed to strong fields. One JT distortion pathway is highlighted in the green box: $T_d \rightarrow C_{3v} \rightarrow C_{2v}$. The C_{3v} configuration leads to atomic hydrogen emission, while the C_{2v} configuration results in molecular hydrogen formation.

rangements, as introduced in Chapter 2, Section 2.3. As shown in Fig. 5.20, the JT distortion follows the geometric evolution: $T_d \rightarrow C_{3v} \rightarrow C_{2v}$. The C_{3v} symmetry leads to proton emission, while the C_{2v} configuration results in molecular hydrogen formation. By comparing Pathway H^0 and Pathway H_2^0 , it is possible to extract the JT distortion time from

C_{3v} to C_{2v} .

A published paper in 2021 [66] investigated the Jahn-Teller effect in methane cations by comparing the fragmentation channels discussed above with a similar approach to the one used in this thesis. Their measurements reveal that the $CH_2^+ + H_2^+$ channel reaches the same KER value approximately 20 fs later than the $CH_3^+ + H^+$ channel as shown in Fig. 5.21. This 20 fs time delay between the two channels is interpreted as the JT distortion time from C_{3v} to C_{2v} .

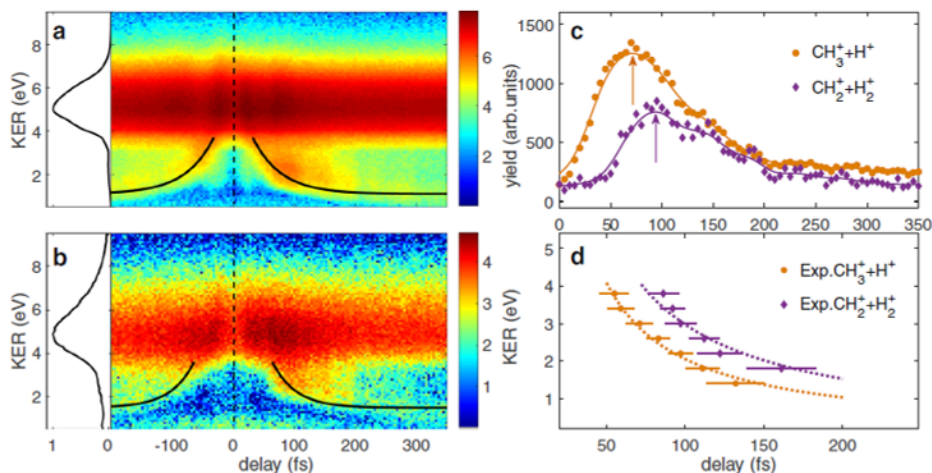


Figure 5.21. Comparison between two channels of $CH_3^+ + H^+$ and $CH_2^+ + H_2^+$ from the reference [66]. (a) Time-dependent KER from channel $CH_3^+ + H^+$. (b) Time-dependent KER from channel $CH_2^+ + H_2^+$. (c) Time-dependent yield variation for both channels at KER = 3.0 eV. (d) Extracted KER time-dependency for two channels.

A similar comparison can be made with our measurements, as shown in Fig. 5.22. In our case, the yield rate is observed at a KER value of (3.0 ± 0.1) eV, and the peak difference is approximately 50 fs, compared to 20 fs in the previous study [66]. The different evolution times can be attributed to differences in laser intensity and pulse duration. The duration of the pulse employed in this thesis is one-third of theirs, while the laser intensity is comparable in both cases. One possible explanation for the observed peak difference is that the potential energy surfaces are modified differently under varying laser conditions, such as pulse shape, pulse duration, spectrum, etc. Firstly, for both experiments (Li's [66] and the thesis), the higher cation A states can not be completely neglected. Secondly, multiple JT distortion pathways of CH_4^+ could directly lead to the C_{2v} geometry without passing through C_{3v} [65]. The final fragmentation channel $CH_2^+ + H^+$ originates from the C_{2v} configuration but does not necessarily transition through C_{3v} . Moreover, both experiments are conducted with the NIR field. The strong-field nature of NIR pulse excitation (including coupling between excited states during the laser pulse) makes it difficult to capture a state-resolved

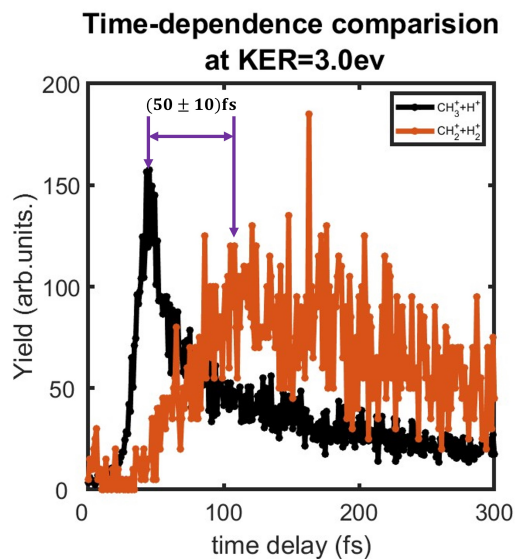


Figure 5.22. Time-dependent comparison between the $CH_3^+ + H^+$ and $CH_2^+ + H_2^+$ channels from our measurements. Both curves are taken at $KER = 3.0$ eV, similar to Fig. 5.21 (c), where the peak position difference between the two channels is 20 fs. In our measurement, this peak difference is (50 ± 10) fs, as indicated by the purple arrows.

picture of the JT effect. The reason is the following: due to the low photon energy (1.5 eV at 800 nm), all dissociation pathways proceed through multiphoton processes. As a result, multiple photofragmentation processes are mixed and compete with the JT distortion, making it ambiguous to conclude the initial cation states. A more detailed explanation of these effects will need to be confirmed by theoretical studies with defined laser pulses.

5.5 Summary of this Chapter

To summarize the dissociation of atomic hydrogen and molecular hydrogen from methane cations, the most simple but useful observation is that neutral fragments and ionic fragments can be differentiated by analyzing their emission angles relative to the laser polarization.

The H^0 primarily dissociates from the ground X electronic state of methane cations through a C_{3v} geometry, while the H^+ is formed via the excited A state of the cations. Single-pulse measurements reveal that H^0 is emitted isotropically, while H^+ is preferentially ejected along the laser polarization axis. The dominant channel is the H^0 dissociation pathway from the ground X state.

The distinct angular momentum characteristics of these two pathways are utilized in a pump-probe experiment, where the kinetic energy release (KER) signatures of both pathways overlap. Through angular momentum analysis, we observe that the branching ratios between these two channels vary with time delay. At short time delays, the H^+ channel is

dominant, while the H^0 channel prevails at longer time delays.

The dissociation of molecular hydrogen exhibits similar characteristics: H_2^0 , induced from the C_{2v} geometry of the ground X state, is ejected isotropically. The neutral H_2^0 channel is also the dominant channel in single-pulse measurements. H_2^+ , is dissociated from the electronically excited A state. It is found that H_2^+ is emitted along the laser polarization. In the pump-probe scheme, the charged H_2^+ dominates at early time delays, while the neutral H_2 becomes prominent at longer time delays.

Since the X state is a three-fold degenerate state, it undergoes the Jahn-Teller (JT) effect by transitioning from its tetrahedral T_d symmetry to a C_{3v} configuration and finally reaching its potential minimum in the C_{2v} configuration. During this distortion process, the C_{3v} configuration leads to the fragmentation channel of:



while the C_{2v} configuration results in:



By measuring the distinct time dependencies of these two channels, the JT-induced molecular evolution time from C_{3v} to C_{2v} can be extracted as (50 ± 10) fs.

However, due to the non-negligible contribution from the A state, the JT characterization time obtained here is not state-resolved but rather represents an average over different electronic states.

In summary, the multiphoton processes induce multiple photofragmentation pathways, making it extremely challenging to differentiate the electronic states of cations. We present a direct experimental method to distinguish the electronic cation states X and A through angular momentum analysis. Additionally, our NIR experiments confirm that the fragmentation patterns reflect Jahn-Teller (JT)-induced structural dynamics in methane cations. By combining angular momentum analysis with time-resolved measurements, our approach provides new insights into ultrafast molecular fragmentation processes under strong laser fields.

Chapter 6

Three-Body Fragmentation of CH₄

Methane can dissociate into more than two fragments under strong laser fields. This chapter examines the three-body dissociation channel $CH_2^+ + H^+ + H^+$. As discussed earlier, strong-field ionization induces significant geometric distortion in methane. Depending on the instant molecular geometry at the probe pulse, different fragmentation pathways may occur, ultimately yielding the same final products: $CH_2^+ + H^+ + H^+$.

The mixture of multiple pathways makes it challenging to distinguish between these processes. This chapter aims to disentangle the different fragmentation pathways through detailed analysis and to clarify the origin of each pathway.

This chapter is structured as follows: Four distinct dissociation pathways are identified based on the energy correlation between the two dissociated H^+ fragments. The experimental observations are summarized in Section 6.1. A detailed analysis of the two concerted pathways is presented in Section 6.2, while the two sequential pathways are discussed in Sections 6.3 and 6.4. A comparison and correlation of these pathways are provided in Section 6.2, followed by supporting evidence from classical simulations in Section 6.6. Finally, a summary of this chapter is given in Section 6.7.

6.1 Separating Fragmentation Pathways Using Two-Proton Energy Correlation

For the channels leading to fragments of $CH_2^+ + H^+ + H^+$, the final energy of two H^+ ions is a direct measure of the instantaneous nuclear distance between the released hydrogen and the remaining molecule after the pump pulse. The correlation between these two H^+ ions reflects the geometric distortion of the charged methane ionized by the pump pulse.

A 2024 study [117] explored proton correlation induced by a **single-pulse** measurement with a duration of approximately 30 fs in the same dissociation channel, leading to the frag-

ments $CH_2^+ + H^+ + H^+$. With a relatively low intensity of $1 \times 10^{14} \text{ W/cm}^2$, the proton energy correlation appears in the diagonal region A and non-diagonal region B, as shown in Fig. 6.1(a). The appearance of regions A and B is attributed to the **concerted pathway**, in which the methane molecule undergoes direct triple ionization by a single pulse, forming CH_4^{3+} .

Differences between region A and region B arise from different vibrational stretching modes of CH_4^{3+} . For region A, two protons are stretched symmetrically with respect to the remaining CH_2^+ , which leads to two H^+ appearing on the diagonal line with identical energy. For region B, two protons undergo an asymmetrical stretching mode, leading to different final energies in the non-diagonal lines in the energy correlation plot.

With a higher intensity of $3 \times 10^{14} \text{ W/cm}^2$, another non-diagonal pattern marked as region C appears in Fig. 6.1(b), which is explained as a **sequential pathway**. In the sequential pathway, the dissociation happens not at once but in steps while interacting with the pulse. They explored the possibility of the dissociation process: $CH_4 \rightarrow CH_3^{2+} + H^+ \rightarrow CH_2^+ + H^+ + H^+$.

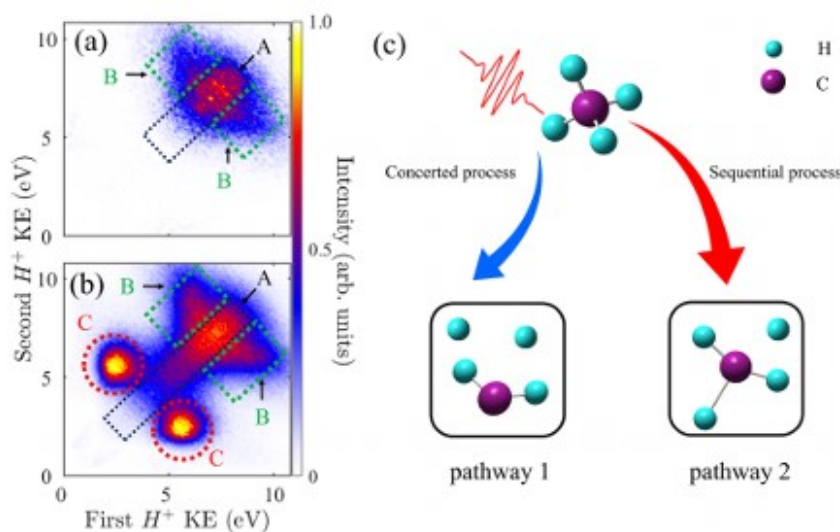


Figure 6.1. Energy correlation between two H^+ from $CH_4^+ + H^+ + H^+$ from single-pulse measurement. The figure is taken from Li [117] without change.

Comparison between Single-Pulse Measurement and Pump-Probe Experiment

Similar results were observed in our single-pulse measurement using a 10 fs pulse at a peak intensity of $3 \times 10^{14} \text{ W/cm}^2$, as illustrated in Fig. 6.2. Both studies are in agreement with each other. The next step involves investigating the mechanism of each pathway in detail using a pump-probe scheme.

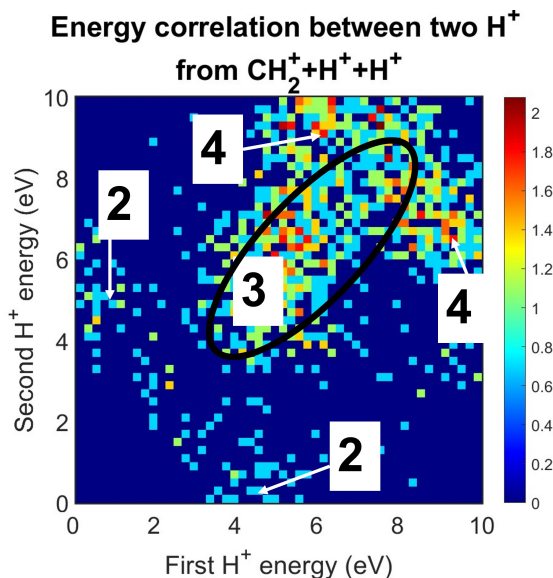


Figure 6.2. Energy correlation between two H^+ fragments produced in the dissociation channel $CH_4 \rightarrow CH_2^+ + H^+ + H^+$, obtained from single-pulse measurement.

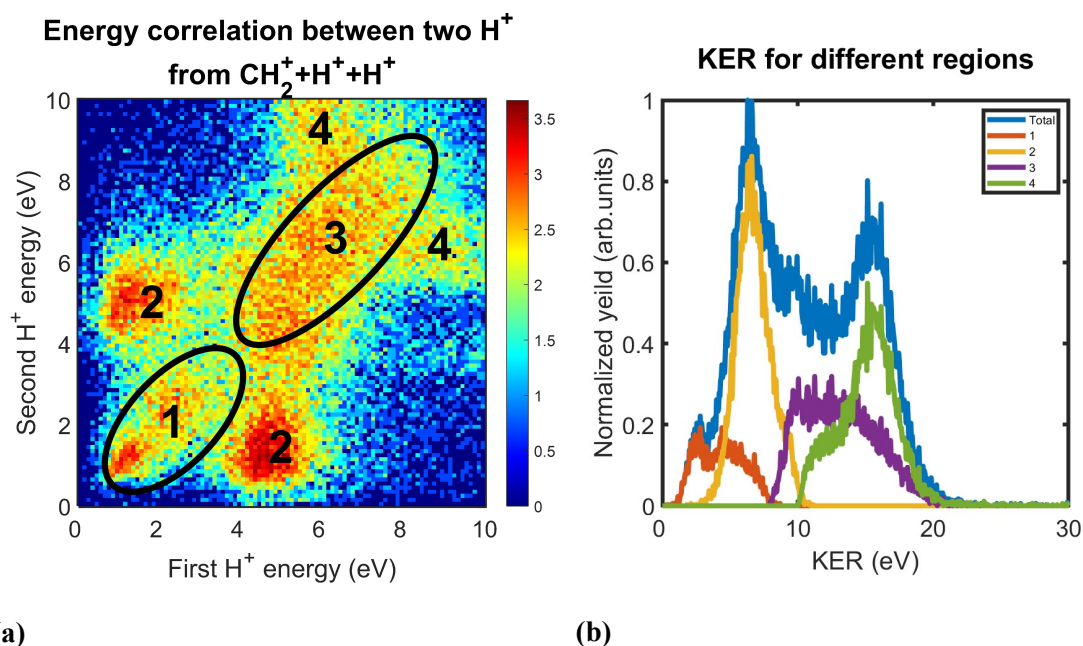


Figure 6.3. Energy correlation between two H^+ from $CH_2^+ + H^+ + H^+$ from the pump-probe measurement, different regions are marked with numbers 1 to 4 in (a). The KER from three fragments coincidence is plotted in (b).

As shown in Fig. 6.3, the energy correlation between the two H^+ ions from the three-body coincidence measurements of the pump-probe experiment is presented. Fig. 6.3 closely resembles Fig. 6.2, where the higher energy diagonal features marked as region 3 and non-diagonal regions marked as regions 2 and 4. The distinct feature of the pump-probe experiment is the low-energy component, designated as region 1, which extends along the diagonal

line originating from region 3.

6.1.1 Pathway Separation

By examining the energy correlation between two H^+ , we confirm that multiple dissociation pathways contribute to the formation of the same final fragments, $CH_2^+ + H^+ + H^+$. To gain a deeper understanding of each pathway and its dynamics, the time-dependent energy correlation of the two protons is presented in Fig. 6.4. For a comprehensive view of the three-body fragmentation process, the time-dependent KER of all three fragments, including CH_2^+ , is shown in Fig. 6.5. Plot (a) illustrates the total KER distribution across all pathways, while plots (b)–(e) display the KER distributions corresponding to regions 1 to 4, respectively.

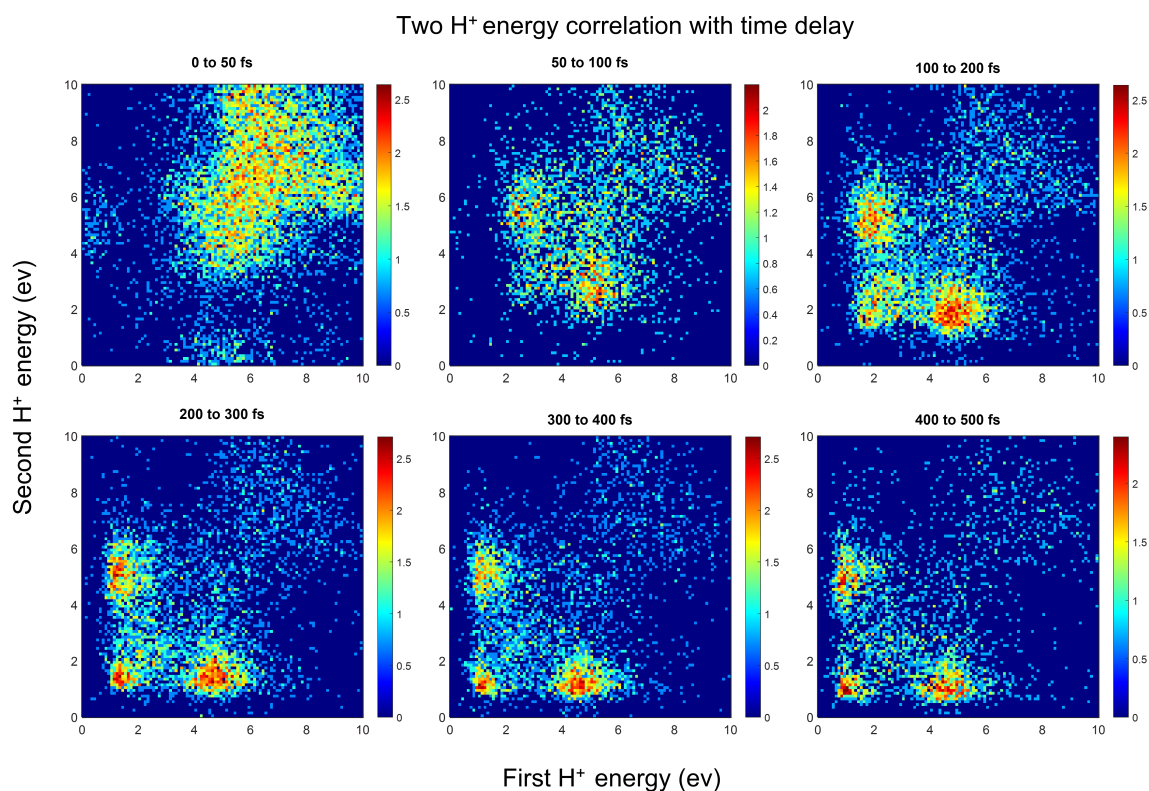


Figure 6.4. The energy correlation between two H^+ ions plotted at different time delays.

From the time-resolved measurements, two distinct features are observed. The first is a **time-independent** constant KER component, primarily originating from regions 3 and 4. (The decrease in color bar intensity for these regions at larger time delays results from the intensity reduction induced by the SLM, as introduced in Chapter 5.) These constant KER features indicate that regions 3 and 4 arise from a direct Coulomb explosion initiated from a higher charged state compared to regions 1 and 2 (which will be explained in the section 6.2). Consequently, these pathways are referred to as **concerted pathways**.

(a)

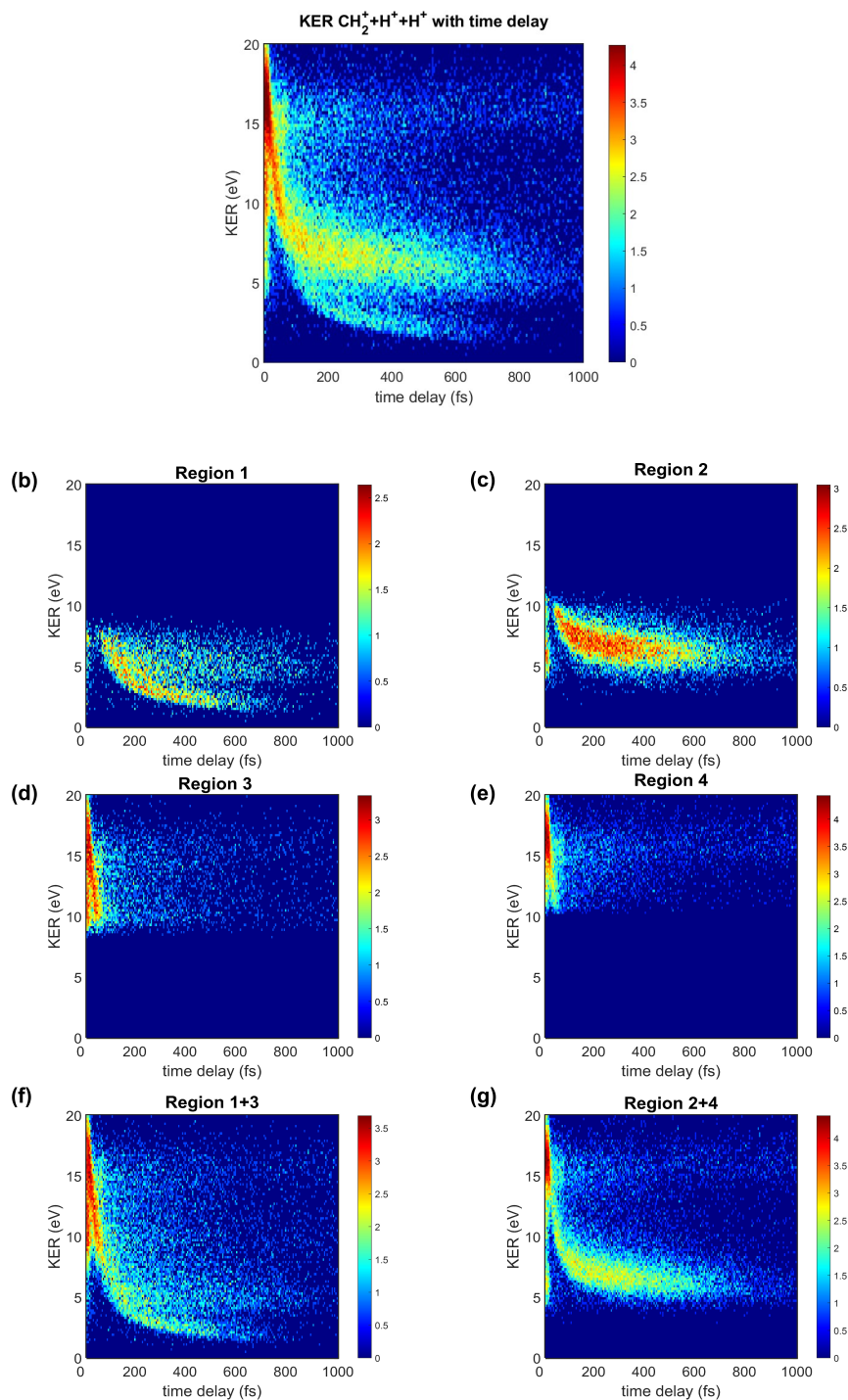


Figure 6.5. (a) Time-dependent KER for $CH_2^+ + H^+ + H^+$. (b)-(e) Time-dependent KER for regions 1 to 4, respectively. (f) Diagonal regions from H^+ correlation: Combined KER time dependency for regions 1 and 3. (g) Non-diagonal regions H^+ correlation: Combined KER time dependency for regions 2 and 4.

The second feature consists of two **time-dependent** KER curves, predominantly contributed by regions 1 and 2. The observed time dependence suggests that these pathways do not result from a single pulse but instead involve sequential interactions with both the pump and probe pulses.

By combining the diagonal regions 1 and 3, Fig. 6.5(f) unexpectedly reveals that the time-dependent signal in region 1 exhibits continuity with the constant KER curve from region 3. This observation suggests that region 1 originates from the same sequential fragmentation process as region 3. In the next, region 1 together with the first 50 fs from region 3 is referred to as the **sequential symmetric region**. Similarly, Fig. 6.5(g) shows that the time-dependent signal from region 2 extends into region 4, indicating a distinct sequential fragmentation pathway, which we refer to as the **sequential asymmetric region**.

As introduced in Chapter 4, the Newton plot reveals the relative correlation between fragments in space. Fig. 6.6 presents the Newton plots for the investigated dissociation pathways. To distinguish between the two H^+ ions and highlight asymmetric contributions, the higher-energy H^+ in each event is designated as the ‘fast’ proton and plotted in the upper part of the Newton plot, while the lower-energy H^+ is classified as the ‘slow’ proton and shown in the lower part. The Newton plot for all regions combined is shown in Fig. 6.6 (a), while the Newton plots for four distinct regions are displayed separately in Fig. 6.6 (b)-(e).

By combining the Newton plots with the analysis of KER time dependence, the key characteristics of the different regions are summarized as follows:

- **Sequential symmetric region:** represents region 1, and the continuous KER component extends up to a delay time of the first 50 fs in region 3. This part only emerges in a pump-probe scheme. Two H^+ ions exhibit the same final energy.
- **Sequential asymmetric region:** represents region 2 and the continuous KER component extends up to a delay time of the first 50 fs in region 4. This channel is observed both in a single pulse measurement and a pump-probe experiment. The feature is one low energy H^+ always corresponds to a high energy H^+ .
- **Region 3 concerted pathway:** Despite the time-dependent signal extending from region 1 to region 3 at the first 50 fs, there are two separate time-independent constant KER curves observed, corresponding to two identical protons. These constant KER lines are peaked at 11 eV and 14 eV, respectively.
- **Region 4 concerted pathway:** Two protons have different final energies, peaking at 8.8 eV and 6.7 eV, respectively, and do not exhibit clear time dependence.

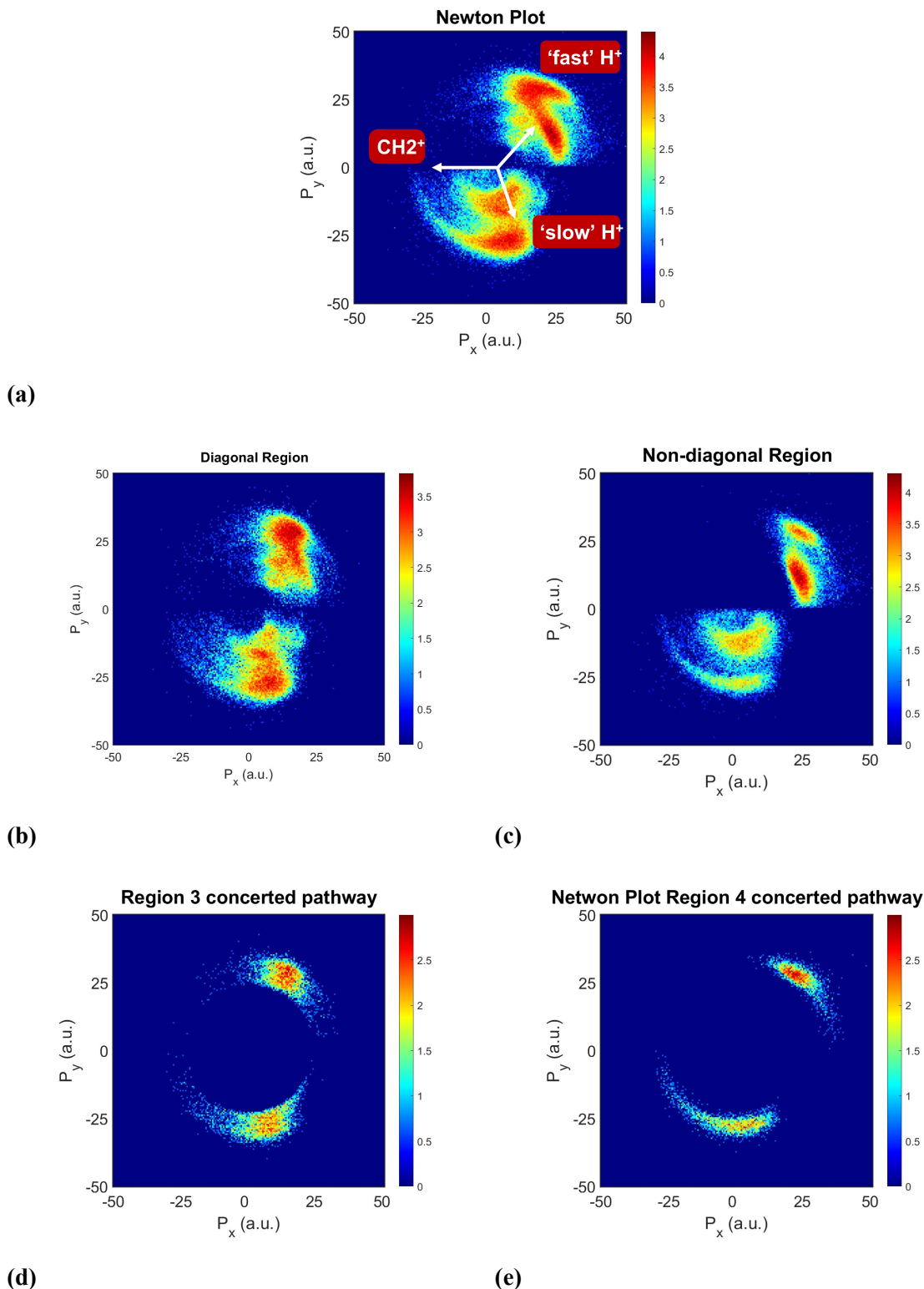


Figure 6.6. (a) Newton plot for all regions integrated. The higher-energy, ‘fast’ proton is placed in the upper plane ($y > 0$), while the lower-energy, ‘slow’ proton is plotted in the bottom half. (b) Newton plot for the diagonal region 1 and the first 50 fs of region 3, which shows a time-dependent continuity with region 1. (c) Newton plot for the non-diagonal region 2 and the first 50 fs of region 4, which shows a time-dependent continuity with region 2. (d) Newton plot for the concerted part of region 3, where the events are time-independent. (e) Newton plot for the concerted part of region 4, where the events are also time-independent.

By analyzing the correlation between the two H^+ ions, four distinct pathways are identified and labeled as separate regions. The next step is to investigate the time dynamics of each process in greater detail.

6.2 Concerted Fragmentation

Concerted fragmentations, corresponding to the time-independent parts of region 3 and region 4, take place within a single pulse, meaning that three electrons are removed during the pulse duration of approximately 10 fs, resulting in relatively higher KER.

The next step is to analyze these two concerted pathways separately. For this, Dalitz plots are presented here to provide an idea of how the energy is distributed between fragments.

Region 3

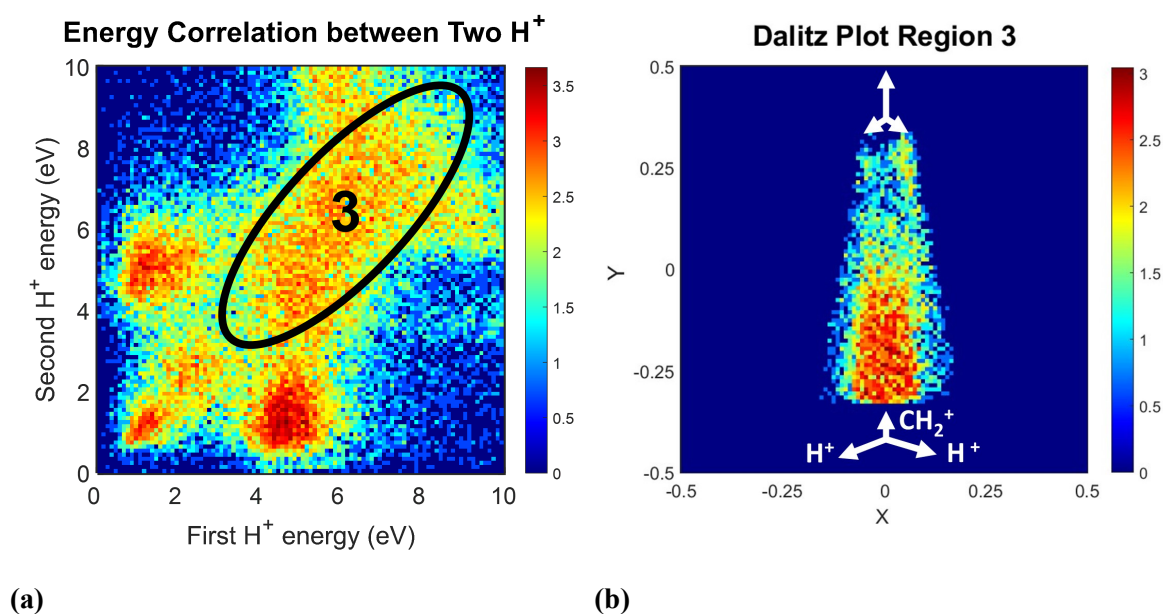


Figure 6.7. (a) Energy correlation between two H^+ ions from three-body fragmentation. Region 3 corresponds to the higher-energy diagonal part without time dependency. (b) Dalitz plot for Region 3. The schematic diagram (white) illustrates that both H^+ ions share the momentum equally. The definition of the Dalitz plot and its corresponding axes can be found in Chapter 4, Section 4.2.3.

Region 3 exhibits equal energy distribution between two protons, as shown in the Dalitz plot of Fig. 6.9 (b). The identical energy of the two H^+ ions suggests that the molecule undergoes a symmetric distortion, where two C-H bonds are identical in length and break simultaneously. This observation aligns with the findings of [117], where the geometry of

CH_4^{3+} was simulated. Their simulation shows that the two C-H bond lengths extend to 4.7 a.u upon Coulomb explosion induced by single-pulse, which directly corresponds to a KER of 14 eV. This value agrees with our measurement results shown in Fig. 6.8.

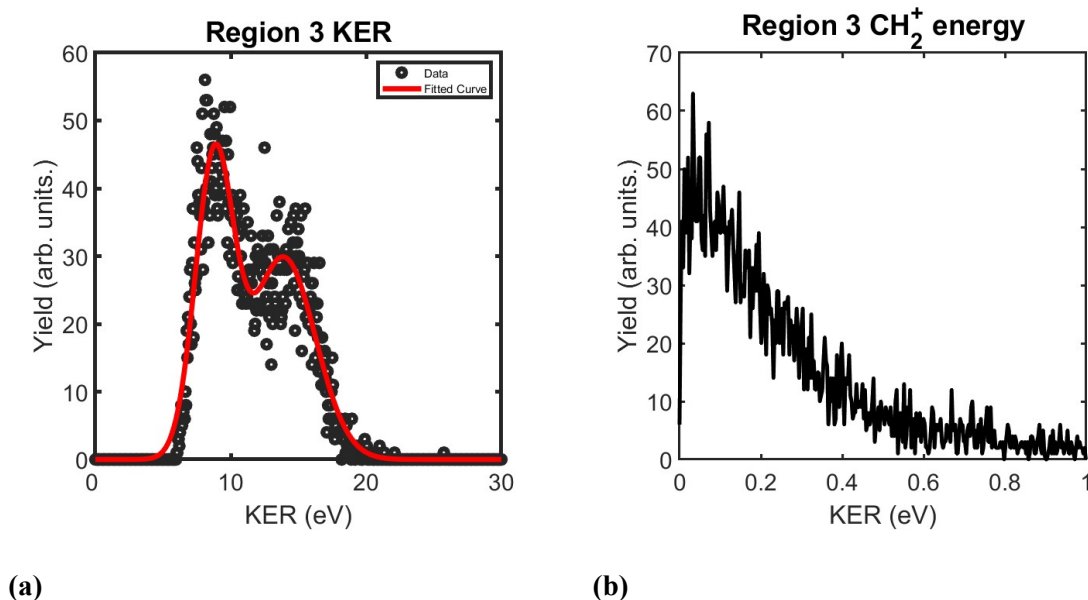
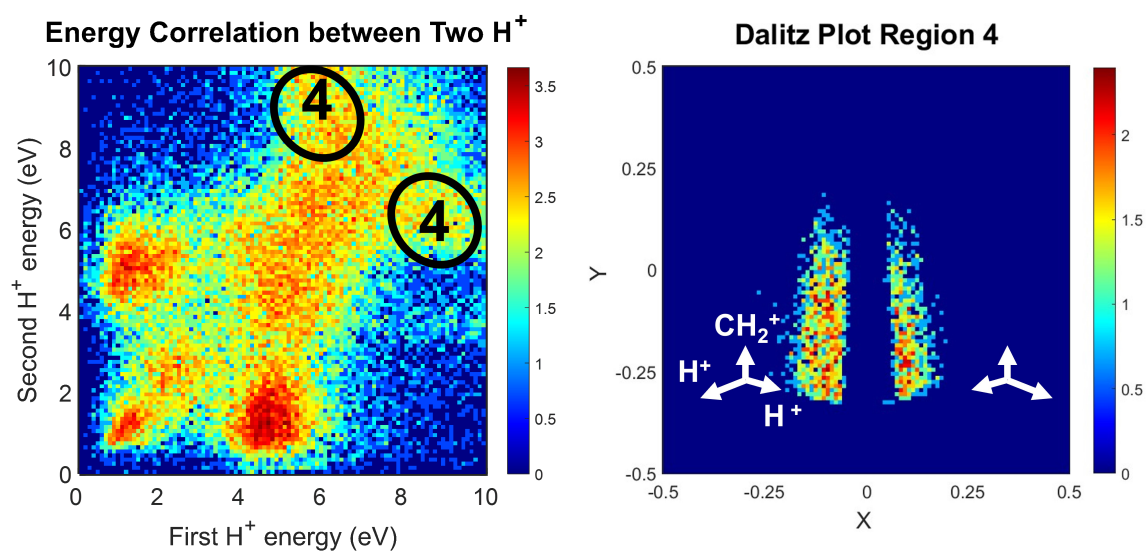


Figure 6.8. (a) Kinetic energy release from region 3 for all three fragments ($CH_2^+ + H^+ + H^+$). As shown, there are two peaks at 8.8 eV and 14 eV. (b) Energy of CH_2^+ from region 3.

However, in addition to the KER peak at 14 eV, our measurements reveal another distinct KER peak at 8.8 eV, as shown in Fig. 6.8 (a). Interestingly, there is only a single peak for CH_2^+ , as shown in Fig. 6.8 (b), indicating that the two KER values are caused by these two identical protons. These two separated peaks are also visible in the Newton Plot of Fig. 6.6 (d), although they are not well resolved due to the broad distribution. Notably, this double-peak effect appears clearly in short-pulse measurements (around 10 fs) which is shown here but is absent in our measurements with a 25 fs pulse duration. The reason is still unclear.

For region 3, we conclude that it results from symmetric bond motion in charged methane. It remains an open question whether this occurs directly from a CH_4^{3+} state or through very fast sequential steps within the pulse duration.

For region 4, the Dalitz plot in Fig. 6.9 (b) shows that the energy is distributed more on one proton compared to the other, indicating an asymmetric bond stretching. The time-independent KER of 16 eV from region 4 is very close to that of region 3, suggesting that both are induced by the same charge state of methane. However, region 4 involves asymmetric bond motions.



(a)

(b)

Figure 6.9. (a) Energy correlation between two H^+ ions from three-body fragmentation. Region 4 corresponds to the higher-energy, non-diagonal part without time dependency. (b) Dalitz plot for Region 4. The schematic diagram (white) illustrates that one H^+ gains more momentum than the other, resulting in the non-diagonal energy correlation observed in (a). The definition of the Dalitz plot and its corresponding axes can be found in Chapter 4, Section 4.2.3.

6.3 Sequential Fragmentation through Hydrogen Release

The sequential asymmetric region includes region 2 and the part continuous to region 4 as shown in Fig. 6.10 (a). As analyzed in the previous section, the different final energy of two H^+ suggests an ‘asymmetric’ distortion of the charged methane ionized by the pump pulses. To illustrate this molecular distortion, the Dalitz plots are presented in Fig. 6.10 (b).

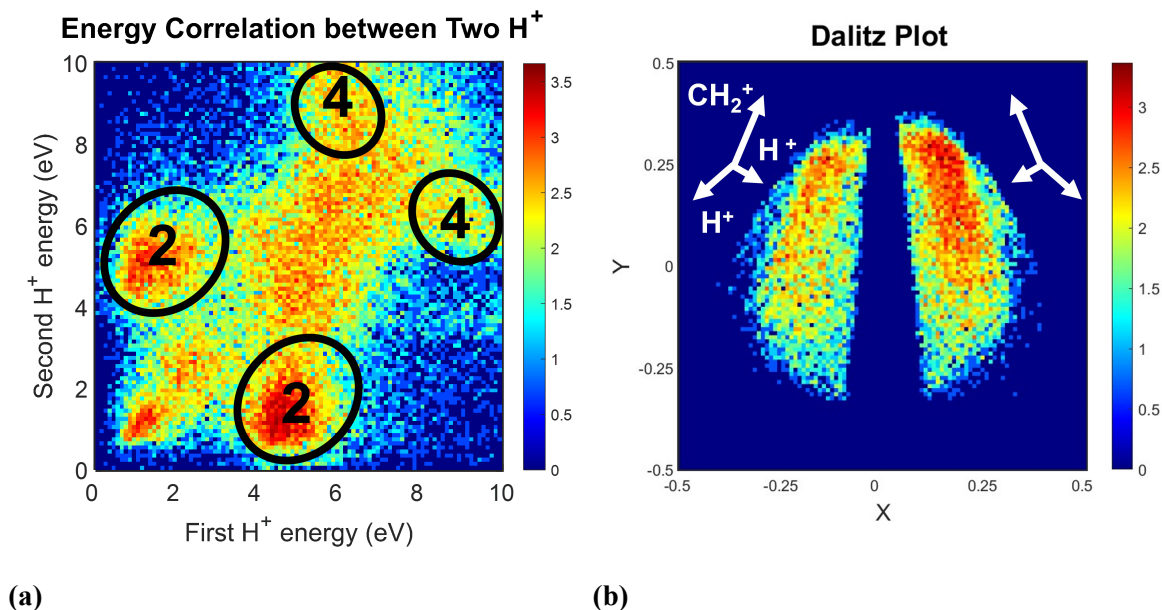


Figure 6.10. (a) Energy correlation between two H^+ ions from three-body fragmentation. The sequential asymmetric region corresponds to the lower-energy off-diagonal region 2 and the time-dependent part of region 4. (b) Corresponding Dalitz plot for region 2. The schematic diagram (white) illustrates that one H^+ acquires less momentum than the other, while CH_2^+ gains more momentum.

A detailed analysis reveals, that both protons exhibit time-dependent behavior, but in different ways, as shown in Fig. 6.11. The time-dependency of the low-energy H^+ is presented in (a), while the fast H^+ is plotted in (b). Clearly, the two H^+ ions exhibit different time-dependencies, further indicating that the two protons are released in separate steps.

Based on the features mentioned above, one possible fragmentation scheme for region 2 is that one H^+ dissociates in the first step of the pump, while the other H^+ dissociates due to the probe. Due to the multiphoton process, it is difficult to determine the charge state of methane after the pump laser, meaning the dissociation could begin from either a CH_4^+ cation or a CH_4^{2+} dication, leading to several possible sequential fragmentation pathways that will be discussed in the following.

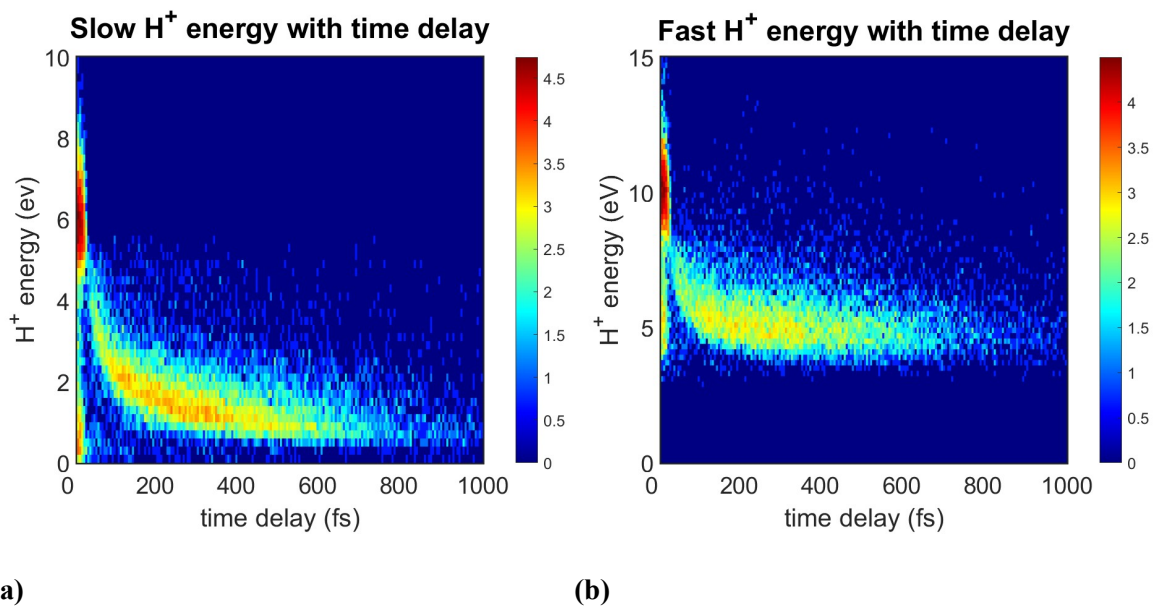


Figure 6.11. (a) Energy of slow H^+ originating from the sequential asymmetric region (region 2 and the time-dependent part of region 4) as a function of time delay. (b) Energy of fast H^+ from the same sequential asymmetric region as a function of time delay.

Possible Fragmentation Processes

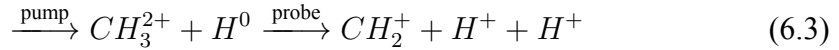
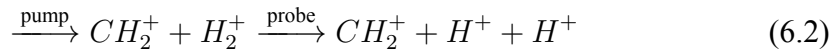
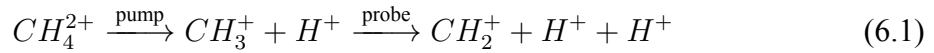
To determine the dissociation pathways, the first step is to list all possible fragmentation processes that could result in the observed ‘asymmetric’ proton distribution. Based on the analysis from the previous section, we focus firstly on the processes where one H^+ leaves the methane molecule.

In order to account for all potential pathways, fragmentation processes are analyzed here based on the charge states of methane after the pump pulse. This analysis aims to determine whether methane is singly or doubly ionized by the pump pulse. Once a specific charge state is assumed, the corresponding fragmentation pathways are analyzed and compared to the measurement data. The detailed charge-state analysis is presented as follows.

Excluding the Pathway through CH_4^{2+} Dication

In this section, all fragmentation pathways resulting from the CH_4^{2+} dication, along with one hydrogen being ejected first, are analyzed and excluded.

If the system reaches the CH_4^{2+} dication, the possible fragmentation pathways are as follows:



- **(6.1) : $CH_4^{2+} \rightarrow CH_3^+ + H^+$** : In this pathway, the methane dication would have already undergone Coulomb explosion into $CH_3^+ + H^+$ during the pump step. As this H^+ originates from a Coulomb explosion, it would rapidly repel from the charged CH_3^+ and remain time-independent in its energy regardless of the arrival of the probe pulse. Since both protons from region 2 exhibit time-dependent features, this pathway can already be excluded. Additionally, the Coulomb-exploded H^+ ion would gain an energy of approximately 4.3 eV, as discussed in Chapter 5 in Fig. 5.7. However, this 4.3 eV does not agree with the energies of either proton shown in Fig. 6.11.
- **(6.2) : $CH_4^{2+} \rightarrow CH_2^+ + H_2^+$** : This pathway can be excluded by comparing it with the $CH_2^+ + H_2^+$ observed in the single-pulse measurement. Following (6.2), the Coulomb explosion of $CH_2^+ + H_2^+$ is induced by the pump pulse, resulting in the same fragments as those observed in a single-pulse measurement. Upon the probe pulse, the H_2^+ dissociates into two H^+ ions. During the probe, the CH_2^+ dissociated from the first pump pulse does not interact further, at least its energy should not decrease as observed. In other words, the CH_2^+ detected in region 2 of the three-body channel in the pump-probe measurement should have the same final energy as the CH_2^+ detected in the two-body channel of the single-pulse measurement.

As shown by the red curve in Fig. 6.12, the final energy of CH_2^+ from the single-pulse measurement is centered around 0.55 eV, with a width of approximately 0.22 eV. In contrast, the CH_2^+ from region 2, represented by the black curve in Fig. 6.12, peaks around 0.2 eV with a distribution width of 0.4 eV. Clearly, the CH_2^+ from region 2 possesses less energy, indicating that it was not generated through the $CH_2^+ + H_2^+$ pathway.

- **(6.3) : $CH_4^{2+} \rightarrow CH_3^{2+} + H^0$** : For (6.3), several theoretical studies suggest that CH_3^{2+} is short-lived [115] [118] [119], meaning it rapidly dissociates into $CH_2^+ + H^+$. Under the influence of Coulomb forces, the two charged particles repel each other, resulting in a time-independent, high-energy H^+ . However, this behavior contradicts the experimental observations.

The above analysis excludes the possibility of dissociating from the CH_4^{2+} dication charged state.

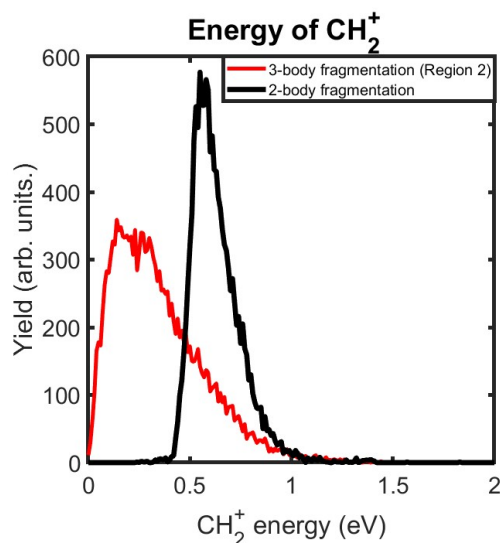
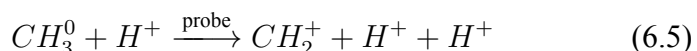
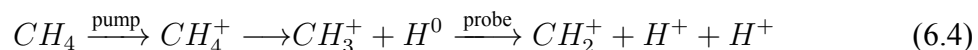


Figure 6.12. Energy of CH_2^+ from region 2 of the three-body dissociation channel (black) and from the two-body dissociation channel $CH_2 + H_2^+$ (red).

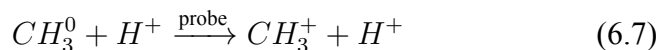
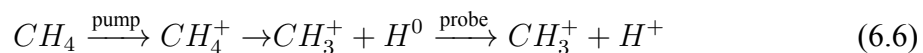
Validating the Pathway through CH_4^+ Cation

If the reaction begins with the CH_4^+ cation, where one H atom dissociates upon interaction with the pump pulse, the possible pathways are outlined below, with schematic representations provided in Fig. 6.13.

The pathways plotted in Fig. 6.13 can be written as:



The first step induced by the pump laser follows the same reaction pathway as the two-body reactions described in (5.3) and (5.4):



If the first dissociated H^+ is induced along this pathway, its time dependence, as shown in Fig. 6.14 (a), should match the characteristics (energy and angular momentum distributions) of the two-body pump-probe experiment in Chapter 5.

In terms of energy, the H^+ ion from the two-body $CH_3^+ + H^+$ channel ranges from 0.3 eV to 4 eV (Fig. 6.14 (b)), while the slow H^+ from the three-body channel is plotted in Fig. 6.14(a). Their similar time dependence suggests a common origin. In terms of angular momentum distribution, the slow H^+ from the three-body channel (black, Fig. 6.15 (a)) closely resembles that of the two-body case (red, same plot). Furthermore, the time-dependent

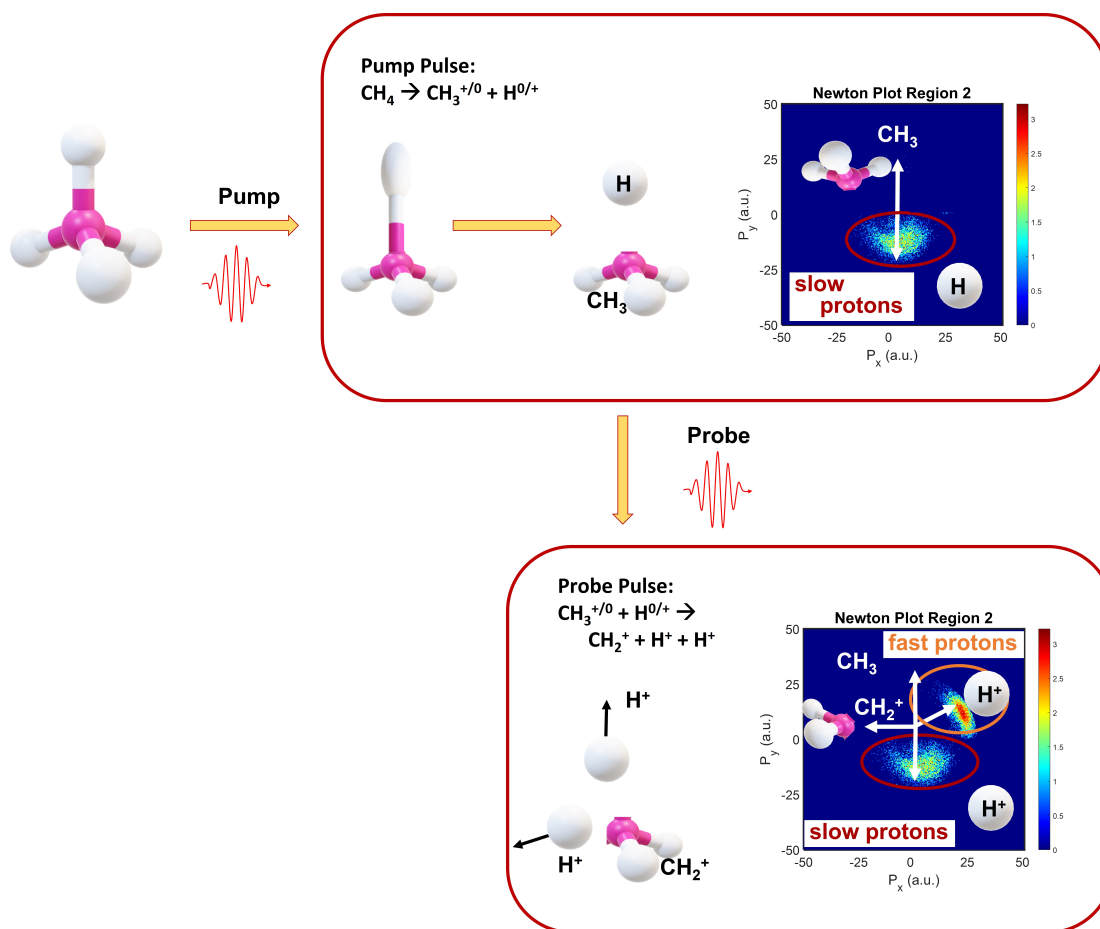


Figure 6.13. Schematic representation of the fragmentation pathway leading to region 2. Following excitation by the pump pulse, the methane cation undergoes bond stretching, resulting in the departure of one hydrogen. Upon interaction with the probe pulse, another hydrogen dissociates.

H^+ emission angle from the three-body channel, shown in Fig. 6.15 (b), follows the same trend as the two-body case in Fig. 5.10.

Based on the comparison with the two-body reaction channel, we conclude that the most probable origin for region 2 is the dissociation of the CH_4^+ cation. In the first step, one H^0/H^+ is ejected, followed by the production of a second H^+ with higher energy through a Coulomb explosion induced by the probe pulse. In the previous section, all possible fragmentation pathways arising from the CH_4^{2+} dication are analyzed and systematically excluded. This examination ultimately confirms that the dissociation pathway originates from the CH_4^+ cation, as described in the channels above.

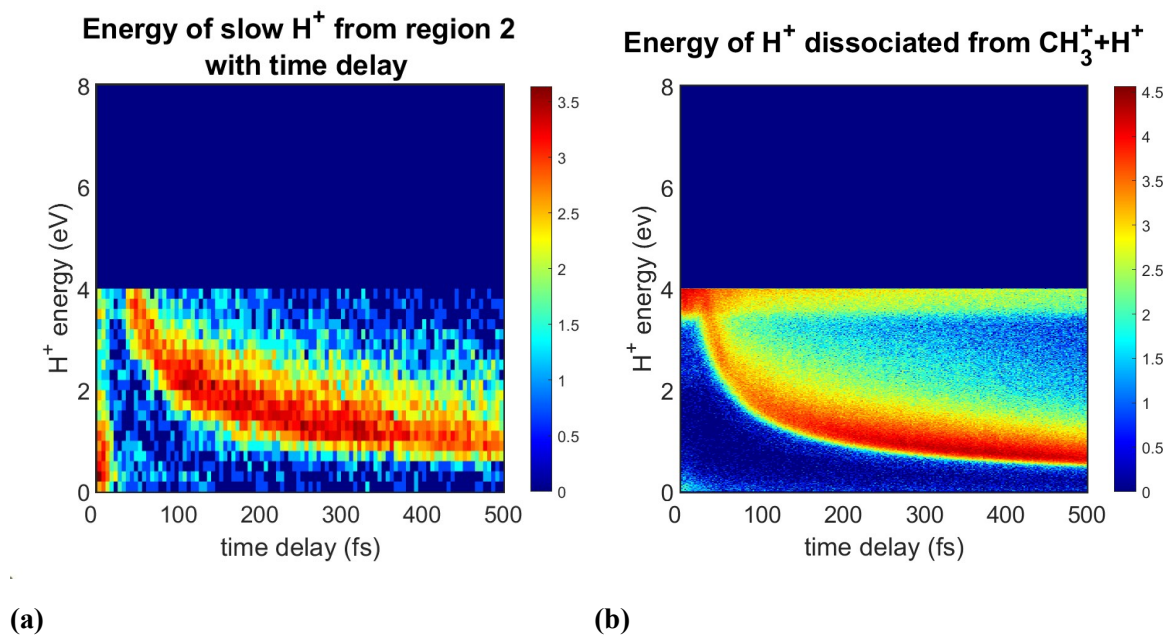


Figure 6.14. (a) Time-dependent H^+ energy distribution from region 2 of the three-body dissociation channel $CH_2^+ + H^+ + H^+$. (b) Time-dependent energy of H^+ from the two-body dissociation channel $CH_3^+ + H^+$.

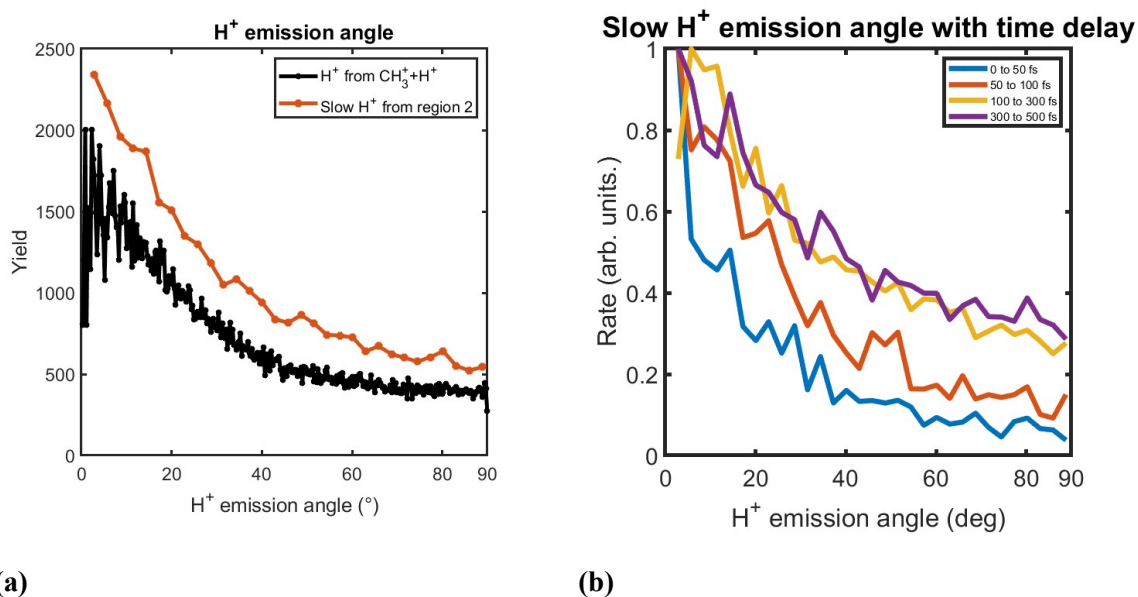


Figure 6.15. (a) Time integrated yield of H^+ as a function of emission angle for the two-body and three-body dissociation channels. The black curve corresponds to the two-body dissociation channel $CH_3^+ + H^+$, while the red curve represents H^+ from region 2 of the three-body channel. (b) Time-dependent H^+ emission angle from region 2 of the three-body dissociation channel $CH_2^+ + H^+ + H^+$.

6.4 Sequential Fragmentation through Molecular Hydrogen Release

Apart from observing protons with different energies, two H^+ ions with identical energies are located along the diagonal line, corresponding to region 1 and region 3 in Fig. 6.16 (a). Recalling the time dependency of this region indicates that they are generated from a sequential process with stable intermediate states after the pump. The symmetric feature from Fig. 6.16 (b) suggests that the two protons are correlated and released simultaneously from two identical C-H bonds of methane. If one hydrogen dissociates first, the two H^+ ions can't exhibit identical energy and time dependence.

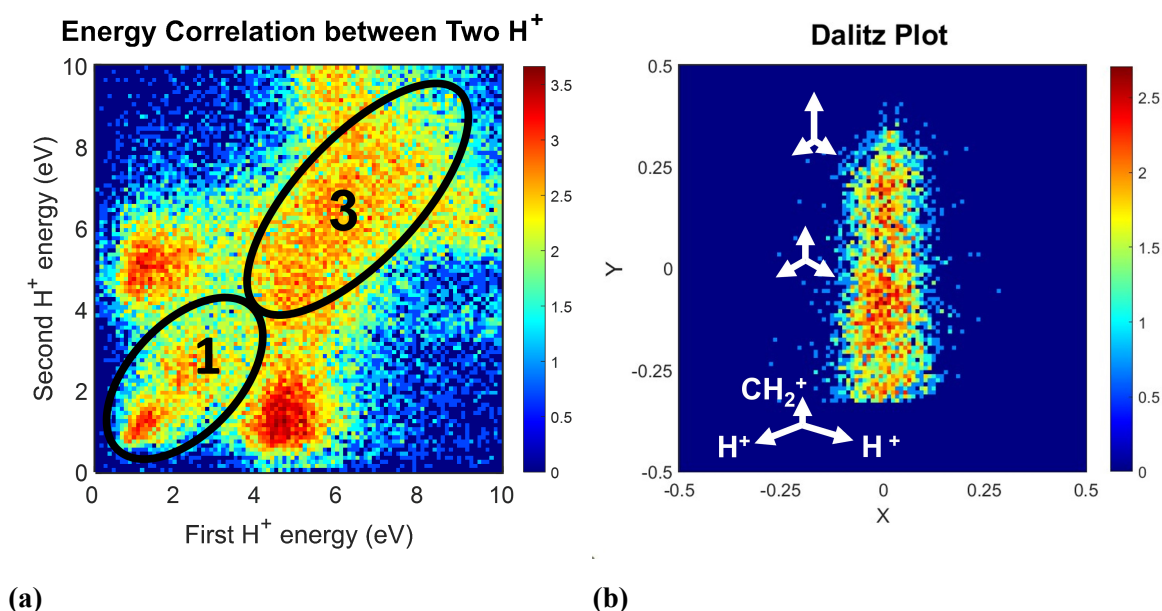


Figure 6.16. (a) Energy correlation between two H^+ ions from three-body fragmentation. The sequential symmetric region corresponds to the lower-energy diagonal region 1 and the time-dependent part of region 3. (b) Corresponding Dalitz plot for region 1. The schematic diagram (white) illustrates that two H^+ share equally the momentum.

Assuming two hydrogen atoms being released from methane at the same time, there are three possible cases:

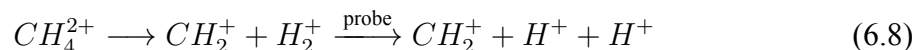
- (1) $H^+ + H^+$: In this case, the Coulomb force will cause the two H^+ ions to repel each other rapidly, resulting in no time dependence.
- (2) $H^+ + H^0$ or $H^0 + H^0$, In both cases, a natural phenomenon occurs: at a specific nuclear distance, the two hydrogen atoms can readily form H_2 or H_2^+ . This explains why the two protons tend to acquire the same energy and exhibit the same time dependence.

Possible Fragmentation Processes

Here, the same analysis procedure is applied to determine the origin of region 1, as previously done for region 2. Subsequently, all possible fragmentation pathways from different charge states that could lead to the formation of $H_2^{+/0}$ are analyzed.

Excluding the Pathway through CH_4^{2+} Dication

As analyzed above, $H_2^{+/0}$ forms as an intermediate state following the pump pulse. If the molecule ionizes to CH_4^{2+} under this condition, the possible fragmentation pathways involving $H_2^{+/0}$ are as follows:



In this case, the pump step induces a Coulomb explosion, resulting in $CH_2^+ + H_2^+$, identical to the Coulomb explosion observed in the single-pulse measurement.

Fig. 6.17 compares the CH_2^+ energy for both cases. As shown, the CH_2^+ from the sequential symmetric region peaks at 0.03 eV (black), while the CH_2^+ generated by the single-pulse Coulomb explosion peaks at 0.55 eV (orange). The clear difference between these peaks indicates that they do not originate from the same step. Therefore, this pathway is no longer considered as the origin.

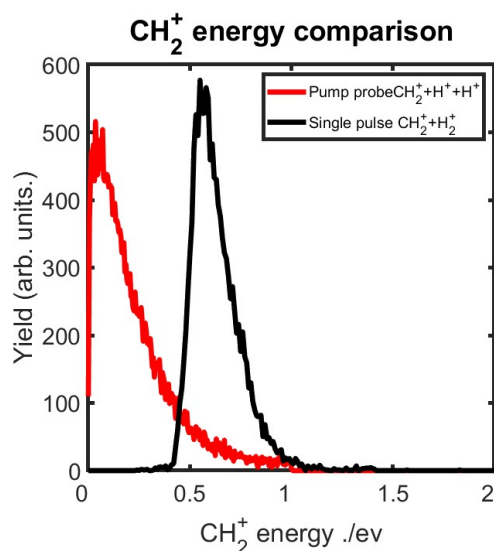


Figure 6.17. Energy of CH_2^+ from the sequential symmetric region, as defined in Section 6.1.1, of the three-body process (black), and from the two-body dissociation channel $CH_2 + H_2^+$ (red).

Validating the Pathway through CH_4^+ Cation

If the reaction (chain) induced by the probe pulse starts from CH_4^+ cation produced in the pump pulse, then all possible pathways through a $H_2^{+/0}$ are shown in Fig. 6.18. The corresponding pathways are:

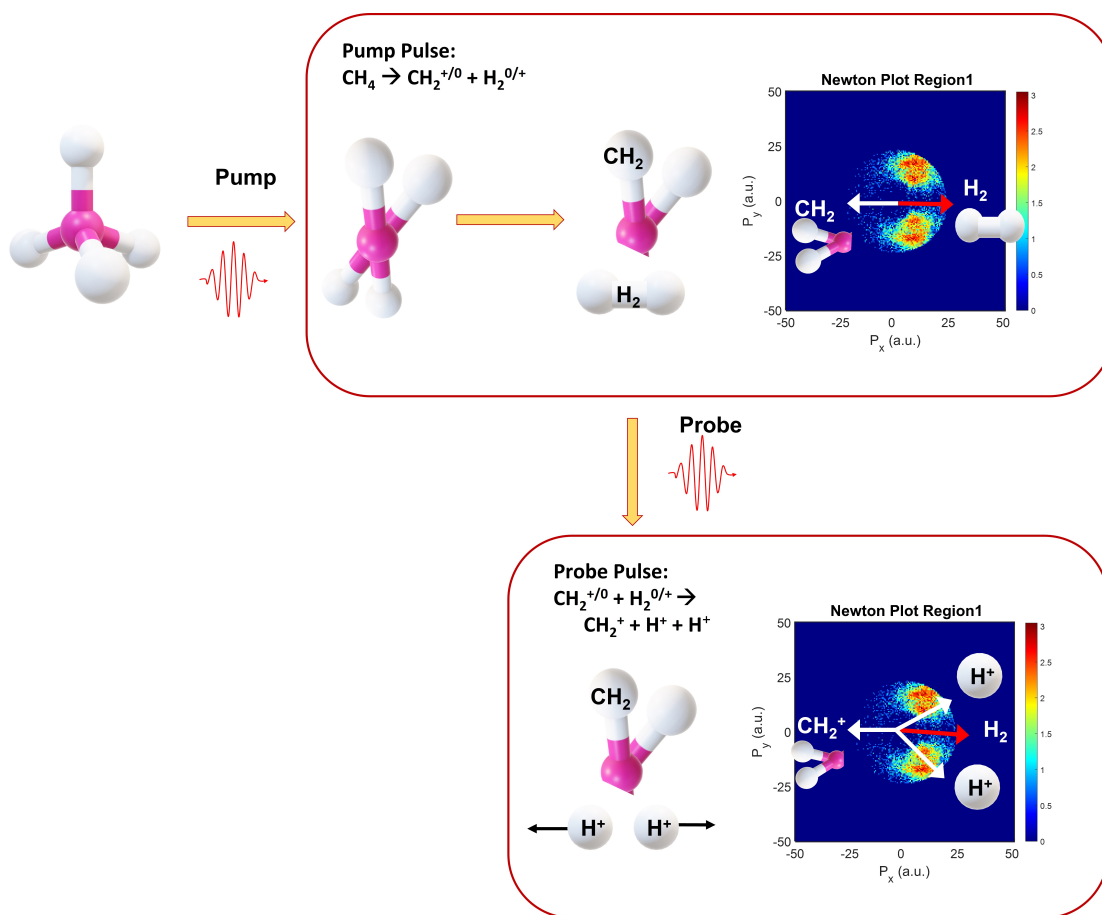
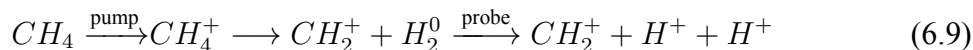
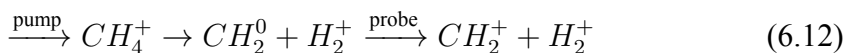
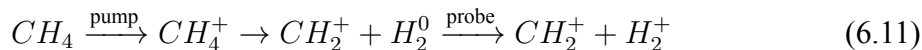


Figure 6.18. Schematic representation of the fragmentation pathway leading to region 1. Following the pump pulse, the methane cation vibrates and reaches C_{2v} geometry, resulting in molecular hydrogen release. The probe pulse then induces the dissociation of two protons.

The first step induced by the pump laser follows the same reaction pathway as the two-body reactions described in (5.7) and (5.8):



If H_2^+/H_2^0 is generated in the pump pulse and dissociates into two H^+ ions upon the probe,

the probe pulse would include the process: $H_2^+ \rightarrow H^+ + H^+$ or $H_2^0 \rightarrow H^+ + H^+$, which should be comparable to the well-studied case of a real H_2 molecule in a laser field.

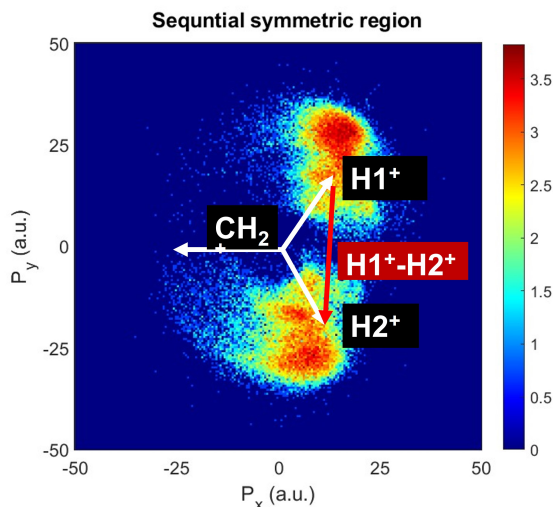


Figure 6.19. Newton plot for symmetric regions 1 and 3. As illustrated, the higher-energy ‘fast’ proton is denoted as $H1^+$ in the upper plane, while the lower-energy ‘slow’ proton is plotted in the lower half-plane and labeled as $H2^+$. The arrows indicate the direction of the emitted momentum vectors. The vector difference between the two H^+ ions, $|H1^+ - H2^+|$, represents the relative momentum obtained by the intermediate H_2 , excluding the component from CH_2^+ .

The relative energy of H_2 can be calculated from the Newton plot shown in Fig. 6.19. Since the momentum vectors of the two protons are fixed on the fragmentation plane, marked as $H1^+$ and $H2^+$ ($H1^+$ and $H2^+$ are noted for differentiating two H^+), the difference between the two proton vectors, $|H1^+ - H2^+|$, represents the momentum of H_2 obtained during the pump pulse.

Extracted Information from Fig. 6.19			
Momentum [in a.u.]	9.0	16.8	28.4
Energy [in eV]	0.6	1.67	5.9
$H1^+-H2^+$ distance [in a.u.]	25	8.0	2.27

Table 6.1. Momentum, energy, and the distance between two protons $H^+ - H^+$ for three peaks from Fig. 6.19.

After obtaining the relative momentum vector, the relative energy of each proton can be calculated from $|H1^+ - H2^+|$, as shown in Fig. 6.20. Three distinct momentum ring

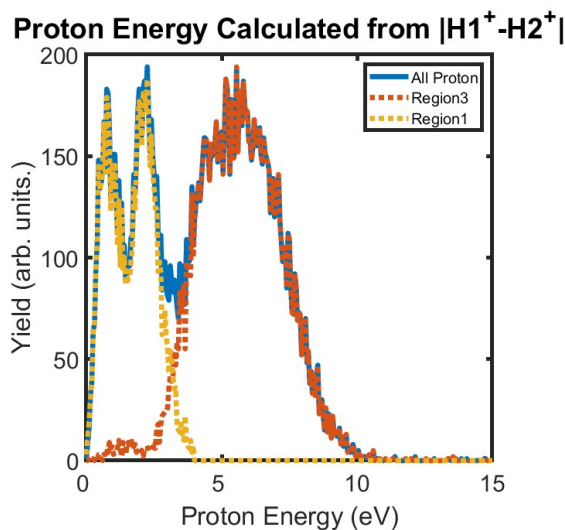


Figure 6.20. Calculated energy from the momentum vector $|H1^+ - H2^+|$ as shown in Fig. 6.19, representing the kinetic energy of the dissociated H_2 after the pump pulse. The yellow curve corresponds to the contribution from Region 1, while the orange curve represents the part from Region 3. The overall energy is shown in blue.

structures from Fig. 6.19 correspond to three peaks in the energy plot in Fig. 6.20. From the kinetic energy of each proton, the H-H distance can be calculated, as listed in the table. 6.1.

In the table, the three columns represent the three ring structures shown in Fig. 6.19. The highest energy of $|H1^+ - H2^+|$ corresponds to the shortest distance, which is 2.27 a.u., close to the equilibrium distance of H_2^+ at 2 a.u. Additionally, as introduced in Chapter 2, Section 2.4.3, the typical dissociative ionization spectra of H_2 in a single-pulse measurement serve as a useful reference for examining the H_2 dissociated from methane in the pump pulse. The measured proton energy from H_2 dissociation by A. Rudenko is shown in Fig. 6.21. This figure presents measurements obtained with a 7 fs single pulse in the solid black curve, and the red curve is taken from our measurement from Fig. 6.20. By overlaying these two results, a strong similarity is observed, further supporting the conclusion that H_2 is formed as an intermediate fragment during methane three-body fragmentation. One thing that needs to be noticed is that the H_2^0 formed in our case is not necessarily in the ground state, but probably in excited states which can not be resolved.

So far, we concluded that region 1 is induced by the singly charged CH_4^+ cation, with the formation of H_2 as an intermediate fragment during the fragmentation of methane.

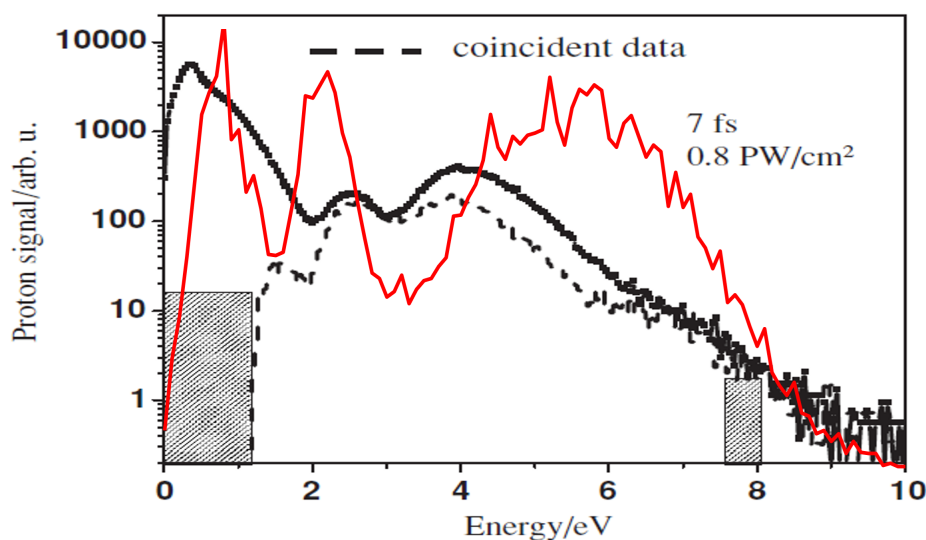


Figure 6.21. Comparison between the relative proton energies of H_2 dissociated from methane and the results from an H_2 measurement conducted by A. Rudenko, as reported in [27]. The solid black curve from the reference represents the proton energy distribution measured from a 7 fs single-pulse measurement without coincident detection of two protons. The dashed black curve from the reference corresponds to the coincidence condition. The red curve added here represents the results from methane, corresponding to the same data presented in Fig. 6.20 in logarithmic scale. More details of the H_2 dissociation mechanism in strong laser fields are introduced in Chapter 2, section 2.4.3.

6.5 Connections between Different Pathways

The next question, and perhaps the most obvious one, is why region 1 appears only in pump-probe measurements and not in the single-pulse case. One key observation is from the time-dependent KER plot shown in Fig. 6.5 (f), where region 3 is continuous with region 1 at time zero. This continuity suggests that both regions are associated with the same geometry configuration.

Based on the analysis of the time-dependent behavior of region 1, H_2 plays the role of an intermediate product. This agrees with the explanation for region 3, where two C-H bonds extend symmetrically, leading to a similar structure similar to H_2 . The critical question is whether these two hydrogen atoms are first dissociated as an H_2 or are directly released as two protons.

For region 3, two protons are directly released within a single pulse.

For region 1, two equally stretched hydrogen atoms form a molecular hydrogen molecule during the pump pulse. The formation time of H_2 is approximately 10 fs, as discussed in Chapter 5, where the H_2^+ signal in a pump-probe experiment is absent at the first 10 fs time delay, and start to emerge at around 10 fs. This 10 fs time can be interpreted as the bond formation time for H_2 , which agrees with the findings of [67]. In their study, using an X-ray probe directly targeting the inner shell, it was demonstrated that 10 fs corresponds to the time required for methane to distort into its C_{2v} geometry. This geometry is also identified as one of the most probable fragmentation pathways leading to H_2^0 , as analyzed in [66] and in Chapter 5.

The threshold energy for methane to dissociate into $CH_2^+ + H_2$ is 15.1 eV, as shown in Table 5.1, meaning that the molecule must absorb at least ten photons to reach this threshold and form H_2 . This process is most likely to occur near the peak intensity of the laser pulse.

If ionization occurs at the peak of the laser pulse, then after the additional 10 fs required for H_2 formation, the pulse intensity decreases significantly, making further ionization of H_2 unlikely. Consequently, a second probe pulse is required to ionize the dissociated H_2 , which explains why region 1 appears exclusively in the pump-probe measurement but not in the single-pulse scheme.

Moreover, it is observed that the branching ratio of region 1 increases with higher laser intensity. This is illustrated in Fig. 6.22, where measurements are performed at three different intensities in a pump-probe scheme, with both the pump and probe pulses having a duration of 25 fs and equal intensity. The results demonstrate that the branching ratio of region 1 increases as the peak intensity increases.

A similar analysis is applied to the relationship between region 2 and region 4. The KER range, together with its time-independent nature, suggests that a single pulse induces an

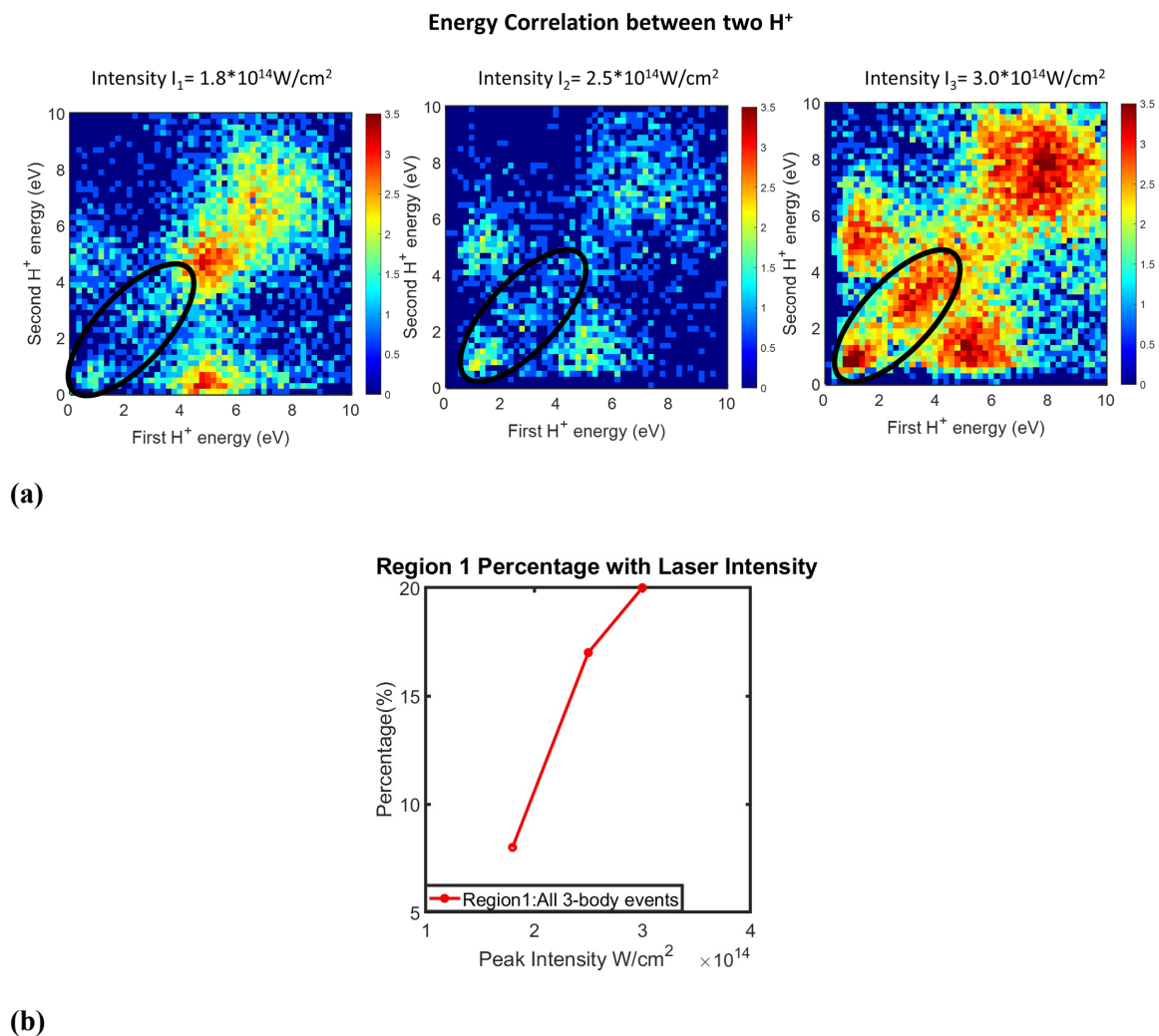


Figure 6.22. (a) Energy correlation between two H^+ ions at three different intensities. (b) Percentage of region 1 events relative to all three-body fragmentation events at three different intensities.

asymmetric distortion in methane molecules. Notably, the KER from region 2 is continuous to the first 50 fs time delay of region 4, as shown in Fig. 6.5.

The main distinction between region 2 and region 1 is that region 2 appears in both single-pulse measurements and pump-probe experiments. This can be attributed to two factors: On the one hand, it takes an even shorter time for the methane cation to dissociate into $CH_3^+ + H^+$, as demonstrated in Fig. 5.7 in the previous chapter, where the dissociation signal is observed approximately at time zero. On the other hand, it requires less energy to reach $CH_3^+ + H^0$ (approximately 14 eV), allowing the dissociation to occur at an earlier stage before the laser peak. This facilitates further absorption of energy within the pulse duration, enabling ionization of the neutral fragment.

Moreover, it requires less energy to ionize H^0 compared to H_2 , making this process more favorable. In the case of H release, the lower energy threshold permits the process

to occur within a single-pulse measurement. The intensity dependence also explains why region 2 is absent at low field intensities but becomes observable at higher intensities, as reported in [117].

6.6 Simulation

To confirm and understand the fragmentation pathways discussed above, a classical simulation based on Coulomb force and Newton dynamics is performed based on the code from F.Trost [120]. First, the simulation methods are briefly introduced, followed by the presentation of the simulation results. The calculations quantitatively reproduce the measured Newton plots.

6.6.1 Simulation Methods

To mimic the three-body fragmentation process of $CH_2^+ + H^+ + H^+$, we employ backward reasoning to prepare three particles, labeled as $[CH_2, H1, H2]$ (where H1 and H2 are named for illustration purposes). The final step of the simulation mimics the probe pulse, which initiates the Coulomb interaction among the three particles. The position and velocity of each particle are determined based on the dynamics before the arrival of the probe pulse, corresponding to the intermediate states reached by the system following the pump pulse and its subsequent evolution. The calculation flowchart is shown in Fig. 6.23.

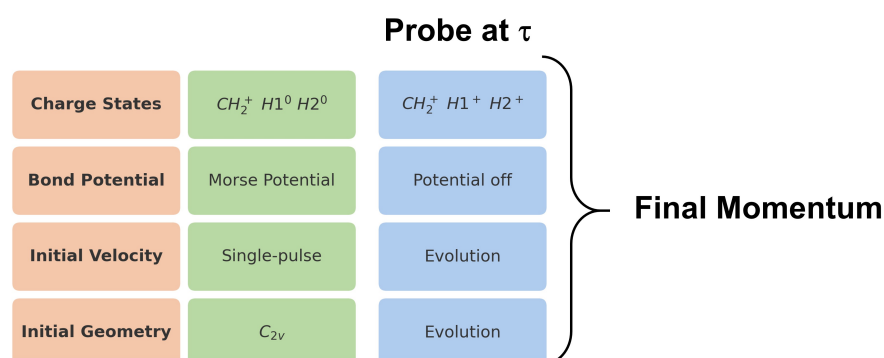


Figure 6.23. Calculation Flowchart. The system is initialized with three fragments: $[CH_2, H1, H2]$. The initial conditions include Charge State, Bond Potential, Initial Velocity, and Initial Geometry. For the four regions, initial parameters are individually selected based on the analysis in previous sections. After an evolution time τ , a ‘probe’ induces a Coulomb explosion. Instantly at τ , the system’s charge state transitions to $[CH_2^+, H1^+, H2^+]$, and the bond potential is turned off. At each step, particle positions and velocities are updated. The calculation terminates when the Coulomb potential drops below 1% of its initial value.

The starting point of this simulation is designed to replicate the system immediately after the pump pulse. For different pathways involving distinct intermediate states, the simulation parameters are derived from the analysis results presented in the previous section. By integrating experimental observations with simulation results, we achieve a deeper understanding of the fragmentation dynamics.

Parameter Selection

To prepare the system state at time zero, which represents the system immediately after the pump pulse, four parameters are considered:

- **Charge states:** As analyzed in the previous section, in regions 1 and 2, the charge state of the system after the pump pulse is a singly charged CH_4^+ . To distribute this single charge within a three-particle system, the dissociation pathways discussed in Equations (6.7)-(6.9) are followed. For instance, in region 1, the system is represented as $[CH_2^+, H1^0, H2^0]$.
- **Initial velocity:** Since the simulation involves dissociation into neutral fragments, the dissociation velocity is a crucial factor for the system's evolution. Without an initial velocity, the system cannot evolve if there is only one charged particle. The initial velocity values are first estimated based on the momentum distribution of each fragment from single-pulse measurements and further optimized by comparing the results with the final Newton plot.
- **Initial geometry:** The initial geometry directly determines the particles' evolution coordinates. Additionally, the geometry influences the molecular potential surface evolution during the pump pulse and dictates the fragmentation pathways. Therefore, it is essential to consider the initial geometry carefully for each pathway. For region 1, where sequential fragmentation occurs via H_2 formation, the process follows a C_{2v} geometry, as explained in Chapter 5. In contrast, region 2 adopts an initial C_{3v} geometry, as it involves the ejection of an H atom during the pump pulse. If different geometries are used, the calculated results will vary accordingly, as shown in the examples in Appendix D. For regions 3 and 4, a tetrahedral T_d geometry is used.
- **Potential/interaction between particles:** For system evolution before the probe pulse, the dominant process is the interaction between the three particles, based on the fragmentation pathway. Taking region 1 as an example, the two hydrogen atoms can interact via the Morse potential of H_2 .

Morse potential: To describe the potential between nuclei, many models have been developed successfully to mimic the real potential energies, such as Lennard-Jones potential, Buckingham Potential, Mie Potential, etc. Among them, Morse potential is implemented well with diatomic molecules, like H_2 or H_2^+ . The Morse potential is written as:

$$V(R) = D_e[1 - e^{-a(R-R_e)}]^2 \quad (6.13)$$

In which, R_e is the equilibrium bond length (the distance at which the potential energy is minimized). D_e is the dissociation energy (the depth of the potential well).

determines the width of the potential well. Here is a table of the parameters to mimic H_2 and H_2^+ :

Table 6.2. Morse potential parameters for H_2 and H_2^+ .

Parameter	H_2 (Hydrogen Molecule)	H_2^+ (Hydrogen Molecular Ion)
D_e [in eV]	4.75	3.40
R_e [in Å]	0.74	0.74
a [in Å ⁻¹]	1.95	2.00

Lennard-Jones Potential: To describe the dissociation process in region 2, we consider the scenario in which, upon interaction with the pump pulse, a charged H^+ and a neutral CH_3 fragment are formed. After the probe pulse, CH_2^+ and an additional H^+ undergo Coulomb explosion. To model the binding potential between CH_2 and this H , the Lennard-Jones potential is employed:

$$V(R) = 4\epsilon \left[\left(\frac{\sigma}{R} \right)^{12} - \left(\frac{\sigma}{R} \right)^6 \right], \quad (6.14)$$

where ϵ represents the depth of the potential well, and σ is the distance at which the potential becomes zero. For CH_3 , ϵ is set to 0.03 a.u., optimized through parameter fitting, and σ is initialized to the distance between CH_2 and the remaining H at the beginning of the dissociation process.

Evolution

After the system is prepared, the next step is to evolve until the probe pulse is applied. When the probe arrives at time τ , an instantaneous Coulomb process occurs. At this point (τ), the charge states change to $[CH_2^+, H^+, H^+]$, and the bond potential is switched off.

Thus far, the simulation process for each event has been introduced, with the trajectory recorded for analysis. To incorporate experimental resolution, a Gaussian distribution is applied to the initial velocity and initial position, with a specified standard deviation for the desired number of events. The resulting statistical data are then compared with the experimental observations.

6.6.2 Simulation Results

Here are the selected calculation results for each region; additional results with varied conditions are provided in Appendix D.

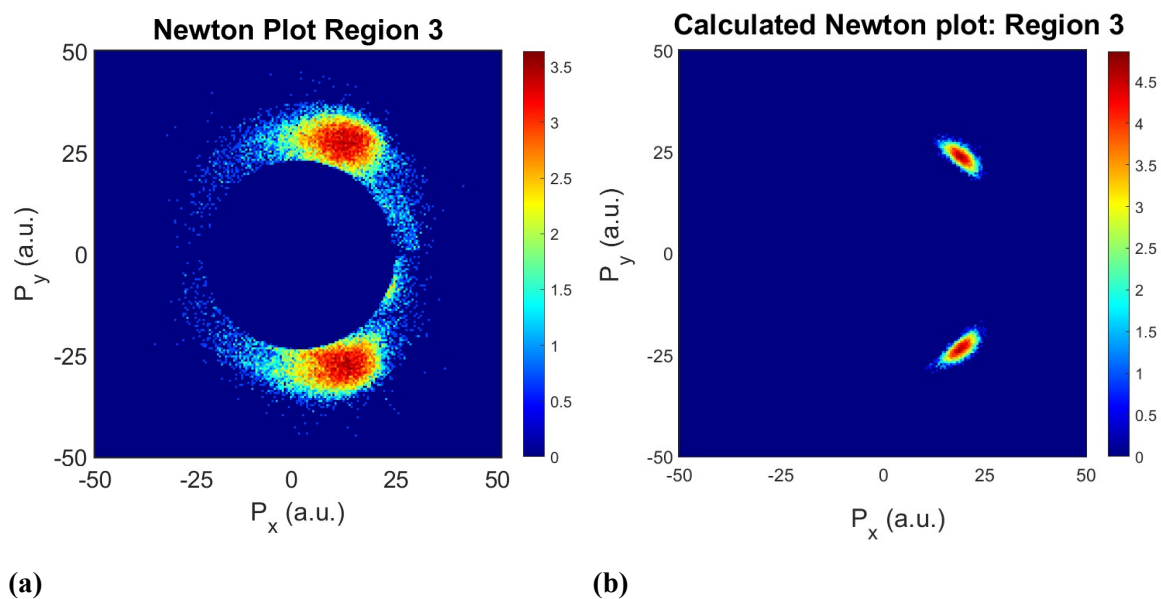
Region 3 and Region 4: Concerted Fragmentation

Figure 6.24. (a) Newton plot for region 3 from experimental measurements. (b) Calculated results with a T_d geometry.

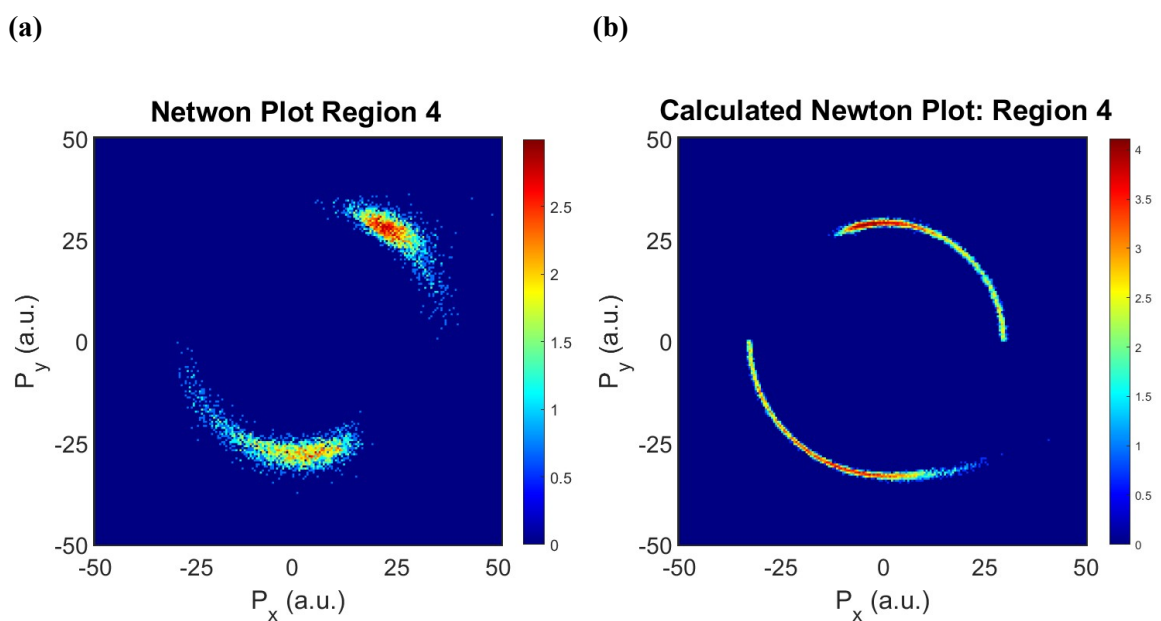


Figure 6.25. (a) Newton plot for region 4 from experimental measurements. (b) Calculated results with a T_d geometry.

For the concerted pathways leading to regions 3 and 4, the simulation is initialized with a doubly charged dication.

For region 3, as it involves a symmetric stretching mode of two hydrogen atoms, similar to H_2 , we initialize the charge distribution with CH_2^+ carrying two charges and assign the remaining charge to the center of mass of the two hydrogen atoms.

For region 4, since it is induced by an asymmetric motion, where one hydrogen atom leaves first, we assign the two charges in the system as $[CH_2^+, H^+, H]$.

For both regions 3 and 4, as they are time-independent and occur within a single pulse, we simulate this process by changing the charge states to $[CH_2^+, H^+, H^+]$ at approximately $t = 10$ fs, which corresponds to the duration of the laser pulse. No binding potential is included in the simulation. The T_d geometry is employed for both regions.

The comparison between the experimental measurements and the simulation results is presented in Fig. 6.24 for region 3 and Fig. 6.25 for region 4.

Region 1: Molecular H_2 formation

Firstly, Fig. 6.26 presents the experimental time-resolved Newton plot for region 1, serving as a reference for comparison with the calculations.

To set up the simulation for region 1, the initial configuration follows Equation (6.8), as previously described. The system begins with $[CH_2^+, H1^0, H2^0]$, where a Morse potential is applied to the neutral H_2^0 molecule.

To determine the initial geometry, the study from [67] suggests that methane cation would likely distort into its C_{2v} geometry within $(10 \pm 2)fs$, leading to H_2^0 formation.

The simulation is carried out at fixed probing times $t = 50, 100, 200, 300, 400, 500$ fs separately. For each probing time, 5000 trajectories are computed. The calculation results are shown in Fig. 6.27, where the simulation reproduces the experimental data features, including the momentum amplitude at different time delays and the double ring structures.

To understand the origin of these features, the trajectories of all three fragments are plotted, distinguishing between the outer ring ($|P_x| > 20$ a.u. and $|P_y| > 20$ a.u.) in Fig. 6.28 (a) and the inner-ring in Fig. 6.28 (b). For the outer ring in Fig. 6.28 (a), the trajectories of the two neutral hydrogen atoms indicate oscillation under the influence of the Morse potential, until the probe pulse initiates the Coulomb explosion, causing the two charged H^+ ions to separate. In contrast, for the inner ring in Fig. 6.28 (b), the two neutral hydrogen atoms are not deeply trapped by the Morse potential, leading to a larger nuclear distance and corresponding to smaller final momenta.

These double-ring structures are influenced by the equilibrium bond length of the potential wall, the initial positions of the two hydrogen atoms, and their initial velocities. This emphasizes the critical role of the initial configuration of the methane cation. Additional simulation results can be found in the appendix.

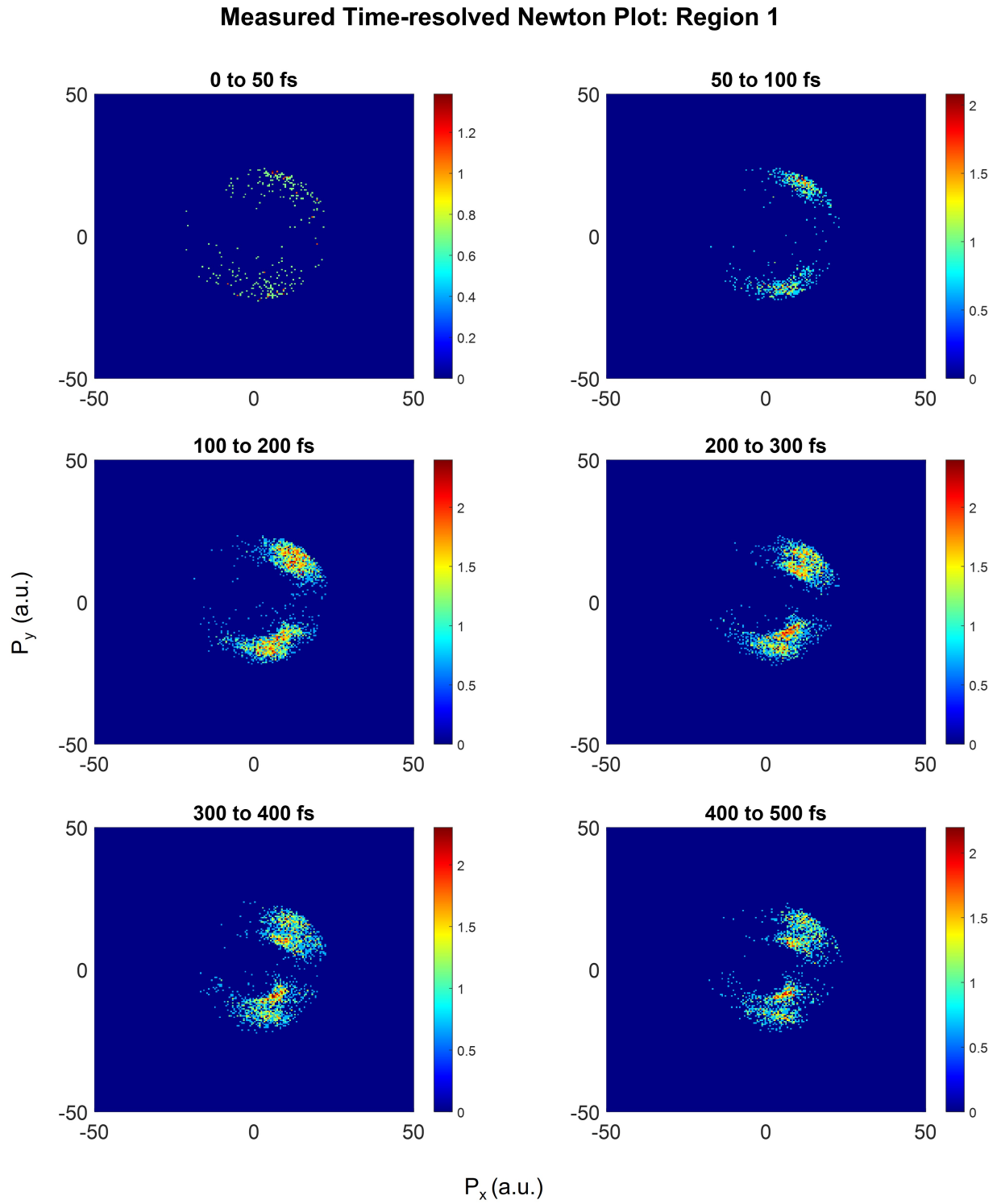


Figure 6.26. Newton plot of region 1 at different time delays from experimental measurements.

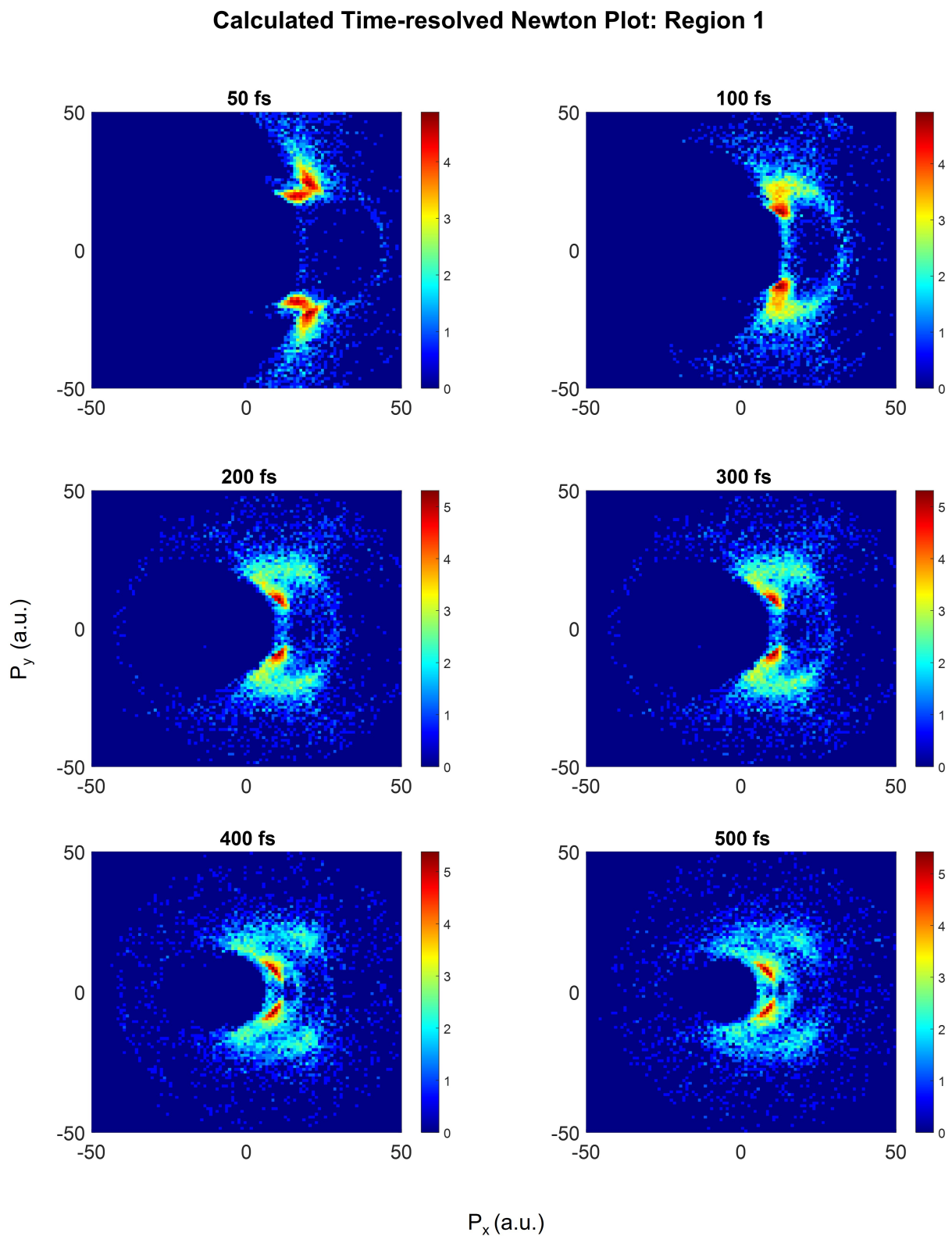


Figure 6.27. Calculated Newton plot for region 1 based on a C_{2v} geometry configuration.

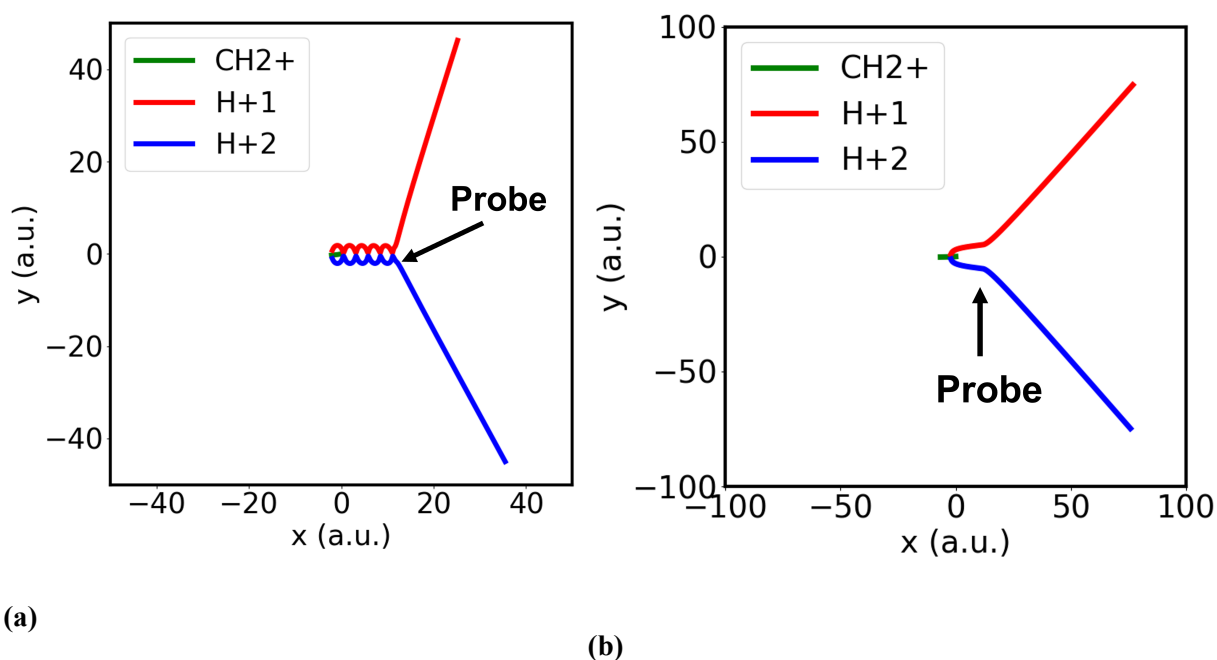


Figure 6.28. Trajectories from outer-ring and inner-ring events, respectively. The arrow labeled ‘probe’ indicates the trajectory changes at the probe delay time τ . (a) Trajectory from the outer-ring event. (b) Trajectory from the inner-ring event.

Region 2: Proton Emission

For simulating region 2, the system is initialized with a charge state of $[CH_2^0, H1^+, H2^0]$. A Lennard-Jones potential is applied to the neutral fragments between CH_2 and H to mimic the vibrational excited CH_3 , as discussed in Section 6.4. The C_{3v} geometry is employed for region 2 calculations, as it is the most probable configuration leading to the H emission pathway, as previously discussed.

Fig. 6.29 shows the Newton plot at different time delays from experimental measurements, while the calculated results are presented in Fig. 6.30. The computed results closely resemble the main structure of the measured data. However, the remaining question is whether the first hydrogen atom leaves the molecule as a proton or as a neutral H . This question connects back to the discussion in Chapter 5. To further clarify this, molecular dynamics (MD) simulations need to be conducted to provide additional insights.

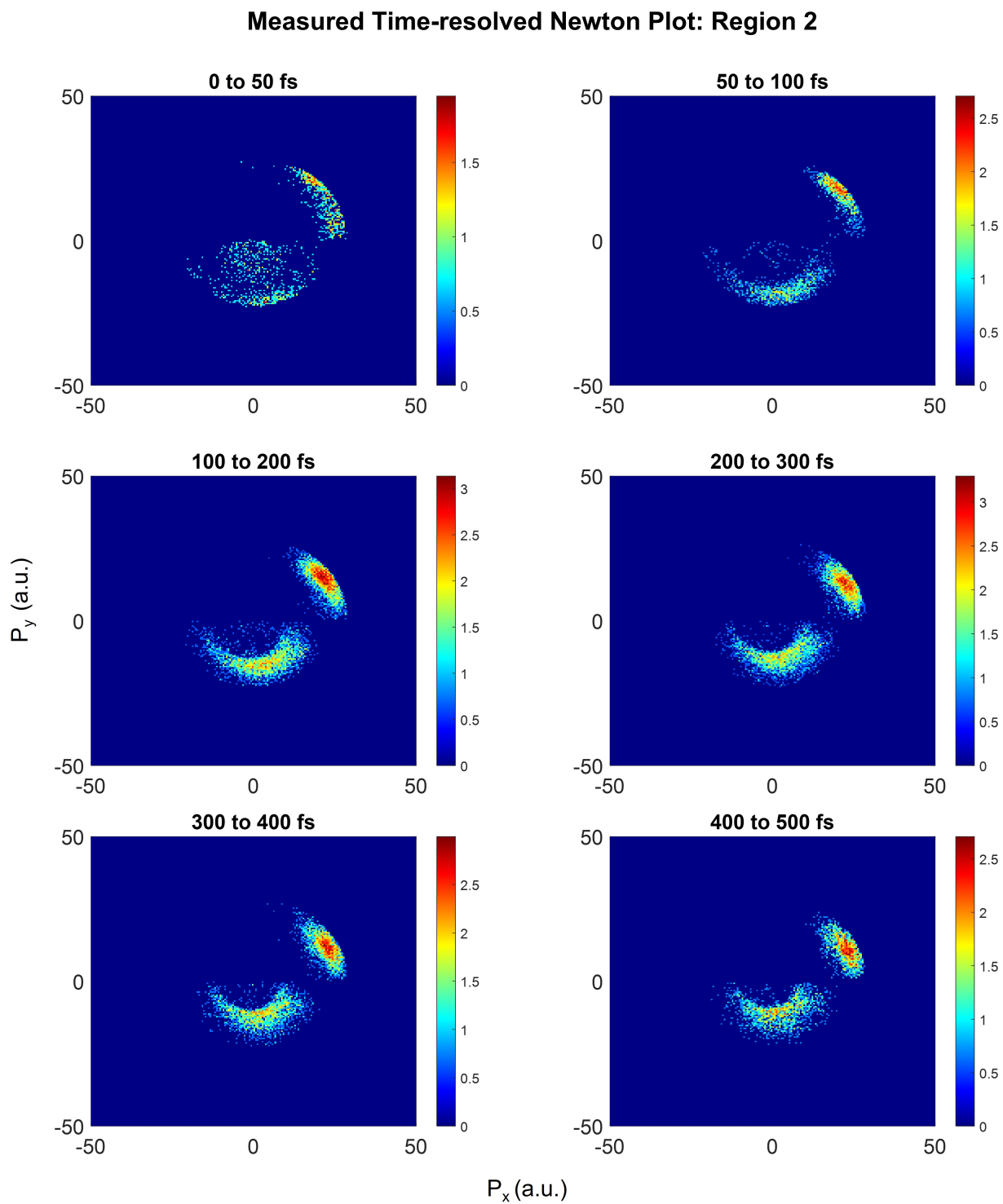


Figure 6.29. Newton plot of region 2 at different time delays from experimental measurements.

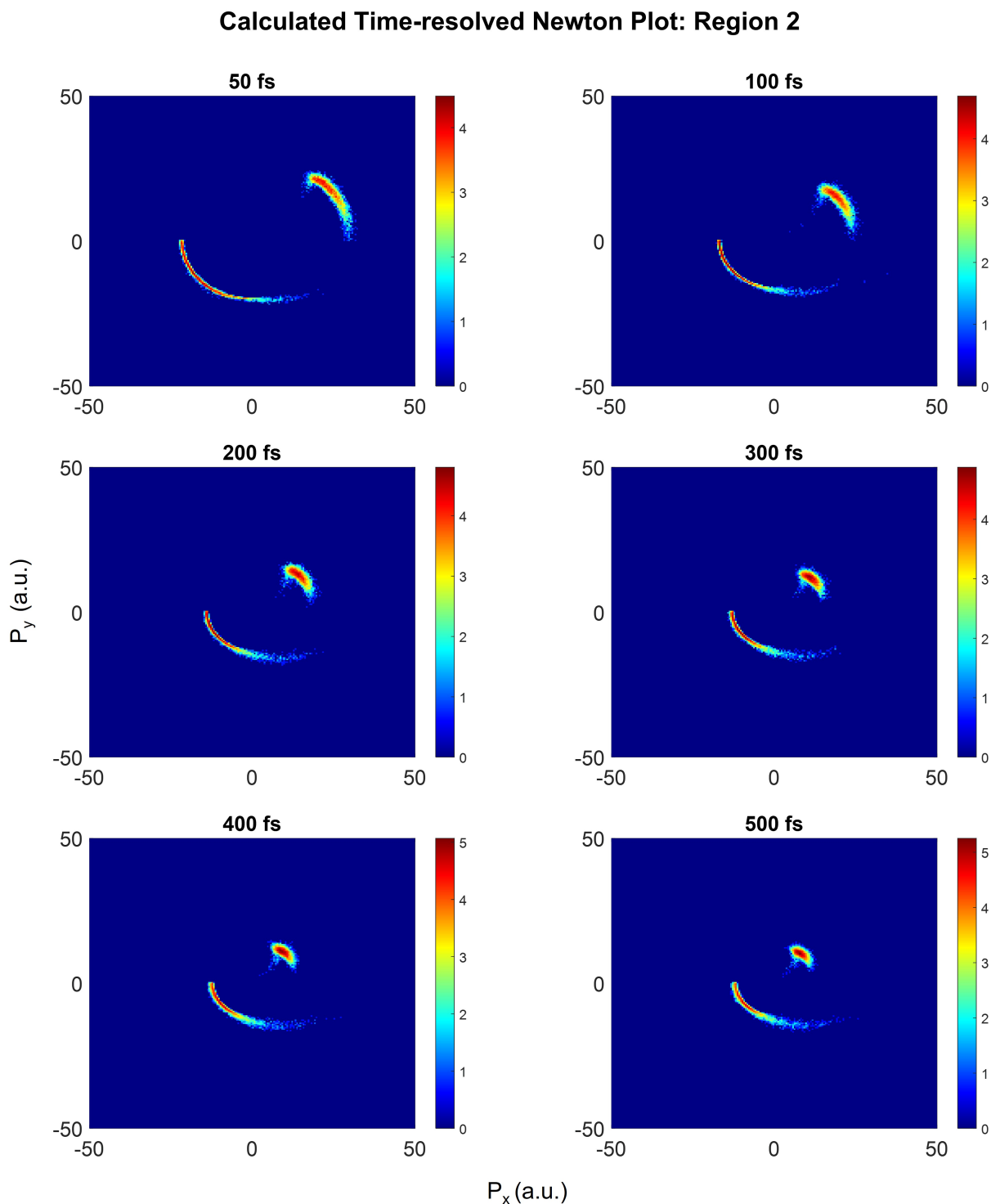


Figure 6.30. Calculated Newton plot for region 2 based on a C_{3v} geometry configuration.

Limitation of The Simulation

Firstly, the simulation does not consider the dynamic interaction processes with the laser during the pump pulse. Instead, it begins from the post-pump state, as inferred from the experimental results.

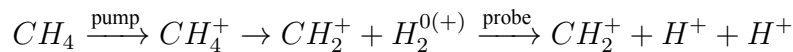
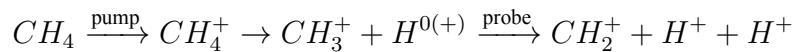
Second, charge distribution is not explicitly considered. Instead, $[CH_2^+, H1^+, H2^+]$ are treated as point charges.

Moreover, the initial parameters require further refinement to fully capture the complexities of the system.

Given these limitations, the simulation does not provide a complete representation of the photofragmentation process. However, due to its simplicity and its ability to quantitatively reproduce the measured results, it still strengthens the conclusions drawn from the experimental data, as discussed in previous sections.

6.7 Conclusion

To conclude the three-body fragmentation process of $CH_2^+ + H^+ + H^+$, the correlation between the energy release of the two protons reveals four distinct regions, each corresponding to a different fragmentation pathway. Through pump-probe experiments and KER-time dependency analysis, these four regions are assigned as follows: two concerted fragmentation processes originating from higher charged states with different symmetric modes, and two sequential fragmentation processes through methane cation states. The sequential pathways are as follows:



To identify the fragmentation pathways, dedicated analyses are done by comparing the intermediate fragments with known information from the previous chapter. For the pathway involving H_2 as an intermediate fragment, the observed features closely resemble the strong-field ionization dynamics of a real H_2 molecule. Additionally, classical simulations qualitatively reproduce the key characteristics of these pathways, supporting the experimental observations.

Additionally, in the simulation, the C_{2v} geometry is applied to the sequential pathway via H_2 , while the C_{3v} symmetry is used for the sequential pathway where H is formed. This approach successfully reproduces the time-resolved structures of Regions 1 and 2. This further supports the idea that, under the influence of the Jahn-Teller (JT) effect, methane cations undergo distinct geometric distortions, including C_{2v} and C_{3v} . These different cationic geometries, in turn, lead to their corresponding fragmentation pathways.

This conclusion further strengthens the connection between the two-body fragmentation channels discussed in Chapter 5 and the three-body processes analyzed in this chapter, highlighting the crucial role of the JT-induced molecular rearrangement process.

Chapter 7

H_3^+ Formation from CH_4

Photodissociation

H_3^+ plays a critical role in the early universe's chemical evolution, it serves as a proton donor, facilitating the creation of many molecular bonds and contributing to early star formation processes [121]. As a result, the formation of H_3^+ has been a major research focus. H_3^+ formation has also been observed from several molecules with ultrafast, strong laser pulses in recent years [122–124].

In addition to its observation, significant efforts have been made to understand the mechanism of H_3^+ formation [125]. One possible pathway is the roaming mechanism, which has been used to explain various chemical reactions [126, 127], which is also applied to H_3^+ formation. H_3^+ forms in organic molecules via double ionization, where neutral H_2 roams around the doubly charged fragment and captures an H^+ by chance. Wang *et al.* [53] investigated the roaming mechanism in ethanol, demonstrating that H_3^+ formation occurs through proton transfer to the neutral H_2 molecule leading to the formation of H_3^+ , in competition with electron transfer from neutral H_2 leading to the formation of H_2^+ . Their study also shows the H_3^+ formation time to be approximately 296 ± 87 fs. H_3^+ can also form along a minimum-energy pathway without requiring neutral H_2 roaming, making it generally faster than the roaming process. In ethane, an H_3^+ formation time of 120 fs has been observed by Y. Zhang, *et al.* [128], attributed to transient state formation.

In the case of methane, its four protons significantly provide the probability of H_3^+ formation. H_3^+ formation from methane has been observed with ion collisions [70] and also with laser fields [129]. However, the mechanism is still not clear and the time-resolved measurements are missing. In this thesis, using the same experimental setup described in the previous chapters, H_3^+ formation was observed in methane. Notably, time-dependent signals are detected in pump-probe measurements, shedding light on H_3^+ generation. Due to its simplicity, methane is a model system for investigating H_3^+ formation dynamics under

strong laser fields.

7.1 Experimental H_3^+ Observations

Although the H_3^+ peak does not directly appear in the time-of-flight spectrum due to its low yield, it can still be identified from the PIPICO plot, as marked in Fig. 4.8, and also shown here in Fig. 7.1.

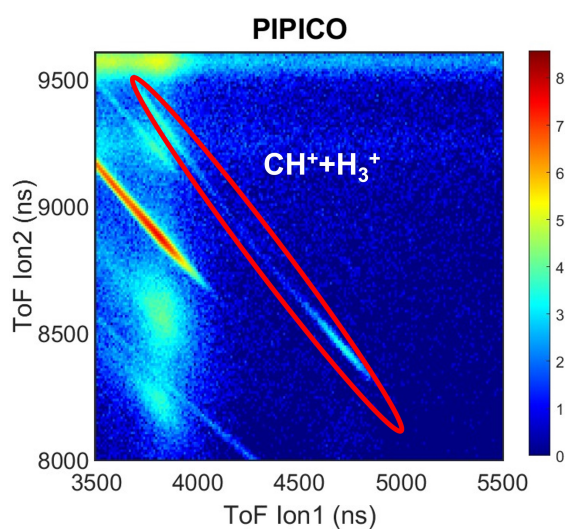


Figure 7.1. Coincidence line of $H_3^+ + CH^+$ from PIPICO plot.

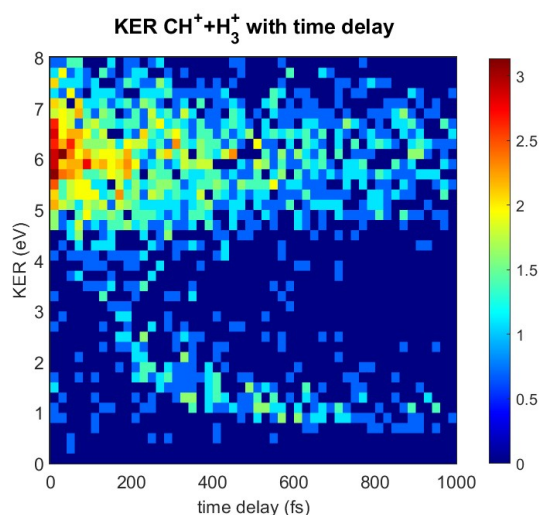


Figure 7.2. Time-dependent KER in the $CH_4 \rightarrow CH^+ + H_3^+$ dissociation

The KER time-dependency is plotted in Fig. 7.2, which is again made up of two parts:

the time-independent constant line and the time-dependent KER curve, where the H_3^+ signal shows up at $(140 \pm 10)fs$.

7.2 Time-independent Channel

In our previous chapter, we learned that the time-independent signal in both: $CH_4 \rightarrow CH_3^+ + H^+$ and $CH_4 \rightarrow CH_2^+ + H_2^+$ arises from Coulomb explosion from methane dication. However, in the case of H_3^+ formation, it is challenging to give a straightforward explanation due to its unique structure. As previously discussed, the formation of H_3^+ generally involves more dynamics, such as transient states or roaming mechanisms, in which the charged molecules reach the specific stable structure of H_3^+ .

As discussed earlier, the time-independent channel also appears in single-pulse measurements. This is illustrated in Fig. 7.3, which compares the KER from single-pulse measurements for the Coulomb explosion channels involving H^+ , H_2^+ , and H_3^+ . As shown in Fig. 7.3 (a), the KER for the $CH_2^+ + H_2^+$ channel (red) and the $CH_3^+ + H^+$ channel (blue) are similar, both peaking at 4.5 eV. However, the KER for the $CH^+ + H_3^+$ channel is significantly higher at 5.85 eV, consistent with the findings of Y. Zhang *et al.* [70] in 2019. Their work interprets this as a proton migration through a transient state of $[H_2-CH_2]^{2+}$.

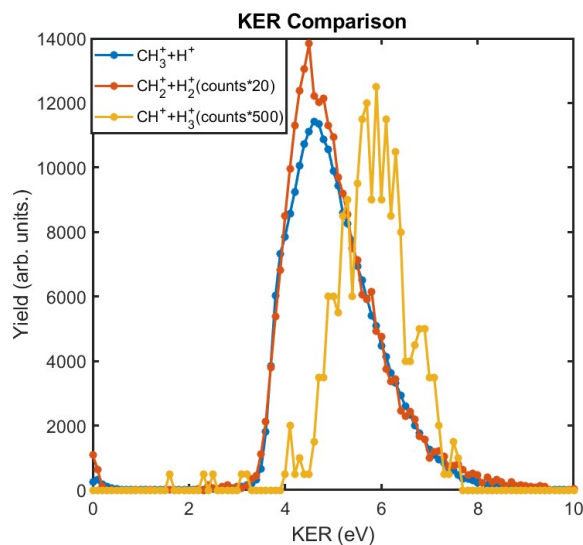
As discussed at the beginning of this chapter, if H_3^+ is formed during a roaming process, the mechanism involves the generation of neutral H_2 together with CH_2^{2+} . In this scenario, the neutral H_2 roams around the CH_2^{2+} dication, and at some point, a proton transfer occurs, resulting in the formation of H_3^+ . This roaming process is expected to be time-independent with respect to the second probe pulse.

Since there is no direct observation to identify the assumption, several related channels are compared in the following.

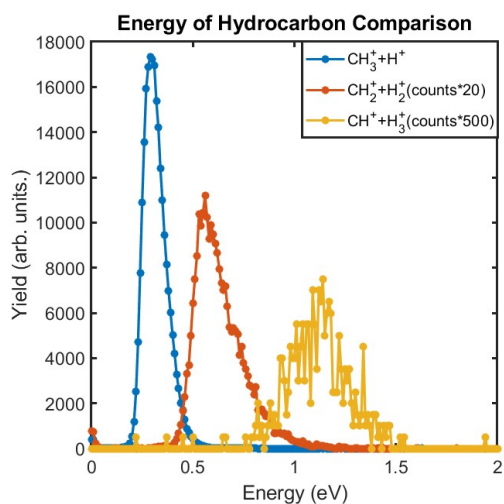
Comparison with Channel $H_2^+ + CH_2^+$

As Wang *et al.* [53] demonstrated in the case of ethanol, the proton transfer channel (H_3^+) competes with the electron transfer channel (H_2^+). Electron transfer can also occur from the neutral H_2 to CH_2^{2+} , leading to the formation of H_2^+ coincident with CH_2^+ . Like the roaming process, the electron transfer mechanism is also time-delay independent. For both processes, the precursor product is $[H_2-CH_2]^{2+}$. The probe pulse in a pump-probe experiment plays a critical role by interrupting the slow roaming process, breaking the dicationic precursor $[H_2-CH_2]^{2+}$. At short delay times, both the proton transfer and electron transfer processes are effectively interrupted by the probe pulses, resulting in reduced formation of H_3^+ and H_2^+ . As the delay time increases, the probe pulse no longer disrupts the roaming process,

(a)



(b)



(c)

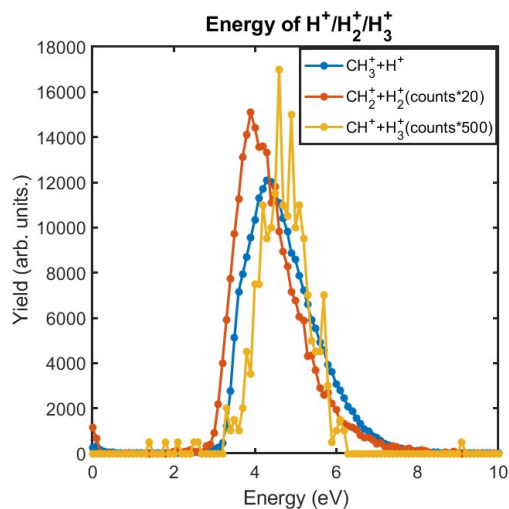


Figure 7.3. Comparison of kinetic energy release (KER) among different Coulomb explosion channels from the **single-pulse** measurement. Fragments from $CH_4^{2+} \rightarrow CH_3^+ + H^+$ are shown in blue, $CH_4^{2+} \rightarrow CH_2^+ + H_2^+$ in red, and $CH_4^{2+} \rightarrow CH^+ + H_3^+$ in yellow. (a) Comparison of the complete fragment KER for the three channels. (b) Energy of CH_3^+ , CH_2^+ , and CH^+ from their respective channels. (c) Energy of H^+ , H_2^+ , and H_3^+ from their respective channels.

allowing both channels to proceed fully. This results in the count rates for both H_3^+ and H_2^+ reaching their respective maxima and stabilizing at a plateau.

However, in this particular experiment of methane, due to low signal statistics and fluctuations in the laser parameters, an increase in count rates with delay time could not be

conclusively determined. Further investigations with improved experimental stability and higher statistics are needed to draw definitive conclusions.

Comparison with Channel $CH_2^{2+} + H_2^+$

Another interesting phenomenon arises if the precursor is indeed $[H_2-CH_2]^{2+}$. Channel $CH_4^{2+} \rightarrow CH_2^{2+} + H_2^+$ would share the precursor with H_3^+ formation channel of $CH_4^{2+} \rightarrow CH^+ + H_3^+$. This section discusses the reason why we consider $CH_2^{2+} + H_2^+$ is result by $[H_2-CH_2]^{2+}$.

During the process in which $CH_2^{2+} + H_2^0$ is formed, if H_2 gets sufficient energy or if the potential energy barrier for dissociation is low, direct dissociation of H_2 could occur. When a neutral H_2 molecule is generated by the pump pulse, the probe pulse has a certain probability of further ionizing this neutral H_2 into H_2^+ , allowing it to be detected.

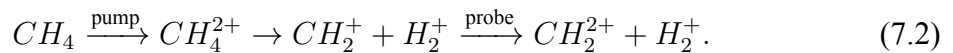
The complete process is detected as the coincidence channel of:



This channel is only appearing with a pump-probe scheme with time dependency.

As illustrated in Fig. 7.4 (a), the kinetic energy release (KER) of the $CH_2^{2+} + H_2^+$ channel is plotted as a function of the time delay. Firstly, this channel appears exclusively in the time-dependent region and does not exhibit a constant KER line. This observation suggests that the pulse intensity in the experiment is insufficient to induce direct triply ionized methane, which would otherwise lead to the formation of $CH_2^{2+} + H_2^+$ with a time-independent signal.

To confirm that pathway (7.1) is the only possible mechanism, the following alternative dissociation pathway is excluded:



If the pump-induced Coulomb explosion were responsible, the KER of $CH_2^+ + H_2^+$ would be approximately 4.65 eV, independent of time delay, as shown in Fig. 5.15. Upon interaction with the probe pulse, the Coulomb-exploded CH_2^+ would undergo further ionization, leading to an increase in energy. However, this prediction does not match the observations in Fig. 7.4.

Thus, the dissociation process is described as equation (7.1). Next is to analyze whether neutral H_2 is roaming around the CH_2^{2+} .

From Fig. 7.4 (a), where H_2^+ appears from time zero, indicating an instantaneous neutral H_2 dissociation rather than a roaming process. The red curve in Fig. 7.4 (a) is fitted with the Coulomb energy equation $E = \frac{2}{R_0 + v_0\tau}$. From this fit, the dissociation velocity for H_2 is determined to be 0.0051 a.u., while the dissociation velocity for H_3^+ in Fig. 7.4 (b) is 0.0026

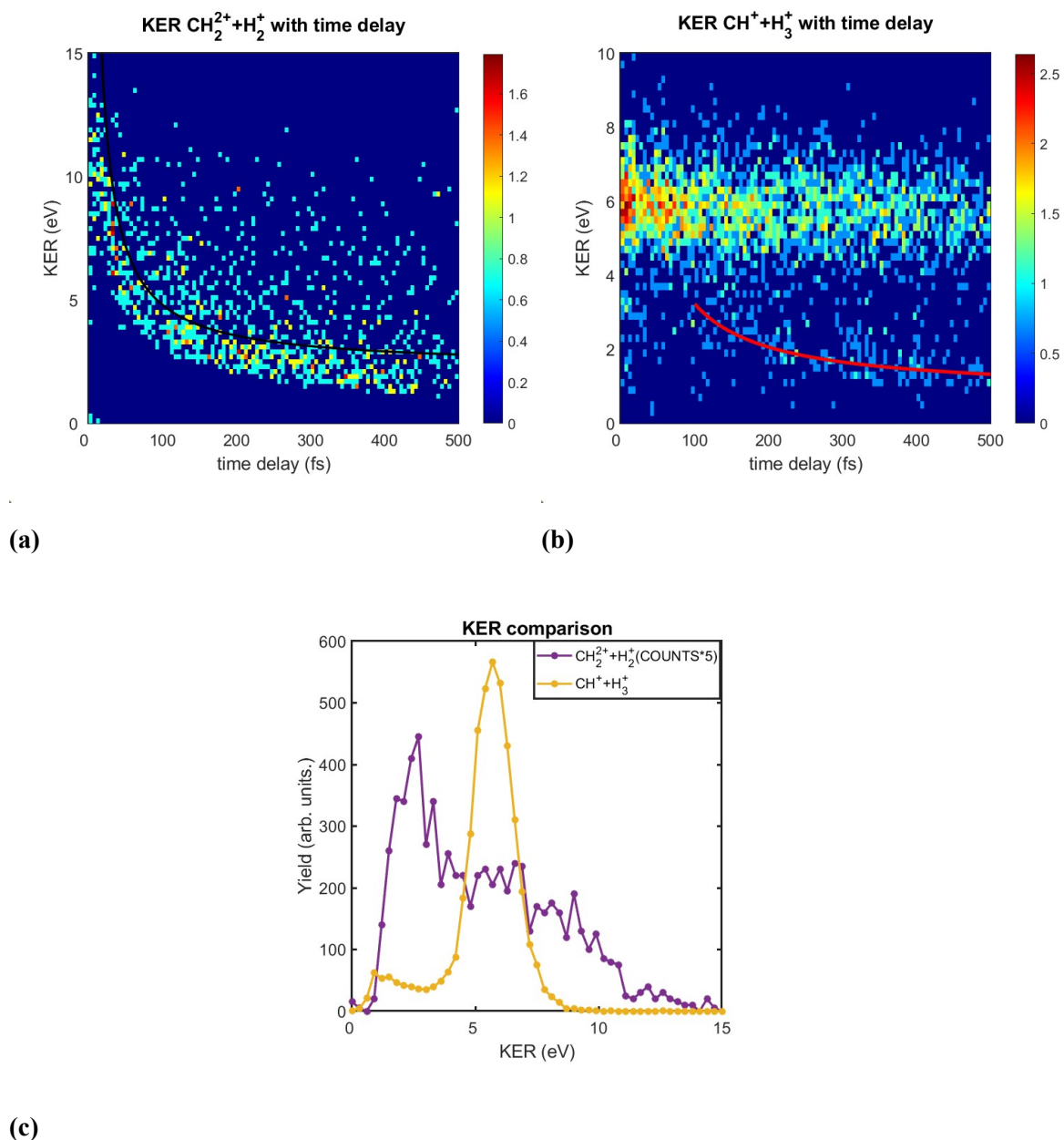


Figure 7.4. Comparison between channel $CH_4^{2+} \rightarrow CH_2^{2+} + H_2^+$ and $CH_4^{2+} \rightarrow CH^+ + H_3^+$. (a) $CH_2^{2+} + H_2^+$ KER with time delay. (b) $CH^+ + H_3^+$ KER with time delay. The time-dependent part is fitted with the red curve. (c) Time-integrated KER of two fragmentation channels.

a.u. This further demonstrates that if the neutral H_2 carries sufficient energy, it undergoes direct dissociation rather than a slower roaming process with a lower velocity.

So far, it can be concluded from the $CH_2^{2+} + H_2^+$ channel that neutral H_2 has been formed, in coincidence with CH_2^{2+} . However, whether there is a certain proportion of neutral H_2 roaming around to catch another H^+ from the CH_2^{2+} is not proven with pure experimental observations. To confirm that the roaming mechanism is the dynamics process for

this case, further calculations and additional evidence are required.

7.3 Time-dependent Channel

For the time-dependent part, since we observe a similar structure for the generation of H and H_2 as described in Chapter 5, it is not surprising to find a comparable structure here. The KER comparison between different channels in the pump-probe experiment is shown in Fig. 7.5. From this comparison, no additional information is revealed compared to the time-independent case. The constant KER peak at 5.85 eV remains unaffected by the probe. Additionally, the dissociation peak appears near the other two channels.

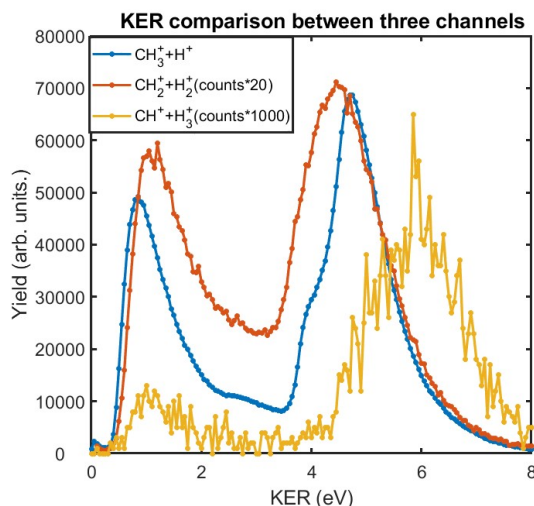
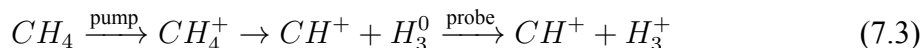
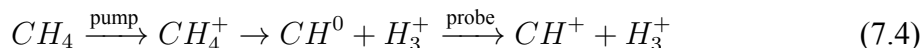


Figure 7.5. Comparison of kinetic energy release (KER) among different fragmentation channels from the **pump-probe** measurement. KER of $CH_3^+ + H^+$ is shown in blue, $CH_2^+ + H_2^+$ in red, and $CH^+ + H_3^+$ in yellow.

However, one significant difference is that H_3^0 is inherently unstable. In this context, the following pathway is not possible:



Another potential pathway is :



However, this pathway is also unlikely, as the formation of H_3^+ requires three hydrogen atoms to achieve a stable three-center bonding structure. This process likely involves intermediate steps, indicating a dynamic rearrangement within the molecule before the direct formation of H_3^+ .

So far, no reasonable explanation has been established for the time dependency of H_3^+ formation. Further calculations are required to investigate the transient states, which may provide a clearer understanding of the mechanisms.

Chapter 8

Summary and Outlook

Few-cycle NIR laser pulses with a duration of 10 fs are created using a spatial light modulator (SLM). By exploiting the birefringence properties of the SLM combined with precise phase modulation, the time delay between the two pulses—pump and probe—is accurately controlled. These pulses are then used in a series of experiments.

Upon ionization by strong NIR fields, methane, one of the simplest molecules, undergoes photoexcitation, ionization, and fragmentation. These processes encode valuable information about molecular structural dynamics. Using a Reaction Microscope, ionic fragments are detected in coincidence and analyzed, providing a comprehensive understanding of molecular dynamics of methane in strong laser fields.

Atomic and Molecular Hydrogen Ejection from CH_4^+ Fragmentation

By tracing the hydrogen motion in a **single-pulse measurement**, it has been found depending on the ejection charge states, the neutral H is emitted isotropically while the proton is emitted parallel to the laser polarization direction. The difference in angular momentum distribution makes it possible to resolve these two pathways mixed KER in a pump-probe experiment. Additionally, from the branching ratio between the pathways leading to neutral hydrogen and protons, we found that in the single-pulse measurement, neutral hydrogen is the dominant fragmentation product. By increasing laser intensity, the proton channel gets enhanced, but the dominant channel is still leading to neutral hydrogen. This reveals that these two pathways originate from different methane cation states. The ground $X(1t_2)^{-1}$ state leads to the neutral hydrogen release, while the excited $A(2a_1)^{-1}$ state results in the proton dissociation. By increasing the laser intensity, the chance to reach the higher A cation states is enhanced.

In **pump-probe measurements**, a time-delayed probe pulse induces a Coulomb explosion (CE) in the molecule, revealing the instantaneous molecular structure through the kinetic energy release and the emission direction of the fragments. Through charge exchange

(CE), both hydrogen and hydrocarbon fragments become ionized, making it originally difficult to determine whether the hydrogen atom was produced in the pump pulse as a neutral species or as H^+ . This distinction can be made based on the characteristic angular momentum distributions observed in the single-pulse measurement.

The branching ratio between these two pathways varies with time delay: at shorter time delays, the proton pathway is dominant, whereas at longer time delays, the neutral hydrogen pathway—which is the dominant channel in the single-pulse measurement—gradually emerges. As a result, the total dissociation yield increases with time delay. The possible explanation is that the neutral H dissociation is delayed in a pump-probe measurement.

A similar distinction is observed in molecular hydrogen formation, where H_2 can be produced in the pump pulse either as a neutral molecule (H_2) or a charged ion (H_2^+). The neutral pathway is found to originate from the ground X state of CH_4^+ , which is the dominant dissociation channel and exhibits an isotropic distribution in the single-pulse measurement. However, in the pump-probe scheme, the neutral pathway (H_2) is absent at short time delays and gradually appears as the time delay increases.

In addition, molecular hydrogen is found to be formed in the same pump-probe measurements within a timescale of 10 fs, which is the timescale that includes the carbon-hydrogen bond breaking and new hydrogen bond creation.

By comparing the atomic and molecular hydrogen cases, the distortion time of the methane cation due to the Jahn-Teller effect can be characterized. Assuming that the $CH_3^+ + H^+$ pathway originates from a C_{3v} geometry, while the $CH_2^+ + H_2^+$ pathway arises from a C_{2v} configuration, the time difference between these two fragmentation processes represents the potential surface evolution time. From this thesis, this evolution time is determined to be approximately 50 fs.

To further investigate proton motion and identify specific transition states, advanced theoretical calculations are required in collaboration with theoreticians. Molecular dynamics (MD) simulations provide a valuable tool to examine the branching ratios between different pathways, offering insights into the intermediate states. When combined with quantum calculations [65], MD simulations can be initialized with more accurate initial states under the laser field, making it more reliable to further develop the molecular trajectories.

Three Body Fragmentation of CH_4

Using the observation of three-ion coincidence ($CH_2^+ + H^+ + H^+$), **four distinct pathways** leading to the same final fragments have been identified.

Two of these pathways are concerted, meaning that the Coulomb explosion occurs within a single pulse, resulting in no time dependency.

The major difference between these two concerted pathways is as follows: In one path-

way (region 3 in the H^+ energy correlation plot), the two hydrogen-carbon bonds stretch symmetrically, resulting in both protons getting the same final kinetic energy. In contrast, in the other concerted pathway, the hydrogen-carbon bonds stretch asymmetrically, leading to an unequal energy distribution between the two protons.

For the two time-dependent sequential pathways, both have been identified to originate from the singly ionized methane cation.

- **Sequential Fragmentation through Atomic Hydrogen Release:**



Firstly, we observed that the two protons do not leave the molecule simultaneously, resulting in an unequal final energy distribution. This is reflected as a non-diagonal distribution in the two protons energy correlation plot, corresponding to region 2 and the time-dependent part of region 4. This asymmetric dissociation was analyzed using methods such as Newton plots and Dalitz plots.

To further confirm that the intermediate charge state after the pump pulse is CH_4^+ , an effective approach is to compare the individual fragments with atomic hydrogen release in the two-body dissociation process discussed in Chapter 5. This comparison is valid because hydrogen release occurs from the same ionic state in both two-body and three-body dissociation processes.

Based on the identified intermediate charge state, a classical simulation is performed. The resulting time-resolved momentum plots further support the pathway dynamics analysis.

- **Sequential Fragmentation through Molecular Hydrogen Release:** Another sequential fragmentation process involves molecular hydrogen formation in the intermediate state after the pump pulse. Since the resulting two protons are equal in final energy, they appear in the diagonal lines in the two protons energy correlation plot, corresponding to region 1 and the time-dependent part of region 3.



By calculating the relative energy of the intermediate H_2 , we found that the H_2 produced via methane fragmentation exhibits characteristics typical of strong-field ionization of natural H_2 , namely sequential dissociation and charge-resonance-enhanced ionization (CREI).

In addition, this three-body fragmentation pathway via H_2 formation is observed only in the pump-probe scheme and not in single-pulse measurements. This suggests that the formation of H_2 requires a few femtoseconds within highly intense laser pulses.

In summary, experimental results on the three-body fragmentation of methane provide detailed insights into molecular dynamics. To gain a deeper understanding, such as resolving different cationic states, more advanced computational methods are required.

H_3^+ Formation from CH_4 Photodissociation

The formation of H_3^+ remains an open topic of discussion, both time-independent and time-dependent channels. For the time-independent pathway, it is not yet to be determined whether the process is induced by an H_2 roaming mechanism or a transition state, which requires confirmation through molecular simulations. For the time-dependent pathways, more refined and reasonable assumptions are necessary to advance the understanding of the dynamics.

Outlook

Molecular dynamics under strong fields enables the investigation of many fundamental atomic and molecular phenomena, such as the Jahn-Teller (JT) effect in rapid molecular rearrangements, molecular potentials in strong fields, and the coupling between electronic and nuclear motion. Nowadays, with the rapid development of ultrafast intense laser pulses, improvements in imaging techniques, and advancements in computational methods, it has become possible to resolve molecular dynamics in these aspects.

Despite extensive studies on methane and its cations, many questions remain unresolved. As one of the simplest nonlinear molecules, methane serves as an ideal system for studying the JT effect. In this thesis, the strong-field nature of NIR pulse excitation—including coupling between excited states during the laser pulse—makes it challenging to capture a state-resolved picture of the JT effect. We believe that using an XUV single-photon pump pulse with fixed photon energy can help remove multiphoton contributions and enable the unambiguous identification of cationic states. If this approach is combined with high-resolution ion imaging, it could also provide access to vibrational states.

On the other hand, understanding molecular dynamics under strong NIR fields is crucial. The complexity of molecular structures makes them highly sensitive to light-induced coupling. Developing theoretical models to describe the nonadiabatic coupling between electronic and nuclear motion beyond the Born-Oppenheimer approximation remains both challenging and intriguing.

By recording molecular transformations in a controlled manner, it becomes feasible to effectively record and reconstruct a molecular movie, capturing ultrafast structural changes in real-time.

Appendix A

Coincident Channel of $CH^+ + H_2^+ + H^+$

In addition to the three-body dissociation pathway $CH_4 \rightarrow CH_2^+ + H^+ + H^+$, the channel $CH^+ + H_2^+ + H^+$ is also observed under the same pump-probe conditions as in Chapters 5 and 6. These two channels exhibit similar characteristics, which will be discussed in the following sections.

First, the dissociated H^+ and H_2^+ energy correlation is shown in Fig. A.1. It exhibits four regions similar to the energy correlation plot of H^+ with H^+ in Fig. 6.3.

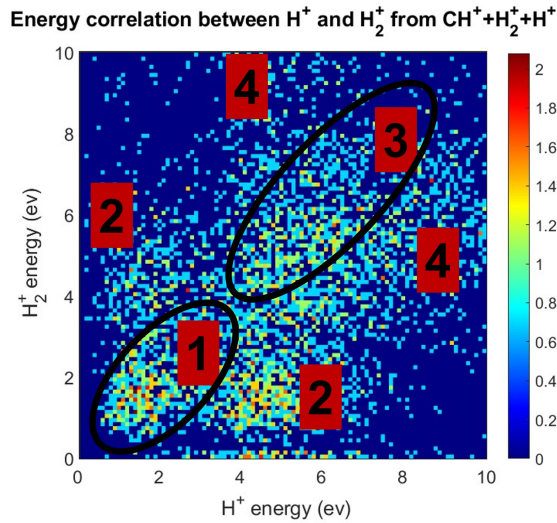


Figure A.1. Energy correlation between H_2^+ and H^+ in the dissociation channel $CH^+ + H_2^+ + H^+$. Numbers 1–4 indicate the four pathways, corresponding to regions 1–4 in the plot.

Next, the time-integrated KER for all three fragments in the dissociation channel $CH^+ + H^+ + H_2^+$ is presented in Fig. A.2(a). The time-dependent KER distribution is shown in Fig. A.2(b), where two distinct time-dependent KER curves originate from regions 1 and 2, respectively, while the time-independent parts correspond to regions 3 and 4.

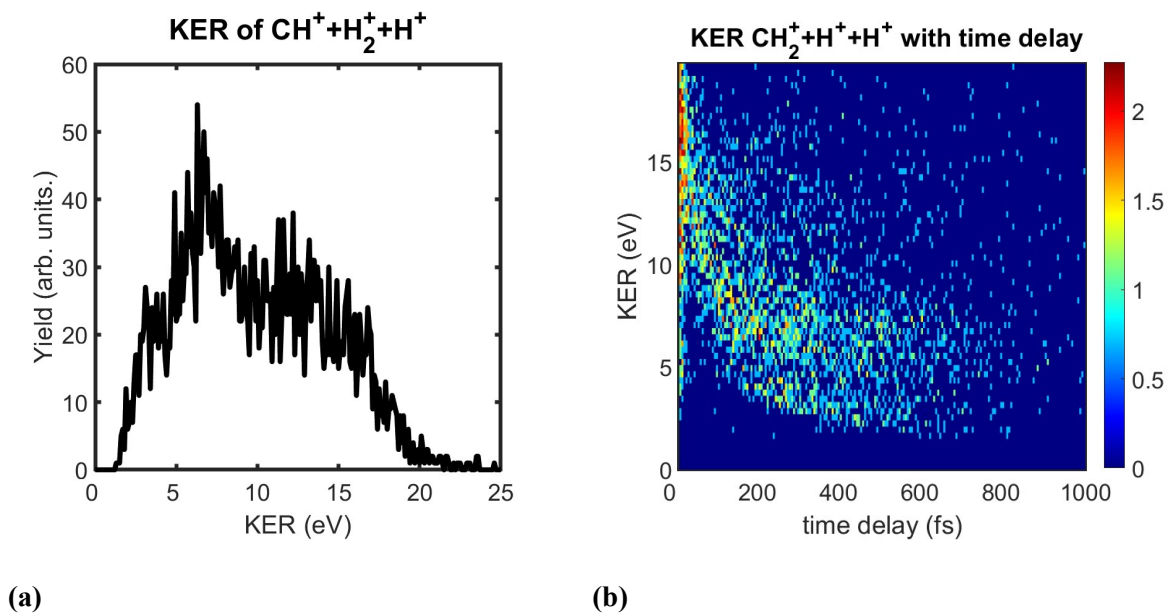


Figure A.2. (a) Time-integrated KER of channel $CH^+ + H_2^+ + H^+$. (b) Time-resolved KER distribution.

Last, the time-integrated Newton plot and Dalitz plot for all regions are presented in Fig A.3.

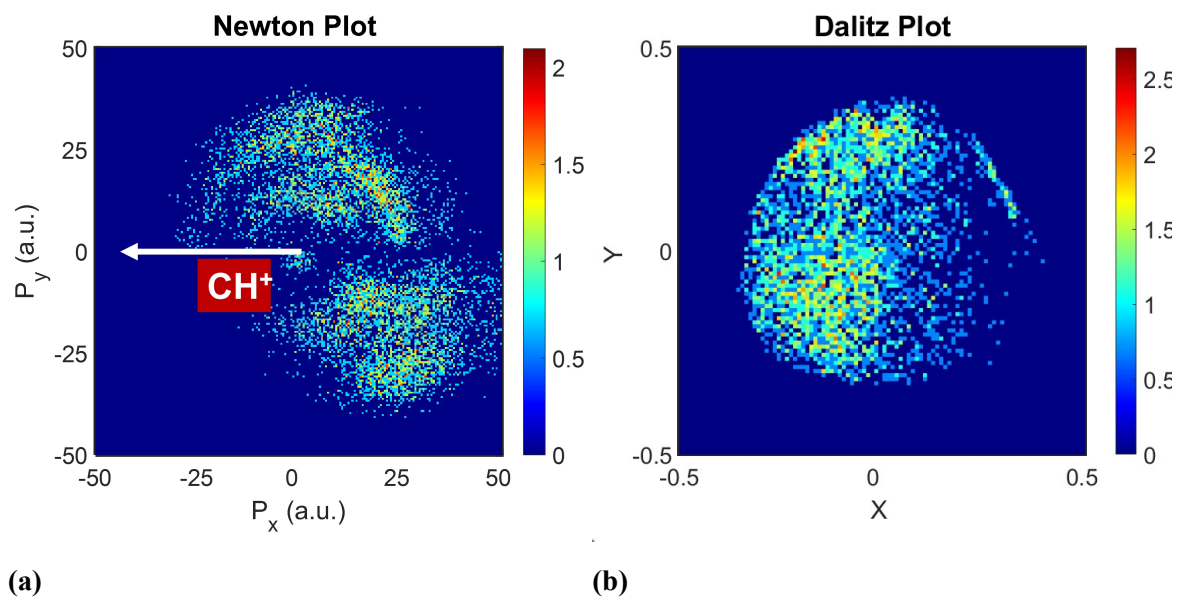


Figure A.3. (a) Newton plot: CH^+ is fixed in the negative x-direction, with H^+ plotted in the upper plane and H_2^+ in the lower plane. (b) Dalitz plot: H^+ is positioned at the left corner, H_2^+ at the bottom-right corner, and CH^+ at the top corner.

Appendix B

Experiments with Horizontally Polarized Pulses

The experiments here follow the same laser conditions as described in the thesis, with a laser intensity of 3×10^{14} W/cm² and a 10 fs pulse duration. The only difference is laser polarization: in the main text, it is vertically polarized along the spectrometer direction, whereas in this appendix, it is horizontally polarized, **perpendicular** to the spectrometer's z-axis.

Results with horizontal polarization are provided for comparison with the vertical case. The results remain consistent, further supporting the conclusions of this thesis.

B.1 Single-pulse Measurement

B.1.1 Hydrogen Emission

In the single-pulse measurement, we examine again the single ionized channel of:



The fragments CH_3^+ and H^+ display distinct angular momentum distributions, as illustrated in Fig. B.1(a) and (b). This observation confirms again that CH_3^+ is ejected isotropically, whereas H^+ is predominantly emitted along the laser polarization direction.

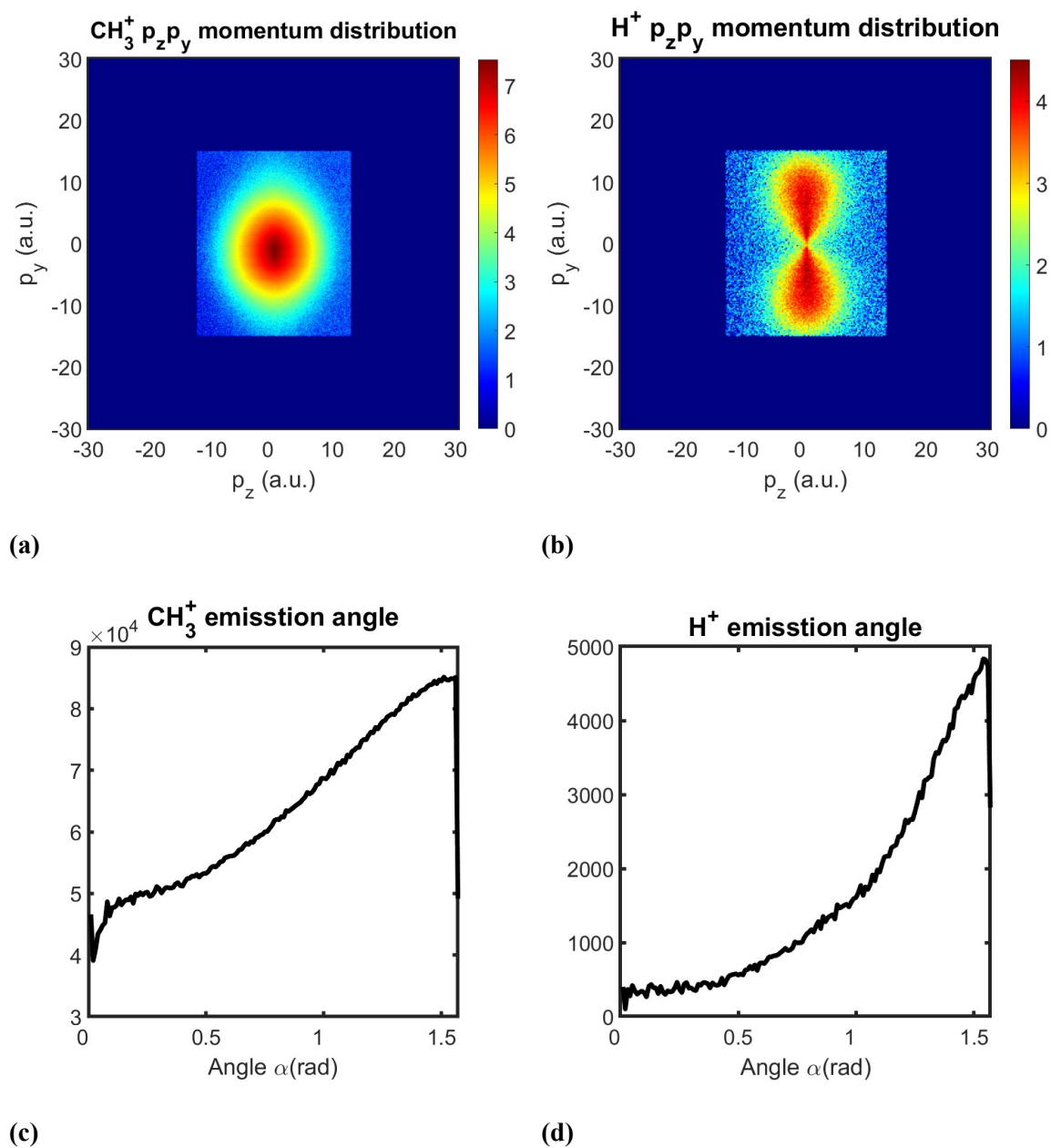


Figure B.1. Comparison with Fig 5.3, but for a horizontally polarized single-pulse measurement. (a) Momentum distribution of CH_3^+ from the $CH_3^+ + H^0$ channel. (b) Momentum distribution of H^+ from the $CH_3^0 + H^+$ channel. (c) Yield of dissociated CH_3^+ as a function of the emission angle relative to the laser polarization. (d) Yield of dissociated H^+ as a function of the emission angle relative to the laser polarization.

B.1.2 Molecular Hydrogen Emission

The single-pulse induced CH_2^+ and H_2^+ from single-ionization CH_4^+ are examined in Fig. B.2.

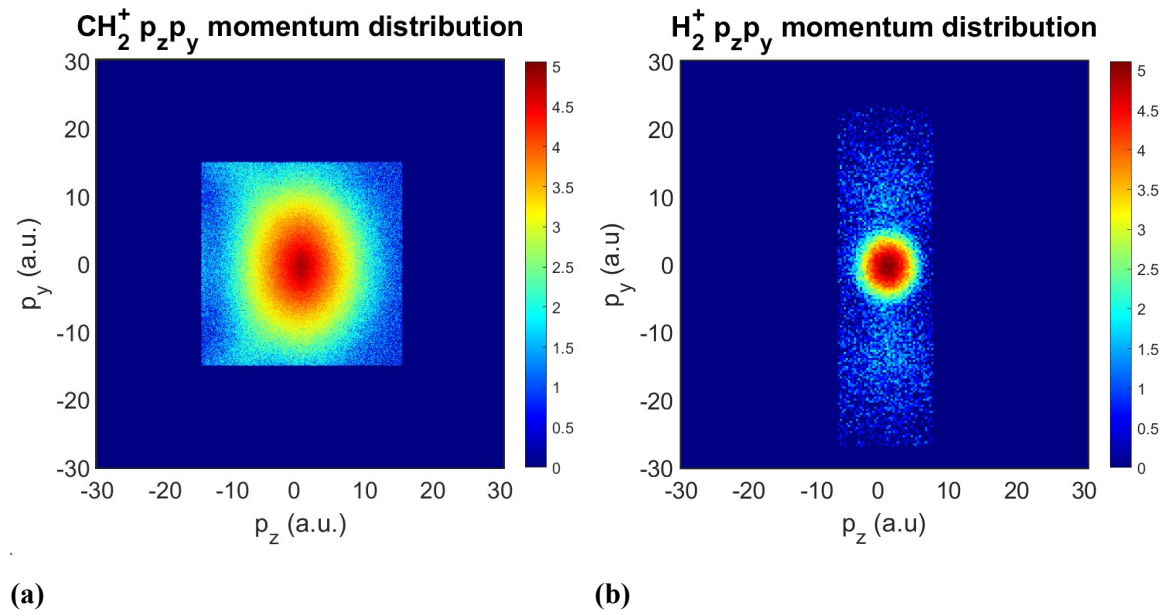


Figure B.2. Comparison with o Fig 5.13, but for a horizontally polarized single-pulse measurement. (a) Momentum distribution of CH_2^+ from the $CH_2^+ + H_2^0$ channel. (b) Momentum distribution of H_2^+ from the $CH_2^0 + H_2^+$ channel.

B.2 Pump-Probe Measurements: Comparison of Atomic Hydrogen and Molecular Hydrogen Emission

Here are the pump-probe measurement results with horizontally polarized laser pulses.

Coincidence Channel of $CH_3^+ + H^+$

As shown in Fig B.3, the KER of fragments resulting from channel $CH_4 \rightarrow CH_3^+ + H^+$ is plotted. Both time-independent and time-dependent KER are observed.

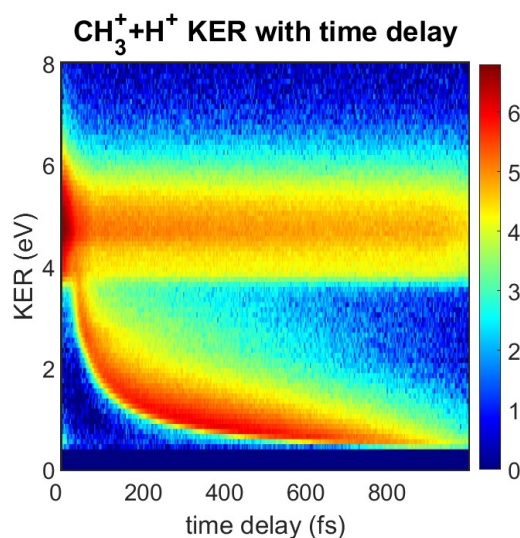


Figure B.3. Comparison with Fig. 5.7. The kinetic energy release as a function of time delay for the fragmentation channel $CH_3^+ + H^+$.

As discussed in Chapter 5, two pathways contribute to the time-dependent KER. However, making use of the angular momentum distribution character from these two pathways, a distinguish can be realized as shown in Fig. B.4.

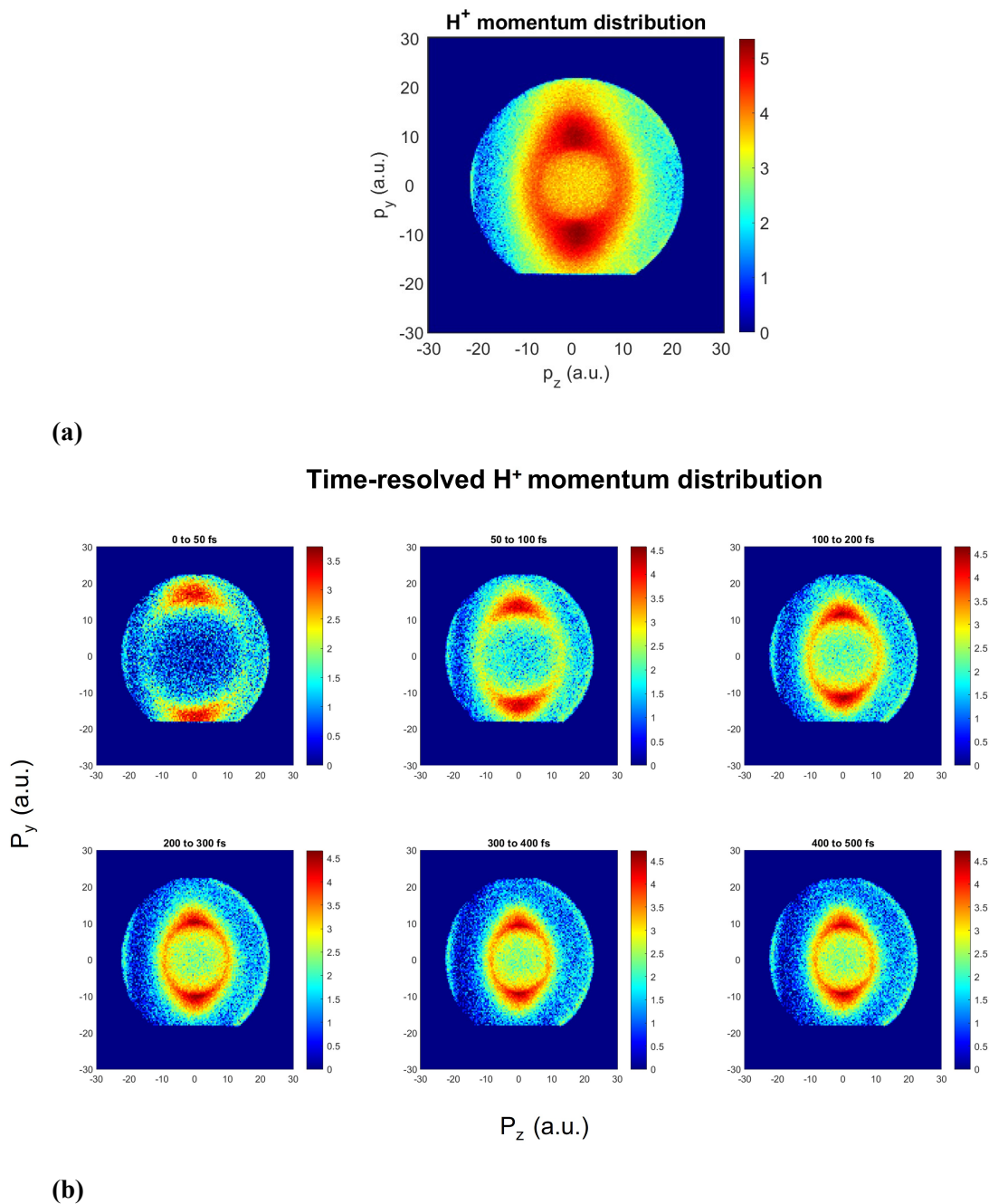


Figure B.4. Comparison with Fig. 5.9, but for the horizontal polarization. (a) H^+ momentum distribution integrated over all time delays and (b) H^+ momentum distribution at different time slices.

Coincidence Channel of $CH_2^+ + H_2^+$

The KER time dependency of the dissociation channel $CH_2^+ + H_2^+$ is presented in Fig B.5. The time-integrated H_2^+ momentum distribution is shown in Fig B.6(a), while the time-resolved results are displayed in Fig B.6(b).

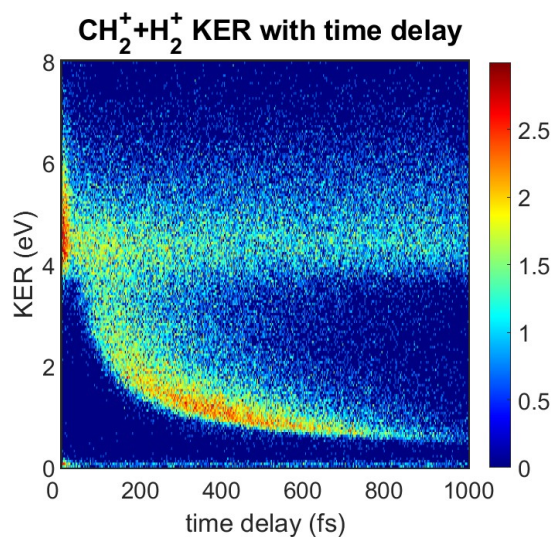


Figure B.5. Comparison to Fig 5.15, showing the kinetic energy release of the dissociation channel $CH_2^+ + H_2^+$ as a function of time delay under horizontally polarized light.

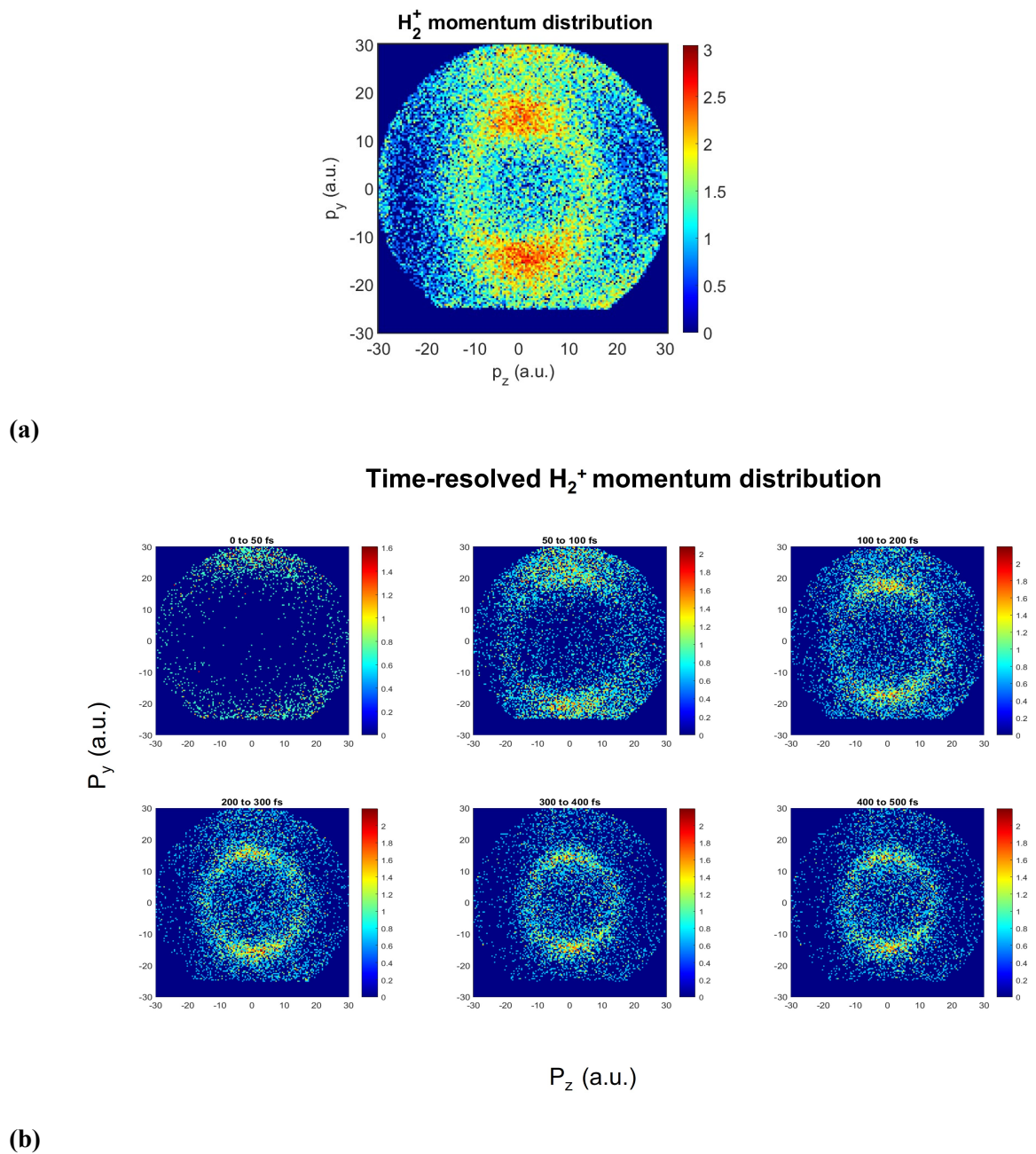


Figure B.6. Similar as Fig. 5.17, but with the horizontal polarized light. (a) H_2^+ momentum distribution integrated over all time delays. (b) H_2^+ momentum distribution at different time slices.

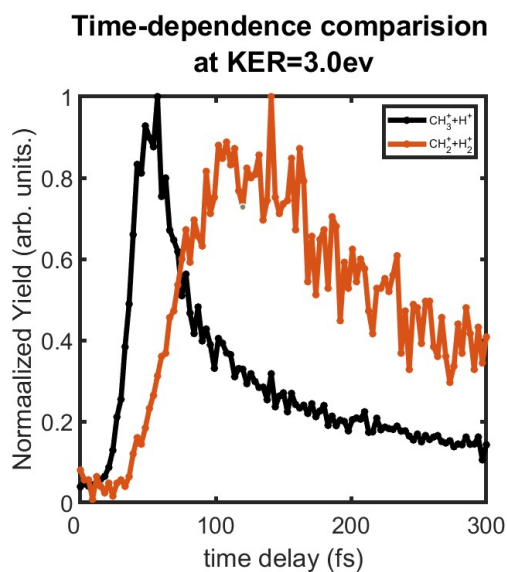


Figure B.7. Comparison with Fig. 5.22. Time-dependent comparison between two dissociation channels. (a) Yield variation over time at KER = 3.0 eV.

To provide a comparable analysis between the channels $CH_3^+ + H^+$ and $CH_2^+ + H_2^+$, as conducted in Section 5.4 of Chapter 5, Fig. B.7 presents their time dependence when the fragments reach a KER of 3.0 eV. The time difference peak between these two channels is interpreted as the cation evolution time from C_{3v} to C_{2v} geometry, which agrees with the same value as in Chapter 5, approximately 50 fs.

B.3 Three Body Coincidence

For the dissociation channel of $CH_2^+ + H^+ + H^+$ measured with horizontally polarized pulses, the energy correlation between two H^+ is plotted for horizontally polarized light in Fig. B.8. Again, we can see four regions as we separated in Chapter 6. However, in the higher-energy regions (regions 3 and 4), the detection efficiency is lower due to highly energetic fragments escaping the detector. (This effect is particularly pronounced for horizontally polarized light, as the fragments acquire greater transverse momentum, causing them to reach the chamber wall before reaching the detector.)

B.3.1 Energy Correlation between Two H^+

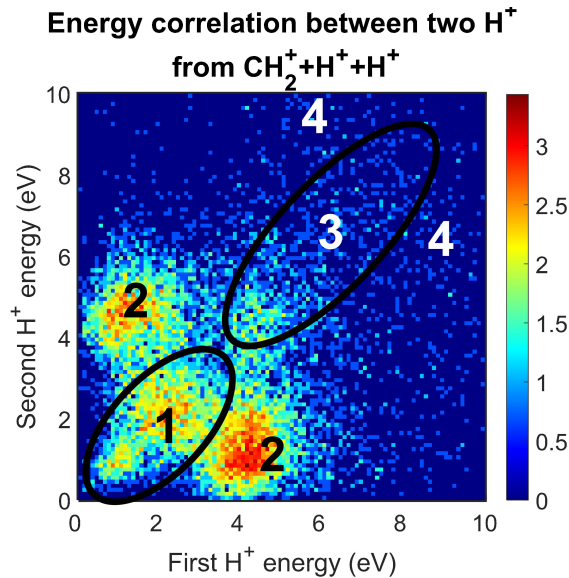


Figure B.8. Comparison with Fig. 6.3. Energy correlation between two H^+ from $CH_2^+ + H^+ + H^+$ with horizontally polarized pulses.

B.3.2 Characteristics of the Four Pathways

In Fig. B.9(a), the KER of the three fragments is plotted as a function of time delay. The time-dependent KER distributions for the four separated regions are shown in Fig. B.9(b)–(e). For each region, the KER time-dependent features are consistent with the results from Chapter 6, as shown in Fig. 6.5.

In Fig. B.10, Newton plots are presented. The key characteristics of each region remain consistent with those in Fig. 6.6 for vertically polarized light.

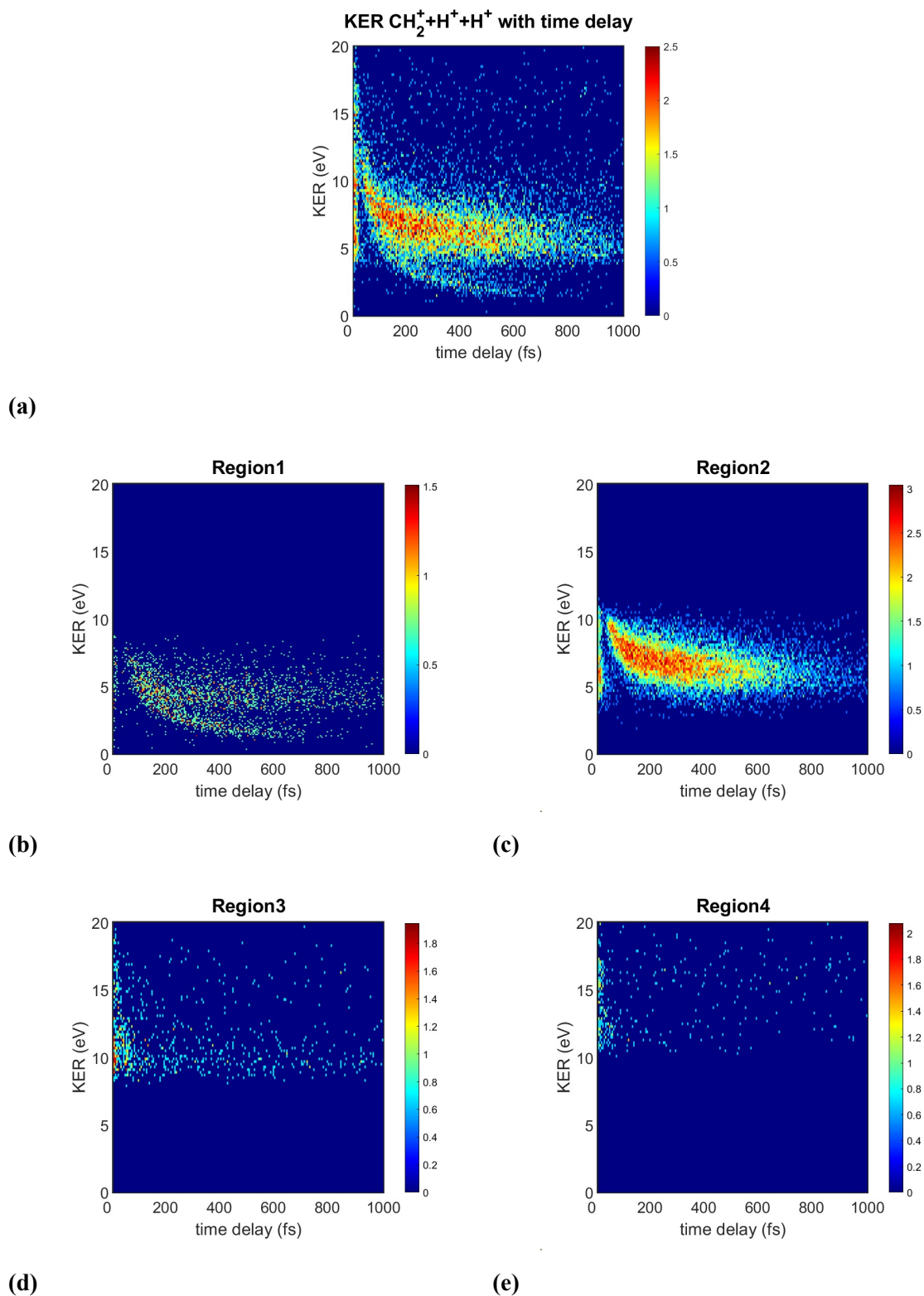


Figure B.9. (a) $CH_2^+ + H^+ + H^+$ time-dependent KER. (b)-(e) time-dependent KER for region 1 to region 4, separately.

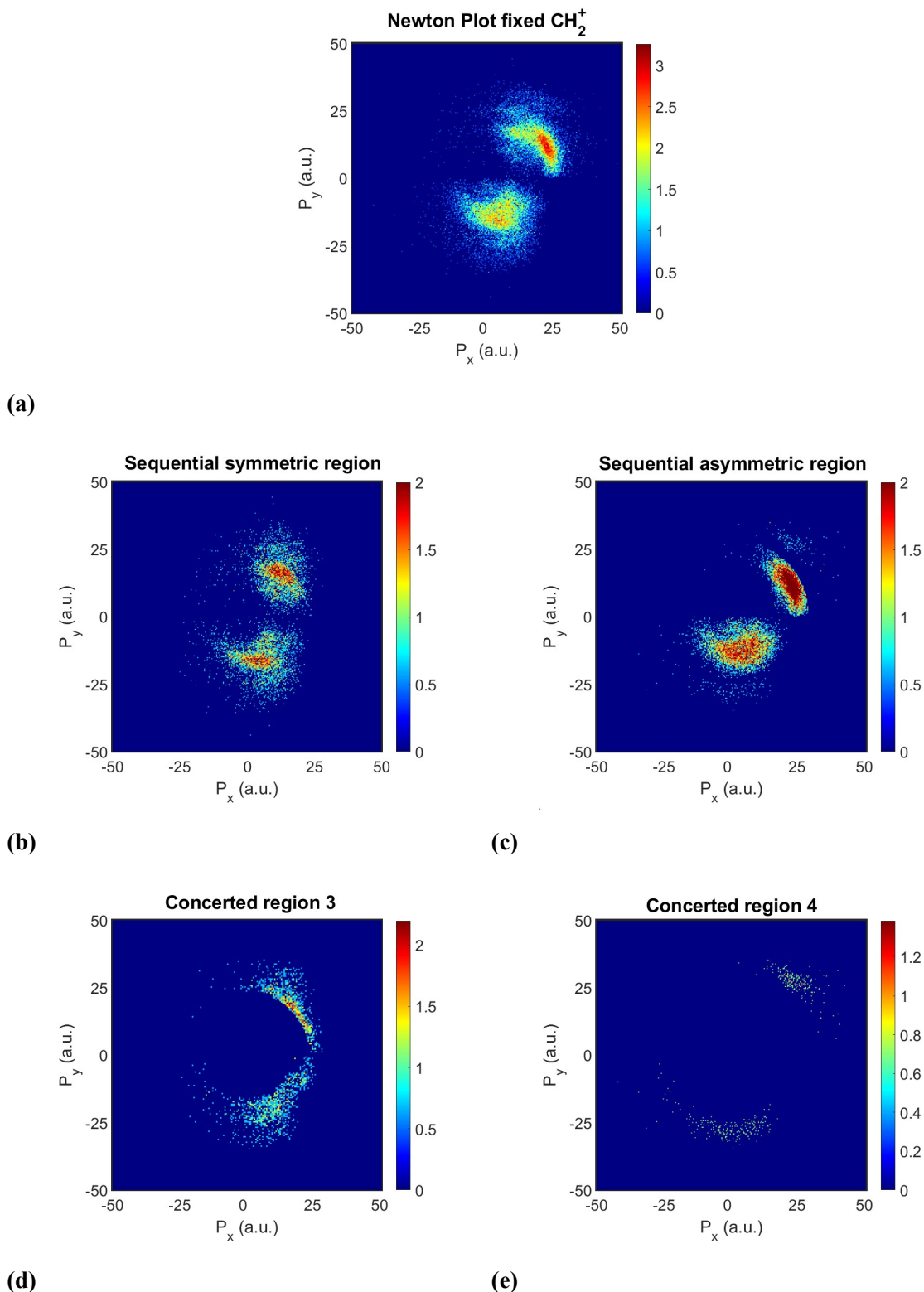


Figure B.10. Comparison with o Fig 6.6. □a) Netwon plot for all regions integrated. The higher energy fast 'proton' is put on the upper plane ($y > 0$) while the low energy 'slow' proton is plotted on the bottom half. (b). Newton plot for diagonal region 1 and part of region 3, which can be seen to continue with region 1. (c) Newton plot for nondiagonal region 2 and part of region 4 where can be seen continue with region 2. (d) Newton plot for region 3 concerted part, where the events are time-independent. (e) Newton plot for region 4 concerted part, where the events are time-independent.

B.4 The Formation of H_3^+

Notably, H_3^+ is also observed under horizontally polarized light. In Fig. B.11, the KER of the $CH^+ + H_3^+$ channel is plotted as a function of time delay. As discussed in Chapter 7, both time-independent and time-dependent KER components are present.

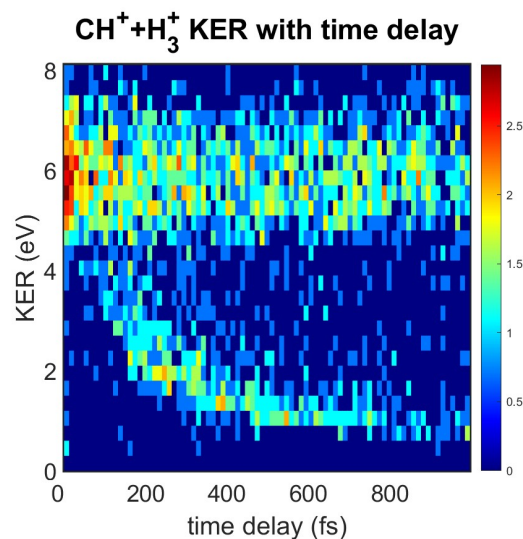


Figure B.11. Comparison with Fig. 7.2. The KER of the dissociation channel $CH^+ + H_3^+$ as a function of time delay under horizontally polarized light.

Appendix C

SLM Alignment Procedure

Figure C.1 presents an actual photo of the SLM setup in the laboratory.

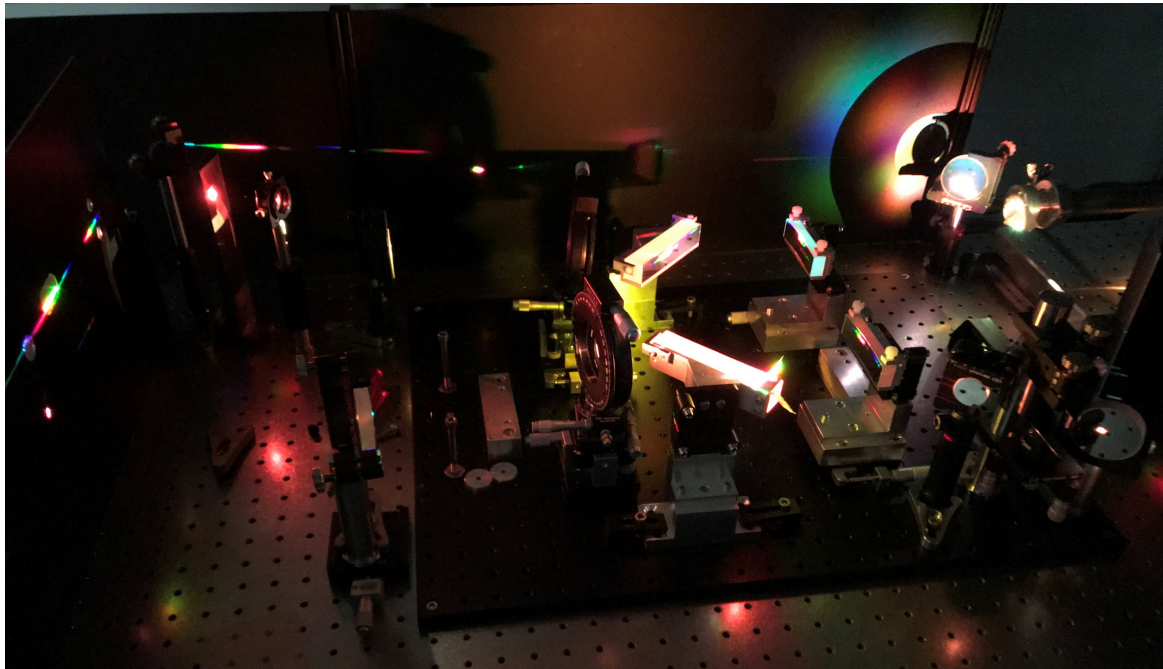


Figure C.1. ‘Pulse shaper’ set-up in the lab.

As shown in Chapter 3 with the SLM 4-f geometry design in Fig. 3.4, to align the pulse shaper, the following procedure needs to be followed:

C.1 Alignment with Optics

All the 4-f related optics together with the SLM are installed in a breadboard for flexibility. For alignment purposes, a He-Ne laser is used. Before installing any optics, four irises are put in front of the requested position for two Folding mirrors (FM) and cylindrical lenses

(CM). Beforehand, a pair of periscopes are installed centered with two side cylindrical lenses (CM) center for guiding the beam from both sides.

Two plane folding mirrors(FM) need to be installed first. Two irises are set horizontally with the breadboard for guiding the He-Ne laser passing through. Once the beam is aligned horizontally through both apertures, a plane mirror is placed in the input beam and adjusted so that the reflected beam passes through the Fourier plane and reaches the iris at the second mirror. Afterward, the plane mirror can be removed, and the alignment laser is coupled on the other side. These alignment steps are then repeated on the other side in the same way. Two folding flat mirrors are installed on both sides to check if the reflected beams are hitting the iris position for the cylindrical lenses.

The next step is to install two cylindrical mirrors(CM). These two CMs are installed one by one. To install a cylindrical mirror, place it at the position of the target iris. The beam should then reflect onto itself while passing through the iris center, ensuring proper alignment for the second CM. This procedure needs to be repeated several times until both lenses are installed properly.

Positioning the translation stage for the cylindrical lenses is more critical and challenging due to the long Rayleigh length of the cylindrical mirror. A simple approach is to place a paper near the Fourier plane for initial optimization, with fine-tuning left for later adjustments.

C.2 Grating Alignment

Installing the grating is a more challenging task. To install a single-sided grating, the CM on the same side must first be removed. The grating holder is then roughly positioned, with a silver mirror temporarily installed in place of the grating.

The next step is to direct the beam through a plane mirror on one side, across the Fourier plane, and onto a plane mirror on the opposite side for reflection. The cylindrical mirror on the opposite side focuses these two beams onto the silver mirror which was positioned in the grating holder. Since the broadband spectrum will eventually pass horizontally through the planar mirrors at different positions, it is critical to ensure that the focus on the grating (or the silver mirror during setup) remains consistent.

This can be achieved by introducing two parallel beams with a slight horizontal separation. The focal points of both beams should overlap on the silver mirror, which can be adjusted by vertically tuning the cylindrical mirror. To ensure both beams are reflected along their original paths, the grating holder must be slightly tilted. During the alignment process, it is crucial to confirm that the two beams remain parallel and at the same height.

After coarse tuning, the gratings can be installed using the actual femtosecond laser at

$\lambda = 785 \text{ nm}$. The holographic grating is designed to maximize the intensity of the ± 1 diffraction orders, with an incident angle of 10.8° , which matches the diffraction angle. It is crucial to ensure the correct orientation of the grating, as using the wrong side will result in a mismatch between the diffraction and incident angles.

The next step involves introducing broadband spectrum light and carefully checking for spatial dispersion at long distances for different frequencies. This can be done by blocking certain frequency components and observing the beam shape and position at a distant location.

C.3 SLM Installation

The last step is to put the SLM into the 4-f setup, which is trivial only if the SLM is fixed and aligned with the horizontal line. Otherwise, the Fourier plane does not overlap with the SLM plane.

C.4 Fine-Tuning and Final Verification

Due to its complexity in ensuring the perfect alignment, several methods are introduced to check the alignment with the fine-tuning and the daily maintenance.

C.4.1 Optical Methods

In practice, the first indication of good alignment is the output power, after the grating, the transmission efficiency is around eighty percent for red light at $\lambda = 785 \text{ nm}$, and the total output from the '4f' set-up should be higher than 50 percent.

C.4.2 Dispersion Measurement

As indicated before, it is very difficult to conclude with the perfect alignment by geometry and optical examinations, the best way is to measure the dispersion directly. Several methods can measure the spectral phase, here are the methods used in this lab. The fastest way to check pulse duration/dispersion is by introducing air plasma with a concave mirror or lens. With an $f=2.5 \text{ cm}$ lens and 100 mW power, it must be possible to see a clear plasma in the air under the condition of a short pulse $t < 50 \text{ fs}$.

The first method is auto-correlation pulse duration measurement, which has been introduced in Chapter 3. Since the 4-f set-up should not introduce any additional propagation-induced dispersion, the pulse duration before and after the pulse shaper should remain the same if no external phase control is done by the SLM. Here are some examples. Fig C.2

shows the incoming pulse with a duration of $25\text{ fs}(\pm 5)\text{ fs}$ measured by an autocorrelator with the intensity correlation scheme introduced in Chapter 3.

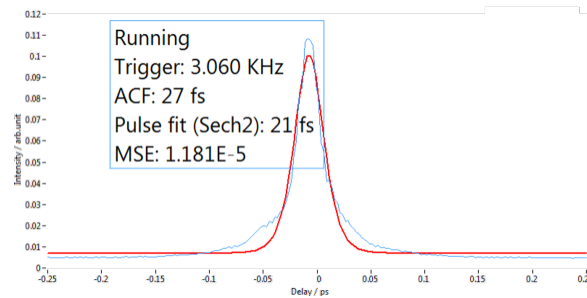


Figure C.2. Autocorrelation of the incoming pulse, with a measured pulse duration of $25(\pm 5)\text{ fs}$.

If the '4f' setup is misaligned, the measured pulse duration after the pulse shaper may be shorter, longer, or chirped, as shown in Fig. C.3 (a)–(c), respectively.

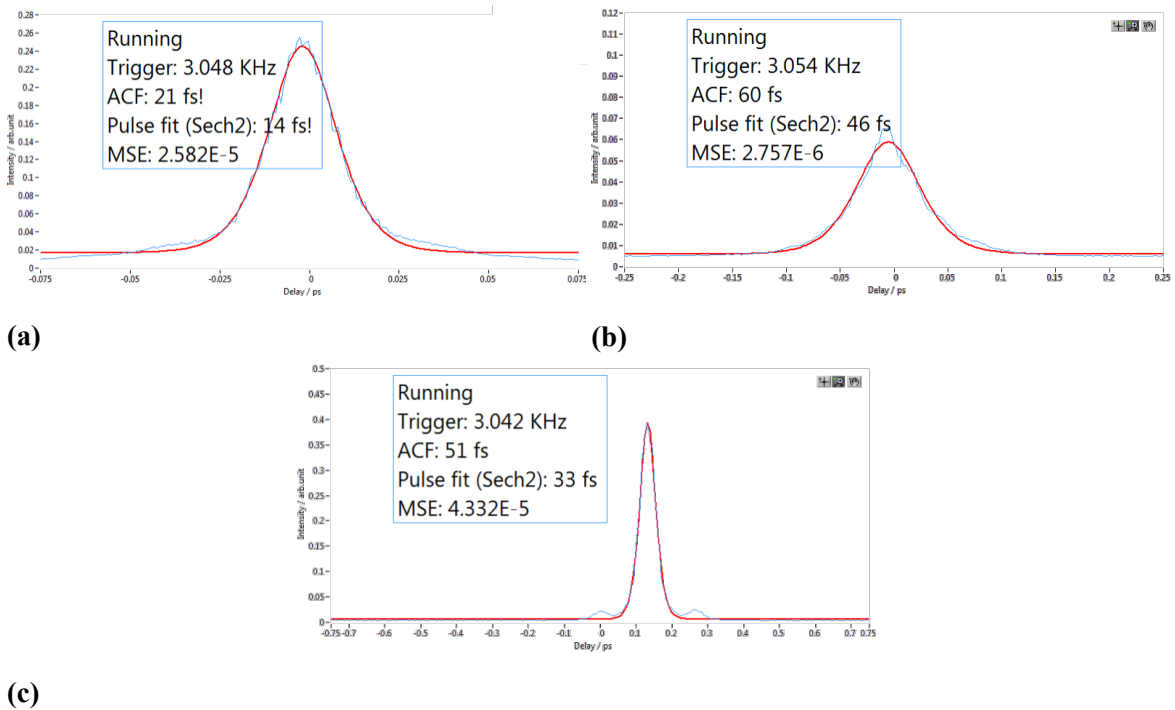


Figure C.3. Measured autocorrelation traces of the output pulse from the pulse shaper under misalignment. (a) The output pulse has a measured duration of 14 fs, shorter than the incoming 25 fs pulse. (b) The output pulse is longer than the input pulse. (c) Two side peaks appear on either side of the main output pulse, indicating the creation of a pre-pulse by the SLM.

C.4.3 Alignment Examination with the Reaction Microscope

As introduced in Chapter 3, ReMi is used as feedback for pulse compression. A shorter pulse results in higher laser intensity, leading to an increased ionization count rate in the ReMi. Therefore, ReMi serves as a final check for alignment and further optimization.

First, a pair of wedges can be installed after the SLM. Moving the wedges by a few μm should cause a significant change in the count rate, but only if the pulse duration is short.

Additionally, as discussed in Chapter 3, when two delayed pulses overlap, they interfere with each other. This interference pattern can be observed by recording the ionization count rate as a function of phase delay, as shown in Fig. C.4.

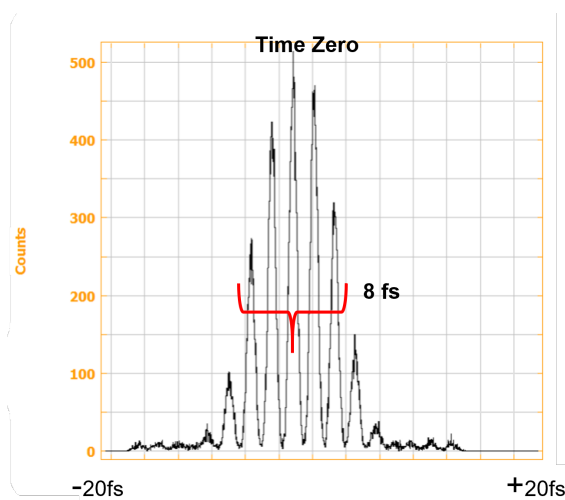


Figure C.4. Measured pulse duration using ReMi. The x-axis represents the time delay between two pulses, ranging from -20 fs to +20 fs, with a time step of 0.1 fs. By estimating the full width at half maximum of the interference pattern, the pulse duration is determined to be approximately 8 fs. This is the pulse employed in this thesis.

Appendix D

Supplemented classical simulations

D.1 Region 1

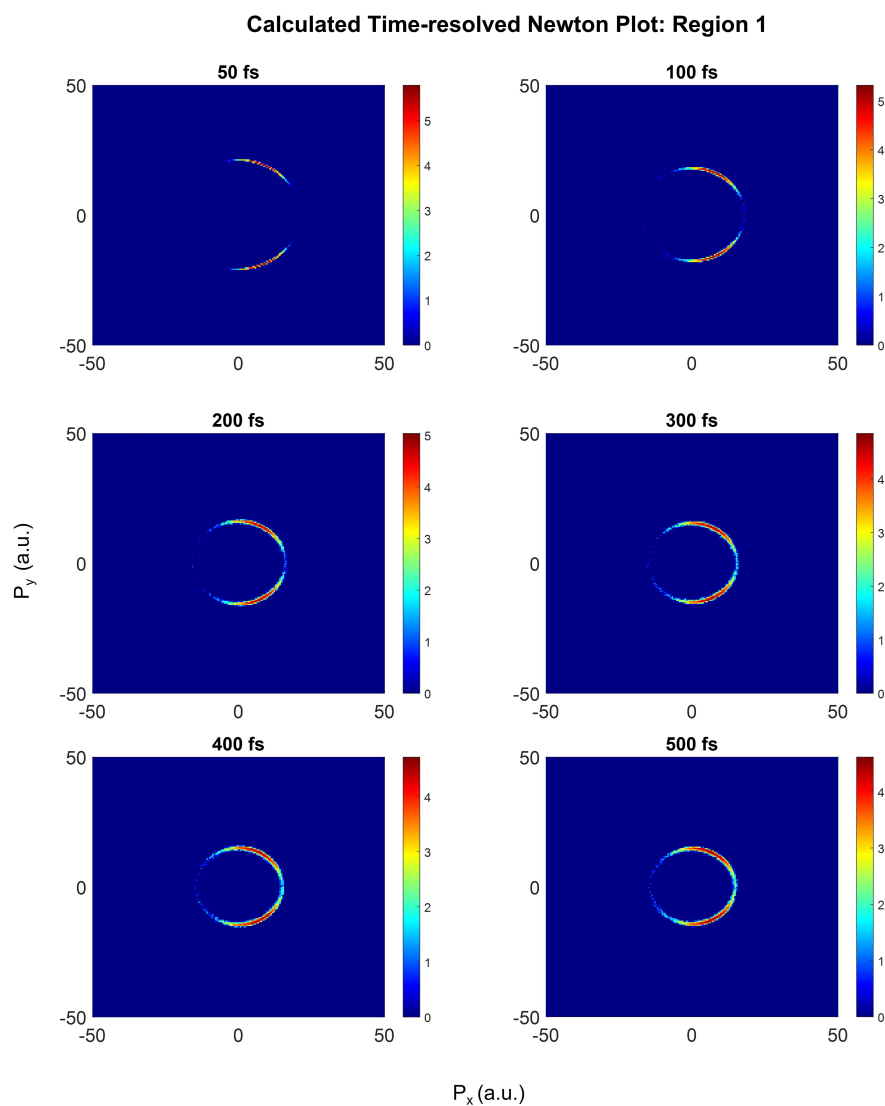


Figure D.1. Initial Geometry. This figure presents the calculated results after changing the initial geometry from T_d to C_{2v} .

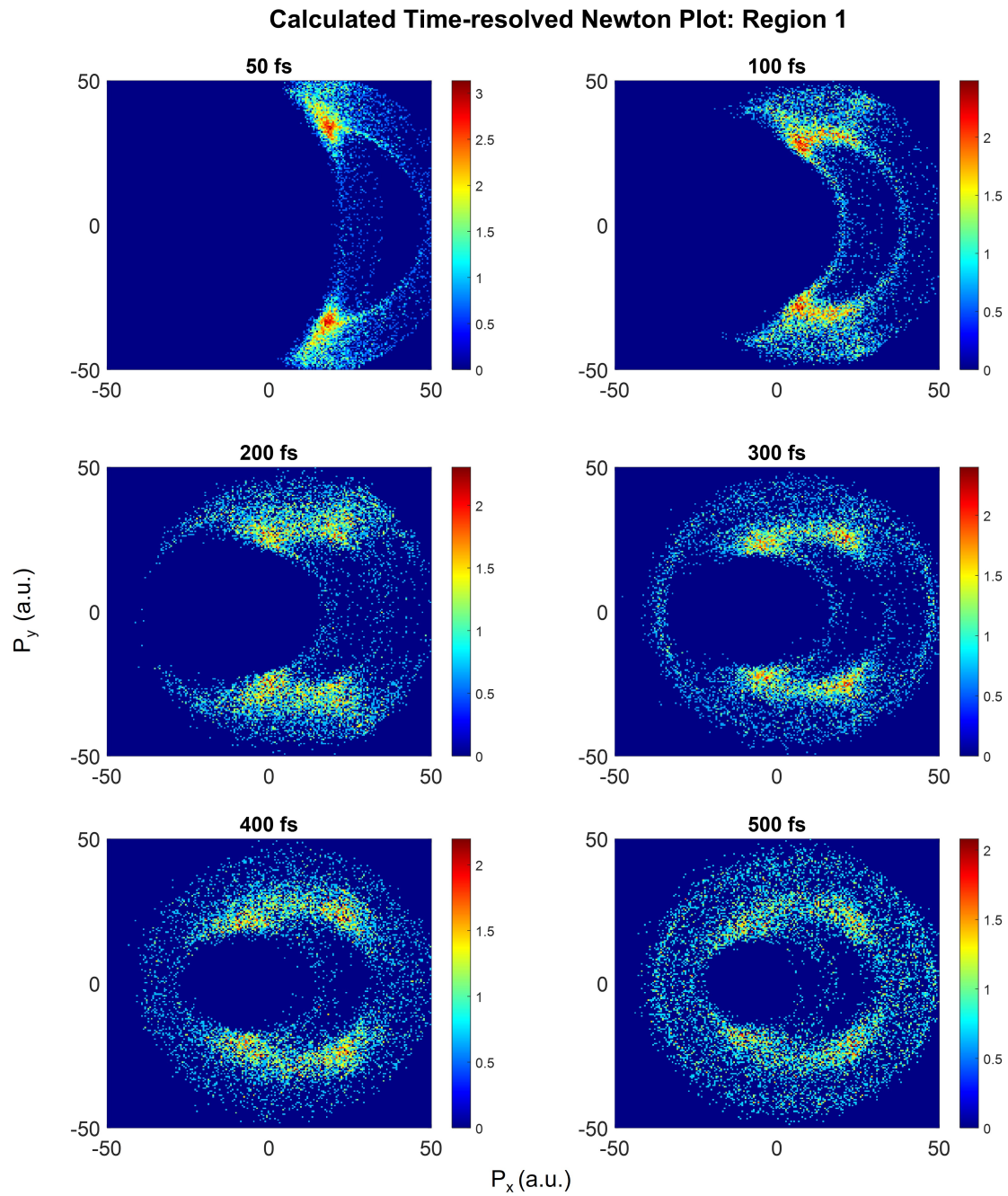


Figure D.2. Initial Velocities: If all initial settings remain the same as in Fig. 6.27, but the initial dissociation velocity is modified, the resulting Newton plots exhibit a significant shape change, as shown in this figure.

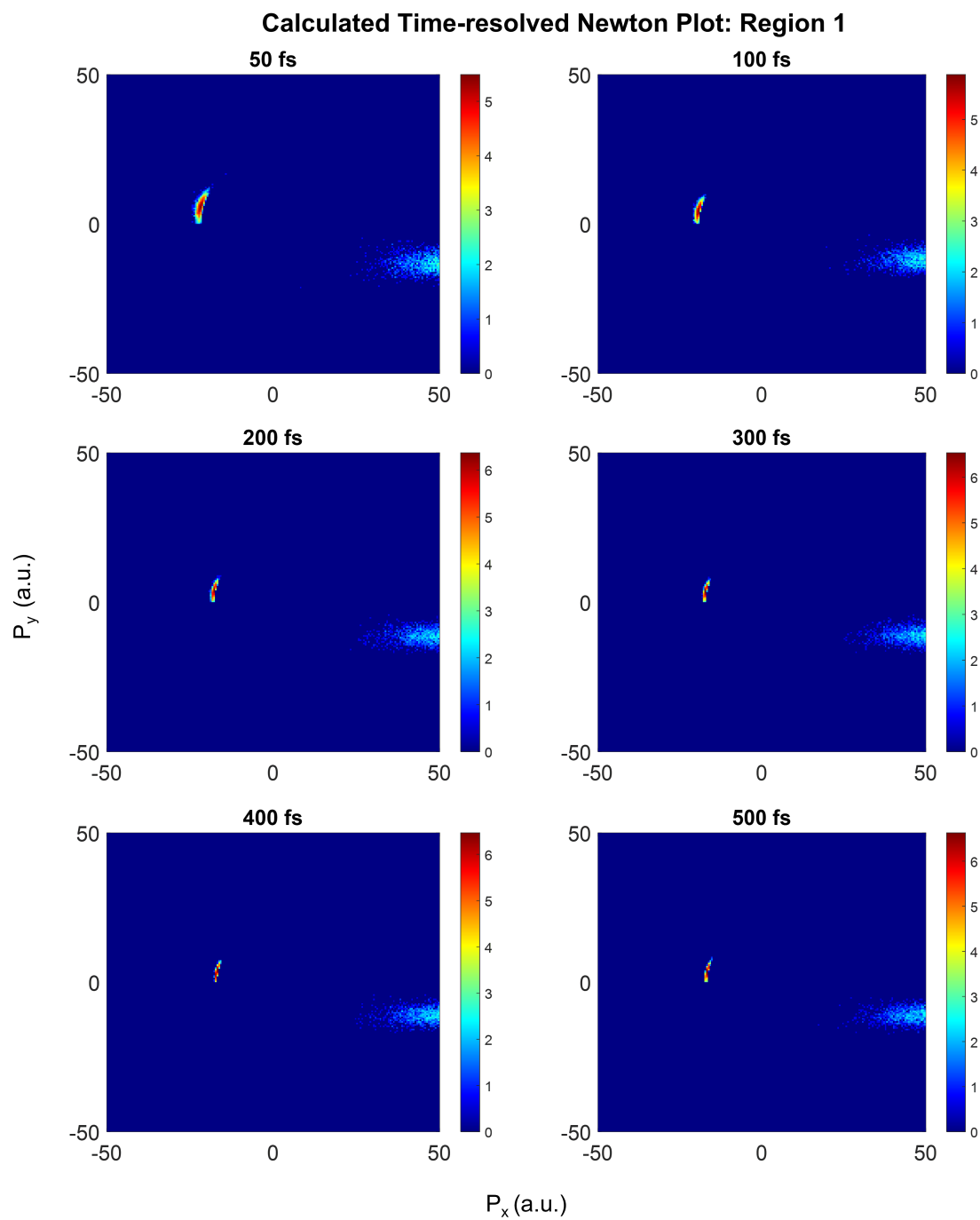


Figure D.3. Morse Potential: By setting the equilibrium bond length R_e as the initial distance between the two hydrogen atoms, the calculated results are presented in this figure.

D.2 Region 2

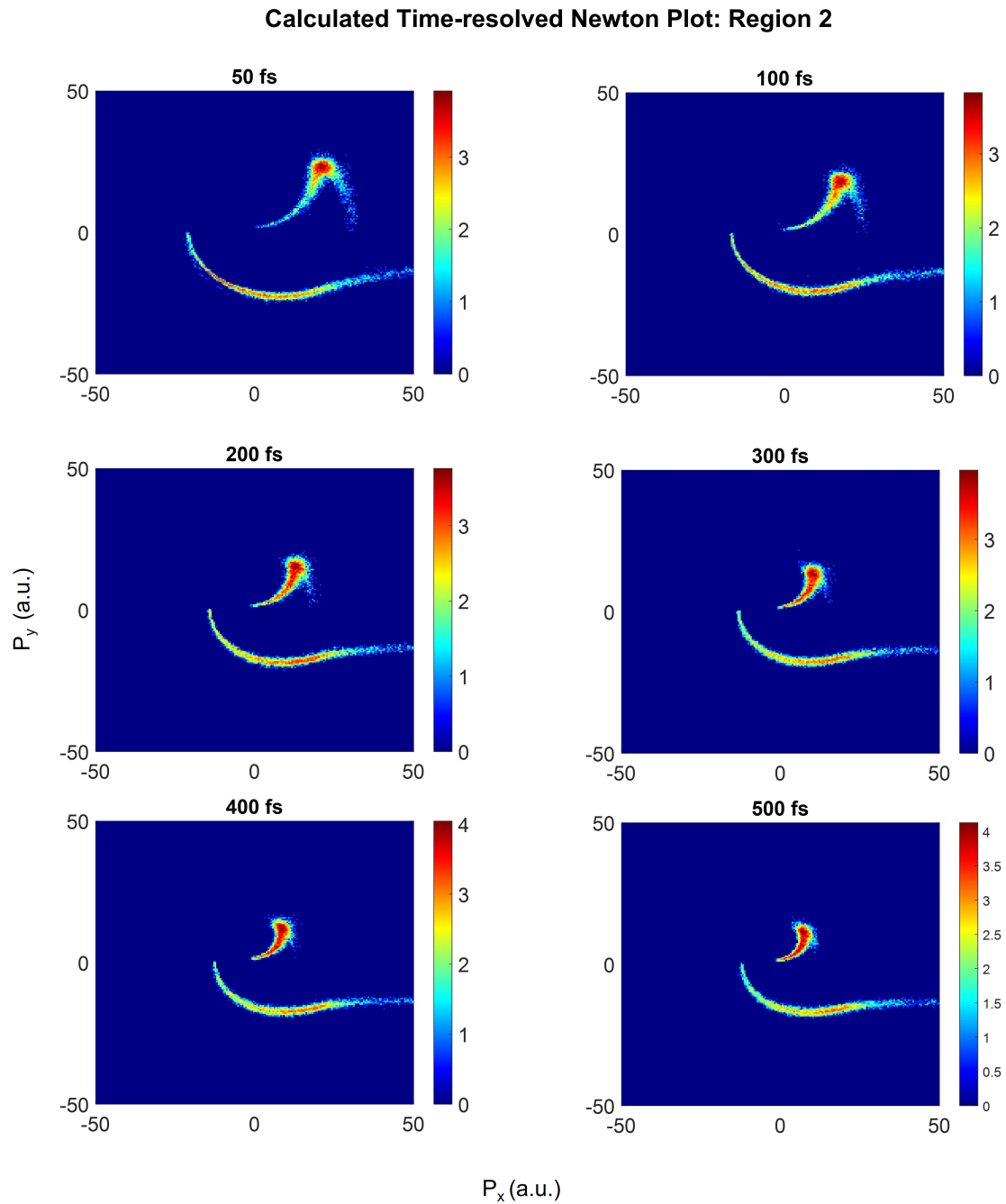


Figure D.4. Lennard-Jose Potential: By shifting the position where the potential is zero from the initial distance between CH_2 and hydrogen to 1.2 times this value, the calculated results are presented in this figure.

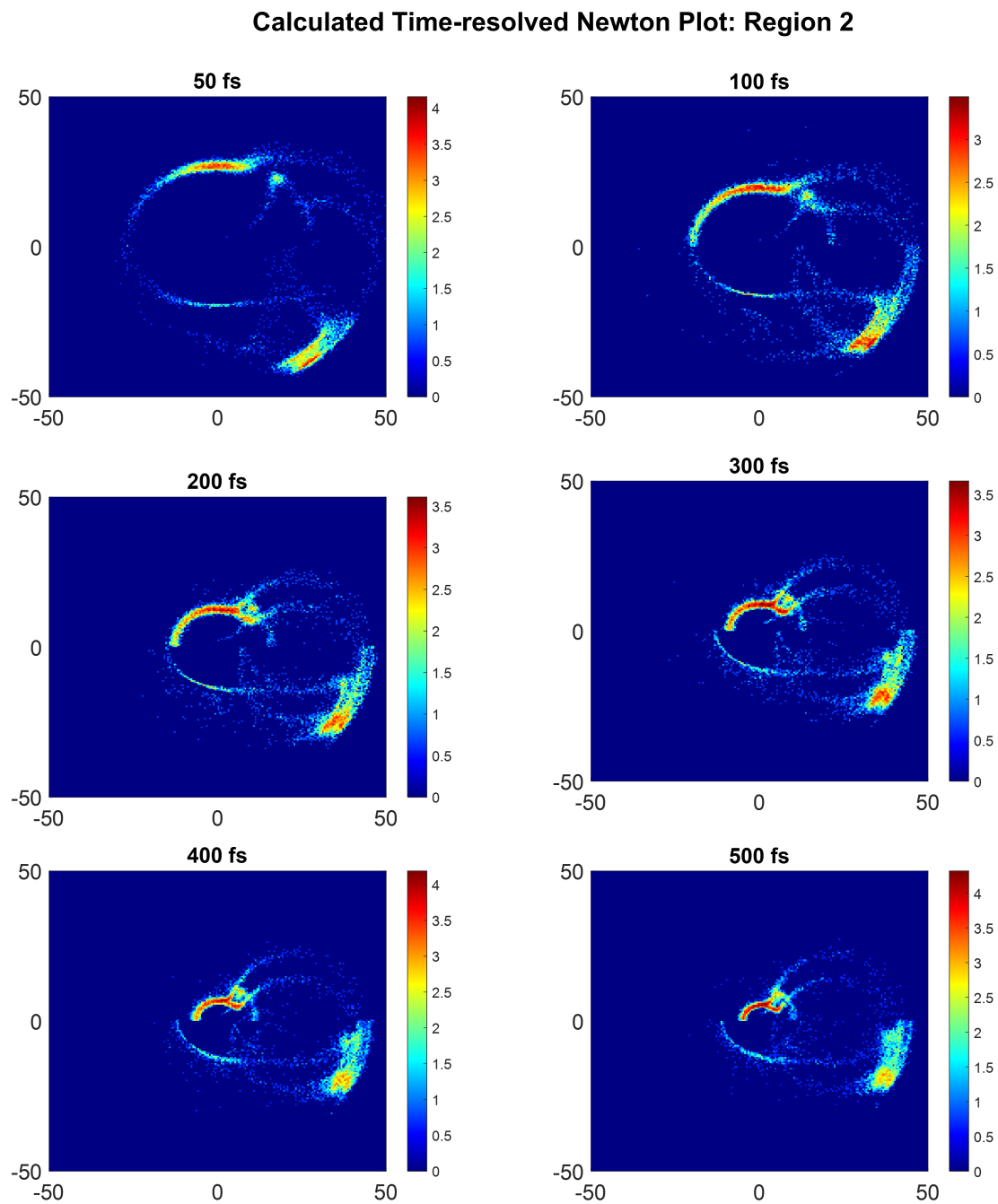


Figure D.5. Lennard-Jose Potential: By changing the depth of the potential wall from 0.03 a.u. to 0.1 a.u., the calculated results are presented in this figure.

Bibliography

- [1] R. Moshhammer, B. Feuerstein, D. Fischer, A. Dorn, C.D. Schröter, J. Deipenwisch, J. R. Crespo López-Urrutia, C. Höhr, P. Neumayer, J. Ullrich, H. Rottke, C. Trump, M. Wittmann, G. Korn, and W. Sandner. Non-sequential double ionization of ne in intense laser pulses: a coincidence experiment. *Opt. Express*, 8(7):358–367, Mar 2001.
- [2] Sylvia Berryman. Ancient Atomism. In Edward N. Zalta and Uri Nodelman, editors, *The Stanford Encyclopedia of Philosophy*. Metaphysics Research Lab, Stanford University, Fall 2008 edition, 2008.
- [3] Henry Enfield Roscoe and Arthur Harden. *A New View of the Origin of Dalton's Atomic Theory: A Contribution to Chemical History, Together with Letters and Documents Concerning the Life and Labours of John Dalton, Now for the First Time Published from Manuscript in the Possession of the Literary and Philosophical Society of Manchester*. Macmillan and Company, 1896.
- [4] J.J. Thomson. Xxiv. on the structure of the atom: an investigation of the stability and periods of oscillation of a number of corpuscles arranged at equal intervals around the circumference of a circle; with application of the results to the theory of atomic structure. *The London, Edinburgh, and Dublin Philosophical Magazine and Journal of Science*, 7(39):237–265, 1904.
- [5] E. Rutherford. Lxxix. the scattering of α and β particles by matter and the structure of the atom. *The London, Edinburgh, and Dublin Philosophical Magazine and Journal of Science*, 21(125):669–688, 1911.
- [6] N. Bohr. I. on the constitution of atoms and molecules. *The London, Edinburgh, and Dublin Philosophical Magazine and Journal of Science*, 26(151):1–25, 1913.
- [7] Michael Creutz. *Quarks, Gluons and Lattices*. Cambridge Monographs on Mathematical Physics. Cambridge University Press, 2023.
- [8] Albert Einstein. Zur Quantentheorie der Strahlung. *Phys. Z.*, 18:121–128, 1917.

- [9] T. H. MAIMAN. Stimulated optical radiation in ruby. *Nature*, 187(4736):493–494, 1960.
- [10] W. Sibbett, A. A. Lagatsky, and C. T. A. Brown. The development and application of femtosecond laser systems. *Opt. Express*, 20(7):6989–7001, Mar 2012.
- [11] Donna Strickland and Gerard Mourou. Compression of amplified chirped optical pulses. *Optics Communications*, 55(6):447 – 449, 1985.
- [12] Ahmed H. Zewail. Laser femtochemistry. *Science*, 242(4886):1645–1653, 1988.
- [13] Ahmed H. Zewail. Femtochemistry: Atomic-scale dynamics of the chemical bond. *The Journal of Physical Chemistry A*, 104(24):5660–5694, 2000.
- [14] P. B. Corkum. Plasma perspective on strong field multiphoton ionization. *Phys. Rev. Lett.*, 71:1994–1997, Sep 1993.
- [15] K. J. Schafer, Baorui Yang, L. F. DiMauro, and K. C. Kulander. Above threshold ionization beyond the high harmonic cutoff. *Phys. Rev. Lett.*, 70:1599–1602, Mar 1993.
- [16] A. McPherson, G. Gibson, H. Jara, U. Johann, T. S. Luk, I. A. McIntyre, K. Boyer, and C. K. Rhodes. Studies of multiphoton production of vacuum-ultraviolet radiation in the rare gases. *J. Opt. Soc. Am. B*, 4(4):595–601, Apr 1987.
- [17] M Ferray, A L’Huillier, X F Li, L A Lompre, G Mainfray, and C Manus. Multiple-harmonic conversion of 1064 nm radiation in rare gases. *Journal of Physics B: Atomic, Molecular and Optical Physics*, 21(3):L31, feb 1988.
- [18] Philippe Antoine, Anne L’Huillier, and Maciej Lewenstein. Attosecond pulse trains using high-order harmonics. *Phys. Rev. Lett.*, 77:1234–1237, Aug 1996.
- [19] Ferenc Krausz and Misha Ivanov. Attosecond physics. *Rev. Mod. Phys.*, 81:163–234, Feb 2009.
- [20] Stephen R. Leone. Profile of pierre agostini, anne l’huillier, and ferenc krausz: 2023 nobel laureates in physics. *Proceedings of the National Academy of Sciences*, 121(5):e2321587121, 2024.
- [21] Linda Young, Kiyoshi Ueda, Markus Gühr, Philip H Bucksbaum, Marc Simon, Shaul Mukamel, Nina Rohringer, Kevin C Prince, Claudio Masciovecchio, Michael Meyer, Artem Rudenko, Daniel Rolles, Christoph Bostedt, Matthias Fuchs, David A Reis, Robin Santra, Henry Kapteyn, Margaret Murnane, Heide Ibrahim, François

- Légaré, Marc Vrakking, Marcus Isinger, David Kroon, Mathieu Gisselbrecht, Anne L'Huillier, Hans Jakob Wörner, and Stephen R Leone. Roadmap of ultrafast x-ray atomic and molecular physics. *Journal of Physics B: Atomic, Molecular and Optical Physics*, 51(3):032003, jan 2018.
- [22] Kiyoshi Ueda, Emma Sokell, Stefan Schippers, Friedrich Aumayr, Hossein Sadeghpour, Joachim Burgdörfer, Christoph Lemell, Xiao-Min Tong, Thomas Pfeifer, Francesca Calegari, Alicia Palacios, Fernando Martin, Paul Corkum, Giuseppe Sansone, Elena V Gryzlova, Alexei N Grum-Grzhimailo, Maria Novella Piancastelli, Peter M Weber, Tobias Steinle, Kasra Amini, Jens Biegert, Nora Berrah, Edwin Kukk, Robin Santra, Alfred Müller, Danielle Dowek, Robert R Lucchese, C William McCurdy, Paola Bolognesi, Lorenzo Avaldi, Till Jahnke, Markus S Schöffler, Reinhard Dörner, Yann Mairesse, Laurent Nahon, Olga Smirnova, Thomas Schlathölder, Eleanor E B Campbell, Jan-Michael Rost, Michael Meyer, and Kazuo A Tanaka. Roadmap on photonic, electronic and atomic collision physics: I. light–matter interaction. *Journal of Physics B: Atomic, Molecular and Optical Physics*, 52(17):171001, aug 2019.
- [23] J Ullrich, R Moshhammer, A Dorn, R Dörner, L Ph H Schmidt, and H Schmidt-Böcking. Recoil-ion and electron momentum spectroscopy: reaction-microscopes. *Reports on Progress in Physics*, 66(9):1463, aug 2003.
- [24] André T. J. B. Eppink and David H. Parker. Velocity map imaging of ions and electrons using electrostatic lenses: Application in photoelectron and photofragment ion imaging of molecular oxygen. *Review of Scientific Instruments*, 68(9):3477–3484, 1997.
- [25] Till Jahnke, Sebastian Mai, Surjendu Bhattacharyya, Keyu Chen, Rebecca Boll, Maria Elena Castellani, Simon Dold, Avijit Duley, Ulrike Frühling, Alice E. Green, Markus Ilchen, Rebecca Ingle, Gregor Kastirke, Huynh Van Sa Lam, Fabiano Lever, Dennis Mayer, Tommaso Mazza, Terence Mullins, Yevheniy Ovcharenko, Björn Senfftleben, Florian Trinter, Atia Tul Noor, Sergey Usenko, Anbu Selvam Venkatachalam, Artem Rudenko, Daniel Rolles, Michael Meyer, Heide Ibrahim, and Markus Gühr. X-ray coulomb explosion imaging reveals role of molecular structure in internal conversion, 2024.
- [26] Arne Senfftleben, Thomas Pflüger, Xueguang Ren, Alexander Dorn, and Joachim Ullrich. Electron impact ionization of spatially aligned hydrogen molecules. *Journal of Physics: Conference Series*, 194(5):052021, nov 2009.

- [27] A Rudenko, B Feuerstein, K Zrost, V L B de Jesus, T Ergler, C Dimopoulou, C D Schröter, R Moshhammer, and J Ullrich. Fragmentation dynamics of molecular hydrogen in strong ultrashort laser pulses. *Journal of Physics B: Atomic, Molecular and Optical Physics*, 38(5):487, feb 2005.
- [28] Thomas Brabec and Ferenc Krausz. Intense few-cycle laser fields: Frontiers of non-linear optics. *Rev. Mod. Phys.*, 72:545–591, Apr 2000.
- [29] L. J. Frasinski, J. H. Posthumus, J. Plumridge, K. Codling, P. F. Taday, and A. J. Langley. Manipulation of bond hardening in H_2^+ by chirping of intense femtosecond laser pulses. *Phys. Rev. Lett.*, 83:3625–3628, Nov 1999.
- [30] R R Freeman and P H Bucksbaum. Investigations of above-threshold ionization using subpicosecond laser pulses. *Journal of Physics B: Atomic, Molecular and Optical Physics*, 24(2):325, jan 1991.
- [31] Andreas Fischer, Alexander Sperl, Philipp Cörlin, Michael Schönwald, Helga Rietz, Alicia Palacios, Alberto González-Castrillo, Fernando Martín, Thomas Pfeifer, Joachim Ullrich, Arne Senfleben, and Robert Moshhammer. Electron localization involving doubly excited states in broadband extreme ultraviolet ionization of H_2 . *Phys. Rev. Lett.*, 110:213002, May 2013.
- [32] J. Itatani, J. Levesque, D. Zeidler, Hiromichi Niikura, H. Pépin, J. C. Kieffer, P. B. Corkum, and D. M. Villeneuve. Tomographic imaging of molecular orbitals. *Nature*, 432(7019):867–871, 2004.
- [33] J.C. Williamson, M. Dantus, S.B. Kim, and A.H. Zewail. Ultrafast diffraction and molecular structure. *Chemical Physics Letters*, 196(6):529–534, 1992.
- [34] W Fuß, W.E Schmid, and S.A Trushin. Time-resolved dissociative intense-laser field ionization for probing dynamics: Femtosecond photochemical ring opening of 1,3-cyclohexadiene. *Journal of Chemical Physics*, 112(19):8347–8362, may 2000.
- [35] Hans Jakob Wörner and Frédéric Merkt. Jahn–teller effects in molecular cations studied by photoelectron spectroscopy and group theory. *Angewandte Chemie International Edition*, 48(35):6404–6424, 2009.
- [36] J W Rabalais, T Bergmark, L O Werme, L Karlsson, and K Siegbahn. The jahn-teller effect in the electron spectrum of methane. *Physica Scripta*, 3(1):13, jan 1971.
- [37] M. N. Paddon-Row, D. J. Fox, J. A. Pople, K. N. Houk, and David W. Pratt. Dynamic jahn-teller effect in methane radical cation. location of the transition structures

- for hydrogen scrambling and inversion. *Journal of the American Chemical Society*, 107(25):7696–7700, 1985.
- [38] Kenji Furuya, Katsumi Kimura, Yasuhiro Sakai, Toshinobu Takayanagi, and Nobuaki Yonekura. Dissociation dynamics of CH_4^+ core ion in the $2a_1$ state. *The Journal of Chemical Physics*, 101(4):2720–2728, 08 1994.
- [39] Stefanie Kerbstadt. Aufbau und charakterisierung eines hochauflösenden polarisationspulsformers für femtosekunden-superkontinua. mathesis, Carl von Ossietzky Universität Oldenburg, May 2016.
- [40] T. Zuo and A. D. Bandrauk. Charge-resonance-enhanced ionization of diatomic molecular ions by intense lasers. *Phys. Rev. A*, 52:R2511–R2514, Oct 1995.
- [41] Z. Vager, R. Naaman, and E. P. Kanter. Coulomb explosion imaging of small molecules. *Science*, 244(4903):426–431, 1989.
- [42] M. Born and R. Oppenheimer. Zur quantentheorie der molekeln. *Annalen der Physik*, 389(20):457–484, 1927.
- [43] H. A. Jahn, E. Teller, and Frederick George Donnan. Stability of polyatomic molecules in degenerate electronic states - i—orbital degeneracy. *Proceedings of the Royal Society of London. Series A - Mathematical and Physical Sciences*, 161(905):220–235, 1937.
- [44] H. A. Jahn and William Henry Bragg. Stability of polyatomic molecules in degenerate electronic states ii-spin degeneracy. *Proceedings of the Royal Society of London. Series A - Mathematical and Physical Sciences*, 164(916):117–131, 1938.
- [45] Horst Köppel, David R. Yarkony, and Heinz Barentzen, editors. *The Jahn-Teller Effect: Fundamentals and Implications for Physics and Chemistry*. Springer Series in Chemical Physics. Springer Berlin, Heidelberg, 1 edition, 2009. eBook ISBN: 978-3-642-03432-9, Hardcover ISBN: 978-3-642-03431-2, Softcover ISBN: 978-3-662-51909-7.
- [46] Isaac Bersuker. *The Jahn-Teller Effect*. Cambridge University Press, 2006.
- [47] I. B. Bersuker. Modern aspects of the jahn-teller effect theory and applications to molecular problems. *Chemical Reviews*, 101(4):1067–114, 2001. PubMed-not-MEDLINE.

- [48] Brian E. Applegate, Timothy A. Barckholtz, and Terry A. Miller. Explorations of conical intersections and their ramifications for chemistry through the jahn–teller effect. *Chem. Soc. Rev.*, 32:38–49, 2003.
- [49] Edward Condon. A theory of intensity distribution in band systems. *Phys. Rev.*, 28:1182–1201, Dec 1926.
- [50] Th. Ergler, B. Feuerstein, A. Rudenko, K. Zrost, C. D. Schröter, R. Moshhammer, and J. Ullrich. Quantum-phase resolved mapping of ground-state vibrational d_2 wave packets via selective depletion in intense laser pulses. *Phys. Rev. Lett.*, 97:103004, Sep 2006.
- [51] Tomas Ekeberg, Dameli Assalauova, Johan Bielecki, Rebecca Boll, Benedikt J. Daurer, Lutz A. Eichacker, Linda E. Franken, Davide E. Galli, Luca Gelisio, Lars Gumprecht, Laura H. Gunn, Janos Hajdu, Robert Hartmann, Dirk Hasse, Alexandr Ignatenko, Jayanath Koliyadu, Olena Kulyk, Ruslan Kurta, Markus Kuster, Wolfgang Lugmayr, Jannik Lübke, Adrian P. Mancuso, Tommaso Mazza, Carl Nettelblad, Yevheniy Ovcharenko, Daniel E. Rivas, Max Rose, Amit K. Samanta, Philipp Schmidt, Egor Sobolev, Nicusor Timneanu, Sergey Usenko, Daniel Westphal, Tamme Wollweber, Lena Worbs, Paul Lourdu Xavier, Hazem Yousef, Kartik Ayyer, Henry N. Chapman, Jonas A. Sellberg, Carolin Seuring, Ivan A. Vartanyants, Jochen Küpper, Michael Meyer, and Filipe R. N. C. Maia. Observation of a single protein by ultrafast x-ray diffraction. *Light: Science & Applications*, 13(1):15, 2024.
- [52] M. Hofmann, D. Trabert, A. Geyer, N. Anders, J. Kruse, J. Rist, L. Ph. H. Schmidt, T. Jahnke, M. Kunitski, M. S. Schöffler, S. Eckart, and R. Dörner. Subcycle resolved strong field ionization of chiral molecules and the origin of chiral photoelectron asymmetries. *Phys. Rev. Res.*, 6:043176, Nov 2024.
- [53] Enliang Wang, Nora G Kling, Aaron C LaForge, Razib Obaid, Shashank Pathak, Surjendu Bhattacharyya, Severin Meister, Florian Trost, Hannes Lindenblatt, Patrizia Schoch, Matthias Kübel, Thomas Pfeifer, Artem Rudenko, Sergio Díaz-Tendero, Fernando Martín, Robert Moshhammer, Daniel Rolles, and Nora Berrah. Ultrafast roaming mechanisms in ethanol probed by intense extreme ultraviolet free-electron laser radiation: Electron transfer versus proton transfer. *The Journal of Physical Chemistry Letters*, 14(18):4372–4380, 2023.
- [54] Komang G. Y. Arsana, Giovanni M. Saladino, Bertha Brodin, Muhammet S. Toprak, and Hans M. Hertz. Laboratory liquid-jet x-ray microscopy and x-ray fluorescence

- imaging for biomedical applications. *International Journal of Molecular Sciences*, 25(2), 2024.
- [55] Linsen Li, Yu-chen Karen Chen-Wiegart, Jiajun Wang, Peng Gao, Qi Ding, Young-Sang Yu, Feng Wang, Jordi Cabana, Jun Wang, and Song Jin. Visualization of electrochemically driven solid-state phase transformations using operando hard x-ray spectro-imaging. *Nature Communications*, 6(1):6883, 2015.
- [56] Kirsten Schnorr, Michal Belina, Sven Augustin, Hannes Lindenblatt, Yifan Liu, Severin Meister, Thomas Pfeifer, Georg Schmid, Rolf Treusch, Florian Trost, Petr Slavíček, and Robert Moshhammer. Direct tracking of ultrafast proton transfer in water dimers. *Science Advances*, 9(28):eadg7864, 2023.
- [57] Alexandra J. Feinberg, Felix Laimer, Rico Mayro P. Tanyag, Björn Senfftleben, Yevheniy Ovcharenko, Simon Dold, Michael Gatchell, Sean M. O. O’Connell-Lopez, Swetha Erukala, Catherine A. Saladrigas, Benjamin W. Toulson, Andreas Hoffmann, Ben Kamerin, Rebecca Boll, Alberto De Fanis, Patrik Grychtol, Tommaso Mazza, Jacobo Montano, Kiana Setoodehnia, David Lomidze, Robert Hartmann, Philipp Schmidt, Anatoli Ulmer, Alessandro Colombo, Michael Meyer, Thomas Möller, Daniela Rupp, Oliver Gessner, Paul Scheier, and Andrey F. Vilesov. X-ray diffractive imaging of highly ionized helium nanodroplets. *Phys. Rev. Res.*, 4:L022063, Jun 2022.
- [58] T. Jahnke, R. Guillemin, L. Inhester, S.-K. Son, G. Kastirke, M. Ilchen, J. Rist, D. Traubert, N. Melzer, N. Anders, T. Mazza, R. Boll, A. De Fanis, V. Music, Th. Weber, M. Weller, S. Eckart, K. Fehre, S. Grundmann, A. Hartung, M. Hofmann, C. Janke, M. Kircher, G. Nalin, A. Pier, J. Siebert, N. Strenger, I. Vela-Perez, T. M. Baumann, P. Grychtol, J. Montano, Y. Ovcharenko, N. Rennhack, D. E. Rivas, R. Wagner, P. Ziolkowski, P. Schmidt, T. Marchenko, O. Travnikova, L. Journal, I. Ismail, E. Kukk, J. Niskanen, F. Trinter, C. Vozzi, M. Devetta, S. Stagira, M. Gisselbrecht, A. L. Jäger, X. Li, Y. Malakar, M. Martins, R. Feifel, L. Ph. H. Schmidt, A. Czasch, G. Sansone, D. Rolles, A. Rudenko, R. Moshhammer, R. Dörner, M. Meyer, T. Pfeifer, M. S. Schöffler, R. Santra, M. Simon, and M. N. Piancastelli. Inner-shell-ionization-induced femtosecond structural dynamics of water molecules imaged at an x-ray free-electron laser. *Phys. Rev. X*, 11:041044, Dec 2021.
- [59] X. Li, A. Rudenko, M. S. Schöffler, N. Anders, Th. M. Baumann, S. Eckart, B. Erk, A. De Fanis, K. Fehre, R. Dörner, L. Foucar, S. Grundmann, P. Grychtol, A. Hartung, M. Hofmann, M. Ilchen, Ch. Janke, G. Kastirke, M. Kircher, K. Kubicek, M. Kunitzki, T. Mazza, S. Meister, N. Melzer, J. Montano, V. Music, G. Nalin, Y. Ovcharenko,

- Ch. Passow, A. Pier, N. Rennhack, J. Rist, D. E. Rivas, I. Schlichting, L. Ph. H. Schmidt, Ph. Schmidt, J. Siebert, N. Strenger, D. Trabert, F. Trinter, I. Vela-Perez, R. Wagner, P. Walter, M. Weller, P. Ziolkowski, A. Czasch, D. Rolles, M. Meyer, T. Jahnke, and R. Boll. Coulomb explosion imaging of small polyatomic molecules with ultrashort x-ray pulses. *Phys. Rev. Res.*, 4:013029, Jan 2022.
- [60] Chelsea E. Liekhus-Schmaltz, Ian Tenney, Timur Osipov, Alvaro Sanchez-Gonzalez, Nora Berrah, Rebecca Boll, Cedric Bomme, Christoph Bostedt, John D. Bozek, Sebastian Carron, Ryan Coffee, Julien Devin, Benjamin Erk, Ken R. Ferguson, Robert W. Field, Lutz Foucar, Leszek J. Frasinski, James M. Glowia, Markus Gühr, Andrei Kamalov, Jacek Krzywinski, Heng Li, Jonathan P. Marangos, Todd J. Martinez, Brian K. McFarland, Shungo Miyabe, Brendan Murphy, Adi Natan, Daniel Rolles, Artem Rudenko, Marco Siano, Emma R. Simpson, Limor Spector, Michele Swiggers, Daniel Walke, Song Wang, Thorsten Weber, Philip H. Bucksbaum, and Vladimir S. Petrovic. Ultrafast isomerization initiated by x-ray core ionization. *Nature Communications*, 6(1):8199, 2015.
- [61] J. Berkowitz, J. P. Greene, H. Cho, and B. Ruscić. The ionization potentials of CH_4 and CD_4 . *The Journal of Chemical Physics*, 86(2):674–676, 01 1987.
- [62] Donald A. McQuarrie and John D. Simon. *Physical Chemistry: A Molecular Approach*. University Science Books, Sausalito, Calif., 1997. Includes index.
- [63] C. R. Brundle, M. B. Robin, and Harold Basch. Electronic energies and electronic structures of the fluoromethanes. *The Journal of Chemical Physics*, 53(6):2196–2213, 09 1970.
- [64] Yasuhito Ohta and Koji Ohta. Interconversion behavior of the C-H bond in the CH_2 radical cation: Ab initio molecular dynamics study. *Journal of Computational Chemistry*, 25(15):1910–1919, 2004.
- [65] Cayo E. M. Gonçalves, R. D. Levine, and F. Remacle. Ultrafast geometrical reorganization of a methane cation upon sudden ionization: an isotope effect on electronic non-equilibrium quantum dynamics. *Phys. Chem. Chem. Phys.*, 23:12051–12059, 2021.
- [66] M. Li, M. Zhang, O. Vendrell, Z. Guo, Q. Zhu, X. Gao, L. Cao, K. Guo, Q. Q. Su, W. Cao, S. Luo, J. Yan, Y. Zhou, Y. Liu, Z. Li, and P. Lu. Ultrafast imaging of spontaneous symmetry breaking in a photoionized molecular system. *Nature Communications*, 12(1):4233, Jul 2021.

- [67] Enrico Ridente, Diptarka Hait, Eric A. Haugen, Andrew D. Ross, Daniel M. Neumark, Martin Head-Gordon, and Stephen R. Leone. Femtosecond symmetry breaking and coherent relaxation of methane cations via x-ray spectroscopy. *Science*, 380(6646):713–717, 2023.
- [68] E Kukk, G Prümper, R Sankari, M Hoshino, C Makochekanwa, M Kitajima, H Tanaka, H Yoshida, Y Tamenori, E Rachlew, and K Ueda. Electronic state dependence in the dissociation of core-ionized methane. *Journal of Physics B: Atomic, Molecular and Optical Physics*, 40(18):3677, sep 2007.
- [69] Jyoti Rajput, Diksha Garg, A. Cassimi, X. Fléchar, J. Rangama, and C. P. Safvan. Addressing three-body fragmentation of methane dication using “native frames”: Evidence of internal excitation in fragments. *The Journal of Chemical Physics*, 159(18):184303, 11 2023.
- [70] Y. Zhang, B. Wang, L. Wei, T. Jiang, W. Yu, R. Hutton, Y. Zou, L. Chen, and B. Wei. Proton migration in hydrocarbons induced by slow highly charged ion impact. *The Journal of Chemical Physics*, 150(20):204303, 05 2019.
- [71] Jyoti Rajput, Diksha Garg, A. Cassimi, A. Méry, X. Fléchar, J. Rangama, S. Guilous, W. Iskandar, A. N. Agnihotri, J. Matsumoto, R. Ahuja, and C. P. Safvan. Unexplained dissociation pathways of two-body fragmentation of methane dication. *The Journal of Chemical Physics*, 156(5):054301, 02 2022.
- [72] R Flammini, M Satta, E Fainelli, G Alberti, F Maracci, and L Avaldi. The role of the methyl ion in the fragmentation of CH_2^{2+} . *New Journal of Physics*, 11(8):083006, aug 2009.
- [73] Sydney Leach. State-to-state studies of the dissociation of doubly-charged molecular cations: methane dication revisited. *Journal of Molecular Structure*, 157(1):197–214, 1987.
- [74] Y. Zhang, T. Jiang, L. Wei, D. Luo, X. Wang, W. Yu, R. Hutton, Y. Zou, and B. Wei. Three-body fragmentation of methane dications produced by slow Ar^{8+} -ion impact. *Phys. Rev. A*, 97:022703, Feb 2018.
- [75] Heide Ibrahim, Catherine Lefebvre, André D Bandrauk, André Staudte, and François Légaré. H_2 : the benchmark molecule for ultrafast science and technologies. *Journal of Physics B: Atomic, Molecular and Optical Physics*, 51(4):042002, jan 2018.
- [76] Jon H. Shirley. Solution of the schrödinger equation with a hamiltonian periodic in time. *Phys. Rev.*, 138:B979–B987, May 1965.

- [77] S. Chu. Floquet theory and complex quasivibrational energy formalism for intense field molecular photodissociation. *Journal of Chemical Physics*, 75(5):2215–2221, 1981.
- [78] Domagoj Pavicic. *Coulomb Explosion and Intense-Field Photodissociation of Ion-Beam H₂⁺ and D₂⁺*. PhD thesis, Ludwig-Maximilians-Universität München, April 2004.
- [79] G. Jolicard and O. Atabek. Above-threshold-dissociation dynamics of h₂⁺ with short intense laser pulses. *Phys. Rev. A*, 46:5845–5855, Nov 1992.
- [80] A. Giusti-Suzor, X. He, O. Atabek, and F. H. Mies. Above-threshold dissociation of h₂⁺ in intense laser fields. *Phys. Rev. Lett.*, 64:515–518, Jan 1990.
- [81] F. Légaré, I. V. Litvinyuk, P. W. Dooley, F. Quéré, A. D. Bandrauk, D. M. Villeneuve, and P. B. Corkum. Time-resolved double ionization with few cycle laser pulses. *Phys. Rev. Lett.*, 91:093002, Aug 2003.
- [82] A. S. Alnaser, T. Osipov, E. P. Benis, A. Wech, B. Shan, C. L. Cocke, X. M. Tong, and C. D. Lin. Rescattering double ionization of d₂ and h₂ by intense laser pulses. *Phys. Rev. Lett.*, 91:163002, Oct 2003.
- [83] Patrick Froß. *Electron-nuclear correlation, singly-excited Rydberg states and electron emission asymmetry in multiphoton ionization of H₂*. PhD thesis, Ruperto-Carola-University of Heidelberg, Germany, 2020.
- [84] Nicolas Camus. *Non-sequential double ionization of atoms with phase-controlled ultra-short laser pulses*. PhD thesis, Ruperto-Carola-University of Heidelberg, Germany, 2013.
- [85] Lutz Fechner. *High-resolution experiments on strong-field ionization of atoms and molecules: test of tunneling theory, the role of doubly excited states, and channel-selective electron spectra*. PhD thesis, Ruperto-Carola-University of Heidelberg, Germany, 2014.
- [86] R. Thurston, J. Heritage, A. Weiner, and W. Tomlinson. Analysis of picosecond pulse shape synthesis by spectral masking in a grating pulse compressor. *IEEE Journal of Quantum Electronics*, 22(5):682–696, 1986.
- [87] A. M. Weiner, J. P. Heritage, and E. M. Kirschner. High-resolution femtosecond pulse shaping. *J. Opt. Soc. Am. B*, 5(8):1563–1572, Aug 1988.

- [88] A.M. Weiner, D.E. Leaird, J.S. Patel, and J.R. Wullert. Programmable shaping of femtosecond optical pulses by use of 128-element liquid crystal phase modulator. *IEEE Journal of Quantum Electronics*, 28(4):908–920, 1992.
- [89] Matthias Wollenhaupt, Andreas Assion, and Thomas Baumert. *Femtosecond Laser Pulses: Linear Properties, Manipulation, Generation and Measurement*, pages 937–983. Springer New York, New York, NY, 2007.
- [90] Geoffrey New. *Introduction to Nonlinear Optics*. Cambridge University Press, 2011.
- [91] M. E. Fermann, V. da Silva, D. A. Smith, Y. Silberberg, and A. M. Weiner. Shaping of ultrashort optical pulses by using an integrated acousto-optic tunable filter. *Opt. Lett.*, 18(18):1505–1507, Sep 1993.
- [92] Erik Zeek, Kira Maginnis, Sterling Backus, Ulrich Russek, Margaret Murnane, Gérard Mourou, Henry Kapteyn, and Gleb Vdovin. Pulse compression by use of deformable mirrors. *Opt. Lett.*, 24(7):493–495, Apr 1999.
- [93] J. Agostinelli, G. Harvey, T. Stone, and C. Gabel. Optical pulse shaping with a grating pair. *Appl. Opt.*, 18(14):2500–2504, Jul 1979.
- [94] J. Desbois, F. Gires, and P. Turnois. A new approach to picosecond laser pulse analysis shaping and coding. *IEEE Journal of Quantum Electronics*, 9(2):213–218, 1973.
- [95] Jenoptik Optical Systems HmbH, Goeschwitzer Strasse 25, 07745 Jena. *SLM-S640d USB/Ethernet*, jan 2018.
- [96] S. Kerbstadt, K. Eickhoff, T. Bayer, and M. Wollenhaupt. Odd electron wave packets from cycloidal ultrashort laser fields. *Nature Communications*, 10(1):658, 2019.
- [97] David E. Goldberg. *Genetic Algorithms in Search, Optimization and Machine Learning*. Addison-Wesley Longman Publishing Co., Inc., USA, 1st edition, 1989.
- [98] Hans-Paul Schwefel. Evolution and optimum seeking. In *Sixth-generation computer technology series*, 1995.
- [99] P. Neining, M. Mikulla, P. Döring, M. Dammann, F. Thome, S. Krause, D. Schwantuschke, P. Brückner, C. Friesicke, and R. Quay. Advances in gan devices and circuits at higher mm-wave frequencies. *e-Prime - Advances in Electrical Engineering, Electronics and Energy*, 4:100177, 2023.
- [100] J. Ajayan and D. Nirmal. A review of inp/inalas/ingaas based transistors for high frequency applications. *Superlattices and Microstructures*, 86:1–19, 2015.

- [101] Daniel J. Kane and Rick Trebino. Single-shot measurement of the intensity and phase of an arbitrary ultrashort pulse by using frequency-resolved optical gating. *Opt. Lett.*, 18(10):823–825, May 1993.
- [102] Peter Baum and Eberhard Riedle. Design and calibration of zero-additional-phase spider. *J. Opt. Soc. Am. B*, 22(9):1875–1883, Sep 2005.
- [103] J. Itatani, F. Quéré, G. L. Yudin, M. Yu. Ivanov, F. Krausz, and P. B. Corkum. Attosecond streak camera. *Phys. Rev. Lett.*, 88:173903, Apr 2002.
- [104] Joachim Ullrich and Viatcheslav Shevelko, editors. *Many-Particle Quantum Dynamics in Atomic and Molecular Fragmentation*, volume 1 of *Springer Series on Atomic, Optical, and Plasma Physics*. Springer Berlin, Heidelberg, 1 edition, 2003. Published: 23 July 2003, Hardcover ISBN: 978-3-540-00667-1, Softcover ISBN: 978-3-642-05626-0, eBook ISBN: 978-3-662-08492-2.
- [105] R. Dörner, V. Mergel, O. Jagutzki, L. Spielberger, J. Ullrich, R. Moshhammer, and H. Schmidt-Böcking. Cold target recoil ion momentum spectroscopy: a ‘momentum microscope’ to view atomic collision dynamics. *Physics Reports*, 330(2):95–192, 2000.
- [106] Horst Schmidt-Böcking, Joachim Ullrich, Reinhard Dörner, and Charles Lewis Cocke. The coltrims reaction microscope—the spyhole into the ultrafast entangled dynamics of atomic and molecular systems. *Annalen der Physik*, 533(9):2100134, 2021.
- [107] Nicolas Camus. Komponenten eines reaktionsmikroskops.
- [108] RoentDek Handels GmbH. *The fADC8 fast sampling ADC unit*. Accessed: 20.07.2020.
- [109] Jyoti Rajput, T. Severt, Ben Berry, Bethany Jochim, Peyman Feizollah, Balram Kaderiya, M. Zohrabi, U. Ablikim, Farzaneh Ziaee, Kanaka Raju P., D. Rolles, A. Rudenko, K. D. Carnes, B. D. Esry, and I. Ben-Itzhak. Native frames: Disentangling sequential from concerted three-body fragmentation. *Phys. Rev. Lett.*, 120:103001, Mar 2018.
- [110] Elias Abboud. Viviani’s theorem and its extension. *The College Mathematics Journal*, 41(3):203–211, 2010. Full publication date: May 2010.
- [111] Ulrich Galster, Frank Baumgartner, Ulrich Müller, Hanspeter Helm, and Martin Jungen. Experimental and quantum-chemical studies on the three-particle fragmentation of neutral triatomic hydrogen. *Phys. Rev. A*, 72:062506, Dec 2005.

- [112] M Schulz, D Fischer, T Ferger, R Moshhammer, and J Ullrich. Four-particle dalitz plots to visualize atomic break-up processes. *Journal of Physics B: Atomic, Molecular and Optical Physics*, 40(15):3091, jul 2007.
- [113] Kazuki Yoshikawa, Manabu Kanno, Hao Xue, Naoki Kishimoto, Soki Goto, Fukiko Ota, Yoshiaki Tamura, Florian Trinter, Kilian Fehre, Leon Kaiser, Jonathan Stindl, Dimitrios Tsitsonis, Markus Schöffler, Reinhard Dörner, Rebecca Boll, Benjamin Erk, Tommaso Mazza, Terence Mullins, Daniel E. Rivas, Philipp Schmidt, Sergey Usenko, Michael Meyer, Enliang Wang, Daniel Rolles, Artem Rudenko, Edwin Kukk, Till Jahnke, Sergio Díaz-Tendero, Fernando Martín, Keisuke Hatada, and Kiyoshi Ueda. Time-resolved photoelectron diffraction imaging of methanol photodissociation involving molecular hydrogen ejection. *Phys. Chem. Chem. Phys.*, 26:25118–25130, 2024.
- [114] Ulrich Wiedemann. Zeitaufgelöste experimente zur fragmentationsdynamik von ch₄ in intensiven, ultra-kurzen laserpulsen. Diplomathesis, Ruperto-Carola-University of Heidelberg, Germany, January 2007.
- [115] C. J. Proctor, C. J. Porter, T. Ast, P. D. Bolton, and J. H. Beynon. Charge stripping reactions of ions formed from methane, ammonia, water and hydrogen sulphide by protonation and by electron impact. *Organic Mass Spectrometry*, 16(10):454–458, 1981.
- [116] Leonardo Baptista and Enio F. da Silveira. A theoretical study of three gas-phase reactions involving the production or loss of methane cations. *Phys. Chem. Chem. Phys.*, 16:21867–21875, 2014.
- [117] Chuanpeng Cao, Min Li, Keyu Guo, Zichen Li, Yang Liu, Yupeng Liu, Kunlong Liu, Yueming Zhou, and Peixiang Lu. Intensity-dependent three-body coulomb explosion of methane in femtosecond laser pulses. *Phys. Rev. A*, 109:023115, Feb 2024.
- [118] D. Mathur, C. Badrinathan, F.A. Rajgara, and U.T. Raheja. Translational energy loss spectrometry of molecular dications from methane. *Chemical Physics*, 103(2):447–459, 1986.
- [119] Y Levy, A Bar-David, I Ben-Itzhak, I Gertner, and B Rosner. Formation of long-lived c₂²⁺ and ch₂²⁺ dications. *Journal of Physics B: Atomic, Molecular and Optical Physics*, 32(15):3973, aug 1999.
- [120] Florian Trost. *Time-resolved Fragmentation of Diiodomethane studied in an XUV Pump-Probe Experiment*. PhD thesis, Ruperto-Carola-University of Heidelberg, Germany, May 2023.

- [121] Takeshi Oka. H_3^+ , the ideal probe for *in situ* measurement of the galactic cosmic rays. *Philosophical Transactions of the Royal Society A: Mathematical, Physical and Engineering Sciences*, 377(2154):20180402, 2019.
- [122] Tomoya Okino, Yusuke Furukawa, Peng Liu, Takayuki Ichikawa, Ryuji Itakura, Kenosuke Hoshina, Kaoru Yamanouchi, and Hidetoshi Nakano. Coincidence momentum imaging of ultrafast hydrogen migration in methanol and its isotopomers in intense laser fields. *Chemical Physics Letters*, 423(1):220–224, 2006.
- [123] Kennosuke Hoshina, Yusuke Furukawa, Tomoya Okino, and Kaoru Yamanouchi. Efficient ejection of h_3^+ from hydrocarbon molecules induced by ultrashort intense laser fields. *The Journal of Chemical Physics*, 129(10):104302, 09 2008.
- [124] N. Kotsina, S. Kaziannis, and C. Kosmidis. Hydrogen migration in methanol studied under asymmetric fs laser irradiation. *Chemical Physics Letters*, 604:27–32, 2014.
- [125] Nagitha Ekanayake, Travis Severt, Muath Nairat, Nicholas P. Weingartz, Benjamin M. Farris, Balram Kaderiya, Peyman Feizollah, Bethany Jochim, Farzaneh Ziaee, Kurtis Borne, Kanaka Raju P., Kevin D. Carnes, Daniel Rolles, Artem Rudenko, Benjamin G. Levine, James E. Jackson, Itzik Ben-Itzhak, and Marcos Dantus. H_2 roaming chemistry and the formation of h_3^+ from organic molecules in strong laser fields. *Nature Communications*, 9(1):5186, 2018.
- [126] D. Townsend, S. A. Lahankar, S. K. Lee, S. D. Chambreau, A. G. Suits, X. Zhang, J. Rheinecker, L. B. Harding, and J. M. Bowman. The roaming atom: Straying from the reaction path in formaldehyde decomposition. *Science*, 306(5699):1158–1161, 2004.
- [127] Joel M. Bowman and Arthur G. Suits. Roaming reactions: The third way. *Physics Today*, 64(11):33–37, 11 2011.
- [128] Yu Zhang, Baihui Ren, Chuan-Lu Yang, Long Wei, Bo Wang, Jie Han, Wandong Yu, Yueying Qi, Yaming Zou, Li Chen, Enliang Wang, and Baoren Wei. Formation of h_3^+ from ethane dication induced by electron impact. *Communications Chemistry*, 3(1):160, 2020.
- [129] Kennosuke Hoshina, Yusuke Furukawa, Tomoya Okino, and Kaoru Yamanouchi. Efficient ejection of h_3^+ from hydrocarbon molecules induced by ultrashort intense laser fields. *The Journal of Chemical Physics*, 129(10):104302, 09 2008.

Acknowledgements

Looking back on these five years, this thesis would never have been possible without the unwavering support of so many people. Everyone's door was always open to me, and I still struggle to find the right words to express how incredible that has been. I have been truly spoiled by all of you. It must be luck that brought me here—because otherwise, I could never have deserved such kindness and generosity.

- **Robert Moshhammer:** Before anyone else, I need to warmly and wholeheartedly thank Robert. As my *Doktorvater*, his outstanding talent, rigorous scientific attitude, and great passion for physics have profoundly shaped my scientific taste. His unique personality, open-mindedness, and kindness created the best 'bubble' in reality (not our 'bubble chamber' this time) to protect me over the years. With the bubble, I own all the freedom to do science work and all the freedom to express myself in any sense. Spending time with Robert is always an adventure, full of surprises (Of course, both sides of surprises, but both are amazing!). He deserves the best acknowledgment (as I promised to him), but at this moment, I only wish I were a novelist so I could express myself better.
- **Thomas Pfeifer:** Thank you, Thomas! Your immense passion for physics, endless patience, limitless ideas, talent for encouragement, and remarkable understanding have made this thesis possible. I have truly enjoyed being part of the division you have built. I have no idea how you manage to take care of everyone and everything so effortlessly—you are as incredible as you are every single day.
- **Claus Dieter Schröter:** No words can capture how impossible it is for anyone to be like Claus Dieter. He is more than just a dictionary of experimental details—without him, no setup would have kept running for this long. Beyond his professional expertise, his kindness, humor, sincerity, spirit, and selflessness make him the most reliable person I know. Without his care, I would not be as happy as I am today.
- **Alexander Dorn:** Without Alexander, everything I wrote would have been wrong. His kindness and support have been invaluable, and I am truly grateful for how much he has helped and spoiled me (including I may have 'borrowed' his milk twice or

three times). I know I can always count on him for assistance. In addition, I must admit—I am jealous of his skiing speed and skills.

- **José Crespo:** Talking to you has always been a pleasure. Your kindness and care, even in the smallest moments, have warmed my heart and encouraged me. I truly appreciate the effort you put into making everyone happier while always offering valuable suggestions.
- **Michael Schulz:** Not only for being a great neighbor next door but also for sharing your insights on CSR experiments and collision physics, which I had no prior knowledge of.
- **Christian Ott:** Thanks for Christian always being around. Not only did he allow me to join the wonderful $\omega - 2\omega$ beamtime, but also for his endless ideas of helium.
- **Wolfgang Quint, Tristan Bereau, and Joao Seco:** Thank you, Wolfgang, for agreeing to be the second referee for this thesis. I am also grateful to Tristan Bereau and Joao Seco for kindly joining my exam committee.
- **Divya:** Without you, Divya, I would have been thousands of times more miserable than I am. You always listen to me, no matter what I am talking about. I cannot think of anyone else who supports me every single day in everything. With you, I never have to pretend to be a better person—something that is not often the case. No matter where you go in the future, I will always wish you the very best.
- **Cristian:** Thank you, Cristian, for always being there whenever I needed help. You bring happiness to everyone and everywhere. Your creativity makes you special wherever you go.
- **Deepthy:** Thank you, Deepthy, for patiently listening to all my ramblings and for sharing everything with me, whether in the office or on the bus.
- **Felix:** Thank you, Felix, for enduring the tough beamtimes with me and for always sharing fun facts. I must have taken at least ten times as many cookies from you!
- **Nikolas:** Thank you, Nikolas, for being my office mate. You had to put up with my absence in the lab during my writing phase, read my thesis, translate my abstracts, and listen to my endless complaints about everything.
- **David:** Thanks, David, for enduring my sadness, anxiety, complaints, endless talking, and bad tempers in the lab. You have witnessed my worst moods and still supported me unconditionally.

- **Florian:** Thank you, Florian, for sharing and teaching me the code I used for simulations. Beyond that, talking to you has always been a pleasure—you are always organized, open-minded, and humorous.
- **Hannes:** Thank you, Hannes, for checking in on my thesis progress from time to time. Discussing physics, coding, and life with you has always been a pleasure.
- **Gergana:** Thank you, Gergana, for always being so positive about my work. Every time after my group seminar, you are always the one giving very positive feedback!
- **Marta:** Thank you for tolerating me as a noisy neighbor and putting up with all the disturbances I caused. Of course, I am also deeply grateful for your constant support and care!
- **Denhi, Hemkumar, and Patrick:** Thanks for introducing me to the lab and the group at the beginning. It was nice to know you!
- **Ranko Grimm, Alexander Von der Dellen, Christian Kaiser, and their co-workers:** Thank you for your technical support, which ensured the success of our experiments.
- **My café table members:** Thank you all for having coffee with me every day. The name list is so long but I remember you all. I cherish our completely divergent topics including physics, bureaucracy, fiction, gossip, and philosophy. You recharge me daily with laughter. So, Robert, I am still waiting for you.
- **My thesis proofreading team:** Special thanks to Alexander Dorn, Divya, Michael, Deepthy, Cristian, Nikolas, Alexander Magunia, Gergana, Marta, Hannes, André, Siddiki, and Chunhai for reading my thesis!

I need to write this acknowledgment at length to say that everyone at MPIK has created the perfect ‘bubble’ for me. Everyone has tried to protect me and support me. Saying ‘thank you’ feels too short to describe how much I owe you all and how much I cherish you. It has been my greatest privilege to meet you all in the best years of my life. The meaning of this thesis extends beyond being a scientific report—it serves as a reminder of the immense support I have received along the way.

- A special thanks to **Kiyoshi Ueda:** I don’t know how you manage to be so amazing at arranging things, taking care of everyone, and helping with physics. I deeply respect you and hope we can work together in the future.
- **Françoise Remacle:** for being interested in the methane project and would like to correlate with me. Of course, thanks to my theoretical teams, they are: **Pandey Gaurav, Manabu Kanno, and Naoki Kishimoto.**

- Beyond my colleagues at work, there are several people I must thank: **Chunhai Lyu, Li Han, Yu He, Shuyuan Hu, Zhiqiu Huang, Zheng Gong, Huixian Li, and Peilun He**. You have filled my life with warmth and support in a foreign country.
- Thank you to **Yifan Wang**, who is far away on the other side of the world but always close to me in spirit.
- Thanks to my family, especially my mother, who is the best mom in my eyes.
- A very deep and special thanks to **Jianshun Gao**, who not only ensured that I was well-fed so that I could finish this thesis but also shared all my happiness and tears—both in the past and in the future. There are no words to express why and how.